Dissertation

submitted to the

Combined Faculty of Natural Sciences and Mathematics

of Heidelberg University, Germany

for the degree of

Doctor of Natural Sciences

Put forward by

M.Sc. Kaustav Dey

born in: Kolkata, India

Oral examination: 20-10-2021

Single-crystal growth, Magnetic and Thermodynamic Investigations of Ilmenite Titanates and Lanthanum Nickelates

Referees: Prof. Dr. Rüdiger Klingeler

Prof. Dr. Maurits W. Haverkort

Abstract

This work presents the single-crystal growth of the ilmenite titanates $M\text{TiO}_3$ (M = Co, Ni) and the perovskite-nickelate LaNiO_3 and their detailed magnetic, structural and thermodynamic investigations. All the single crystals were grown using the floating-zone technique in a four-mirror and a high-pressure optical furnace respectively. Detailed characterization of the LaNiO_3 single-crystals solves the ambiguity concerning its magnetic ground state and emphasizes the importance of oxygen-vacancy defects in nickelates. The full magnetic phase diagram of the easy-plane type NiTiO_3 and CoTiO_3 is constructed for the first time using high-field dilatometry and magnetization measurements. The thermal expansion studies indicate strong magnetoelastic coupling in titanates and Grüneisen analysis yields the corresponding pressure dependencies. The comparison of neutron diffraction, dilatometry and dielectric data indicates the presence of significant magneto-electric coupling in NiTiO_3 and of magneto-dielectric coupling in CoTiO_3. Magnetostriction measurements in the easy-plane exhibit significant lattice changes in low-fields due to domain-rearrangement processes and furthermore show remarkable effects of changing the uniaxial pressure which is also attributable to domain effects. In addition, the crystal growth and magneto-structural characterization of MnTiO_3, $\text{Ni}_{0.25}\text{Mn}_{0.75}\text{TiO}_3$ and $\text{La}_4\text{Ni}_3\text{O}_{10}$ are presented.

Zusammenfassung

Die vorliegende Arbeit beschreibt die Kristallzüchtung der Ilmenit-Titanate $M\mathrm{TiO_3}$ (M = Co, Ni) sowie des Perovskit-Nickelats $\mathrm{LaNiO_3}$ und deren detaillierte magnetische, strukturelle und thermodynamische Untersuchung. Die Einkristalle wurde mithilfe des Zonenschmelzverfahrens in einem konventionallen bzw. einem Hochdruckkristallofen gezüchtet. Die detaillierte Charakterisierung der $\mathrm{LaNiO_3}$ Einkristalle liefert den magnetischen Grundzustand und verdeutlicht den Einfluss von Sauerstoff-Defekten in Nickelaten. Darüber hinaus wird mittels Hochfeld-Dilatometrie und Magnetisierungsmessungen erstmalig die magnetischen Phasendiagramme von $\mathrm{NiTiO_3}$ und $\mathrm{CoTiO_3}$. Die Messungen der thermischen Ausdehnung zeigen eine starke magnetoelastische Kopplung in beiden Titanaten und erlaubt die Bestimmung der jeweiligen Druck-abhängigkeiten mittels Grüneisenanalyse. Der Vergleich der Ergebnisse aus Neutronenstreuung, Dilatometrie und dielektrishcen Messungen zeigt eine signifikante magneto-elektrische Kopplung in $\mathrm{NiTiO_3}$ und belegt die magneto-dielektrische Kopplung in $\mathrm{CoTiO_3}$. Magnetostriktionsmessungen in der leichten Magnetisierungsebene zeigen signifikante Gitterveränderungen in niedrigen Feldern, sowie beachtliche Effekte bei Veränderung des angelegten uniaxialen Druckes, die jeweils durch Domäneneffekte erklärt werden können. Neben den genannten Materialien werden zudem Ergebnisse zur Kristallzüchtung des magneto-elektischen $\mathrm{MnTiO_3}$, von $\mathrm{Ni_{0.25}Mn_{0.75}TiO_3}$ und $\mathrm{La_4Ni_3O_{10}}$ sowie deren magnetische und structurelle Charakterisierung gezeigt.

Contents

Chapter 1

Introduction and background

Transition Metal Oxides (TMOs) are one of the most interesting and widely studied solid systems in which strong electron correlations results in highly exciting and exotic properties [1]. As per Alexandradinata *et al.* [2] a strongly correlated electron system is one in which "*the interactions are so strong or have a character such that theories based on the underlying original bare particles fail even to qualitatively describe the material properties*". The current challenge is that we cannot reliably predict the properties of strongly correlated electron materials. Fortunately for many materials such as purely ionic solids or in some ideal metallic systems where conduction electron screen the long-ranged coulomb interaction, the main properties could be explained using simple models (e.g. free electron Fermi gas) or taking into account a low order approximation (e.g. Fermi liquid theory, exchange interactions in magnetism). However, the presence of strong correlations invalidates such simple models and results in so-called emergent phenomena. In transition metal oxides with outermost d-electrons, unique features and complex collective behaviour arise due to the mutual coupling and competition between charge, spin, orbit and lattice degrees of freedom as shown in Fig. 1.1. As a result, one can find TMOs which are either metallic (eg. $LaNiO_3$, RuO_2) or purely insulating (eg. $BaTiO_3$) in nature, also oxides which show both metallic and insulating properties at different temperatures (e.g. V_2O_3) [1] and oxides with various kinds of spin, charge and orbital ordering (e.g. manganites) [3, 4]. One of the most fascinating discoveries of 20th century is that of high-T_c superconductivity in cuprates by Bednorz and Müller in 1986 [5], which had garnered world-wide attention. It has been more than three decades of intense research effort since then and our understanding of high-T_c still remains inadequate. Apart from the high-T_c's newer research directions based on entanglement and topology [6] in quantum materials such as quantum spin-liquids, quantum criticality and correlated topological materials have emerged. This only indicates that strongly correlated electron problem is going to be one of the central problems in physics for the decades to come [2].

Apart from obvious fundamental interests as mentioned above, TMOs also have far reach-
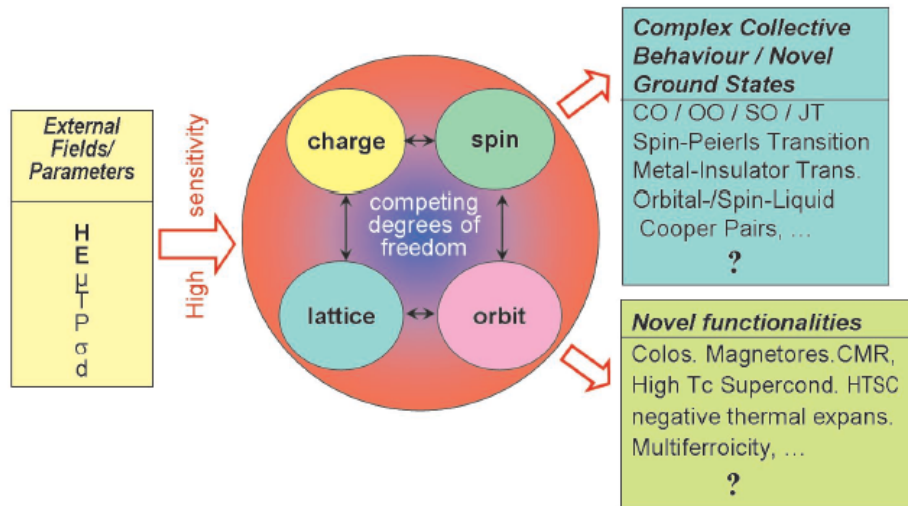
Figure 1.1. Schematic depiction of various possible complex emergent behaviour arising in strongly correlated systems. H, E : magnetic and electric field respectively; μ: chemical potential (doping); T: temperature; P: pressure; σ: strain; d: dimensionality as in bulk vs thin-films; CO: charge order; OO: orbital order; SO: spin-order; JT: Jahn-Teller transition. Taken from Ref. [7]

ing functionalities and applications for the mankind. According to the nobel laureate John B. Goodenough, engineering the transition metal oxides to optimize a given application depends on the understanding of few general concepts such as - (i) the role of the covalent component of the d-orbital bonding; (ii) cooperative static and dynamic d orbital ordering; and (iii) the characteristic transition from localized to itinerant d electron behaviour [8]. One of the famous examples, the discovery of the giant-magnetoresistance (GMR) in magnetic multilayers composed of transition metals formed an important step towards industry application [9, 10]. The emerging field of spintronics and orbitronics which exploits the effect of external magnetic field on electronic spin, charge and d-electron orbital states, and thereby controlling the electric current, are great avenues which aim to transform the future of electronics [3].

In this thesis, two different classes of TMOs namely the lanthanum nickelates (LaNiO$_3$, La$_4$Ni$_3$O$_{10}$) and ilmenite titanates MTiO$_3$ (M = Co, Ni, Mn, Ni$_{0.25}$Mn$_{0.75}$) are investigated. While LaNiO$_3$ is metallic in nature, the titanates are insulating. Lanthanum nickelate exhibits no magnetic order down to the lowest temperatures whereas the ilmenite titanates are long-ranged antiferromagnets. Interestingly, the possibility of titanates to be potential multiferroic materials have resulted in an incremental interest in them. Multiferroicity is another novel phenomenon in TMOs where the magnetism and ferroelecricity which are essential to many forms of current technology are intimately coupled [11]. Several microscopic mechanism depending on the spin-order and its coupling to elastic and lattice degrees of freedom for co-existence of

magnetic order and electric order have been suggested [12] and newer mechanisms and territories are still open to be explored [13]. A variety of promising technological applications such as energy transformation, signal generation and processing, information storage and so on make multiferroics an attractive research topic. In fact, the research in multiferroics is considered a successive hot topic in correlated electron materials after the high-T_c cuprates and the colossal magnetoresistive manganites [13].

The synthesis of bulk single-crystals, thin films and nanostructures play a seminal role is pushing the frontiers of quantum materials [14]. The synthesis of high-T_c cuprates [5], the discovery of the fractional quantum Hall effect in 2D electron gases [15], and observance of type-II multiferroicity in TbMnO$_3$ [16] are some of the examples of materials which challenged the theoretical understanding of the era. In general, bulk synthesis provides the community with large single crystals of both established and new materials [17–19], while the atomic-scale growth techniques enable synthesis of these materials in an epitaxial thin film form and in artificial layered hetero-structures where structural and chemical degrees of freedom can be controlled [14]. As the investigation in strongly correlated electron materials move forward, there is a need to push the well-known techniques - flux, floating zone and Bridgman growth, molecular beam epitaxy, pulsed lased deposition, and chemical vapour deposition etc, [18] extending them to new frontiers. In this thesis, emphasis is on the growth of large, high-quality bulk single crystals using the newly developed high-pressure optical floating zone furnace (see methods sec. 1.3.1). Recent advances in high-pressure floating zone growth has not only made it possible to grow single crystals of several materials for the first time (e.g. rare-earth nickelates [20,21]) but also enabled improvement in the quality of other known materials (e.g. MnTiO$_3$; see appendix B) [19,20,22–24].

The overall body of the thesis is structured as follows. In the following subsections of chapter 1, an introduction and a concise review of the existing relevant research in the ilmenite titanates MTiO$_3$ (M = Mn, Ni, Co) and LaNiO$_3$ is presented. Following this, a summary of the relevant experimental methods employed in the synthesis, characterization and magnetic studies of these bulk single-crystals is described. In chapter 2, experimental results containing single-crystal growth, investigations of magneto-elastic coupling and high-field magnetic phase diagram of easy-plane type NiTiO$_3$ and CoTiO$_3$ is presented. In particular, thermo-dilatometry data of NiTiO$_3$ and CoTiO$_3$ are also shown which facilitates understanding of microscopic mechanism of the magnetoelectric coupling in them. Chapter 3 contains the detailed investigation of magnetic ground state of the high-pressure optical floating-zone grown single-crystals of LaNiO$_3$. Chapter 4 presents important conclusions followed by a final summary and future work. Additional unpublished data on the single-crystal growth and characterization of MnTiO$_3$, Ni$_{0.25}$Mn$_{0.75}$TiO$_3$ and La$_4$Ni$_3$O$_{10}$ are presented in the appendices.

1.1   Ilmenite titanates - MTiO$_3$ (M = Mn, Ni, Co)
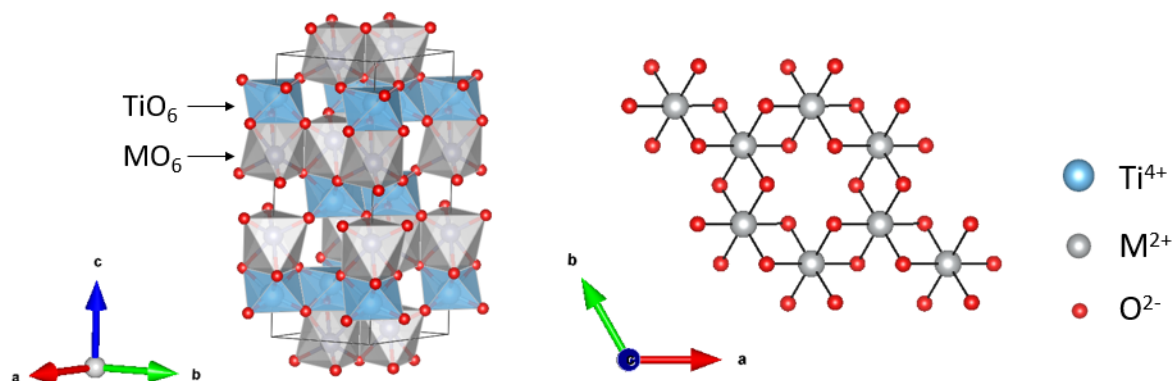
Figure 1.2. (Left) A 3D-view of the ilmenite crystal structure; (Right) The ilmenite crystal structure in the ab plane. Here a, b and c indicate principal crystallographic axes. The images are generated using the VESTA software [25].

Ilmenite titantes are the family of compounds with the general formula MTiO$_3$ where M is either a $3d$ transition element such as Mn (pyrophanite), Fe (ilmenite), Co, Ni or Mg (geikielite) which is a group 2 element. Originally, FeTiO$_3$ a titanium-iron oxide mineral was discovered by William Gregor in 1791, in a stream south of Manaccan (Cornwall) and was named ilmenite [26]. Since then, complete range of mineral chemistries in the (Fe,Mg,Mn,Ti)O$_3$ form has been found naturally on earth. The ilmenites investigated in this thesis, i.e., NiTiO$_3$, CoTiO$_3$, MnTiO$_3$ and Ni$_{0.25}$Mn$_{0.75}$TiO$_3$ have been synthesized firstly in polycrystalline form via the standard high-temperature solid state reactions and subsequently as single crystals using the optical floating-zone technique (see Sec. 1.3). See chapter 2 and appendices B, C for more details on sample synthesis.

The ilmenite crystal structure was solved for the first time in 1934 by Barth and Posnjak, using single crystal x-ray diffraction data on natural FeTiO$_3$ single crystals [27] and subsequently for polycrystalline NiTiO$_3$, CoTiO$_3$ and MnTiO$_3$ using powder x-ray data [28]. All the ilmenites were found to be isostructural and crystallizing in the rhombohedral space group $R\bar{3}$ (SG No. 148) with $a = b \neq c; \alpha = \beta = 90°, \gamma = 120°$. In particular, the ilmenite crystal structure is an ordered corundum structure where the Ti^{4+} and the M^{2+} ions occupy alternate basal plane layers and are face linked in pairs (Fig. 1.2). In a particular basal ab plane, M^{2+} ions are interconnected via O^{2-} ions forming a honeycomb-like structure as shown in Fig. 1.2. The electrostatic repulsion between M^{2+} and Ti^{4+} ions alternately displaces them above and below the hexagonal layers in the ab plane leading to a slight buckling of the hexagonal layers. All the metal M^{2+} ions and the titanium Ti^{4+} ions in the unit cell occupy the Wyckoff position 6c (site symmetry 3.) and the oxygen atoms occupy 18f position (site symmetry 1) in the obverse hexagonal setting.

Table 1.1. The valence electronic configurations of magnetic M^{2+} ions in various ilmenites, corresponding metal-oxygen-metal super-exchange bond-angle ($\angle MOM$) in the ab plane, Néel temperature (Ref. [33]) and the spin-structure of the magnetic ground-state. Note: All the bond angles for NiTiO$_3$, CoTiO$_3$ and MnTiO$_3$ are determined from single-crystal XRD data at 100 K (see chapter 2 and appendix B) and for FeTiO$_3$ from Ref. [27]; the corresponding spin-structures are obtained by neutron diffraction experiments reported in Refs. [34] for NiTiO$_3$ and MnTiO$_3$, [35] for CoTiO$_3$, [36–38] for FeTiO$_3$. For FeTiO$_3$ A-type (S||c+2°) means a collinear spin-structure with spins canted away by 2° from c axis.

Ilmenite	Ion(M^{2+})	$\angle MOM$	T_N	Spin-struc.
MnTiO$_3$	[Ar]3d^5 (S=5/2)	88.41	64 K	G-type (S||c)
FeTiO$_3$	[Ar]3d^6 (S=2)	93.93	56 K	A-type (S||c+2°)
CoTiO$_3$	[Ar]3d^7 (S=3/2)	89.94	38 K	A-type (S || ab)
NiTiO$_3$	[Ar]3d^8 (S=1)	90.35	22 K	A-type (S || ab)

The ilmenites are insulating in nature. Hence, it is evident that the magnetism arises due to the presence of localized unpaired electrons in the $3d$ levels of the transition elements (see Table. 1.1). Therefore, crystal-field theory is appropriate for the description of single-ion properties and superexchange theory for the description of inter-atomic magnetic interaction. A brief description of the relevant single-ion properties and predominant superexchange pathways is described below. For more details on the theory of magnetic properties of ilmenites, see Ref. [29].

The crystal field effect arises due to the static electric field produced by the surrounding oxygen ions, resulting in breaking of the d orbital degeneracy. In ilmenites, all the M^{2+} ions are in the high-spin state and are surrounded by octahedra of O^{2-} ions, which features a slight trigonal distortion. Hence, the single-ion properties and subsequently the magnetic anisotropy, is determined firstly by cubic crystal field which splits the d orbitals, followed by the combined effect of trigonal distortion and spin-orbit coupling acting as a small perturbation [29–31]. Note that the spin-orbit coupling is usually small for $3d$ elements as compared to $4d$, $5d$ or the rare-earths owing to the partial or complete quenching of the orbital angular momentum [32]. In the following, a brief description of the crystal field and spin-orbit effect on the M^{2+} ions in the ilmenites is made.

For Ni^{2+} ion, the cubic crystal field splits the orbital levels leaving an orbital singlet ($L = 0$, $S = 1$) as the lowest level. The resulting $S = 1$ spin-state will remain so under the influence of either spin-orbit or trigonal field alone. However, the anisotropy arises due to the combined effect of spin-orbit coupling (λ) and trigonal field (δ), mixing the upper states to the lower states as a second order perturbation (resulting in a δ/λ term). The anisotropy favours the

spins to point in the ab plane and results in a rather isotropic g-factor. Note that the dipole-dipole interaction also adds to the anisotropy which in this case too, favours the spins to be in the ab plane [29]. The isotropic g-factor determined by electron spin resonance [33, 39] and susceptibility experiments [33, 40, 41] amounts to $g = 2.23(2)$ (See Chapter 2 for magnetization data on NiTiO$_3$).

For Co^{2+}, the cubic crystal-field splits the seven-fold orbital state with a triplet state ($L = 1$, $S = 3/2$) as the lowest. In this case the spin-orbit coupling becomes more predominant than in Ni^{2+} case because of partial quenching of the orbital momentum. Hence spin-orbit coupling acts alongwith the trigonal distortion term, in the first order perturbation theory resulting in six doublet energy levels [30]. At low-enough temperatures, the lowest Kramers doublet is the only occupied state and the physics is dictated by a spin-orbit coupled pseudospin-1/2 ground state. Recent inelastic neutron scattering (INS) experiments on CoTiO$_3$ have found the spin orbit coupling parameter to be $\lambda = 28(1)$ meV and crystal field splitting $\Delta = 45(6)$ meV [42]. A huge anisotropy of the $g-$factor with $g_{ab}/g_c = 1.6$ for the pseudospin was obtained from INS, favouring the spins to point in the ab plane.

Fe^{2+} also exhibits an unquenched orbital momentum ($L = 1$) and the combined spin-orbit and trigonal distortion results in a considerable Ising anisotropy pointing spins along the c axis [29]. However FeTiO$_3$ will not be discussed here in great detail as is not studied in the current work. Mn^{2+} is an S-state ion with half-filled shell ($S = 5/2$), hence resulting in no net orbital momentum and the interaction with the crystalline electric field is exceedingly small. The resultant isotropic g-factor determined from the resonance [43] and susceptibility measurements [33, 44] is close to the free-electron value of 2. The anisotropy arises chiefly due to dipole-dipole interaction.

It is evident from the description of single-ion properties that the ilmenites form an interesting series of compounds where the magnetic ground states vary depending on the metal M^{2+} ion. All the ilmenites exhibit an antiferromagnetic ground state at low-temperatures with varying spin-structure. See table. 1.1 for the long-range antiferromagnetic transition temperatures T_N and the corresponding ground-state spin structure. See Fig. 1.3 for a schematic on different types of spin structure realized for ilmenites.

Fig. 1.4 shows the dominant superexchange pathways that drive the long-ranged antiferromagnetic order in ilmenites [29]. The dominant interaction J_1 contains two contributions: a neighbouring cation-cation interaction via direct overlap of t_{2g} orbitals and a near 90° cation-anion-cation (M-O-M) interaction as listed in Table 1.1. Note that the cation-anion-cation involves coupling of t orbital of one cation and e_g orbital of the other. Since the e_g orbitals are half-filled in all ions and t_{2g} orbitals are half-filled in Mn^{2+}, but more than half-filled in Fe^{2+}, Co^{2+} and Ni^{2+}, it follows from superexchange rules that $J_1^{Mn} < 0$ and $J_1^{Fe} > 0$, $J_1^{Co} > 0$, $J_1^{Ni} > 0$ [29]. All the other interactions are mediated via the M-O-O-M pathways and are rel-

A-type (S || ab)   **A-type (S || c)**   **G-type (S || c)**
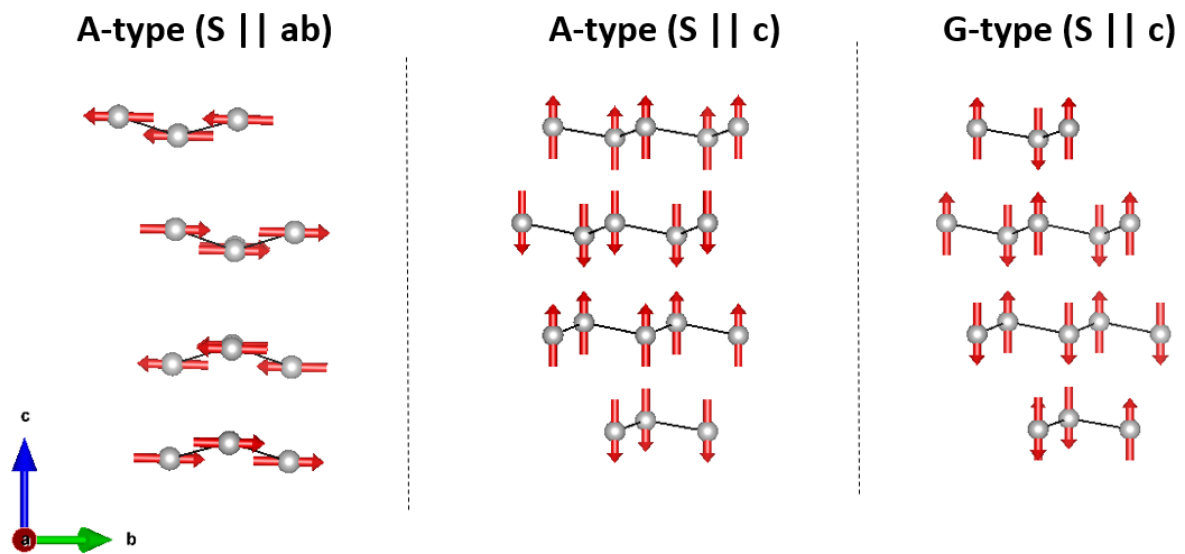
Figure 1.3. Schematic representation of various spin-structure of the ground state realised by ilmenite titanates depending on the magnetic-ion (Mn^{2+}, Co^{2+}, Ni^{2+} and Fe^{2+}) involved. The grey spheres represent the magnetic ions and the arrows indicate their respective spin (S) direction.
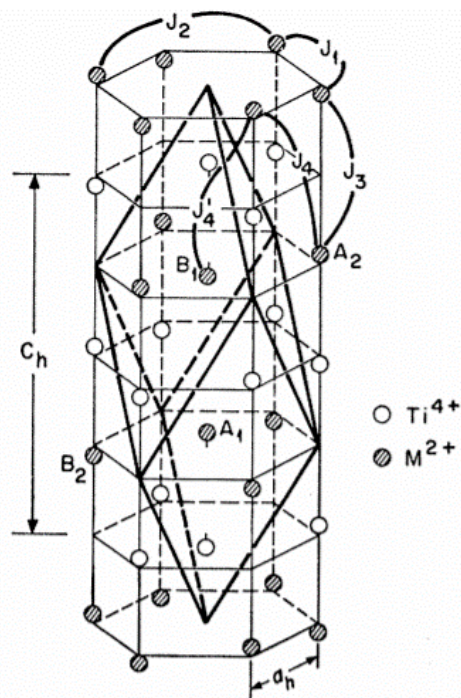
Figure 1.4. Ilmenite structure comprising of metal M^{2+} ions and titanium ions with principal super-exchange pathways J_1, J_2, J_3, J_4 and J'_4. Taken from Ref. [29].

atively weak. Since the out-of-plane interactions require e_g orbitals each containing only one electron, these interactions are expected to be antiferromagnetic and weak compared to J_1 [29].

As predicted from crystal-field and superexchange theory, both $NiTiO_3$ and $CoTiO_3$ exhibit easy-plane type or the A-type spin-structure. In particular, the spins in the ab plane are ferromagnetically arranged, with each layer coupled antiferromagnetically to the next layer. The spin-structure of $NiTiO_3$ was solved for the first time by Shirane $et\ al.$ [34] in 1959 and $CoTiO_3$ by Newnham $et\ al.$ [35] in 1964 and recently revisited by Elliot $et\ al.$ [45]. Both the structures were solved by means of powder neutron diffraction experiments, where the additional magnetic peaks were observed corresponding to the propagation vector $K = (0, 0, 3/2)$. Subsequently, the magnetic susceptibility [33, 40, 41, 44] and electron-spin resonance experiments [33] were reported starting from the 1960s which complemented well with the proposed spin-structure. It is to be noted that, most of the macroscopic results on $NiTiO_3$ and $CoTiO_3$ have been limited to polycrystalline materials till today. First single-crystal growth of $CoTiO_3$ and $NiTiO_3$ was reported by Watanabe $et\ al.$ [40] in 1980, but with limited details and subsequently by others using flux [46] and the floating-zone method [47, 48].

$MnTiO_3$ was relatively more intensely investigated in the past decades in both single and poly-crystalline form (see Ref. [44, 49] for details on floating-zone growth). The magnetic structure was solved by means of powder neutron diffraction experiment by Shirane $et\ al.$ [34] in 1959. $MnTiO_3$ exhibits G-type antiferromagnetic order (propagation vector $K = (0, 0, 0)$) below 64 K with spins pointing along the c direction (See Fig. 1.3). Magnetization measurements with magnetic-field along the easy c axis exhibit a spin-flop transition at 6 T [50] as expected for an uniaxial antiferromagnet. Interestingly, the magnetic susceptibility measurements exhibited a broad peak at 100 K which is above the $T_N = 64$ K, reminiscencing a quasi-2D behaviour [51]. The heat capacity measurements exhibit a sharp lambda-shaped anomaly at T_N but only 55% of magnetic entropy was found to be consumed below T_N [52]. Following this, a flurry of quasi-elastic and inelastic scattering experiments [51, 53–56] and an ESR study [57] were conducted between 1970s and 1990s to study the critical properties of $MnTiO_3$ close to the phase transition. Akimitsu $et\ al.$ in 1970 [51] found out by means of quasi-elastic magnetic scattering that, the sublattice moment from 64° to 56° follows a power law $(T_N - T)^\beta$ with $\beta = 0.32 \pm 0.01$, as in a 3D antiferromagnet in contrast to 2D magnetism. Interestingly, the following neutron scattering studies in 1974 [53] and 1977 [54] at temperatures above T_N, indicated a gradual cross-over from 3D to 2D character by measuring the change in scattering profile on increasing temperature. This study showed that $MnTiO_3$ is a quasi-2D antiferromagnet. The exchange interaction parameters were determined from a spin-dynamics study by Todate $et\ al.$ [55] in 1986 and it was revealed that the 2D antiferromagnetic properties are realized by accidental cancellation of inter-layer exchange interaction.

The magnetic properties of the ilmenites as described above, have been a matter of inves-
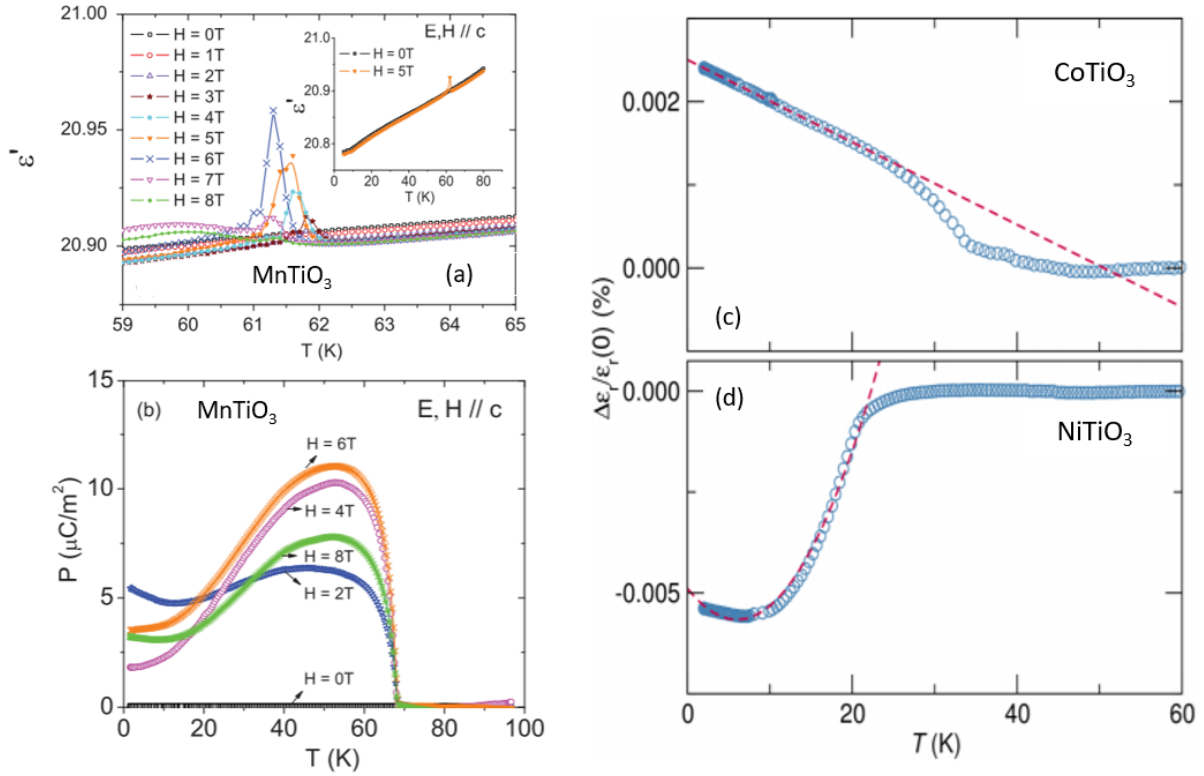
Figure 1.5. (a) Temperature dependence of the dielectric constant of MnTiO$_3$ for magnetic field applied along the c axis and (b) electric polarization of MnTiO$_3$ under various constant magnetic field [58]; relative changes in the dielectric constant versus temperature at zero external magnetic field for (c) CoTiO$_3$ and (d) NiTiO$_3$ [44]. See the text for more details.

tigation since the 1950s and are well understood within the proposed theoretical framework. However, exciting new and puzzling discoveries have been made in the past decade, which has lead to a resurgence of interest in these materials. The following section briefly summarizes the latest relevant results.

The observation of linear magnetoelectric coupling in the single-crystals of MnTiO$_3$ for the first time in 2011 by Mufti *et al.* [58] re-kindled interest in the ilmenites family as a whole. The dielectric function (ϵ) exhibits no anomalies for the measured temperature range at $B= 0$ T. Interestingly, on application of magnetic-field, sharp anomalies appear in ϵ at the Néel temperature T_{N} for $H, E||c$ (see Fig. 1.5 (a),(b)). Subsequently the onset of electric polarization was observed below T_{N} as shown in Fig. 1.5 which scales linearly with applied external magnetic field up to 3 T, indicating that MnTiO$_3$ is a linear magnetoelectric material. No anomalies were observed for $E, H \perp c$; $H||c, E \perp c$ or $H \perp c, E||c$ [58]. Note that all the measurements were made after cooling from the paramagnetic state in finite magnetic and electric fields to avoid any domain effects.

From the reported magnetic structure of MnTiO$_3$, the magnetic symmetry below T_{N} for MnTiO$_3$ is $R\bar{3}'$, which theoretically allows for the linear magnetoelectric effect, with non-zero

tensor elements $\alpha_{xx} = \alpha_{yy}, \alpha_{zz}$ and $\alpha_{xy} = -\alpha_{yx}$ [58, 59]. Here α is a magnetoelectric coefficient. Furthermore, the investigation of magnetic symmetry by means of second harmonic generation experiments above the spin-flop field (i.e. $B > 6$ T) reveal that $MnTiO_3$ has a spin-structure symmetry similar to Cr_2O_3 [59]. Note that Cr_2O_3 has a similar ground state spin-structure as that of $MnTiO_3$ and exhibits linear magnetoelectric effect too [60]. In the spin-flop phase, Cr_2O_3 exhibits toroidal moments [61], which makes $MnTiO_3$ a candidate material to study toroic order [59]. Experimentally, epitaxially grown thin films of $MnTiO_3$ on sapphire substrates exhibited spin-flopping similar to bulk crystals leading to the conclusion that the films had ferrotoroidic structure [62].

As mentioned above, the absence of any dielectric changes in zero magnetic-field at T_N was taken initially by Mufti *et al.* as an indication for lack of exchange-striction (and hence appreciable spin-lattice coupling) in $MnTiO_3$ [58]. Polarization dependent x-ray absorption experiments by Chen *et al.* [63] in 2014 revealed a strong asymmetric charge distribution due to strongly anisotropic O $2p$-Mn $3d$ orbital hybridization $(p - d)$, indicating that a spin-dependent-metal-ligand hybridization mechanism behind the magnetically induced ferroelectricity in $MnTiO_3$. In a $p-d$ hybridization mechanism, a local electric polarization $\Delta P \propto$ exists between transition metal and the ligand due by hybridization [64, 65]. Here S is the spin and e is the vector connecting the transition metal and ligand. This mechanism is fundamentally related to the single-ion properties and hence indicates that spin-lattice coupling in $MnTiO_3$ should be considered more seriously than described by Mufti *et al.*. Interestingly, the thermal evolution of the lattice parameters measured by X-ray diffraction exhibited deviations from the high-temperature behaviour in the spin-correlated regime and in the magnetically ordered phase [66]. Furthermore, new crystallographic incommensurate supercell peaks were observed in recent neutron diffraction experiments which exist up to highest measured temperatures of 300 K and exhibit both temperature and magnetic field dependence, revealing that the effect of spin-lattice coupling in $MnTiO_3$ cannot be neglected for $MnTiO_3$ [67]. The origin of additional structural peaks and in particular spin-lattice coupling in $MnTiO_3$ are still poorly understood and need further systematic investigations.

Following $MnTiO_3$, dielectric spectroscopy measurements were made on polycrystalline samples of $CoTiO_3$ and $NiTiO_3$ by Harada *et al.* [44]. Significant anomalies were observed for both the compounds at their respective T_N (see Fig. 1.5) in zero external magnetic field, revealing significant magnetodielectric coupling [44]. A strong dependence of dielectric permittivity on the applied external magnetic field was observed near T_N and the dielectric loss measurements indicated that all the observed effects were intrinsic [44]. Note that in contrast to $MnTiO_3$, both $CoTiO_3$ and $NiTiO_3$ exhibit dielectric anomalies in zero external magnetic field, indicating that an exchange striction mechanism may be responsible for the observed effects. Further detailed investigations are needed on the single crystals of ilmenites to understand their

magnetic and nuclear structures, and the underlying spin-lattice coupling effects. This forms one of the principal questions which is investigated in this thesis.
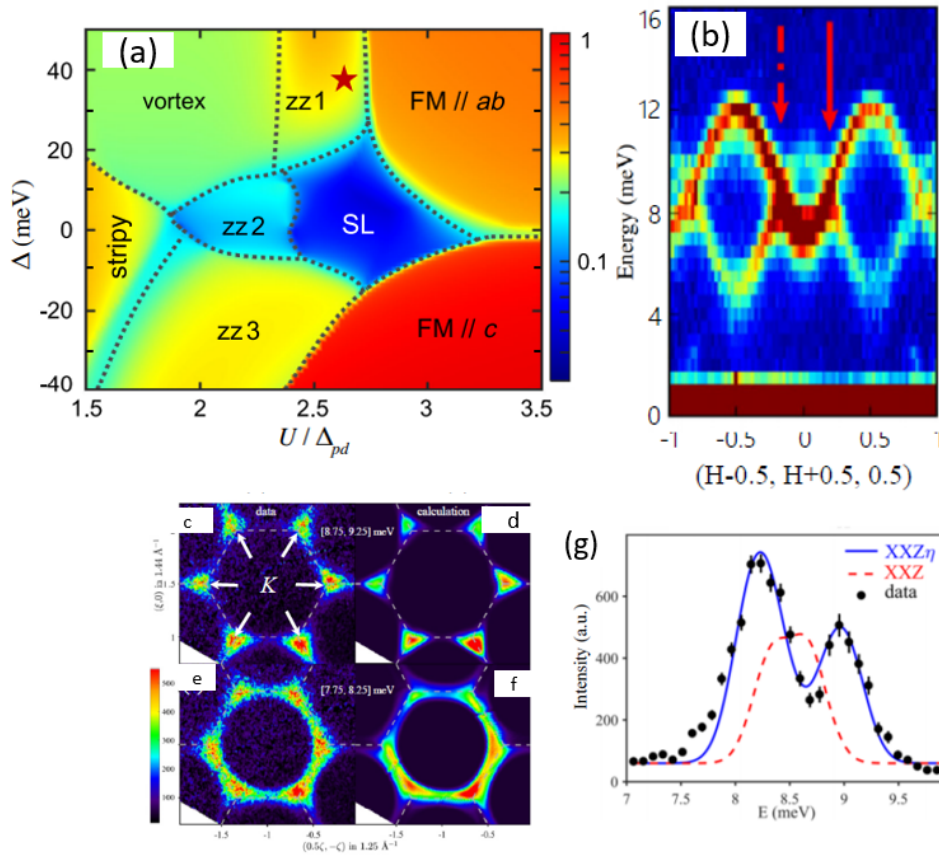
Figure 1.6. (a) Theoretically predicted magnetic phase diagram of honeycomb cobaltates. SL represents Kitaev spin-liquid phase, FM represents ferromagnetic states with moments in ab plane and along c axis, ZZ represents different zig-zag states (from Ref. [68]); (b) neutron scattering intensity map of magnons in CoTiO$_3$. Arrows indicate the Dirac points where two linear magnon bands cross (from Ref. [42]); (c-f) experimental and calculated momentum intensity maps (from Ref. [45]); (g) average energy scan centered at K-points in (c). The experimental data shows two clear peaks, which can be resolved by an XXZ model with an additional bond-dependent anisotropy labelled by η (from Ref. [45]).

Recent inelastic neutron scattering studies on magnon topology in CoTiO$_3$ and theoretical predictions on the realization of Kitaev spin-liquid states for cobaltates have attracted tremendous attention to CoTiO$_3$ [68, 69]. Initially, it was believed that only $4d$ and $5d$ systems, where significant spin-orbit coupling come into play, provide the ideal platform to realize exotic states of matter such as quantum spin-liquids [70]. In contrast, $3d$ elements were largely neglected because the spin-orbit coupling was not strong enough (owing to partial or full quenching in a cubic crystal-field) to support orbital magnetism for Kitaev physics. However, recent theoretical investigations by Liu *et al.* Ref. [68, 69] suggest that for $3d$ cobaltates, orbital moments

remain active and in-fact generate a Kitaev model as the leading term in the Hamiltonian. The trigonal crystal field was identified as the key parameter deciding the strength of non-Kitaev terms in $3d$ compounds [68, 69]. A rich phase diagram (as seen in Fig. 1.6 (a)), displaying various magnetic phases arising from spin-orbit entangled pseudospin 1/2 Co^{2+} ions on a honeycomb lattice, as a function of trigonal field Δ and the ratio of Coulomb repulsion U and the charge-transfer gap Δ_{pd} was predicted [68, 71]. Following the theoretical proposals, several new materials for example BaCo$_2$(AsO$_4$)$_2$ [72], Na$_3$Co$_2$SbO$_6$ [73], Na$_2$Co$_2$TeO$_6$ [73, 74] and CoTiO$_3$ [68] with Co-based honeycomb structures have been under intense experimental investigation. Neutron diffraction experiments indicate that, a variety of magnetic ground states as predicted in Fig. 1.6 (a) are indeed realized in cobaltates, for example: spin-spiral state in BaCo$_2$(AsO$_4$)$_2$ [72], zig-zag order in Na$_3$Co$_2$SbO$_6$ [75] and Na$_2$Co$_2$TeO$_6$ [74] and FM$\|ab$ order in CoTiO$_3$ [35] as discussed above. As the trigonal crystal field is identified as a crucial parameter, tuning it by doping or applied external uniaxial pressure has been suggested to push the materials close to the spin-liquid ground state [68].

The magnon dispersion studies on CoTiO$_3$ by means of INS experiments have been of particular interest due to non-trivial magnon band topology. In particular, a gapless Dirac cone as shown in Fig. 1.6(b) has been revealed by INS experiments [42, 45]. An azimuthal modulation around the linear touching Dirac points has been observed [45] (see Fig. 1.6 (c,e)), which is considered as a fingerprint of a topologically non-trivial magnon band structures [76]. Interestingly, an evidence for bond-dependent exchange interactions is obtained from recent inelastic neutron scattering (INS) results, which is in line with theoretical predictions. The theoretical calculation as shown in Fig. 1.6 (d,e) by means of a $XXZ\eta$ model, where η represents the bond-dependent exchange anisotropies explains the data very well [45]. An average energy scan around Dirac point exhibits two peaks feature (see Fig. 1.6(g)) which can only be explained well by the $XXZ\eta$ model, providing a conclusive evidence of the presence of bond-dependent anisotropic exchange in CoTiO$_3$ [45]. Furthermore, a spectral gap of 1 meV at low energy was observed in high-resolution neutron diffraction experiments which is beyond the XXZ model [45]. It was indicated that a quantum order-by-disorder mechanism involving bond-dependent interactions could explain such a gap [45]. However, a small in-plane gap was also observed for NiTiO$_3$ by means of high-frequency electron spin-resonance mechanism [39]. A bond-dependent anisotropic mechanism suggested for CoTiO$_3$ is unlikely for NiTiO$_3$(exhibits quenching of orbital moment) and a magnetoelastic origin of this small gap must be investigated in further detail.
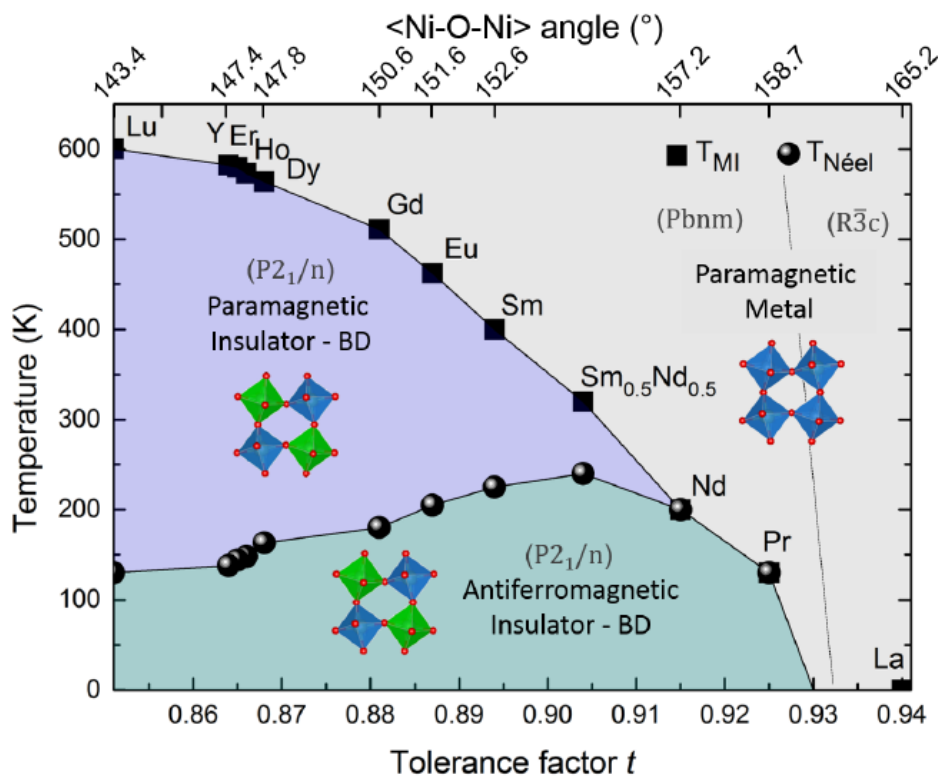
Figure 1.7. The phase diagram of RNiO$_3$ family showing the evolution of the structure, metal-insulator transition and Néel temperature as a function of tolerence factor (t) and the <Ni-O-Ni> bond angle. $R\bar{3}c$, $Pbnm$ and $P2_1/n$ indicate space groups corresponding to the rhombohedral, orthorhombic and monoclinic crystal structures, respectively. Taken from Ref. [77]

1.2 Lanthanum nickelate - LaNiO$_3$

LaNiO$_3$ belongs to the perovskite nickelate family RNiO$_3$, where R is a trivalent rare earth $R = La, Pr, Nd, ...Lu$. The RNiO$_3$ family exhibit a fascinating phase diagram as shown in Fig. 1.7 and are intensely investigated since last three decades. All the members of the family except for $R = La$ exhibit metal-to-insulator transition (MIT) with the transition temperature decreasing with decreasing size of R cation. Consequently, the evolution of nickelate phase diagram is correlated to the Goldschmidt tolerance factor $'t'$ ($t = d_{R-O}/\sqrt{2}d_{Ni-O}$ where d is the ionic bond distance between R-O and Ni-O respectively) and the <Ni-O-Ni> bond angle. A structural transition concomitant to MIT is observed where the unit cell volume expands by 0.2%. The resultant insulting phase (monoclinically distorted) is characterized by a Ni-O bond length disproportion with two inequivalent Ni sites. At high-temperatures, all the compounds are metallic and paramagnetic, and exhibit orthorhombic crystal structure except for $R = La$, which exhibits a rhombohedral structure. While LaNiO$_3$ remains paramagnetic down to low temperatures, other members exhibit an antiferromagnetic ground state. Interestingly, for $R = Pr$ and Nd, the MIT occurs simultaneously with a Néel transition whereas for the others, MIT takes

place at a higher temperatures than the spin-ordering transitions. The RNiO$_3$ family provides a fascinating example of the coupling of electronic, structural and spin-degrees of freedom where the underlying microscopic mechanisms are still intensely debated. Theoretical principles of nickelate physics shall not be described in this brief introduction however the focus will be set on LaNiO$_3$. See the reviews [77–79] and references therein for a comprehensive overview on experimental results and theoretical understanding of the nickelates.

From the synthesis point of view, nickel adopts the Ni^{3+} valence state in RNiO$_3$ and hence high temperatures and pressures are instrumental in synthesizing them. Demazeau *et al.* [80] in 1971 synthesized the nickelates for the first time by reacting R$_2$O$_3$, NiO and KClO$_3$ in a sealed platinum capsule at 950^0 C with in situ pressures of 60 kbar. Lacorre *et al.* [81] synthesized them by reacting oxides at 1000^0 C and 200 bar oxygen pressure. As a result, most of the research in bulk nickelates until 2017 had been limited to polycrystalline samples only, with the largest single crystals available were about 100 μm [82] in size. The availability of nickelate single crystals have been scarce even today due to the challenging conditions required to grow them. Hence, considerable efforts have been made in the synthesis of thin films in which high-crystallinity could also be achieved at lower pressures. A plethora of experimental studies on thin film nickelates exists which have not only improved the understanding of nickelate physics but also opened the doors to several applications. In this thesis, only bulk samples have been investigated. For interesting and comprehensive reviews on thin film research in nickelates see Ref. [77, 79, 83].

Bulk LaNiO$_3$ which has been investigated in this thesis, deviates from the rest of nickelates as discussed above and shown in the nickelate phase diagram (Fig. 1.7). LaNiO$_3$ remains paramagnetic [84–86], metallic [85, 86] and rhombohedral [87, 88] until the lowest measured temperatures of $T = 1.5$ K. The static paramagnetic susceptibility (χ) is well described by a dominant temperature independent Pauli term (χ_P) with an additional small Curie-term (χ_C) in the temperature range 100-300 K [85] (see Fig. 1.8(a)). A stronger temperature dependence of χ observed at lower temperatures, i.e., $T < 100$ K (see Fig. 1.8(a)) is accounted well for by a Curie contribution arising due to extrinsic quasi-free Ni^{2+} moments [85]. A positive temperature coefficient of electrical resistivity which is typical of metals is observed down to 4.2 K, where resistivity varies almost linearly with temperature for $T \geq 200\ K$, and in contrast it varies as T^2 for $T < 50$ K [84–86] (see Fig. 1.8(b)). Interestingly, both the measured Pauli paramagnetic susceptibility χ_p and the linear temperature coefficient of the specific heat γ show enhancement well above their free electron-gas values indicating that LaNiO$_3$ is a correlated paramagnetic metal [84–86].

Although, the magnetic and electronic properties of LaNiO$_3$ have been well investigated since 1980s, recent experimental and theoretical works in the past five years cast doubt on the rhombohedral, paramagnetic metallic ground state. Notably, pair density function analysis

of the neutron diffraction data [89, 90] indicated that on the nanoscale the local symmetry is broken at the Ni sites due to oxygen distortions and hence the local structure is best described by the monoclinic $P2_1/n$ symmetry. Furthermore, Alaska Subedi by means of DFT calculations [91] indicated that, several structures lie close in energy with orthorhombic $Pnma$ marginally preferred over $R\bar{3}c$, and both structures are stabilized by octahedral breathing distortions and an antiferromagnetic ground state which is in contrast to the previous magnetization studies.
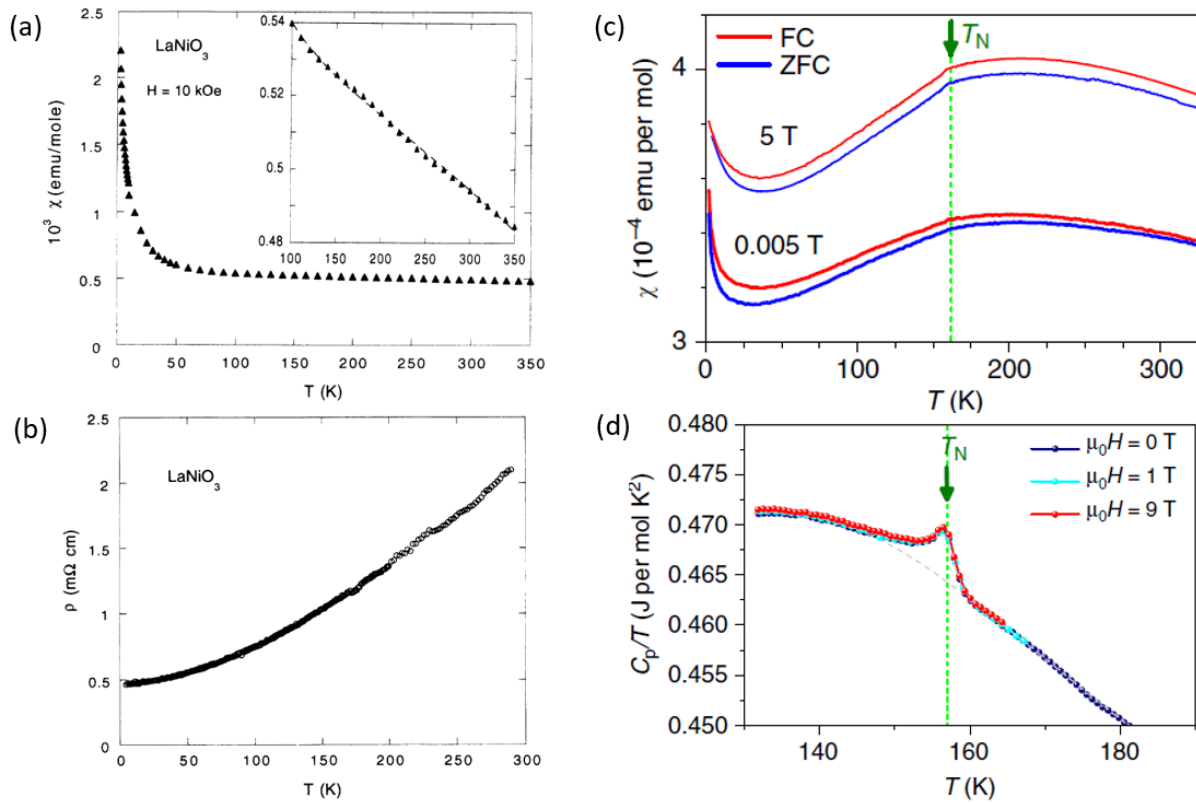
Figure 1.8. (a) Static magnetic susceptibility χ vs. T and (b) electrical resistivity ρ vs. T for polycrystalline LaNiO$_3$ taken from ref. [85]; (c) χ vs. T of single crystalline LaNiO$_3$ exhibiting a kink at around 157 K and the corresponding (d) specific heat data taken from Ref. [92].

Note that until 2017, all the investigations on the bulk nickelates have been limited to only polycrystalline samples. Extreme conditions for synthesis of nickelates such as high-temperature and pressure as described above rendered it difficult to grow large single crystals. The presence of high-quality single crystals of appreciable size is indispensable in understanding the fundamental electronic and structural properties especially in the nickelates. Due to recent technological advances in the high-pressure optical floating-zone furnace (see Methods 1.3.1) [19, 22, 23] it was possible to grow macroscopic LaNiO$_3$ single crystals for the first time.

LaNiO$_3$ single crystals were grown for the first time by Zhang *et al.* [20] in 2017 at the Argonne National Laboratory, USA and subsequently by Guo *et al.* [92] in 2018 at the Max-Planck-Institute, Dresden. Both the groups employed the optical floating zone technique where

Zhang *et al.* used an elevated O$_2$ pressure of 50 bar whereas Guo *et al.* employed 150 bar respectively. The high-resolution single crystal X-ray diffraction studies by both the groups re-confirmed the rhombohedral $R\bar{3}c$ space group. Interestingly, the static magnetic susceptibility measurements by both the groups exhibited a clear distinction as compared to the previous polycrystalline data. The magnetization behaviour of single crystals was neither Pauli-like nor Curie-like and exhibited a broad hump at 200 K as shown in Fig. 1.8(c). The low-temperature upturn was ascribed to the tiny paramagnetic impurities similar to the polycrystalline case. Surprisingly, Guo *et al.* [92] observed an anomalous kink in magnetization at 157 K (see Fig. 1.8 (c)). Their specific heat measurements as shown in Fig.1.8(d) also exhibited a clear peak at 157 K indicative of a long-ranged antiferromagnetic transition. However such anomalies were surprisingly not observed in magnetization and specific heat data on the single crystals grown by Zhang *et al.* [20] or in any previously published data on polycrystalline samples. Furthermore, the neutron scattering measurements by Guo *et al.* [92] revealed new quarter integer peaks in their single crystals with propagation vector (1/4,1/4,1/4) similar to other insulating rare-earth nickelates.

Note that several oxygen deficient phases of lanthanum nickelate, i.e., LaNiO$_{3-x}$ have previously been reported in the literature [93–95] with dramatically different physical properties. For example, LaNiO$_{2.5}$ exhibits antiferromagnetism at around $T_{\mathrm{N}} = 150$ K [95] and LaNiO$_{2.75}$ exhibits ferromagnetism at $T_c \approx 230$ K [93]. Several other oxygen deficient phases with $0 \leq x \leq 0.5$ also exist with slightly differing T_{N} and T_c [93, 95]. Even the electrical properties is reportedly different than the parent LaNiO$_3$ with a metal-insulator transition observed for $x \geq 0.25$ [93]. Note that such oxygen deficient impurity phases may also be present during the synthesis of LaNiO$_3$ and one needs to carefully quantify the oxygen deficiency.

As a matter of fact, samples were reportedly more stoichiometric for Guo *et al.* [92] ($x = 0.003$) as compared to Zhang *et al.* [20] ($x = -0.015$). However, the LaNiO$_3$ single crystal grown by Wang *et al.* [96] at 130 bar O$_2$ pressure exhibited similar stoichiometry ($x = -0.020$) to that of Zhang *et al.*. Surprisingly, on reducing the as-grown LaNiO$_{3-x}$ samples purposefully from $x = 0.020$ to $x = 0.076$, Wang *et al.* [96] observed anomalies in the magnetization and specific heat data at around 150 K. Furthermore, neutron diffraction studies on the reduced samples also exhibited additional temperature dependent Bragg peaks below 150 K at quarter integer points similar to GuO *et al.* [92]. Notably, such quarter integer peaks were found to be absent in the as-grown samples which is in line with Zhang *et al.* [20] results. Hence there exists an ambiguity in the ground state properties of LaNiO$_3$. Solving for the ground state of LaNiO$_3$ is essential even for other nickelates where the electronic and magnetic properties are still under intense investigation.

1.3 Methodology

In this section, a brief description of the most important experimental techniques employed in this thesis are discussed. For more details on experimental techniques refer to the subsequent chapters.

1.3.1 Single-crystal growth by optical floating-zone technique
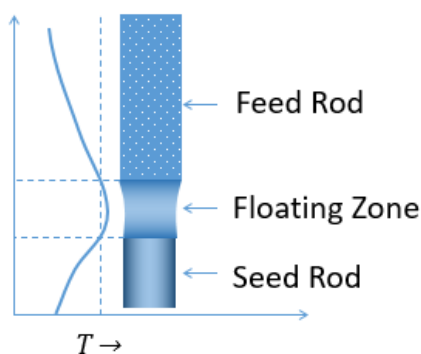
Figure 1.9. A schematic showing the feed, seed rods and the liquid zone assembly in an optical floating zone process. The solid curve shows the temperature profile along the z-direction.

All the oxide materials investigated in this thesis were grown using the optical floating-zone (OFZ) technique. OFZ is a high-temperature, crucible free technique to grow relatively large (up to several cm) high-quality single-crystals of technological and fundamental interest. In short, this technique involves two cylindrical-shaped ceramic rods typically several cm long, mounted in a vertical configuration with their tips at a focal point of ellipsoidal mirrors (see Fig. 1.10). Xenon or halogen lamps of several kW in power, located at the other focal point of the mirror configuration are used to melt the tips of the polycrystalline rods. The melted tips are brought together to establish a liquid-zone also called as the floating zone between the feed (top) and seed (bottom) rods. The entire assembly comprising the rods and liquid zone (as shown in Fig. 1.9) are then moved along the vertical direction at a certain rate (typically few mm per hour) resulting in cooling of the liquid zone and crystallization on the seed rod. Maintaining a stable floating zone is crucial for the growth of large single crystals, and is achieved by a delicate balance of several parameters during the growth such as - lamp power, pulling rates, rotation rates of the rods, atmosphere and pressure applied during the growth and melting properties of the material involved. A comprehensive review of the OFZ technique, it's advantages and disadvantages can found in refs [17, 97]. A brief introduction to the optical floating zone furnaces and typical parameters employed to grow the ilmenites and lanthanum nickelates

is described below. Further details on the growth of specific materials are given in subsequent chapters.

High-pressure optical floating-zone furnace
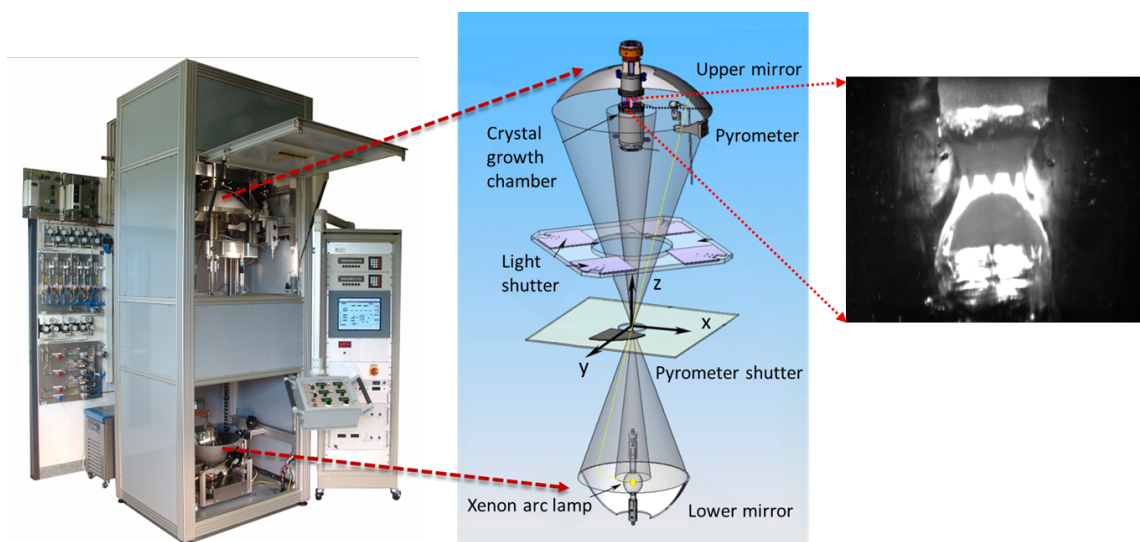
Figure 1.10. (Left) A picture of the high-pressure (150 bar) optical floating-zone furnace (HKZ Sci-Dre) [98]; (centre) schematic of the relevant components of the HKZ furnace. Adapted from [22, 23]; (right) a real-time image of the LaNiO$_3$ floating-zone at 100 bar O$_2$ pressure.

The high-pressure optical floating-zone furnace (HKZ, Sci-Dre), as shown in Fig. 1.10, consists of two elliptical mirrors in the vertical configuration which are used to focus light from a 3.5 kW xenon short arc lamp. The furnace can be operated up to a maximum pressure of 150 bar which makes it possible to grow new materials, previously impossible with low-pressure furnaces (for example see the crystal-growth of LaNiO$_3$ in chapter 3). The entire growth process takes place inside a transparent quartz/sapphire cylinder tightened with a combination of brass, o-rings and teflon disks which enables maintaining high-pressure. In the Heidelberg furnace the growth can be performed either in argon or in oxygen atmospheres with a typical flow-rate of 0.1-1 lt/min. A higher flow rate is usually favourable for materials exhibiting higher-volatility [17, 97]. Temperatures in excess of 2000° C can be achieved depending on the absorption of individual materials, using the power shutter system of the light beam, to facilitate melting of feed and seed rods and form a molten-zone. Typical growth rates of 1-8 mm/h is applied to grow the materials in this thesis (higher for congruently-melting materials) along with counter rotation of feed and seed rods for better mixing and temperature stability of the molten-zone [17, 97]. The vertical temperature profile in and around the molten-zone is measured using an *in-situ* pyrometer.

Four-mirror optical floating-zone furnace
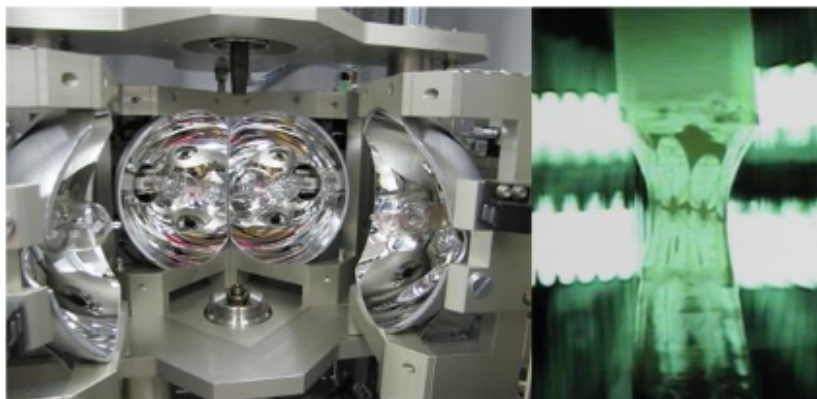
Figure 1.11. (Left) A picture of the four semi-ellipsoidal mirrors of the CSC furnace; (right) Real-time image of the floating-zone during $CoTiO_3$ crystal growth process at ambient pressure.

Apart from employing a two-mirror high-pressure OFZ furnace as described above, a four-mirror floating-zone furnace (Crystal System Corporation, Japan) comprising of four semi-ellipsoidal mirrors with halogen lamps (at IISER Pune, India) was also used to grow single-crystals. Unlike the vertical configuration of mirrors (as in Fig. 1.10), the horizontal configuration (Fig. 1.11) ensures a larger vertical temperature gradient along the rods which is sometimes beneficial for a better grain selection [97]. Note that a larger temperature gradient may also result in an increased cracking due to thermal stress and hence a highly dense feed and seed rods must be employed for successful growth. In this thesis, the easy-plane type ilmenites, i.e., $NiTiO_3$ and $CoTiO_3$ were grown using the four-mirror furnace with 4×150 W halogen lamps in ambient/1 bar over-pressure conditions in air and O_2 atmospheres. Note that the four mirror furnace can only be operated to a maximum pressure of up to 10 bar and hence lanthanum nickelates ($LaNiO_3$ and $La_4Ni_3O_{10}$) cannot be ideally grown in these furnaces.

1.3.2 Single-crystal characterization

Powder X-ray diffraction

The phase identification of the polycrystalline materials and in particular of the grown single-crystals were investigated by means of powder x-ray diffraction experiments (PXRD). Prior to a PXRD measurement, the single crystalline pieces are pulverized by grinding for about 30 min, using a mortar and pestle to form a homogeneous powder comprising of small crystallites. The experiments were carried out by I. Glass at the Geosciences Institute, Heidelberg University using a 'Bruker D8 Advance Diffractometer' with monochromatic Cu-Kα source ($\lambda = 1.5405$ Å) in the Bragg-Brentano geometry. The diffraction patterns were typically in the 2θ range of 15-

$90°$ with a step width of $0.02°$ and an integration time of 1 s for a short measurement and of 10 s for a long measurement. The phase identification was done by comparing the obtained PXRD patterns with the previous data in literature using the MATCH software [99] and the DIFFRAC.EVA software [100].

The Rietveld refinements were done using the FULL-PROF suite 2.0 software [101] on the obtained PXRD patterns (long-measurement) to additionally check for the phase purity and to refine the lattice parameters. The refinements were performed against a starting model obtained using crystallographic information files from ICSD database [102]. The relevant parameters which were refined are - the scale factor, zero error, background correction (usually a polynomial with six-coefficients), lattice parameters, Debye-Waller factor, FWHM parameters, asymmetry and the atomic-coordinates. A full occupation of the corresponding atomic sites were assumed while refinements. A multi-phase refinement was also performed to quantitatively estimate the content of the additional impurity phases, if at all present.

Polarized Optical Microscopy
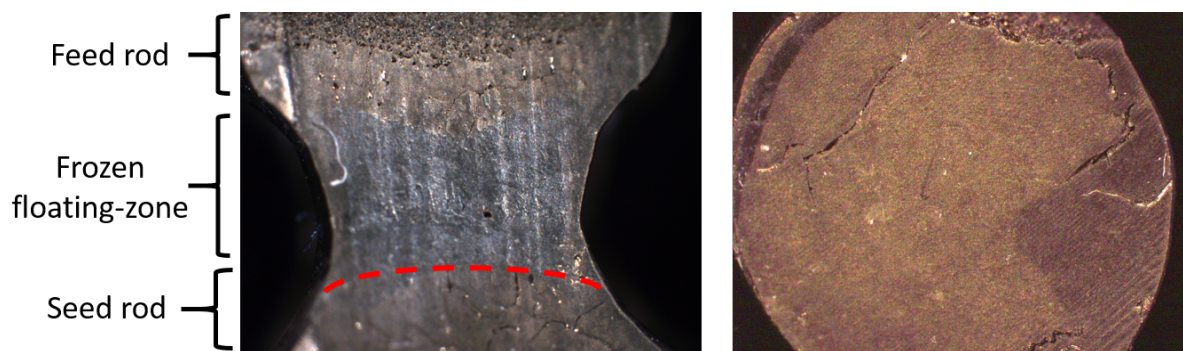
Figure 1.12. (Left) Polarized optical microscopy image of quenched floating-zone zone of $LaNiO_3$ grown at 100 bar; (right) Polarized microscopy image of the cross-section of disk extracted post-growth from a $LaNiO_3$ boule grown at 80 bar.

To check for defects, shape of the growth front between seed rod and the floating zone and crystallinity of the grown boules, polarized optical microscopy experiments were performed using a Carl Zeiss Axio scope.A1 microscope [103]. For this, thin sections of flat disks were extracted using Diamond wire saw from the grown boules and polished well in SAPHIR 520/530 using silicon carbide paper of different grit sizes. A water based solvent with suspended monocrystallites of Diamond (few microns in size) were used to obtain smooth polished surface. Representative optical microscopy images of the frozen floating zone and the a cross-section from $LaNiO_3$ growth is shown in Fig. 1.12. A convex growth front as seen in 1.12 (left) is considered beneficial for the grain selection [97] process and indicates that the parameters used for growth were suitable. The contrast between the central and the peripheral regions as seen in

Fig. 1.12 (right) indicates the presence of compositional difference between the regions [17,97], which was indeed re-confirmed by other recent macroscopic measurements on $LaNiO_3$ [104]. Such radial difference in composition may especially arise in a high-pressure optical floating zone growth due to additional cooling effects of the peripheral regions.

SEM and EDX
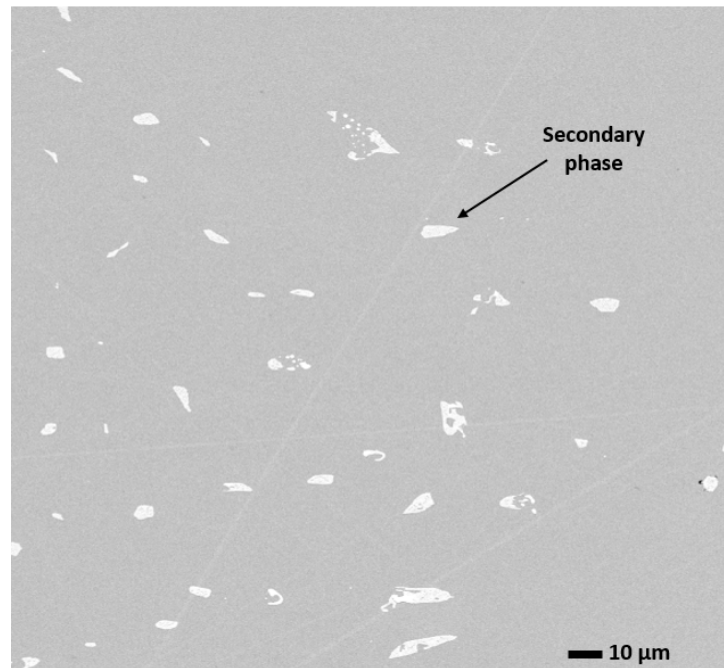
Figure 1.13. A representative scanning electron micrograph image of $NiTiO_3$ single crystal grown in argon atmosphere at 5 bar pressure. The white spots represent a precipitated secondary phase.

To study the surface morphology and elemental composition of the grown crystals, scanning electron microscopy (SEM) and energy dispersive x-ray analysis(EDX) were performed respectively. The experiments were performed on polished single crystals by Lennart Singer of Kirchhoff Institute for physics, Heidelberg University using a JEOL JSM-7610F SEM and in collaboration with Rabindranath Bag of IISER Pune using a Zeiss Ultra plus SEM. Fig. 1.13 shows a characteristic SEM picture obtained using the JEOL SEM of a $NiTiO_3$ single crystal with secondary phases precipitated (Ni-rich) possibly due to a higher growth rate.

Laue back-scattered diffraction

The Laue back-scattered diffraction experiments were performed rigorously to check for single-crystallinity of the grown boules and to orient the obtained single-crystals. The as-grown boules or single crystalline pieces were mounted on a goniometer-stage and the bremsstrahlung (white

X-rays) produced by a conventional tungsten X-ray tube were used to generate diffraction patterns. A typical acceleration voltage of 30 to 40 kV and tube-current of 15 to 20 mA, along with an acquisition time of 300-500 s was employed to obtain good quality images. The sample distance was maintained at approximately 30 mm using the spacer and PSL viewer [105] software was used to process the images. The obtained diffraction patterns were checked and oriented with the help of the expected Laue patterns for respective crystal structures using the Cologne Laue indexation program (CLIP software) [106].

1.3.3   Magnetization

The magnetization measurements presented in this thesis were performed using the Quantum Design magnetic-property measurement system - MPMS-XL and MPMS3 [107]. In particular, the oriented and weighted single-crystals were mounted on a brass-holder equipped with quartz tubes or a quartz holder (for low-moment samples) using vacuum grease for magnetization measurements. In an MPMS, any change in the magnetic flux facilitated by the movement of the magnetic sample produces a current in the pick-up coils. The pick-up coils are connected to the superconducting quantum interference device (SQUID) resulting in a very high-sensitivity of moment detection amounting to less than 10^{-8} emu [107]. In a typical experiment, the variation of the sample magnetization with respect to temperature in the range 2-400 K and in magnetic-fields up to 7 T is measured. The measurements were performed either in the DC or the VSM mode.

The magnetization measurements with respect to rotation angle (θ) were also performed using the rotator option of the MPMS3 to study the magnetic anisotropy of the materials [108]. Note that, the rotator measurements can only be performed in a DC mode. The single-crystals were mounted either on a horizontal rotator to study out of plane, i.e. ab plane to c axis anisotropy or a thin-film rotator to study the anisotropy in the ab-plane. Here a, b and c denote the principal crystallographic directions.

Furthermore, the high-field magnetization measurements in magnetic fields up to 15 T were performed using the vibrating sample magnetometer (VSM) option of the Quantum Design physical property measurement system (PPMS) [109]. Here the oriented single crystalline samples are also mounted on a brass holder with quartz tubes but doesn't feature a SQUID detection technique, hence resulting in a lower magnetic moment sensitivity of 10^{-6} emu as compared to MPMS.

1.3.4   Single-crystal X-ray diffraction

To study in-detail the crystallographic structure of the materials, high-resolution single-crystal X-ray diffraction experiments (S-XRD) were performed. These experiments were performed

by Prof. Dr. Hubert Wadepohl of the Inorganic-Chemistry Institute in Heidelberg University. Small single crystal pieces which are extracted close to the larger oriented single-crystals from as-grown boule were employed, to perform S-XRD at 100 K using Mo $K\alpha$ ($\lambda = 0.71073$ Å) radiation. Further details on the data collection, intensity corrections and analysis can be found in Chapter2.

1.3.5   Single-crystal neutron diffraction
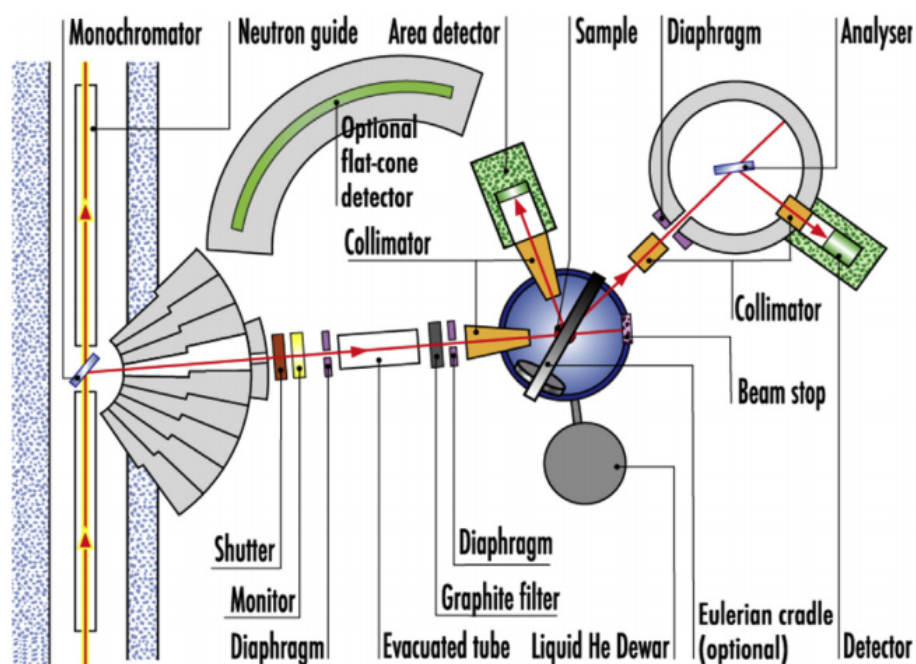
Figure 1.14. Schematic representing the D10 instrument at the Institut Laue-Langevin, Grenoble, France. Taken from Ref. [110].

The crystal structure at lower temperatures (up to 2 K) and the magnetic structure of the single-crystals were studied by means of four-circle single-crystal neutron diffractometer D10 at the Institute Laue-Langevin, Grenoble. The four-circle has Euler geometry. A pyrolytic-graphite (PG) or a Cu (200) crystal can be used as a monochromator to access wavelengths between 1.1 and 6 Å and a vertically focusing pyrolytic graphite is used as an analyser. A neutron flux of $\geq 5 \times 10^6$ cm^{-2}s^{-1} is available. An 80×80 mm^2 two-dimensional microstrip detector for three dimensional resolution in the reciprocal space or a single ^{3}He detector are available. In the four-circle mode, the Eulerian cradle can be equipped with a helium-flow cryostat to access temperatures in the range 0.1 K to 450 K. Pressure cells and cryomagnets (0-15 T) may also be mounted with computer control of double-axis tilt stage to allow limited out of plane access.

All the obtained integrated intensity data of the corresponding nuclear and magnetic Bragg

peaks were refined against the most suitable model using the wfp2k Rietveld program of the WinPLOTR software [111].

Chapter 2

Single-crystal growth, magnetoelastic coupling and magnetic phase diagram of easy-plane type ilmenite titanates

2.1 Magnetic phase diagram and magnetoelastic coupling of NiTiO$_3$

The following chapter has been published in Physical Review B under the title "Magnetic phase diagram and magnetoelastic coupling of NiTiO$_3$" [41]. Copyright ©2021 American Physical Society. All rights reserved.

In the following, contributions of each co-authors are explained in detail, particularly highlighting the specific contribution of K. Dey who is the first and the communicating author.

- The single-crystal growth and characterization (Fig. 1), magnetization measurements and analysis of specific heat (Fig. 2 and Fig. 4(b)), magnetic phase diagram construction (Fig. 6) and Grüneisen analysis (Fig. 8) were performed by K. Dey. Except parts of thermal expansion and magnetostriction discussion, the manuscript draft was written by K. Dey.

- S. Sauerland is a shared first author to this manuscript and performed the thermal expansion (Fig. 3 and Fig. 5) and magnetostriction measurements (Fig. 7). S. Sauerland assisted in Grüneisen analysis and wrote the thermal expansion and magnetostriction discussion part in the paper.

- J. Werner performed the high-field magnetization measurements (Fig. 4) and took part in some discussions.

- Y. Skourski was the local contact at HLD-EMFL, Dresden and supervised the high-field magnetization measurements.

- M. Abdel-Hafiez performed the specific heat measurements (Fig. 2(b)).

- R. Bag assisted in single-crystal growth at IISER Pune using the CSC furnace.

- S. Singh supervised the single crystal growth experiments performed at ambient pressures.

- R. Klingeler supervised the measurements and supported data analysis and manuscript writing.

- All authors proofread the manuscript.

Magnetic phase diagram and magnetoelastic coupling of NiTiO₃

K. Dey,[1,*,†] S. Sauerland,[1,†] J. Werner [1] Y. Skourski,[2] M. Abdel-Hafiez,[3] R. Bag,[4] S. Singh,[4] and R. Klingeler[1,5]

[1]*Kirchhoff Institute of Physics, Heidelberg University, INF 227, D-69120 Heidelberg, Germany*
[2]*Dresden High Magnetic Field Laboratory (HLD-EMFL), Helmholtz-Zentrum Dresden Rossendorf, D-01314 Dresden, Germany*
[3]*Harvard University, Cambridge, Massachusetts 02138, USA*
[4]*Indian Institute of Science Education and Research, Pune, Maharashtra 411008, India*
[5]*Centre for Advanced Materials (CAM), Heidelberg University, INF 225, D-69120 Heidelberg, Germany*

We report high-resolution dilatometry on high-quality single crystals of NiTiO₃ grown by means of the optical floating-zone technique. The anisotropic magnetic phase diagram is constructed from thermal expansion and magnetostriction studies up to $B = 15$ T and magnetization studies in static (15-T) and pulsed (60-T) magnetic fields. Our data allow us to quantitatively study magnetoelastic coupling and to determine uniaxial pressure dependencies. While the entropy changes are found to be of magnetic nature, Grüneisen analysis implies only one relevant energy scale in the whole low-temperature regime. Thereby, our data suggest that the observed structural changes due to magnetoelastic coupling and previously reported magnetodielectric coupling [L. Balhorn, J. Hazi, M. C. Kemei, and R. Seshadri, Phys. Rev. B **93**, 104404 (2016)] are driven by the same *magnetic* degrees of freedom that lead to long-range magnetic order in NiTiO₃.

I. INTRODUCTION

The search for new multiferroics, i.e., materials concomitantly exhibiting various ferroic orders such as magnetic and electric order coupled to each other [1], has revived interest in the family of ilmenite-structured compounds. There are various titanates MTiO₃ (M = Mn, Fe, Co, Ni) which crystallize in the ilmenite structure within the space group R-3. The crystal structure consists of alternate layers of corner sharing TiO₆ and MO₆ octahedra stacked along the c axis [2]. Previous magnetic [3–5] and powder neutron diffraction studies [6–9] report that long-range antiferromagnetic (AFM) order evolving at low temperatures is of the G type for MnTiO₃, and of the A type for FeTiO₃, CoTiO₃, and NiTiO₃. In the ordered phase, the magnetic moments associated with M^{2+} ions are collinearly arranged along the c axis in MnTiO₃ and with a slight spin tilting of $1.6°$ away from the c axis in FeTiO₃. The easy-plane-type AFM order in CoTiO₃ and NiTiO₃ is characterised by spins lying in the ferromagnetic ab layers which are aligned antiferromagnetically along c. In FeTiO₃, the onset of long-range magnetic order, at T_N, is associated with significant changes of the lattice parameters indicating magnetoelastic coupling [9]. Magnetodielectric and polarization measurements on MnTiO₃ show an anomaly in the dielectric permittivity, ϵ, at T_N, while finite polarization is found in applied external magnetic fields indicating that it may realize a linear magnetoelectric material [10]. Both in CoTiO₃ and NiTiO₃, anomalies in ϵ at T_N and a strong field dependent

magnetocapacitance in the ordered state indicate the presence of large magnetodielectric coupling [11]. Furthermore, the observation of Dirac magnons in CoTiO₃ from recent inelastic neutron scattering studies [12] has peaked interest in this series of materials. Despite clear evidence of pronounced magnetodielectric coupling in all known MTiO₃, its origin and mechanism have not yet been elucidated. In order to address this question, we have grown large, high-quality single crystals of NiTiO₃ by means of the optical floating-zone technique under various atmospheres and at different pressure. The single crystals were used for high-resolution studies of thermal expansion and magnetostriction along the crystallographic a and c axes, respectively. Though such investigations have been shown to provide detailed insight into underlying mechanism of multiferroics (see, e.g., Refs. [13–18]), there are no high-resolution dilatometry studies on MTiO₃ single crystals yet. In addition, comparing the magnetic length and entropy changes as detected by thermal expansion coefficients and specific heat allow determining the uniaxial and hydrostatic pressure dependencies by means of Grüneisen scaling. Analysis of the Grüneisen ratio, i.e., the ratio of thermal expansion coefficient and heat capacity, has been particularly suggested by Spaldin *et al.* for the related compound EuTiO₃ as it can clarify the potential multiferroic quantum critical nature [19]. Our dilatometry studies are accompanied by magnetization studies in static (15-T) and pulsed (60-T) magnetic fields which enable constructing the anisotropic phase diagram in NiTiO₃ which has not been established yet.

II. EXPERIMENTAL METHODS

NiTiO₃ powder was prepared via standard solid-state reaction of stoichiometric amounts of NiO and TiO₂ between

---

*kaustav.dey@kip.uni-heidelberg.de
†These authors contributed equally to this work.

1150° and 1350 °C with several intermediate grinding steps. The powder was made into rods of length 10 cm and 5 mm in diameter by hydrostatically pressing the powders at 700 bar and annealing them for 24 h at 1350 °C. Single crystals of $NiTiO_3$ were grown in a four-mirror optical floating-zone furnace (Crystal system corporation, Japan) equipped with 4×150 W halogen lamps at IISER Pune and in a two mirror high-pressure optical floating-zone furnace (HKZ, SciDre) equipped with a 3500-W Xe arc lamp at Heidelberg University. Macroscopic single crystals were grown at 3 mm/h under various atmospheres and up to 5 bar pressure. Phase purity of the powder and the ground single crystals was studied by means of powder x-ray diffraction measurements on a Bruker D8 Advance ECO diffractometer with Cu-Kα source. Laue diffraction in back scattering geometry was performed to study the crystallinity and to orient the single crystals. Structural Rietveld refinements were carried out using the Full Prof suite 2.0 [20].

Static magnetization $\chi = M/B$ was studied in magnetic fields up to 15 T applied along the principal crystallographic axes by means of a home-built vibrating sample magnetometer [21] (VSM) and in fields up to 5 T in a Quantum Design MPMS-XL5 SQUID magnetometer. Pulsed-magnetic-field magnetization was studied up to 60 T at Helmholtz Zentrum Dresden Rossendorf by an induction method using a coaxial pick-up coil system [22]. The pulse raising time was 7 ms. The pulsed-field magnetization data were calibrated using static magnetic field measurements. Specific heat measurements at 0 T and 9 T has been done in a Quantum Design PPMS using a relaxation method. The relative length changes dL_i/L_i were studied on a cuboid shaped single crystal of dimensions $2 \times 1.85 \times 1$ mm^3. The measurements were done by means of a three-terminal high-resolution capacitance dilatometer [23]. In order to investigate the effect of magnetic fields, the linear thermal expansion coefficient $\alpha_i = 1/L_i dL_i(T)/dT$ was studied in magnetic fields up to 15 T. In addition, the field induced length changes $dL_i(B)/L_i$ were measured at various fixed temperatures in magnetic fields up to 15 T and the longitudinal magnetostriction coefficient $\lambda_i = 1/L_i dL_i(B)/dB$ was derived. The magnetic field was applied along the direction of the measured length changes.

III. NiTiO₃ SINGLE CRYSTAL GROWTH

Single crystals of $NiTiO_3$ were grown by the optical floating-zone method using polycrstalline feed and seed rods as starting material. The phase purity of the $NiTiO_3$ powders used for making the feed and seed rods has been studied by means of powder XRD after each sintering step. Rietveld refinement of these data indicates the presence of ilmenite phase (R-3) as well as an additional ($\approx 1\%$) TiO$_2$ (rutile) phase. In order to achieve phase pure high-quality single crystals, a variety of crystal growth experiments were performed under different atmosphere and pressure and by means of both the four-mirror horizontal configuration and two-mirror vertical configuration optical furnaces [24,25]. The optimized growth parameters employed during crystal growth are listed in Table I.

Depending on the growth parameters, the processes summarized in Table I yield mm- to cm-sized single crystals.

TABLE I. Growth parameters, lattice parameters, and phase analysis from the Rietveld refinement of the room temperature powder XRD data of crushed $NiTiO_3$ single crystals. Feed and seed rods were counter-rotated at the same rotation speed.

Furnace	CSC	CSC	HKZ
Atmosphere	O_2	air	Ar
Pressure	Ambient	Ambient	5 bar
Growth rate (rpm)	3	3	4-6
Rotation speed (mm/h)	20	10	15
Latt. parameter a (Å)	5.0304	5.0304	5.0304
Latt. parameter c (Å)	13.7881	13.7845	13.7862
Crystal size	cm	cm	mm
Secondary phase (appr.)	1% TiO$_2$ + NiO	1% TiO$_2$	1% NiO

Figure 1(a) shows a representative $NiTiO_3$ boule grown in air at ambient pressure. The shiny surface of the grown boule indicating the presence of single crystal of several cm in length. Rietveld refinement of powder XRD data of the ground and pulverized single crystalline pieces extracted from the boules [see Fig. 1(b) and Table I] implies the main ilmenite
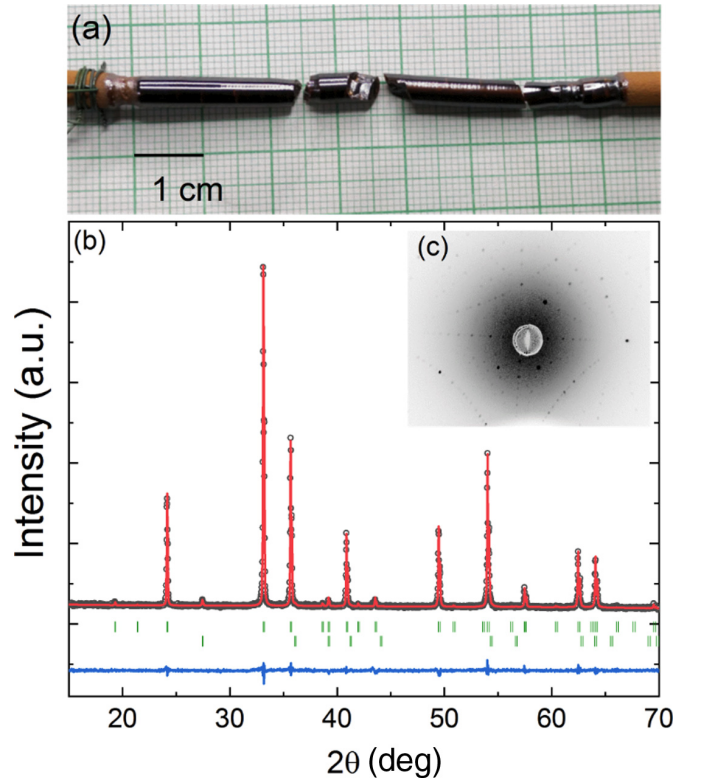
FIG. 1. (a) Picture of a shiny $NiTiO_3$ boule grown in air atmosphere at ambient pressure and (b) Rietveld refinement fit of the room temperature XRD data of a powdered $NiTiO_3$ single crystal. The observed diffraction pattern is shown in black, calculated pattern in red and the difference between the observed and the calculated pattern is shown in blue. The upper vertical ticks in green denote the allowed Bragg positions of the ilmenite phase and the lower ticks denote the Bragg positions of TiO$_2$ in rutile phase. (c) Representative Laue pattern of the $NiTiO_3$ single crystal oriented along (010) direction.

phase as well as an impurity TiO_2 phase of about 1%. When grown in O_2 atmosphere, there is also an additional NiO phase. In order to further investigate the growth process of $NiTiO_3$ and to reduce the secondary phase content, $NiTiO_3$ was also grown under 5 bar pressure in Ar atmosphere. In this case, the resulting boule is mostly of polycrystalline nature with only mm-sized shiny single crystalline regions toward the end of the boule. Phase analysis of a single crystalline piece extracted from this region shows the presence of about 1 % NiO secondary phase while the TiO_2 phase is absent. We conclude that inert atmosphere does not support optical floating-zone-growth of $NiTiO_3$ single crystals. For the magnetic studies presented below, we employ crystals grown in air as they exhibit only a small nonmagnetic impurity phase. Laue diffraction performed at several spots along the length of grown boules confirm the presence of macroscopic cm-sized single crystalline grains with high crystallinity [see Fig. 1(c)]. For the measurements reported below, a cuboid shaped single crystal of dimensions $2 \times 1.85 \times 1$ mm^3 has been extracted from the boule grown in air and oriented along three principal crystallographic directions.

IV. EXPERIMENTAL RESULTS

A. Magnetoelastic coupling

The onset of long-range antiferromagnetic order in $NiTiO_3$ at $T_N = 22.5(5)$ K is associated with pronounced anomalies in magnetic susceptibility and specific heat (Fig. 2). For $T \leqslant T_N$, the susceptibility is anisotropic with a decrease for magnetic fields B applied in the ab plane and attaining a constant value for $B||c$ axis suggesting an easy-plane-type antiferromagnet. This is in accordance with the previous studies [4,6]. At high temperatures, the susceptibility is isotropic and obeys a Curie-Weiss behavior. Fitting the averaged susceptibility [inset to Fig. 2(a)] at $T > 100$ K by means of a Curie-Weiss-like law $\chi = \chi_0 + N_A \mu_{\text{eff}}^2/3k_B(T - \Theta)$ yields $\chi_0 = 1.93 \times 10^{-4}$, the effective magnetic moment $\mu_{\text{eff}} = 3.17(5) \ \mu_B$ and the Weiss temperature $\Theta = -11(1)$ K. Using the spin-only value $S = 1$ for Ni^{2+} implies an effective g factor of 2.24(4). Note, that our measurements yield a smaller value than $\mu_{\text{eff}} = 4.01 \ \mu_B$ previously reported for a single crystal [4] but is similar to the values reported for polycrystalline samples [3,11].

The sharp λ-shaped anomalies in the specific heat [Fig. 2(b)] and in Fisher's specific heat [26] $\partial(\chi_a T)/\partial T$ [Fig. 2(a)] confirm the onset of long-range magnetic order at T_N and also indicate high crystallinity of the single crystal. Furthermore, the anomaly presents a continuous nature of the phase transition. The phonon contribution to the specific heat (c_p^{ph}) has been estimated by fitting the c_p data at temperatures well above T_N by an extended Debye model which includes both Debye and Einstein terms [27]. The model fits very well for temperatures above about 50 K and yields characteristic Debye and Einstein temperatures of $\Theta_D = 786$ K and $\Theta_E = 230$ K, respectively. The sum of the obtained coefficients of the individual terms $n_D = 3.94$ and $n_E = 0.94$ reasonably agrees to the expected value of 5 which reflects the number of phonon modes given by the number of atoms per formula unit. Integrating the magnetic specific heat (c_p-c_p^{ph})/T yields a total magnetic entropy change $S_{\text{mag}} =$
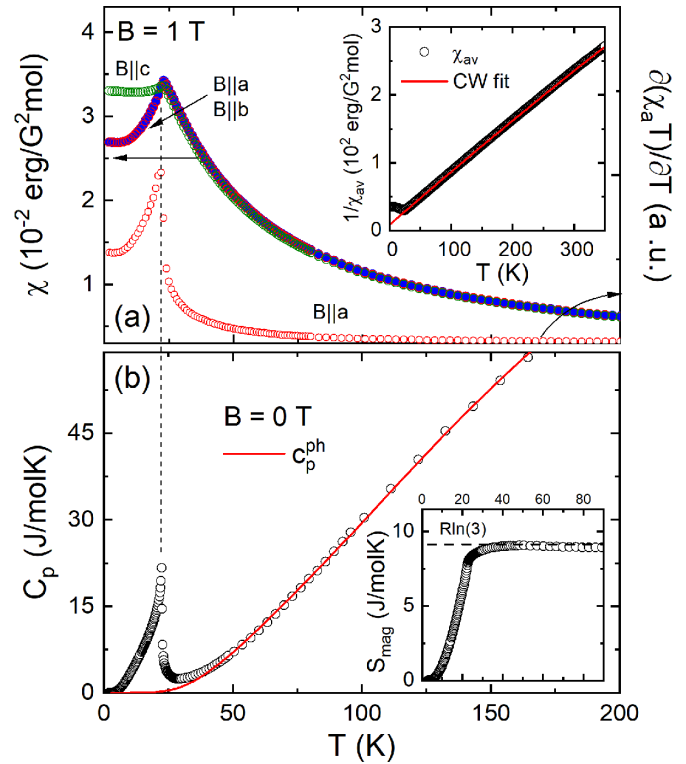
FIG. 2. (a) Temperature dependence of the static magnetic susceptibility $\chi = M/B$ (left axis) and the derivative $\partial(\chi T)/\partial T$ (right axis) at $B = 1$ T applied along main crystallographic directions and (b) temperature dependence of the specific heat c_p in zero magnetic field. The solid line in (b) indicates the phonon specific heat c_p^{ph} obtained by fitting c_p data with a combined Debye and Einstein model well above the magnetic ordering transition (see the text). Insets: (a) Curie-Weiss fit (red line) to the inverse averaged susceptibility $1/\chi_{\text{av}}$. (b) Magnetic entropy changes obtained by integrating (c_p-c_p^{ph})/T.

9.1(1) J/(mol K) which agrees to the theoretically expected value for $S = 1$ Ni^{2+} spins of $R \ln(3) = 9.13$ J/(mol K). We conclude that the entropy changes are of magnetic nature. The measured entropy changes imply that nearly 20% of magnetic entropy is consumed between T_N and 50 K, suggesting the presence of short-range magnetic correlation persisting up to temperatures as high as twice the ordering temperature.

The evolution of long-range magnetic order is associated with pronounced length changes as illustrated by strong anomalies in the uniaxial thermal expansion coefficients α_i ($i = a, c$) and in the relative length changes dL_i/L_i (Fig. 3). The anomalies demonstrate the presence of significant magnetoelastic coupling in $NiTiO_3$. The measured relative length changes shown in the inset of Fig. 3 signal shrinking of the c axis and increase of the a axis on evolution of magnetic order at T_N. The signs of the anomalies indicate positive uniaxial pressure dependence of T_N for pressure along c axis, i.e., $\partial T_N/\partial p_c > 0$, whereas the anomaly in α_a indicates $\partial T_N/\partial p_a$ being negative and considerably smaller. The anomaly in the volume thermal expansion coefficient $\alpha_V = \alpha_c + 2\alpha_a$ implies a significant positive hydrostatic pressure dependency of T_N. In addition, opposite sign of the anomalies in α_a and α_c enables reading-off the data in Fig. 3 that structural effects
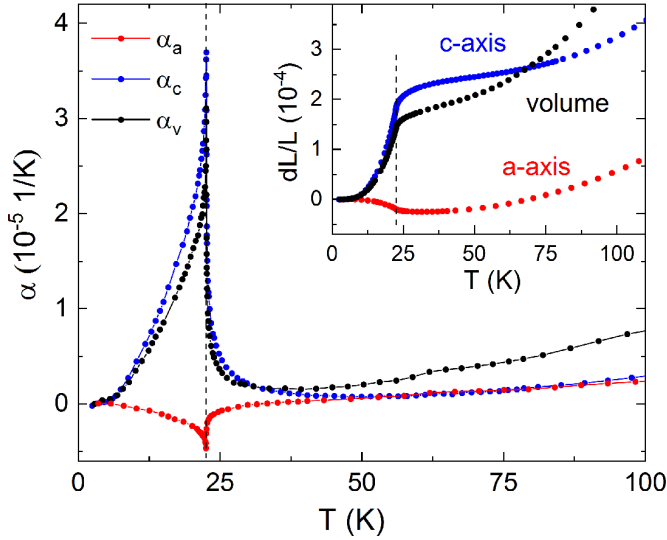
FIG. 3. Thermal expansion coefficients α_i along the crystallographic a and c axes and the volume thermal expansion coefficient α_V. The inset shows the relative length changes dL_i/L_i. Dashed lines mark T_N.

above T_N precursing the onset of long-range order extend up to about 50 K. This coincides with the temperature regime where magnetic entropy changes mark the onset of short-range magnetic correlations.

B. Magnetic phase diagram

The saturation fields and moments at $T = 1.5$ K are deduced from pulsed-field magnetization studies up to 60 T which are shown in Fig. 4(a). For both field directions $B||c$ and $B||a$, the magnetization shows a linear behavior in a wide range of applied fields. The saturation fields nearly coincide and amount to $B_{sat} = 36.0(5)$ T. Also the saturation magnetisations as indicated by the dashed horizontal lines in Fig. 4(a) agree with each other within error bars at $M_{sat} = 2.23(5)$ μ_B/f.u.. For $S = 1$, this yields $g = 2.23(5)$ which agrees well with the value of 2.24(4) derived from the Curie-Weiss fit to the static magnetic susceptibility presented in Fig. 2. A more detailed look at the low-field behavior in Fig. 4(b), at $T = 2$ K, confirms that linearity of M vs. $B||c$ extends to zero magnetic field while nonlinear behavior is observed when the magnetic field is applied along the a axis. To be specific, the derivative of the magnetization with respect to magnetic field shows a broad peak centered at $B^* = 1.20(5)$ T and subsequently a constant behavior [see Fig. 4(b)]. The data suggest spin reorientation which we attribute to finite anisotropy in the ab plane. At $T = 2$ K, the magnetization jump at B^* is estimated to $\Delta M \approx 0.03$ μ_B/f.u. Remaining slight nonlinearity above B^* is indicated by the static magnetic susceptibility measured in magnetic fields up to 15 T [Figs. 4(c) and 4(d)]. While there is no significant field effect for $T > T_N$, the data exhibit a monotonous change for $T < T_N$ at applied fields $B \geqslant 3$ T as compared to $B = 1$ T. Overall, the data confirm spin-reorientation behavior as for $B \geqslant 3$ T (i.e., above B^*) the susceptibility attains an almost constant value below T_N whereas it decreases sharply for $B||a = 1$ T.
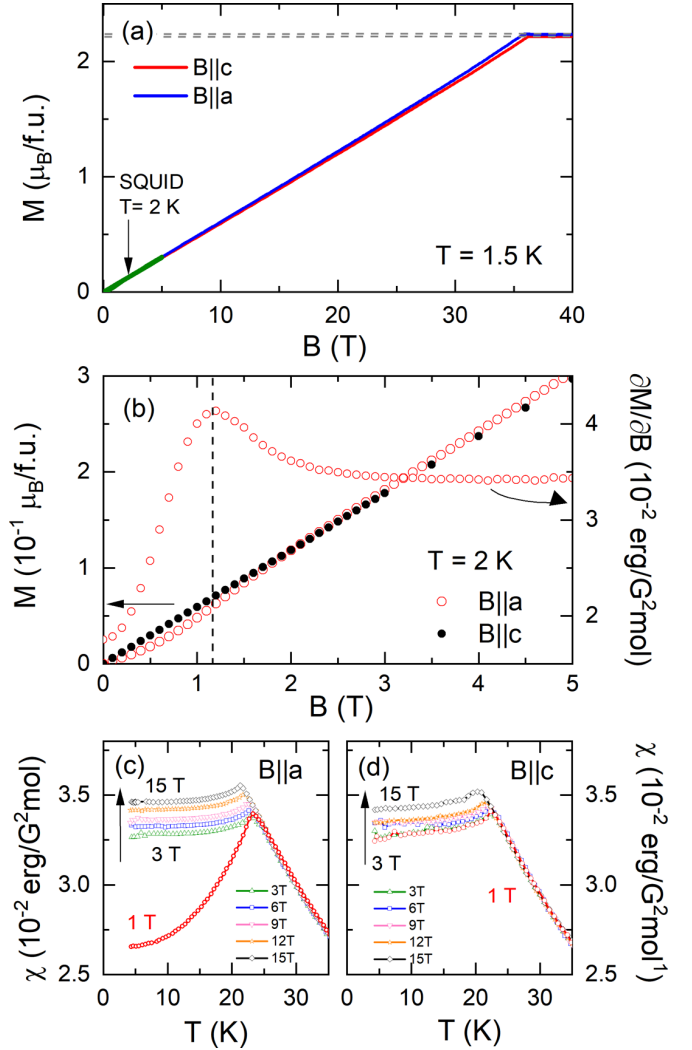
FIG. 4. (a) Pulsed-field magnetization M at $T = 1.5$ K, (b) quasistatic field magnetization M and magnetic susceptibility $\partial M/\partial B$ vs. magnetic field along the a- and c axes, at $T = 2$ K, [(c) and (d)] static magnetic susceptibility $\chi = M/B$ vs. temperature for magnetic fields up to 15 T applied along the a- and c axes, respectively.

In addition, the phase boundary $T_N(B)$ marked as peak in the static susceptibility is determined.

Sharp λ-shaped anomalies observed in α_i ($i = a, c$) in external magnetic fields (Fig. 5) enable to further determine the phase boundaries and to study the magnetic field effect on the lattice parameters. While the shape of the anomalies are not significantly affected by magnetic fields, T_N expectedly shifts to lower temperatures on application of external magnetic fields. For both field directions, a similar shift of $\Delta T_N \approx 1.5$ K is observed when applying $B = 15$ T. This corroborates well with the magnetization data in Figs. 4(c) and 4(d) and signals overlying phase boundaries for B applied along the a and c axes, respectively (see Fig. 6). Corresponding anomalies signaling $T_N(B)$ (or synonymously the temperature dependence of the critical field $B_c(T)$ which signals melting of magnetic order, too) appear in the relative length changes versus magnetic field (Fig. 7) and in the magnetostriction coefficients (see supplemental material, Fig. S1 [34]) and
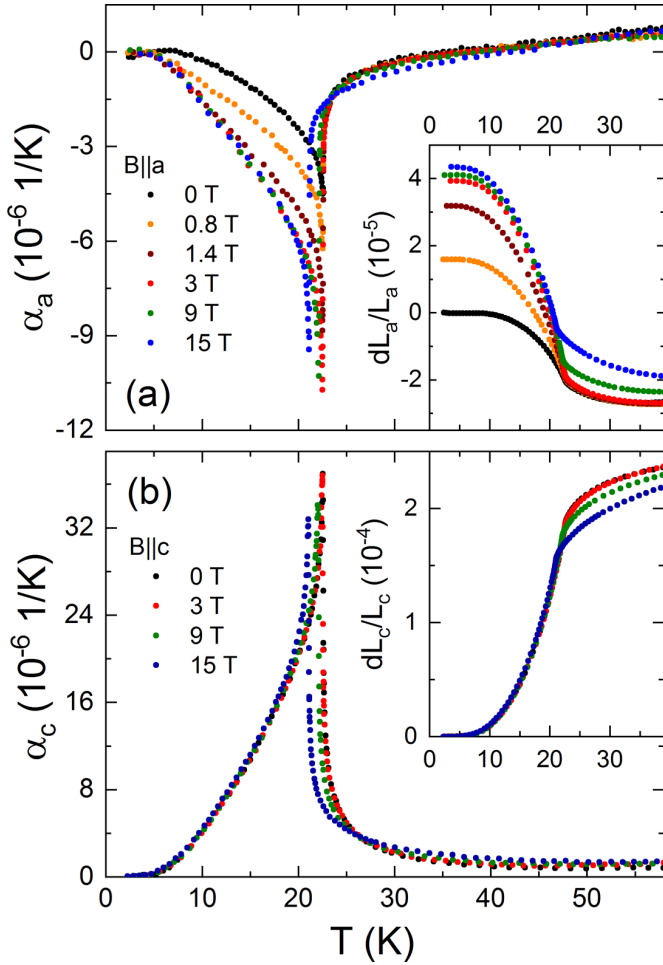
FIG. 5. Thermal expansion coefficients α_i at magnetic fields between 0 T and 15 T applied along the a- and c axes, respectively, of NiTiO$_3$. Insets show the corresponding relative length changes shifted with respect to each other by means of magnetostriction curves, at $T = 30$ K.

FIG. 6. Magnetic phase diagram of NiTiO$_3$ constructed from magnetization $M(T, B)$, dilatometry $L(T, B)$ and specific heat data. Closed (open) markers correspond to magnetic fields applied along the a axis (c axis). Lines are guides to the eye. AFM, SR, PM label the antiferromagnetically ordered, spin-reoriented and paramagnetic phases, respectively.
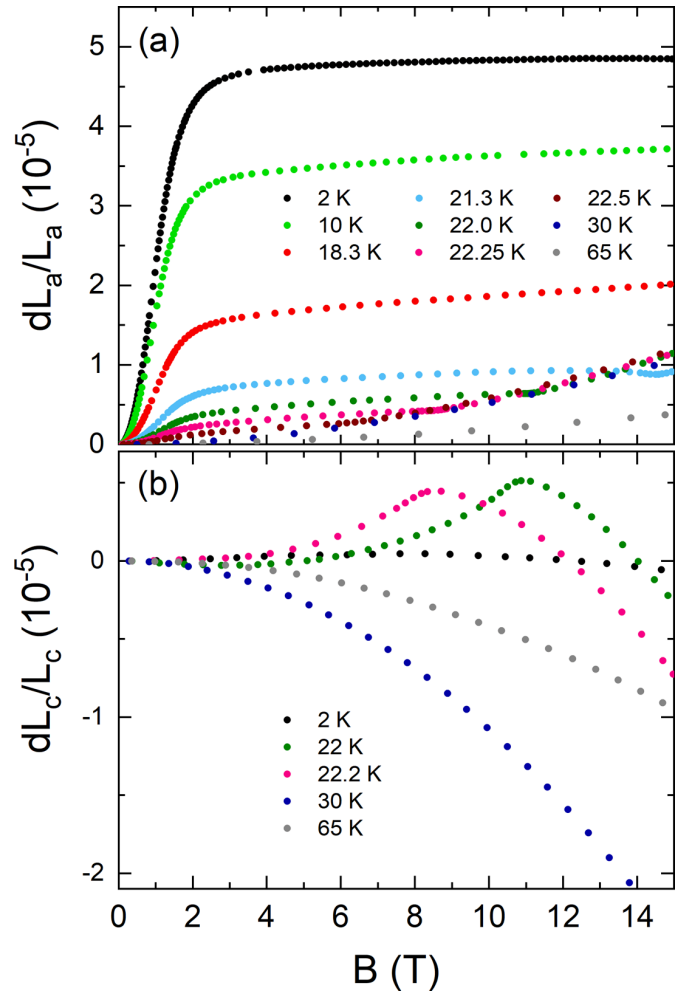
FIG. 7. Relative length changes versus magnetic field applied along a and c axes at different temperatures.

enable constructing the magnetic phase diagram displayed in Fig. 6. To 15 T, $T_N(B)$ obeys a square-root behavior.

The thermal expansion in magnetic field and the magnetostriction data in Figs. 5 and 7, respectively, show small increase of the a axis and decrease of the c axis in magnetic fields applied in the respective directions. Interestingly, except for effects associated with suppression of T_N, there are no large length changes dL_c driven by $B\|c \lesssim 15$ T. Correspondingly, the magnetostriction λ_c, at 2 K (see supplemental material, Fig. S1 [34]), is small and amounts to a few 10^{-7} T^{-1} only. While a similar behavior is found for λ_a at $B\|a \gtrsim 5$ T, there are pronounced length changes at low fields which we associate with spin-reorientation. The corresponding half height of these jump like anomalies in dL_a/L_a is at consistent fields as the peak in $\partial M/\partial B$ and yields B^* (see Fig. 6). Notably, these field-induced changes imply that the total thermal expansion changes in the magnetically ordered phase become considerably larger in applied magnetic fields [see the inset of Fig. 5(a)]. Quantitatively, spin reorientation at 2 K is associated with length changes of $\Delta L_a/L_a \approx 4.8 \times 10^{-5}$. On heating, the size of magnetostriction decreases but,

nonetheless, significantly exceeds length changes observed at $T > T_N$.

C. Discussion

Knowledge on the saturation fields B_{sat} enables estimating the effective antiferromagnetic exchange interaction J_{AF} driving the A-type nature of magnetic order. Applying a two-sublattice mean-field model, the saturation field, at $T = 0$, is determined by interplane interaction and magnetic anisotropy. The fact that B_{sat} does not depend on the magnetic field direction, i.e., $B_{sat}^{\parallel} \simeq B_{sat}^{\perp}$, suggests a negligible effect of the latter. By employing

$$g\mu_B B_{sat} = E(\uparrow\downarrow) - E(\uparrow\uparrow) = 2J_{AF}$$

we obtain the effective interplanar exchange coupling $J_{AF}/k_B = 25.1(5)$ K. Here $E(\uparrow\downarrow)$ denotes the energy associated with the A-type AFM state at $B = 0$ and $E(\uparrow\uparrow)$ that of the fully spin-polarized state at $B > B_{sat}$. In addition, validity of the Curie-Weiss law down to nearly T_N indicates that mean-field equations relating experimental values of the Weiss temperature Θ and the Néel temperature T_N can be used to estimate effective in-plane and interplane couplings J_{FM} and J_{AF}. Following Refs. [28,29], we obtain $J_{AF}/k_B = 25.1(5)$ K which agrees very well with analysis of B_{sat}, and $J_{FM} = 8.5(5)$ K.

Comparing the nonphononic contributions to the thermal expansion coefficient and to the specific heat enables further conclusions on the nature of the associated (i.e., magnetic) entropy changes and on the hydrostatic pressure dependencies. In order to assess the magnetic contribution to the volume thermal expansion coefficient, α_V^{mag}, we have approximated the phonon contribution, α_V^{ph}, by scaling the background specific heat c_p^{ph} (cf. Fig. 2) by means of an appropriate Grüneisen parameter $\gamma^{ph} = \alpha_V^{ph}/c_p^{ph}$ [30]. For that purpose, a Debye-Einstein model with fixed Θ_D and Θ_E of the fit to the specific heat data has been fitted to the high-temperature data of α_V leaving only the two associated lattice Grüneisen parameters γ_D and γ_E as scaling factors. Similarly to the specific heat, at $T \gtrsim 50$ K, α_V is well described by the phonon background α_V^{ph} with $\gamma_D = 2.8 \times 10^{-7}$ mol/J and $\gamma_E = 2.3 \times 10^{-7}$ mol/J as shown in the inset of Fig. 8.

The resulting nonphonon contribution α_V^{mag} to the thermal expansion coefficient is shown in Fig. 8(a) (right ordinate) together with the respective magnetic specific heat data c_p^{mag} (left ordinate). Both quantities are proportional to each other in the entire temperature range, i.e., there is a T-independent Grüneisen parameter describing the ratio of pressure and temperature dependence of entropy changes in this temperature range. This observation clearly implies the presence of a single dominant energy scale ϵ [31]. As entropy changes are of magnetic nature, we conclude that a single magnetic degree of freedom drives the observed nonphonon length and entropy changes. The corresponding scaling parameter obtained is the magnetic Grüneisen parameter [30]

$$\gamma_m = \frac{\alpha_V^{mag}}{c_p^{mag}} = \frac{1}{V}\frac{\partial \ln \epsilon}{\partial p}\bigg|_T = 1.18(3) \times 10^{-6} \text{mol/J}.$$
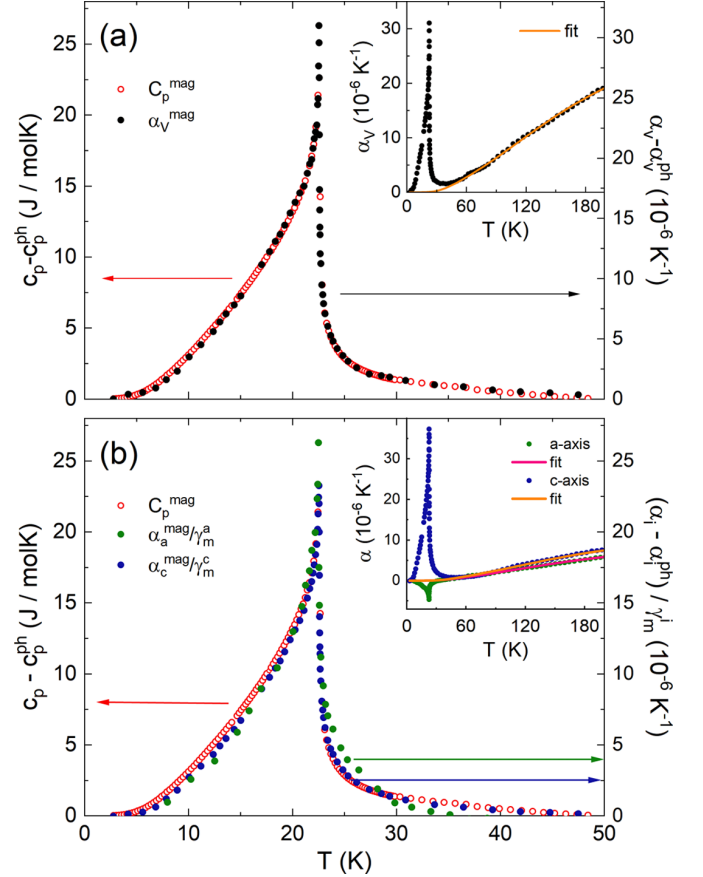
FIG. 8. Grüneisen scaling of the magnetic contributions to the heat capacity (c_p^{mag}) and (a) volume thermal expansion coefficient (α_V^{mag}). The inset shows α_V vs. temperature together with a combined Debye-Einstein fit to the high-temperature data (see the text). (b) Grüneisen scaling with uniaxial thermal expansion coefficients α_a and α_c.

Using the Ehrenfest relation, the obtained value of γ_m enables to determine the hydrostatic pressure dependence of the ordering temperature, i.e., $dT_N/dp = T_N V_m \gamma_m = 1.12(4)$ K/GPa which is deduced using the molar volume of $V_m = 42.01$ cm³/mol. Elaborating Grüneisen scaling for the uniaxial thermal expansion coefficients individually, good proportionality is confirmed between c_p^{mag} and α_a^{mag} and α_c^{mag} as well [Fig. 8(b)]. This yields the uniaxial pressure dependencies of $dT_N/dp_a = -0.21(3)$ K/GPa and $dT_N/dp_c = 1.51(7)$ K/GPa for pressure applied along the a and c axis, respectively. The uniaxial values are fully consistent with the obtained hydrostatic pressure dependence.

On a microscopic level (see supplemental material, Fig. S4 [34]), Ni-O-Ni bonding angles in the ab planes of 90.5(3)° implying nearest-neighbor FM exchange interaction J_{nn} are supposed to increase when hydrostatic pressure is applied, i.e., J_{nn} becomes smaller. The main exchange paths contributing to J_{AF} do not suggest a clear picture which prohibits a qualitative analysis.

Magnetostriction measurements in the paramagnetic regime, i.e., where $M = \chi B$, enable to extract the uniaxial pressure dependence of magnetic susceptibility by exploiting the relation $dL_i/L_i = -1/2V \partial \chi_i/\partial p_i B^2$ [32].

Plotting the data accordingly (see supplemental material Fig. S2 [34]) allows to read off $\partial(\ln \chi_a)/\partial p_a = -1.3\% \, \mathrm{GPa}^{-1}$ and $-0.8\% \, \mathrm{GPa}^{-1}$ at 30 and 65 K, respectively, as well as $\partial(\ln \chi_c)/\partial p_c = +3.1\% \, \mathrm{GPa}^{-1}$ and $+2.2\% \, \mathrm{GPa}^{-1}$ at respective temperatures. Qualitatively, this suggests AFM exchange interactions to be strengthened and FM ones to be weakened by uniaxial pressure along the a axis. While, uniaxial pressure along the c axis is found to result in opposite effects. Considering the results of Grüneisen analysis presented above, i.e., predominance of only one energy scale as well as $\partial T_N/\partial p_a < 0$ and $\partial T_N/\partial p_c > 0$, suggests that the value of T_N is mostly affected by the (in-plane) FM exchange interactions. This is also reflected in the increase of T_N and Weiss temperature θ when substituting Ni over Co to Fe in $M\mathrm{TiO}_3$ whereby even $\theta > 0$ is observed for FeTiO_3 [3].

The phase boundary of spin-reorientation features a very small slope $\partial B^*/\partial T \approx 4 \times 10^{-3}$ T/K. Considering the magnetization jump ΔM at B^* and exploiting the Clausius-Clapeyron relation, we estimate associated entropy changes $\Delta S^* = -(\partial T/\partial B^*)^{-1} \cdot \Delta M^* \approx -8 \times 10^{-4}$ J/(mol K) [33]. This implies only insignificant entropy changes associated with spin reorientation. On the other hand, in applied magnetic fields $B \| a$, our data show that the total thermal expansion changes dL_a/L_a in the magnetically ordered phase become significantly larger (see the inset of Fig. 5). This suggests that Grüneisen scaling which is valid at $B = 0$ T as evidenced by Fig. 8 is broken in magnetic fields $B \| a > B^*$. Somehow correspondingly, uniaxial pressure dependence of B^* is very large. Using the measured jumps in relative length changes ($\Delta L_a/L_a$) and magnetization (ΔM) at B^* and 2 K and exploiting the Clausius-Clapeyron relation yields $\partial B^*/\partial p_a = V(\Delta L_a/L_a)/\Delta M \approx 9.2$ T/GPa. This is a huge value similar to what has been observed, i.e., in TlCuCl_3 [32]. It implies strong effects of uniaxial pressure along the a axis so that applying p_a would strongly enhance the spin reorientation field while it would vanish for tiny hypothetical negative pressure.

Below T_N, due to the presence of small in-plane anisotropy one might assume that magnetostriction would locally distort the lattice to a lower symmetry $P - 1$. While such symmetry breaking has not yet been observed in previous neutron diffraction experiments, the fact that this distortion is expected to increase with application of magnetic field might allow detecting such symmetry breaking when applying external magnetic fields. Above T_N, i.e., in the absence of long-range spin order where short-range correlations are still present as, e.g., indicated by the specific heat data, magnetostriction is relatively large in NiTiO_3. This observation agrees to the fact that both λ_a and λ_c become significantly larger when B exceeds B_c which appears at 21 K $\leqslant T \leqslant$ 22.2 K in the accessible field range (see Fig. 7 and supplemental material, Fig. S1 [34]). We conclude that, in a paramagnetic but yet correlated regime, magnetic fields along the a and the c axes, respectively, yield reorientation of spins which are short-range ordered in this temperature and field ranges.

Recently, anomalies in the electrical permittivity ϵ at T_N and strongly field-dependent magnetocapacitance close to T_N

have been observed in polycrystalline NiTiO_3 indicating the presence of significant magnetodielectric coupling [11]. The shape of the reported temperature dependence of ϵ is very similar to the length and volume changes observed by our thermal expansion measurements (see supplemental material Fig. S3 [34]) indicating an almost linear relation between electrical permittivity and structural distortion below T_N. Conclusively, $\epsilon(T)$ and reported magnetodielectric coupling are directly related to the length changes and the magnetoelastic coupling. Furthermore, driving entropy changes of the low-temperature effects are purely of magnetic nature as evidenced by Grüneisen analysis presented above. We conclude that magnetodielectric coupling is secondarily mediated via structural changes and that magnetic degrees of freedom constitute a single common origin for the dielectric, structural and magnetic changes evolving at and below T_N in NiTiO_3. Note, however, that magnetocapacitance data on polycrystals (at $T = 15$ K) do not show anomalies at B^* though spin reorientation is associated with significant length changes. One might speculate that the polycrystalline nature of samples studied in Ref. [11] masks such effects.

V. SUMMARY

In summary, we report growth and characterization of large and high quality NiTiO_3 single crystals by means of the optical floating-zone technique. The anisotropic phase diagram is constructed by means of pulsed and static magnetization, specific heat, thermal expansion, and magnetostriction data. It features a spin-reorientation transition at $B^* \| a \approx 1.2$ T which is accompanied by pronounced length changes. In addition, high-resolution thermal expansion data are used for detailed analysis of pronounced magnetoelastic coupling in NiTiO_3. Grüneisen scaling of the magnetic contributions to c_p and α_V implies a single magnetic degree of freedom driving the observed length and entropy changes at T_N. Our analysis suggests in-plane ferromagnetic interactions mainly determine the value of T_N. Relating our findings to recently reported strong magnetodielectric effects in NiTiO_3 implies the essential role of structural changes for magnetodielectric coupling and suggests a single magnetic origin of low-temperature dielectric, structural, and magnetic changes in NiTiO_3.

[1] N. A. Spaldin and M. Fiebig, Science **309**, 391 (2005).

[2] T. F. W. Barth and E. Posnjak, Z. Krist. **88**, 265 (1934).

[3] J. J. Stickler, S. Kern, A. Wold, and G. S. Heller, Phys. Rev. **164**, 765 (1967).

[4] H. Watanabe, H. Yamauchi, and H. Takei, J.Magn. Magnetic Mat. **15-18**, 549 (1980).

[5] G. S. Heller, J. J. Stickler, S. Kern, and A. Wold, J. Appl. Phys. **34**, 1033 (1963).

[6] G. Shirane, S. J. Pickart, and Y. Ishikawa, J. Phys. Soc. Jpn. **14**, 1352 (1959).

[7] R. E. Newnham, J. H. Fang, and R. P. Santoro, Acta Crystallogr. **17**, 240 (1964).

[8] Y. Yamaguchi, H. Kato, H. Takei, A. Goldman, and G. Shirane, Solid State Commun. **59**, 865 (1986).

[9] M. Charilaou, D. Sheptyakov, J. F. Löffler, and A. U. Gehring, Phys. Rev. B **86**, 024439 (2012).

[10] N. Mufti, G. R. Blake, M. Mostovoy, S. Riyadi, A. A. Nugroho, and T. T. M. Palstra, Phys. Rev. B **83**, 104416 (2011).

[11] J. K. Harada, L. Balhorn, J. Hazi, M. C. Kemei, and R. Seshadri, Phys. Rev. B **93**, 104404 (2016).

[12] B. Yuan, I. Khait, G.-J. Shu, F. C. Chou, M. B. Stone, J. P. Clancy, A. Paramekanti, and Y.-J. Kim, Phys. Rev. X **10**, 011062 (2020).

[13] C. dela Cruz, F. Yen, B. Lorenz, Y. Q. Wang, Y. Y. Sun, M. M. Gospodinov, and C. W. Chu, Phys. Rev. B **71**, 060407(R) (2005).

[14] C. R. de la Cruz, B. Lorenz, Y. Y. Sun, C. W. Chu, S. Park, and S. W. Cheong, Phys. Rev. B **74**, 180402(R) (2006).

[15] M. Ackermann, L. Andersen, T. Lorenz, L. Bohatý, and P. Becker, New J. Phys. **17**, 013045 (2015).

[16] L. Wang, J. Werner, A. Ottmann, R. Weis, M. Abdel-Hafiez, J. Sannigrahi, S. Majumdar, C. Koo, and R. Klingeler, New J. Phys. **20**, 063045 (2018).

[17] Y. Zhang, M. McDonnell, S. A. Calder, and M. G. Tucker, J. Am. Chem. Soc. **141**, 6310 (2019).

[18] C. P. Grams, S. Kopatz, D. Brüning, S. Biesenkamp, P. Becker, L. Bohatý, T. Lorenz, and J. Hemberger, Sci. Rep. **9**, 4391 (2019).

[19] N. Awadhesh, A. Cano, A. V. Balatsky, and N. A. Spaldin, Nat. Mat. **18**, 223 (2019).

[20] J. Rodríguez-Carvajal, Physica B: Condens. Matt. **192**, 55 (1993).

[21] R. Klingeler, B. Büchner, K.-Y. Choi, V. Kataev, U. Ammerahl, A. Revcolevschi, and J. Schnack, Phys. Rev. B **73**, 014426 (2006).

[22] Y. Skourski, M. D. Kuz'min, K. P. Skokov, A. V. Andreev, and J. Wosnitza, Phys. Rev. B **83**, 214420 (2011).

[23] R. Küchler, T. Bauer, M. Brando, and F. Steglich, Rev. Sci. Inst. **83**, 095102 (2012).

[24] W. Hergett, C. Neef, H. Wadepohl, H.-P. Meyer, M. M. Abdel-Hafiez, C. Ritter, E. Thauer, and R. Klingeler, J.Cryst. Growth **515**, 37 (2019).

[25] C. Neef, H. Wadepohl, H.-P. Meyer, and R. Klingeler, J. Cryst. Growth **462**, 50 (2017).

[26] M. E. Fisher, Philos. Mag. **7**, 1731 (1962).

[27] N. Aschcroft and N. Mermin, *Solid State Physics* (Saunders College, Philadelphia, 1976).

[28] J. B. Goodenough and J. J. Stickler, Phys. Rev. **164**, 768 (1967).

[29] W. Nolting and A. Ramakanth, *Quantum Theory of Magnetism* (Springer, Berlin, 2009).

[30] R. Klingeler, J. Geck, S. Arumugam, N. Tristan, P. Reutler, B. Büchner, L. Pinsard-Gaudart, and A. Revcolevschi, Phys. Rev. B **73**, 214432 (2006).

[31] P. Gegenwart, Rep. Prog. Phys. **79**, 114502 (2016).

[32] N. Johannsen, A. Vasiliev, A. Oosawa, H. Tanaka, and T. Lorenz, Phys. Rev. Lett. **95**, 017205 (2005).

[33] U. Stockert, N. Leps, L. Wang, G. Behr, S. Wurmehl, B. Büchner, and R. Klingeler, Phys. Rev. B **86**, 144407 (2012).

[34] See supplemental material at http://link.aps.org/supplemental/10.1103/PhysRevB.101.195122 for additional magnetostriction data, the comparison of the thermal expansion coefficient and the normalized dielectric permittivity, and a schematic of dominant exchange pathways in $NiTiO_3$.

34

Supplement: Magnetic phase diagram and magneto-elastic coupling of NiTiO$_3$

K. Dey,[1] J. Werner,[1] S. Sauerland,[1] Y. Skourski,[2]

M. Abdel-Hafiez,[3] R. Bag,[4] S. Singh,[4] and R. Klingeler[1,5]

[1]*Kirchhoff Institute of Physics, Heidelberg University,*

INF 227, D-69120 Heidelberg, Germany[*]

[2]*Dresden High Magnetic Field Laboratory (HLD-EMFL),*

Helmholtz-Zentrum Dresden Rossendorf, D-01314 Dresden, Germany

[3]*Harvard University, Cambridge, MA 02138, USA*

[4]*Indian Institute of Science Education and Research, Pune, Maharashtra 411008, India*

[5]*Centre for Advanced Materials (CAM), Heidelberg University,*

INF 225, D-69120 Heidelberg, Germany

(Dated: March 31, 2020)

PACS numbers:
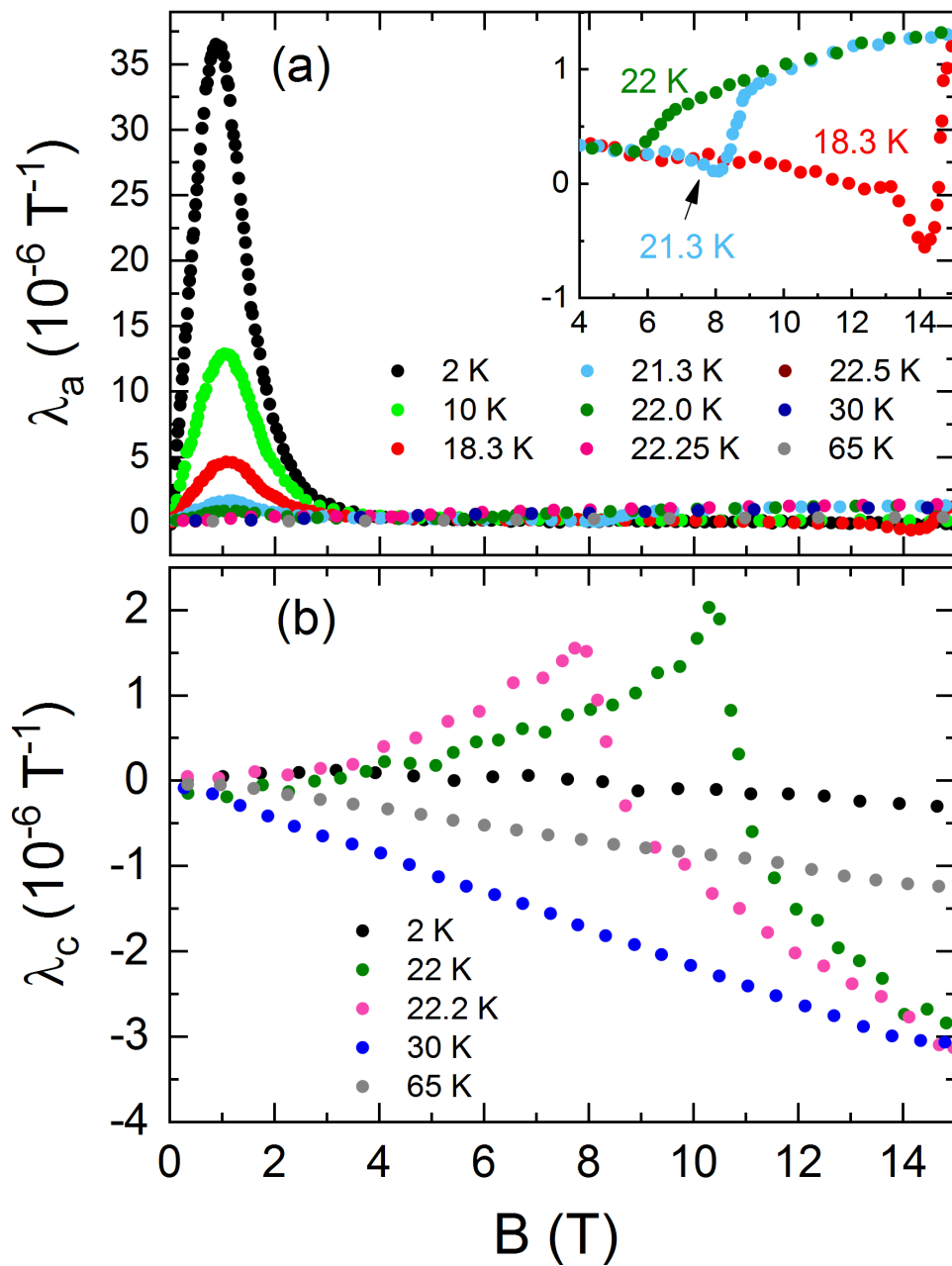
FIG. 1: Linear magnetostriction coefficients (a) λ_a and (b) λ_c vs. magnetic field applied along a and c-axes, respectively. The inset to (a) depicts λ_a at high magnetic fields at 18.3 K, 21.3 K and 22 K.

* Email:kaustav.dey@kip.uni-heidelberg.de
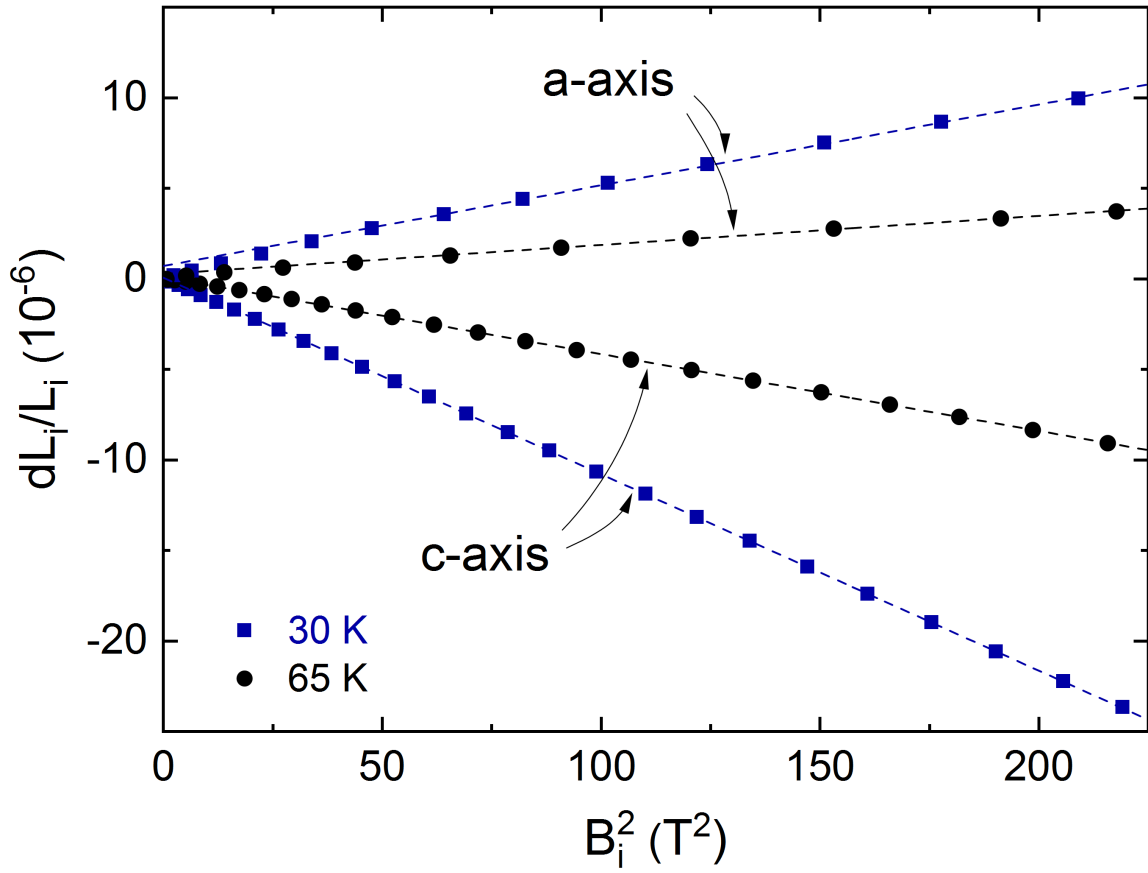
FIG. 2: Magnetostriction along the a- and c-axis, respectively, plotted vs. B^2, at $T > T_{\mathrm{N}}$. Lines are linear fits to obtain the uniaxial pressure dependencies $\partial(\ln \chi_i)/\partial p_i$.
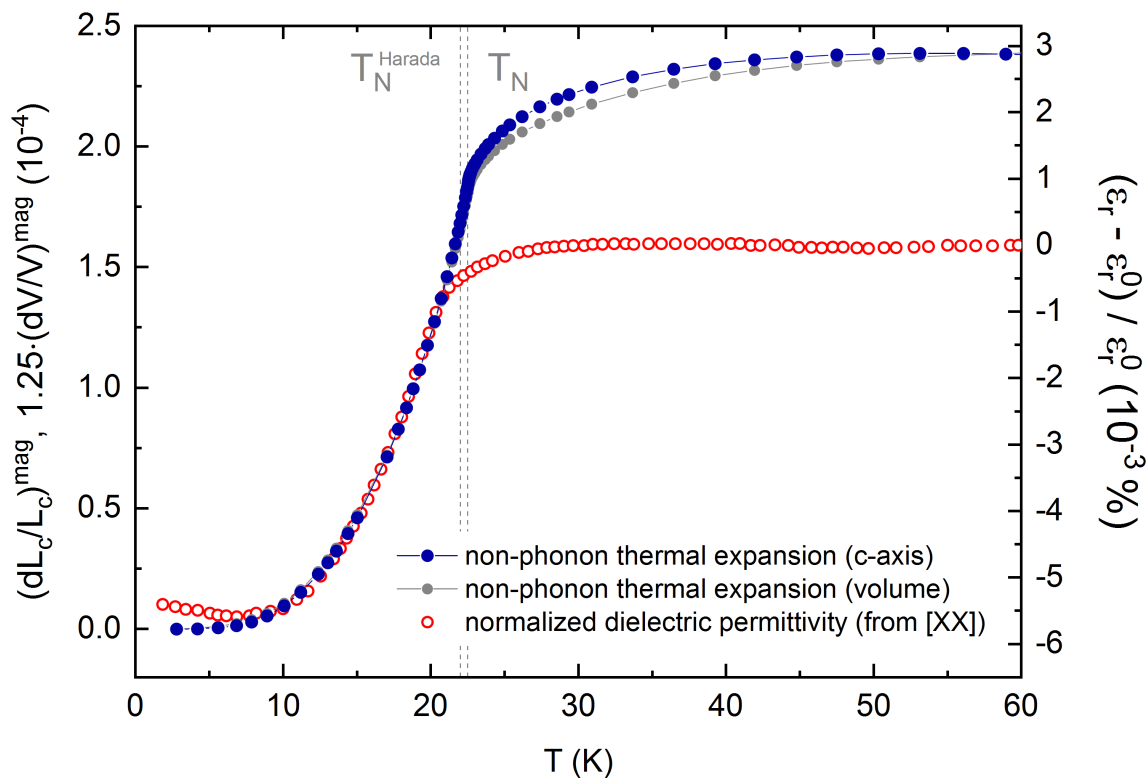
FIG. 3: Magnetic contribution to the thermal expansion and normalised dielectric permittivity taken from Ref. [**?**].
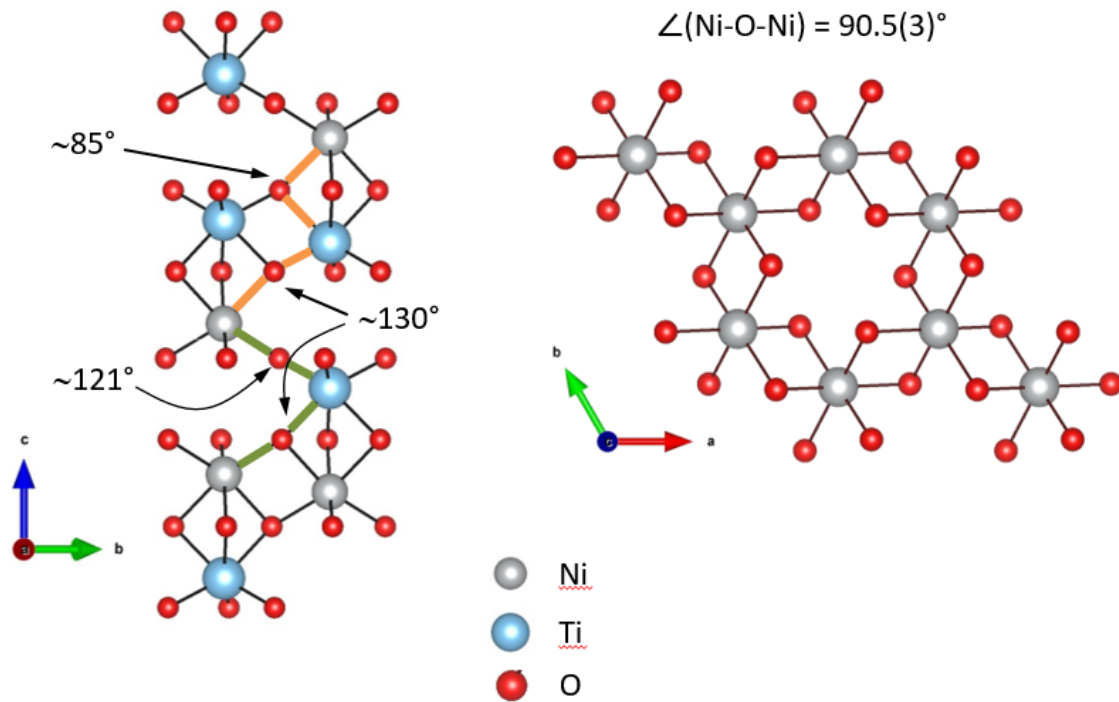
FIG. 4: Crystal structure of NiTiO$_3$ showing (Left) dominant AFM exchange pathways marked by green and orange lines along c axis and (Right) view along c axis in the ab plane. The schematic crystal structure is generated from VESTA software (http://jp-minerals.org/vesta/en/) using a cif file (COD:1544718) from the crystallography open database.

2.2   Magneto-structural coupling in ilmenite-type NiTiO$_3$

The following section has been published in Physical Review B under the title "Magnetostructural coupling in NiTiO$_3$" [112]. Copyright ©2021 American Physical Society. All rights reserved.

In the following, contributions of each co-authors are explained in detail, particularly highlighting the specific contribution of K. Dey who is the first and communicating author.

- All the experiments were performed on single crystals grown by K. Dey. The neutron diffraction proposal writing and experimentation was performed by K. Dey. Magnetization measurements were performed by K. Dey. All the plot making (except Fig. 3 and Fig. 6) and data analysis, in particular explaining the magnetoelectric effect and finding and successfully applying the multidomain phenomenological theory was done by K. Dey. The manuscript draft was written by K. Dey.

- S. Sauerland performed the dilatometry experiments (Fig. 3(a) and Fig. 5(a),(b)).

- B. Ouladdiaf and K. Beauvois were the local contacts at ILL where neutron diffraction experiments were performed. They assisted in writing the neutron diffraction sub-section in the manuscript.

- H. Wadepohl performed and analysed the single-crystal X-ray diffraction experiments. H. Wadepohl assisted in writing the single-crystal x-ray diffraction sub-section in the manuscript.

- R. Klingeler supervised the measurements, supported data analysis and manuscript writing.

- All the authors proofread the manuscript.

Magnetostructural coupling in ilmenite-type NiTiO₃

K. Dey,[1,*] S. Sauerland,[1] B. Ouladdiaf,[2] K. Beauvois,[2] H. Wadepohl,[3] and R. Klingeler[1,4]

[1]*Kirchhoff Institute of Physics, Heidelberg University, INF 227, 69120, Heidelberg, Germany*
[2]*Institut Laue-Langevin, CS20156, 38042 Grenoble Cedex 9, France*
[3]*Institute of Inorganic chemistry, Heidelberg University, 69120, Heidelberg, Germany*
[4]*Center for Advance Materials (CAM), Heidelberg University, INF 227, D-69120, Heidelberg, Germany*

We report the ground state magnetic structure and in-field magnetostrictive effects of NiTiO₃ studied by means of zero-field and in-field single-crystal neutron diffraction, magnetization, and high-resolution dilatometry experiments. Zero-field neutron diffraction on NiTiO₃ single crystals confirms an easy-plane antiferromagnet with a multidomain ground state. Upon application of external magnetic fields, neutron diffraction shows the evolution of domains with spins perpendicular to the applied field. The rotation of spins in the multidomain state exhibits pronounced lattice changes in the magnetostriction measurements. We see magnetization and magnetostriction measurements scale with each other in the multidomain state in accordance with phenomenological theories, revealing the strong coupling of spins to the lattice.

I. INTRODUCTION

Layered honeycomb magnets have been a great avenue for exciting and rich physics since time immemorial. The recent theoretical and experimental studies of Kitaev quantum spin-liquids in Co-based honeycomb materials [1,2], Dirac magnons [3], and topological spin excitations [4] in honeycomb ferromagnets, nonreciprocal magnons in honeycomb antiferromagnets [5], zigzag [6] and incommensurate [7,8] spin ground states or two-dimensional (2D) magnetism in van der Waals materials [9] have resulted in enormous interest in this class of materials. Moreover, the spin-lattice coupling in several honeycomb magnets such as Fe₄Nb₂O₉ [10], Na₃Ni₂SbO₆ [11], and Co₄Nb₂O₉ [12] has resulted in significant magnetoelectric coupling, hence motivating possible technological applications.

Ilmenite titanates with the chemical formula MTiO₃ (M = Mn, Fe, Co, Ni) form an isostructural series of antiferromagnetic (AFM) compounds where magnetic M^{2+} ions in the basal ab plane exhibit a buckled honeycomblike structure. The M^{2+} ions are interconnected via oxygen ions (O²⁻), leading to M-O-M as the dominant superexchange pathway [13]. Along the c axis, the crystal structure exhibits alternating layers of corner-sharing TiO₆ and MO₆ octahedra, resulting in relatively weaker M-O-Ti-O-M superexchange pathways. Depending on the single ion anisotropies of the respective metal ions, various magnetic ground states are realized in ilmenites, for example, uniaxial AFM ground state with spins pointing along the c axis in MnTiO₃ [14] or an easy-plane-type AFM with spins lying in the ab plane for NiTiO₃ and CoTiO₃ [15], respectively.

Although these compounds have been rigorously investigated [13,14,16–18], recent studies evidencing linear magnetoelectric coupling in MnTiO₃ [19], large spontaneous magnetostriction in FeTiO₃ [20], magnetodielectric and magnetoelastic coupling in NiTiO₃ [21,22] and CoTiO₃ [23], respectively, as well as the observance of Dirac magnons in CoTiO₃ [24,25] have piqued enormous interest in this class of materials.

The least investigated compound among the ilmenites family, i.e., NiTiO₃, develops long-range AFM order at T_N = 22.5 K [16,21,22,26]. Recent studies of the dielectric permittivity and the thermal expansion show a pronounced magnetodielectric effect [21] as well as distinct significant magnetoelastic coupling [22]. Notably, at T_N, there is a single dominant energy scale driving the observed structural, magnetic, and dielectric anomalies [22]. In this paper, we study in detail the magnetostructural coupling of NiTiO₃ by means of single-crystal x-ray and neutron diffraction and high-resolution dilatometry. We observe by means of single-crystal neutron diffraction that the macroscopic structural symmetry (R-3) is retained down to the lowest measured temperature of 2 K within the experimental resolution. In addition, the magnetic ground state of NiTiO₃ is solved. At T_N, in addition to long-range AFM order, a significant lattice distortion evolves, revealing large spontaneous magnetostriction in NiTiO₃. In applied magnetic fields, the multidomain ground state evolves to a spin-reoriented single domain state characterized by spins aligned perpendicular to the applied magnetic field. Magnetostriction measurements in the low-field region show pronounced effects due to magnetoelastic domains and remarkably scale with magnetization measurements, confirming both significant magnetostructural coupling and the magnetostructural domain model in NiTiO₃.

II. EXPERIMENTAL METHODS

Macroscopic single crystals of NiTiO₃ were grown by means of the optical floating-zone technique in a four-mirror

---

*kaustav.dey@kip.uni-heidelberg.de

optical floating-zone furnace (CSC, Japan) equipped with 4×150 W halogen lamps. Details of the growth process and characterization the single crystals have been published previously [22]. Single-crystal x-ray intensity data were obtained at 100 K with an Agilent Technologies Supernova-E CCD 4-circle diffractometer (Mo-Kα radiation $\lambda = 0.71073$ Å, microfocus x-ray tube, multilayer mirror optics). Static magnetization $\chi = M/B$ was studied in magnetic fields up to 5 T in a Quantum Design MPMS-XL5 SQUID magnetometer. The relative length changes dL_i/L_i were studied on a cuboid-shaped single crystal of dimensions $2 \times 1.85 \times 1$ mm^3 by means of a three-terminal high-resolution capacitance dilatometer [11,27]. Magnetostriction, i.e., field-induced length changes $dL_i(B)/L_i$, was measured at several fixed temperatures in magnetic fields up to 15 T, and the longitudinal magnetostriction coefficient $\lambda_i = 1/L_i dL_i(B)/dB$ was derived. The magnetic field was applied along the direction of the measured length changes.

Single-crystal neutron diffraction experiments were performed up to 6 T magnetic fields at the D10 beamline of the Institut Laue-Langevin (ILL) at Grenoble, France. To determine the magnetic ground state at $B = 0$ T, the four-circle configuration was used with a 96×96 mm^2 2D microstrip detector. An incident wavelength of 2.36 Å using a vertically focusing pyrolytic graphite (PG) (002) monochromator was employed. A PG filter was used to suppress higher-order contamination to 10^{-4} times that of the primary beam intensity. Measurements were made in the temperature range 2–50 K. The magnetic field-driven evolution of the magnetic structure at $T = 2$ K was studied by mounting the sample in a 6 T vertical cryomagnet and aligned to within $1°$ of magnetic field. The magnetic field was applied along the b axis, limiting the scattering to the $(H, 0, L)$ plane.

III. EXPERIMENTAL RESULTS

A. Single-crystal x-ray diffraction

To the best of our knowledge, the earlier studies of the ilmenite-type NiTiO$_3$ crystal structure have been limited to powder diffraction experiments only [14,22,28]. We have reinvestigated the crystal structure by means of single-crystal high-resolution x-ray diffraction (XRD) at 100 K, using Mo-Kα radiation ($\lambda = 0.71073$ Å). A single-crystal splinter of size $0.16 \times 0.14 \times 0.01$ mm^3 was broken off from a larger specimen and used for data collection. A full shell of intensity data was collected up to 0.4 Å resolution {24 180 reflections, 1028 independent ($R_{int} = 0.05$) of which 1024 were observed [$I > 2\sigma(I)$]}. Detector frames (typically ω, occasionally ϕ scans, scan width $0.5°$) were integrated by profile fitting [29]. Data were corrected for air and detector absorption, Lorentz and polarization effects [30], and scaled essentially by application of appropriate spherical harmonic functions [30–32]. Absorption by the crystal was treated numerically (Gaussian grid) [32,33]. An illumination correction was performed as part of the numerical absorption correction [32]. Space group R-3 was assigned based on systematic absences and intensity statistics (refined obverse centered unit cell on hexagonal axes, Hall group $-R3$, $a = 5.02762(6)$, $c = 13.76711(17)$ Å, $V = 301.369(8)$ Å^3, and $Z = 6$). This choice was confirmed

TABLE I. Fractional atomic coordinates, Wyckoff positions, site occupation, and equivalent isotropic displacement parameters (Å^2) for NiTiO$_3$ at 100 K, as obtained from refinement of model A. (Note: (1) These coordinates are correct but do not form a uniquely bonded set; (2) U_{eq} is defined as one-third of the trace of the orthogonalized U_{ij} tensor. The anisotropic displacement factor exponent takes the form $-2\pi^2[h^2a^{*2}U_{11} + ... + 2hka^*b^*U_{12}]$).

Atom	Site	x	y	z	sof	U_{eq}
Ni	6c	0	0	0.35051 (2)	1	0.00308 (2)
Ti	6c	0	0	0.14422 (2)	1	0.00297 (3)
O	18f	0.35198 (8)	0.03455 (8)	0.08662 (2)	1	0.00421 (4)

by analysis of the symmetry of the phases obtained *ab initio* in P1. The structure was solved by intrinsic phasing [34–36] and refined by full-matrix least-squares methods based on F^2 against all unique reflections [37–40]. Three somewhat different models were employed for the atomic structure factors f_{at} within the independent spherical atoms approximation: conventional f_{at} calculated with neutral atoms [41] for Ni, Ti, and O (model A) and two "ionic" models [41] {f_{at} for Ni^{2+} and Ti^{4+} taken from Ref. [41] and O^{2-} from Ref. [42] (model B) or Ref. [43], respectively (model C)}. An empirical secondary extinction correction [38,44] was applied in each case but proved insignificant. The different models refined to essentially the same structure, with only insignificant differences in key parameters like atom coordinates, R factors, U_{eq} for all atoms, and residual electron density. Ni-O and Ti-O bond lengths agreed within one standard deviation. There was no evidence of cation mixing, and fully occupied sites were employed for all atoms. The results confirm the assignment of the space group and improve on the accuracy of the crystallographic parameters previously obtained from powder XRD and neutron data [14,22,28]. Fractional atomic coordinates, Wyckoff positions, site occupation, and equivalent isotropic displacement parameters for model A are listed in Table I [45].

B. Single-crystal neutron diffraction

The crystal structure at lower temperatures and the magnetic ground state of NiTiO$_3$ were determined by means of single-crystal neutron diffraction. At 50 K, 110 nuclear Bragg reflections were collected. Appropriate correction for extinction, absorption, and Lorentz factor was applied to all the nuclear Bragg peaks. All the nuclear peaks at 50 K were successfully indexed in the R-3 space group with lattice parameters $a = 5.03$ Å and $c = 13.789$ Å.

To clarify the magnetic structure, preliminary reciprocal-space scans (not shown here) were performed at 2 K along the $(0, 0, L)$, $(H, 0, 0)$, and $(H, K, 0)$ directions. The scans reveal a peak of significant intensity emerging at $(0,0,1.5)$, indicative of the propagation vector $\mathbf{k} = (0,0,1.5)$. To determine the detailed magnetic structure, integrated intensities of 187 nuclear reflections allowed within the space group R-3 and 292 satellite magnetic reflections were collected at 2 K. The nuclear structure was firstly refined using FULLPROF program within the R-3 space group. The results of refinement are listed in Table II, and the observed and calculated intensities from the Rietveld fits are shown in Fig. 2(a). No peak splitting or

TABLE II. Parameters for the nuclear structure of NiTiO$_3$ measured at 2 K obtained from refinements of single-crystal neutron diffraction data. The isotropic temperature factors (B_{iso}) of all atoms were refined. [Space group: R-3 (148); Lattice parameters: $a = b = 5.0229(1)$ Å, $c = 13.7720(1)$ Å, $\alpha = \beta = 90°$, and $\gamma = 120°$.]

Atom	Site	x	y	z	B_{iso}(Å^2)
Ni1	6c	0	0	0.3537 (2)	0.00748
Ti1	6c	0	0	0.1338 (5)	0.06643
O1	18f	0.3344 (6)	0.0052 (1)	0.2466 (2)	0.09830

significant broadening was observed within the experimental resolution in respective 2 K nuclear reflections as compared with 50 K, indicating that the macroscopic R-3 symmetry is maintained until the lowest measured temperatures. The nuclear Bragg peaks show no temperature dependence between 2 and 50 K excluding **k** = (0,0,0).

All the finite intensity magnetic peaks are observed at the general position $(H, K, L) + (0,0,1.5)$ with H, K, L satisfying the reflection conditions of the R-3 space group and hence confirming **k** = (0,0,1.5). A few of the observed high-intensity magnetic peaks are listed in Table III. The largest diffraction intensity occurs for the magnetic Bragg peak (0,0,1.5), indicating that the Ni^{2+} moments lie in the ab plane, which had been suggested by previous magnetization measurements [22]. The temperature dependence of the integrated intensity of the commensurate reflection (0,0,1.5) in Fig. 1 shows finite intensity below the magnetic ordering temperature. A power law fit in the critical region using $I \propto M^2 \propto \tau^{2\beta}$, where M is the order parameter and $\tau = 1 - T/T_N$ results in $T_N = 22$ (1) K and $\beta = 0.35(1)$. The obtained value T_N from the power law fit agrees to the one from previous macroscopic studies [16,21,22,26]. The obtained value of the critical parameter $\beta = 0.35(1)$ lies in between the three-dimensional (3D) XY ($\beta = 0.345$) and 3D Heisenberg ($\beta = 0.367$) universality classes. However, the previously reported pulsed-field M vs B measurements revealed an isotropic behavior for $B||ab$ and $B||c$ [22], indicating that Ni^{2+} spins in NiTiO$_3$ are of 3D Heisenberg nature.

The knowledge of the propagation vector **k** = (0,0,1.5) with the Ni^{2+} moments lying in the hexagonal ab plane points

TABLE III. Observed intensities (I_{obs}) of several high-intensity magnetic peaks, as measured in D10 at 2 K and their corresponding calculated intensities (I_{cal}), as discussed in the text.

Q	I_{obs}	I_{cal}
(0,2,2.5)	975 (17)	917
(0,2,5.5)	1410 (27)	1307
(0,−1,5.5)	2481 (36)	2685
(0,0,4.5)	2809 (22)	3348
(1,−2,−1.5)	1923 (20)	2045
(1,−2,4.5)	1755 (22)	1521
(0,−1,2.5)	1787 (17)	1965
(−1,2,4.5)	1812 (48)	1521
(0,−1,8.5)	1729 (109)	1679
(0,0,1.5)	4366 (21)	3942
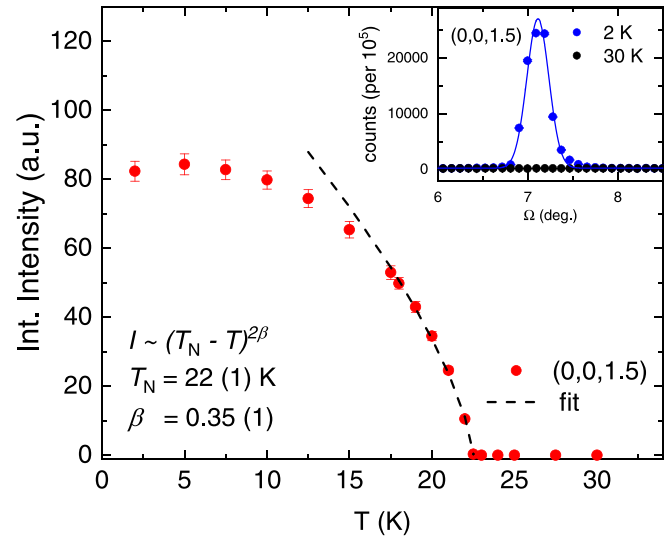
FIG. 1. Temperature dependence of the integrated intensity of the (0,0,1.5) magnetic Bragg peak. The dashed black curve is a fit to the data with the power law $I \sim (T_N - T)^{2\beta}$. The inset shows the Ω scan through the magnetic (0,0,1.5) peak at 2 and 30 K, respectively. The solid blue line is the Gaussian fit to the peak at 2 K. See the text for more details.

toward two possible magnetic models for NiTiO$_3$: (a) ferromagnetic layers stacked AFM along the c axis or (b) AFM layers with the spins aligned ferromagnetically along the c axis. Previous static magnetic susceptibility $\chi = M/H$ vs T measurements reveal the decrease of χ_{ab} below T_N, whereas χ_c stays nearly constant [22,26]. Moreover, the magnetic model (b) implies a zero magnetic structure factor at the position $Q = (0, 0, 1.5)$, contrary to our observation. Hence, model (a) is most suitable to describe the magnetic structure of NiTiO$_3$. The obtained magnetic peaks at 2 K were refined against model (a), and a very good fit was obtained, as shown in Fig. 4(b). The obtained magnetic structure of NiTiO$_3$ reconfirms the structure proposed by Shirane *et al.* [14] based
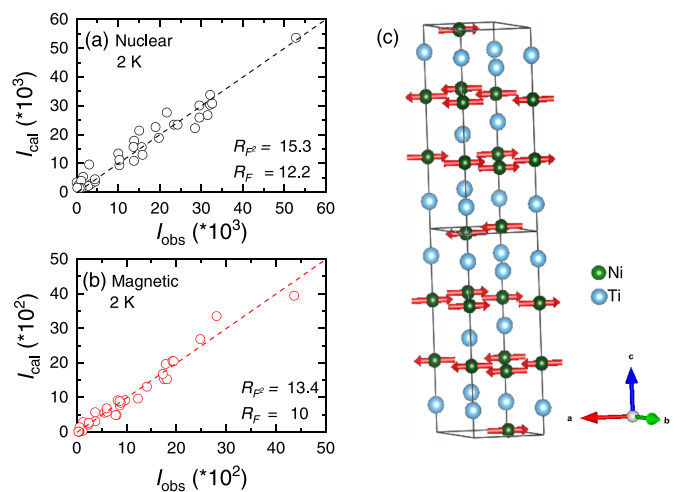
FIG. 2. Comparison between the observed and calculated integrated intensities of the nonequivalent (a) nuclear and (b) magnetic reflections, respectively, at 2 K, and (c) easy-plane-type magnetic structure of NiTiO$_3$, as determined from the refinements at 2 K.
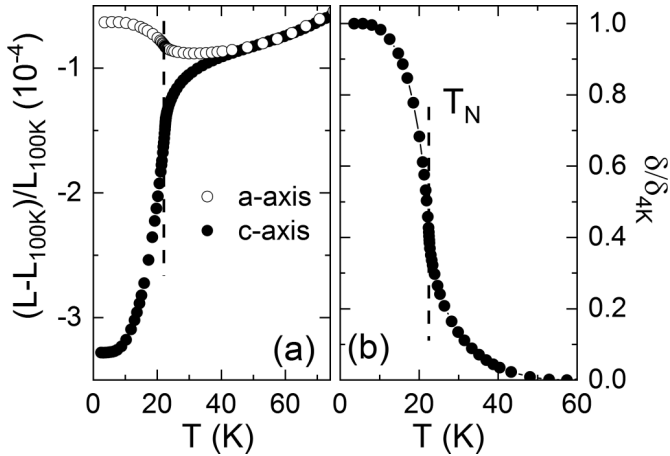
FIG. 3. (a) Relative length changes $dL_i^* = (L_i - L_i^{100\,K})/L_i^{100\,K}$ measured along the principle crystallographic a and c axes, respectively, by means of high-resolution dilatometry. (b) Normalized distortion parameter $\delta/\delta_{4\,K}$, with $\delta = (dL_a^* - dL_c^*)/(dL_a^* + dL_c^*)$. The vertical dashed lines indicate T_N.

on powder neutron data . The observed and calculated intensities of several magnetic peaks are listed in Table III, and the complete magnetic structure of NiTiO$_3$ is schematically represented in Fig. 2(c). At $T = 2$ K, the ordered moment amounts to 1.46 (1) μ_B.
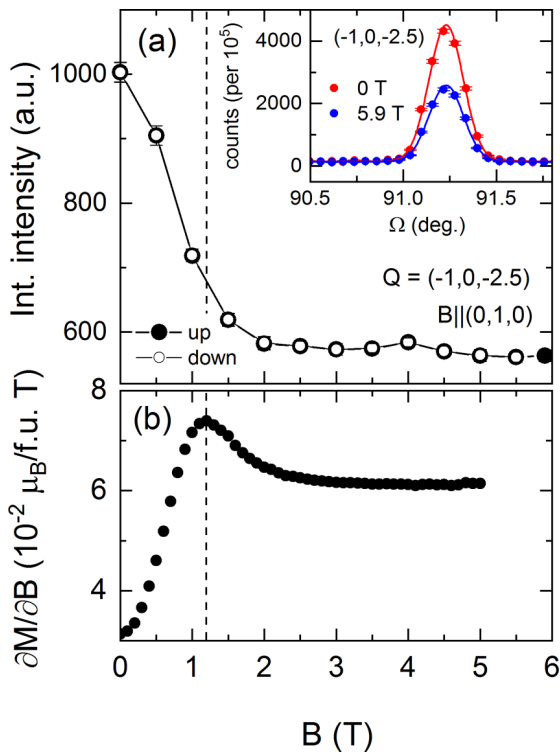
FIG. 4. (a) Integrated intensity of the magnetic $(-1,0,-2.5)$ peak as a function of magnetic field (up and down) and (b) the derivative of static magnetization with respect to magnetic field $\partial M/\partial B$ as a function of magnetic field (from Ref. [22]) at 2 K. The inset to (a) shows the Ω scans through the magnetic $(-1,0,-2.5)$ peak at 0 and 5.9 T. The solid lines in blue and red are Gaussian fits to the peaks at 0 and 5.9 T, respectively.

The crystal symmetry of the basal hexagonal planes is marked by the presence of two sets of three twofold axes. Hence, the in-plane spin configurations rotated by 120° are exactly equivalent, leading to the presence of spin domains (i.e., three domains). Since the refinements are usually performed using the average of the integrated intensities of the equivalent reflections, the directions of the spins cannot be uniquely determined using single-crystal neutron diffraction alone, like the problem existing in the earlier powder diffraction experiments [14]. However, excellent agreement of the integrated intensities between the equivalent reflections ($R_{int} = 1.86\%$ indicates that there are likely three spin domains of equal population with spins rotated by 120° in between the neighboring domains.

C. Magnetostructural-dielectric coupling

The magnetostructural coupling in NiTiO$_3$ has been studied by means of high-resolution capacitance dilatometry. The uniaxial relative length changes $dL_i^* = (L_i - L_i^{100\,K})/L_i^{100\,K}$ ($i = a, c$) [Fig. 3(a)] vs temperature show abrupt changes at T_N, i.e., shrinking of the c axis and expansion along the a axis, which demonstrates significant magnetoelastic coupling in NiTiO$_3$. At higher temperatures $T \geqslant 50$ K, isotropic thermal expansion coefficients result in similar rate of increase of dL_i^* along the a and the c axes, respectively. To further elucidate lattice changes at T_N, the normalized distortion parameter δ/δ_{4K}, with $\delta = (dL_a^* - dL_c^*)/(dL_a^* + dL_c^*)$, is shown in Fig. 3(b).

As evidenced by the distortion parameter, different behavior of the a and c axes starts to evolve gradually below 50 K, while δ sharply jumps at T_N [Fig. 3(a)]. Evidently, the onset of long-range AFM order is associated with a large spontaneous magnetostriction effect, and it implies strong magnetostructural coupling. Spontaneous magnetostriction has also been observed in other ilmenites such as FeTiO$_3$, which however shows a reversed magnetostrictive effect, i.e., expansion of the c axis and shrinking of the a axis [20]. We attribute this difference to the differing magnetic ground states in FeTiO$_3$ and NiTiO$_3$ and corresponding variation in magnetocrystalline anisotropy. Finite distortion δ up to 50 K evidences a precursor phase with short-range order well above T_N. Due to the observed strong magnetoelastic coupling, we conclude the presence of short-ranged spin correlations persisting up to twice the transition temperature. This is corroborated by previous specific heat measurements [22] on NiTiO$_3$, which reveal that nearly 20% of magnetic entropy is consumed between T_N and 50 K. In addition, it has been shown that the **q**-dependent spin-spin correlations couple to the dielectric response via the coupling of magnetic fluctuations to optical phonons, thereby causing a significant magnetocapacitance effect [46]. Accordingly, we conclude that the significant magnetocapacitance of 0.01% and finite magnetostriction recently observed in NiTiO$_3$ well above T_N is due to persisting spin-spin correlations [21,22].

D. Spin reorientation

The effect of magnetic fields applied within the ab plane on the crystal and magnetic structure of NiTiO$_3$ is studied by

means of in-field neutron diffraction at 2 K. Specifically, the magnetic field is applied vertically along the b axis, and the scattering vector lies in the $(H, 0, L)$ plane. Several nuclear and magnetic reflections were measured with rocking curve scans in magnetic fields up to 6 T. As will be discussed below, there is a considerable decrease in intensity upon application of the magnetic field for all magnetic peaks, while in contrast, there is no magnetic field effect on the nuclear peak intensities. A representative scan through the magnetic peak $Q = (-1, 0, -2.5)$ is shown in the inset to Fig. 4.

The magnetization curve displays a nonlinear dependence on magnetic fields applied along the ab plane, as evidenced by the magnetic susceptibility $\chi = \partial M / \partial B$ in Fig. 4(b). The maximum in χ at $B = 1.2$ T is indicative of a spin-reorientation transition. Correspondingly, the integrated magnetic intensity [Fig. 4(a)] shows a continuous decrease in magnetic fields up to 2 T, above which it stays nearly constant at a finite value. Since the magnetic neutron diffraction intensity is proportional to the component of the magnetic moments perpendicular to the scattering vector, this observation indicates that, in magnetic field, the spins are rotated smoothly from three magnetic domains to a single domain state with spins aligned perpendicular to fields >2 T. Between 2 and 6 T, negligible field dependence indicates a very small canting of spins toward the magnetic field. The full width at half maximum calculated using Gaussian fits to nuclear peaks show negligible broadening up to 6 T, indicating that the magnetostriction effects on lattice parameters corresponding to the spin reorientation are below the experimental resolution.

E. Magnetostriction

Applying magnetic fields along the ab plane yields a pronounced increase of the associated lattice parameter in the low-field region ($B < B^* = 2$ T), while there is only small magnetostriction at higher fields (see Fig. 5). Magnetostriction is also reportedly small for fields applied along the c axis [22]. We conclude that this behavior is associated with the field-driven collective rotation of spins, as discussed above and evidenced by Fig. 4. However, as will be discussed below, the magnetization changes do not scale with magnetostriction, and the maxima in $\partial M / \partial B$ and $\partial L_a / \partial B$ do not match each other [see Fig. 8(a)]. The magnetostriction data hence do not correspond to what is expected for a thermodynamic spin-reorientation transition. Instead, the presence of domains has to be involved, and in the following, we will present clear evidence that the data represent the change from a low-field multidomain state to a high-field uniform monodomain one.

To further investigate the effect of in-plane magnetic fields, the intensity evolution of two equivalent magnetic Bragg peaks $(3, 0, 1.5)$ and $(-3, 0, -1.5)$ belonging to two different magnetic domains is displayed in Fig. 5(c). In the multidomain state, the AFM vector is uniform within a single domain and has different directions in different domains. The observed isotropic decrease in intensity of both magnetic peaks upon application of the magnetic field implies that the spins of both domains rotate perpendicularly to the external field direction. The spin-rotation process is completed at 2 T, which hence signals the formation of a spin-reoriented monodomain state. Accordingly, no significant changes in the peak intensities are observed between 2 and 6 T.
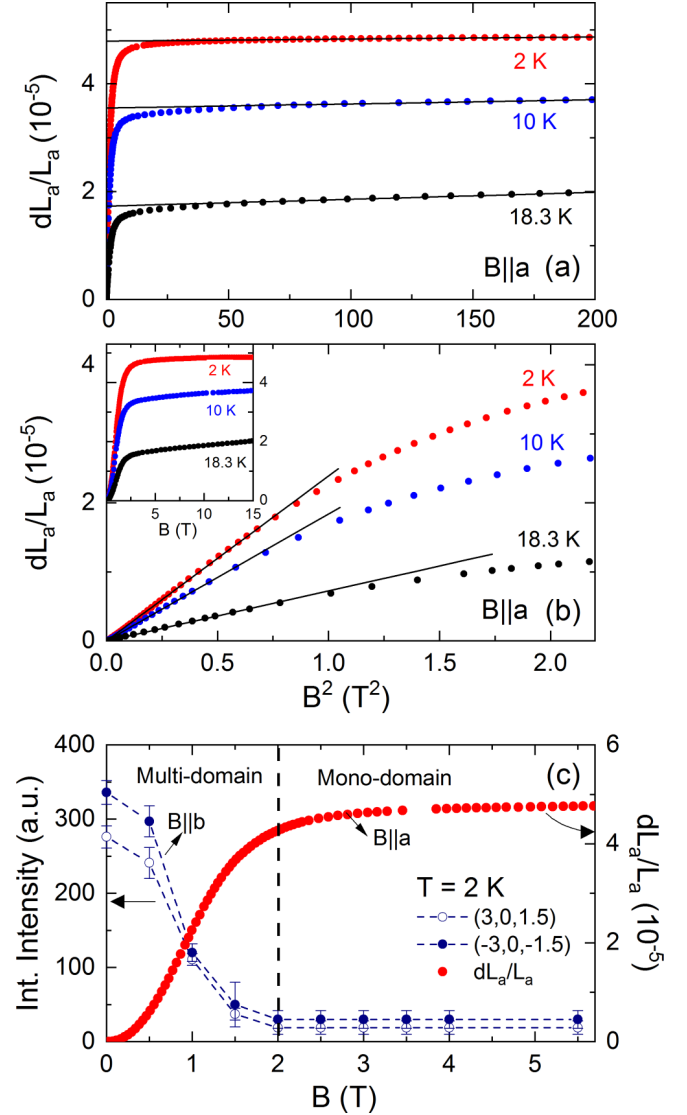
FIG. 5. Relative length changes dL_a / L_a at different temperatures vs the square of magnetic field applied along the crystallographic a axis for (a) magnetic fields up to 14 T, i.e., including the high-field single-domain (homogeneous) phase, and (b) for $B \leqslant 1.5$ T, which is the low-field multidomain phase (see the text). The solid black lines are corresponding linear fits. The inset to (b) shows the relative length changes vs applied magnetic field. (c) Integrated intensity of the equivalent magnetic Bragg peaks $(3, 0, 1.5)$ and $(-3, 0, -1.5)$ vs magnetic field applied along the b axis and (dL_a / L_a) for fields along a axis, at $T = 2$ K. The vertical dashed line separates the multidomain and the monodomain (homogeneous) regions. See text for more details.

IV. DISCUSSION

Comparison of the magnetic order parameter and the relative volume changes with the reported data of the dielectric function by Harada *et al.* [21] elucidates the coupling mechanism between the lattice and the dielectric degrees of freedom in $NiTiO_3$. As displayed in Fig. 6(a), the nonphononic relative volume changes $dV'/V = 2(dL_a / L_a) + (dL_c / L_c)$ which are obtained by subtracting the phononic contribution from dV/V (cf., Ref. [22]) show a very similar temperature dependence, below T_N, as the normalized dielectric permittivity. Note that
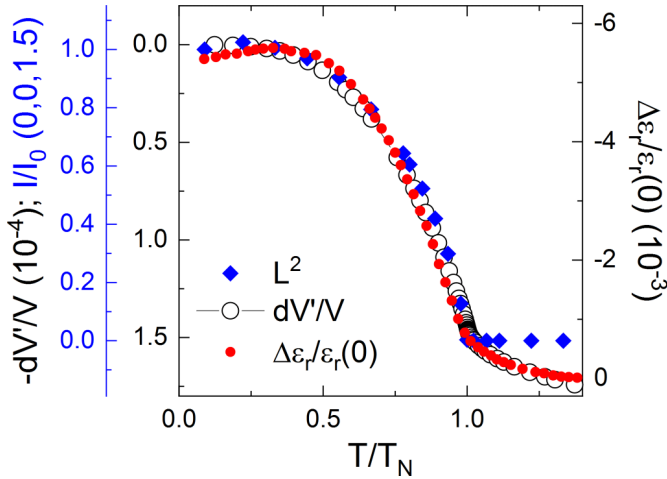
FIG. 6. Temperature dependence of the square of the antiferromagnetic order parameter (L^2), i.e., the normalized integrated intensity of the (0,0,1.5) magnetic Bragg peak, the negative nonphononic volume changes dV'/V, and the normalized dielectric permittivity digitized from Ref. [21].

the polycrystalline sample studied in Ref. [21] displays a slightly lower T_N than the single crystals studied at hand. In general, the length changes can directly affect the experimentally measured permittivity via the relation $\epsilon = Cd/\epsilon_0 A$, where C, ϵ_0, d, and A are sample capacitance, vacuum permittivity, sample thickness, and area, respectively. However, the changes in sample dimensions at T_N are on the order of 10^{-4}, while the relative change in permittivity is an order higher, implying that spontaneous magnetostriction is not the driving mechanism for the observed dielectric changes at T_N. Interestingly, the normalized dielectric permittivity varies as the square of the AFM order parameter L, represented by the normalized integrated intensity of the magnetic (0,0,1.5) Bragg peak in Fig. 6(a). To discuss this, we recall the Landau expansion of the free energy F, in terms of polarization P, and the sublattice magnetization L at zero magnetic field [47]:

$$F = F_0 + \alpha P^2 + \alpha' L^2 + \beta PL + \gamma P^2 L^2 - PE, \quad (1)$$

The dielectric function is obtained as $\partial^2 F/\partial P^2 = \epsilon \propto \gamma L^2$. Hence, Fig. 6(a) qualitatively evidences the presence of magnetodielectric coupling in NiTiO₃. On top of the spin and dielectric changes, the structural changes exhibit similar behavior below T_N. Previously reported magnetic Grüneisen analysis [22] evidences that the entropic changes at T_N are of purely magnetic nature. In our opinion, the spin-phonon coupling is responsible for observed dielectric changes at T_N. In the presence of spin-phonon coupling, the phonon frequency ω can be affected by spin correlation as $\omega = \omega_0 + \lambda \langle S_i.S_j \rangle$, resulting in modification of permittivity via the Lyddane–Sachs–Teller equation $\epsilon_0 = \omega_L^2/\omega_T^2 \epsilon_\infty$, where ϵ_0 and ϵ_∞ are the permittivity at zero frequency and optical frequency, respectively, and ω_L^2 and ω_T^2 are the long-wavelength longitudinal and transverse optical phonon modes, respectively.

It is noteworthy that, apart from spontaneous magnetostriction, an exchange-striction (ES) mechanism may in principle also lead to spontaneous lattice deformation at T_N and be a potential source for dielectric anomaly at T_N. Magnetodi-

electricity fueled by an ES mechanism have been observed in several systems, for example, Y₂Cu₂O₅ [48] and TeCuO₃ [46]. In FeTiO₃, a combination of ES and magnetostriction mechanisms have been suggested for the spontaneous lattice deformation at T_N [20]. For NiTiO₃, an ES mechanism would imply a change in the Ni-O-Ni bond angle in the *ab* plane closer to 90°, favoring ferromagnetic superexchange. However, diffraction experiments reveal that the bond angle increases from 90.34° at 100 K to 90.36° at 2 K (Supplemental Material, Fig. 2 [49]), contrary to predictions of ES. Hence, an ES mechanism is excluded as the origin of lattice distortion at T_N in NiTiO₃.

The crystallographic symmetry of the easy hexagonal plane in NiTiO₃ suggests the presence of three domains with spins rotated by 120° in different domains. Such a spin structure with three domains is often observed in easy-plane-type hexagonal antiferromagnets such as CoCl₂, NiCl₂, and BaNi₂V₂O₈ [50,51]. In NiTiO₃, the magnetostriction data imply that the field-driven changes of the domain structure is associated with structural changes. Indeed, orientational AFM domains are magnetoelastic in nature [52,53] and have previously been observed in various systems, for example, in cubic antiferromagnets RbMnF₃ [54], KNiF₃ and KCoF₃ [55,56], NiO [57], iron-group dihalides CoCl₂ [58] and NiCl₂ [59], the quasi-2D AFM BaNi₂V₂O₈ [51], YBa₂Cu₃O₆.₃ [53], etc. Kalita *et al.* [58–62] have developed phenomenological theories describing the effect of domain redistribution on the magnetostriction for CoCl₂ and NiCl₂. Note that both NiCl₂ and CoCl₂ are easy-plane-type antiferromagnets with similar crystalline symmetry, i.e., trigonally distorted octahedral environment surrounding metal ions, like NiTiO₃ and CoTiO₃ [50,63]. In the following, we will describe the field dependency of the length changes in NiTiO₃ based on the phenomenological theories developed by Kalita *et al.* [58–62].

Both at low magnetic fields $B||a \leqslant 1$ T and at higher fields, the field-induced striction dL_a/L_a varies as the square of the applied magnetic field, as shown in Figs. 5(a) and 5(b). In the latter, i.e., the monodomain state, this is predicted by calculating the equilibrium elastic strain by energy minimization of the magnetoelastic and the elastic contributions to the free energy [58,59]. The magnetostriction in the monodomain state is described by

$$\left(\frac{dL_a}{L_a}\right)(T,B) = \alpha(T)B^2 + \left(\frac{dL_a}{L_a}\right)_s(T,B=0), \quad (2)$$

where $\alpha(T)$ is the temperature-dependent slope, and $(dL_a/L_a)_s(T,H=0)$ is the spontaneous magnetostriction of the monodomain state obtained by extrapolating the linear fit to $B=0$ T. Equation (2) fits well with dL_a/L_a at different temperatures, as shown by the solid black lines in Fig. 5(a). The obtained fit parameters are listed in Table IV. Here, $(dL_a/L_a)_s$ corresponds with a hypothetical spontaneous striction that would be observed if the magnetoelastic domains did not appear at low fields, i.e., if the total spontaneous magnetostriction was not compensated on the whole by summation of strains in different directions in each of the domains.

The magnetostrictive response upon application of magnetic fields in the multidomain state is governed by

TABLE IV. Parameters obtained from fits to the magnetostriction data [Figs. 5(a) and 5(b)] using Eqs. (2) and (3). $(dL_a/L_a)_s$ is the spontaneous magnetostriction (see the text).

T	$(dL_a/L_a)_s(10^{-5})$	B_d (T)	α (10^{-9}) (T^2)
2 K	4.79	1.41	3.8
10 K	3.55	1.38	7.6
18.3 K	1.73	1.55	12.8

domain-wall motion. Specifically, magnetostriction is large due to the associated facilitated rotation of spins. The motion of magnetoelastic domain walls is predominantly reversible in nature [52,55], and the associated length changes again exhibit a square dependence on the magnetic field, which is expressed by

$$\left(\frac{dL_a}{L_a}\right)(T, B) = \left(\frac{dL_a}{L_a}\right)_s(T, B = 0) \times \left(\frac{B}{B_d}\right)^2. \quad (3)$$

Here, H_d is an empirical parameter obtained from the fits (see Table IV). As shown in Fig. 5(b), the experimental data are well described by Eq. (3), which is in line with the predictions of phenomenological models [55,59]. Although the magnetoelastic domains are predominately reversible in nature, a small irreversibility may arise due to pinning of domain walls by crystal defects and imperfections in the crystals. A small remanent striction amounting to ∼1.6×10^{-6}, at $T = 2$ K, is indeed observed in our data (see Supplemental Material, Fig. S1 [49]), which indicates the presence of predominately mobile domain walls [52] in NiTiO$_3$.

Unlike uniaxial antiferromagnets, which show an abrupt magnetization jump at the spin-flop transition as, e.g., observed in MnTiO$_3$ [64], the magnetization in NiTiO$_3$ follows a sickle-shaped field dependence in the nonflopped phase, and the reorientation transition is associated with smooth right bending in M vs B (see Fig. 7). Such characteristic smooth nonlinear variation of magnetization in low fields is a manifestation of the multidomain state where spin reorienta-
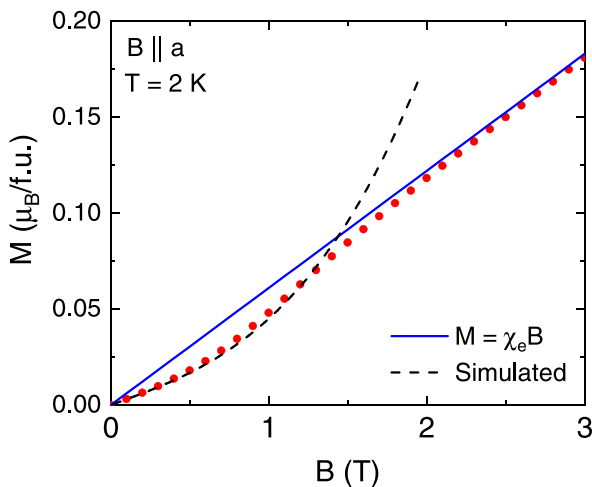
FIG. 7. Magnetization M, at $T = 2$ K, vs applied magnetic field $B\|a$ axis. The solid blue line represents a linear fit to M in the high-field region, and the dashed black line shows a simulation to M at low fields (see the text for more details).
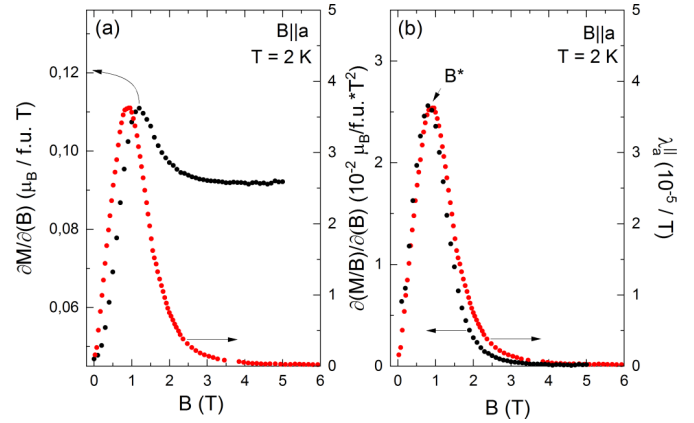
FIG. 8. (a) Scaling of $\partial M/\partial B$, (b) $\partial(M/B)/\partial B$ and $\lambda_a^{\|}$ versus B at $T = 2$ K.

tion takes place gradually by displacement of domain walls [56]. This is described [62] by

$$M = \left(\frac{1}{2}\right)\chi_e B\left[1 + \left(\frac{B}{B_d}\right)^2\right], \quad (4)$$

where χ_e is the high-field magnetic susceptibility. A linear fit to the M vs B curve [22] at $B > 4$ T yields $\chi_e = 0.06$ μ_B/f.u. T, which is represented by the solid blue line in Fig. 7. Using B_d from the analysis of the magnetostriction data (see Table IV) enables us to deduce the field dependence of M. The simulation using Eq. (4) is shown by the dashed line in Fig. 7. It yields a good description of the field-driven evolution of the magnetization in the multidomain state, thereby further confirming the applied phenomenological model. The blue line in Fig. 7 represents the expected magnetization in a single-domain easy-plane AFM with no in-plane anisotropy.

The field-driven disappearance of the multidomain state yields different behavior of the magnetic susceptibility $\partial M/\partial B$ and the magnetostriction $\partial L/\partial B$. This is demonstrated in Fig. 8(a), where the derivative of the magnetization and the longitudinal magnetostriction coefficient $\lambda_a^{\|} = (1/L_a)\partial L_a/\partial(\mu_0 H)$ are shown at $T = 2$ K as a function of B. The data are scaled to match the corresponding peak values. According to the Ehrenfest relation

$$\frac{\partial B^*}{\partial p_i} = V_m \frac{\Delta \lambda_i}{\Delta[\partial M/\partial(\mu_0 H)]}. \quad (5)$$

Using molar volume $V_m = 42.01$ cm^3/mol and $B^* = 0.8$ T [Fig. 8(b)], we obtain the normalized pressure dependency $(1/B^*)\partial B^*/\partial p = 0.8$ kbar^{-1}. Positive magnetostriction in the monodomain phase reveals that [see also Fig. 5(a)] for each domain, the in-plane distortion in magnetic field is such that the lattice expands perpendicular to the spin direction. Hence, applying a uniaxial pressure p will induce an anisotropy in plane favoring domains with spins nearly parallel to p in the multidomain phase.

The scaling of $\partial(M/H)/\partial(\mu_0 H)$ and $\lambda_a^{\|}$ at 2 K in Fig. 8(b) shows that the quantities vary proportional to each other in the multidomain state peaking at B^*. The proportional variation $d(m/H)/dH \sim \lambda_a^{\|}$ is consistent on combining Eq. (3) with Eq. (4) and is a manifestation of the magnetoelastic nature of the domains. The behavior is expected from phenomenolog-

ical theories of magnetoelastic domains which describe the variation of magnetization and length changes by means of a single domain co-alignment parameter and its variation with magnetic field [61].

Apart from a large magnetocrystalline anisotropy which dictates the easy-plane spin structure in $NiTiO_3$, an additional small in-plane anisotropy may arise due to frozen strains in the domain walls [65]. The origin of this in-plane gap in the spin-wave spectrum of easy-plane antiferromagnets have been theoretically predicted [66,67] and experimentally observed in several easy-plane-type antiferromagnets, for example, the dihalides NiCl2 ($\sim$0.3 T) and CoCl2 ($\sim$0.8 T) by means of low-frequency resonance experiments [68]. Interestingly, $CoTiO_3$, which exhibits similar crystallographic and magnetic structure to $NiTiO_3$, shows an in-plane gap of $\sim$1 meV in recent inelastic neutron scattering experiments [24,25]. A frustrated bond anisotropic exchange interaction pinning the order parameters to the crystal axes [24,25] was suggested as the responsible mechanism for small in-plane gap in $CoTiO_3$, which is unlikely for $NiTiO_3$. However, in view of the theoretical predictions and experimental observations listed above, we speculate a small in-plane anisotropy to be present in $NiTiO_3$ corresponding with the frozen strains in magnetoelastic domain walls.

V. SUMMARY

In summary, we have studied in detail the magnetostructural coupling in magnetodielectric $NiTiO_3$ by means of single-crystal neutron diffraction and high-resolution dilatometry. Zero-field neutron diffraction confirms the multidomain A-type spin AFM ordering with preservation of crystallographic R-3 symmetry down to 2 K. Zero-field thermal expansion measurements reveal spontaneous lattice deformation at T_N. The dielectric permittivity ϵ scales with the square of the magnetic order parameter L in line with predictions of Landau theory, hence indicating finite magnetodielectric coupling in $NiTiO_3$. Our analysis suggests the presence of spin-phonon coupling as a responsible mechanism for the dielectric anomaly at T_N in $NiTiO_3$. In-field neutron diffraction shows the evolution of magnetic domains with spins perpendicular to the applied field. The effect of magnetic domains on magnetostriction has been discussed in light of phenomenological multidomain theories. We see magnetization and magnetostriction scale with each other in the multidomain state, revealing strong coupling of spins to the lattice.

[1] R. Zhong, T. Gao, N. P. Ong, and R. J. Cava, Sci. Adv. **6**, eaay6953 (2020).

[2] H. Liu and G. Khaliullin, Phys. Rev. B **97**, 014407 (2018).

[3] S. S. Pershoguba, S. Banerjee, J. C. Lashley, J. Park, H. Ågren, G. Aeppli, and A. V. Balatsky, Phys. Rev. X **8**, 011010 (2018).

[4] L. Chen, J.-H. Chung, B. Gao, T. Chen, M. B. Stone, A. I. Kolesnikov, Q. Huang, and P. Dai, Phys. Rev. X **8**, 041028 (2018).

[5] T. Matsumoto and S. Hayami, Phys. Rev. B **101**, 224419 (2020).

[6] A. I. Kurbakov, A. N. Korshunov, S. Y. Podchezertsev, A. L. Malyshev, M. A. Evstigneeva, F. Damay, J. Park, C. Koo, R. Klingeler, E. A. Zvereva, and V. B. Nalbandyan, Phys. Rev. B **96**, 024417 (2017).

[7] A. Nakua and J. Greedan, J. Solid State Chem. **118**, 402 (1995).

[8] C. Koo, E. A. Zvereva, I. L. Shukaev, M. Richter, M. I. Stratan, A. N. Vasiliev, V. B. Nalbandyan, and R. Klingeler, J. Phys. Soc. Jpn. **85**, 084702 (2016).

[9] K. S. Burch, D. Mandrus, and J.-G. Park, Nature **563**, 47 (2018).

[10] A. Maignan and C. Martin, Phys. Rev. Materials **2**, 091401(R) (2018).

[11] J. Werner, W. Hergett, M. Gertig, J. Park, C. Koo, and R. Klingeler, Phys. Rev. B **95**, 214414 (2017).

[12] N. D. Khanh, N. Abe, K. Matsuura, H. Sagayama, Y. Tokunaga, and T. Arima, Appl. Phys. L **114**, 102905 (2019).

[13] J. B. Goodenough and J. J. Stickler, Phys. Rev. **164**, 768 (1967).

[14] G. Shirane, S. Pickart, and Y. Ishikawa, J. Phys. Soc. Jpn. **14**, 1352 (1959).

[15] R. E. Newnham, J. H. Fang, and R. P. Santoro, Acta Crystallogr. **17**, 240 (1964).

[16] J. J. Stickler, S. Kern, A. Wold, and G. S. Heller, Phys. Rev. **164**, 765 (1967).

[17] G. S. Heller, J. J. Stickler, S. Kern, and A. Wold, J. Appl. Phys. **34**, 1033 (1963).

[18] J. Akimitsu, Y. Ishikawa, and Y. Endoh, Solid State Commun. **8**, 87 (1970).

[19] N. Mufti, G. R. Blake, M. Mostovoy, S. Riyadi, A. A. Nugroho, and T. T. M. Palstra, Phys. Rev. B **83**, 104416 (2011).

[20] M. Charilaou, D. Sheptyakov, J. F. Löffler, and A. U. Gehring, Phys. Rev. B **86**, 024439 (2012).

[21] J. K. Harada, L. Balhorn, J. Hazi, M. C. Kemei, and R. Seshadri, Phys. Rev. B **93**, 104404 (2016).

[22] K. Dey, S. Sauerland, J. Werner, Y. Skourski, M. Abdel-Hafiez, R. Bag, S. Singh, and R. Klingeler, Phys. Rev. B **101**, 195122 (2020).

[23] R. M. Dubrovin, N. V. Siverin, M. A. Prosnikov, V. A. Chernyshev, N. N. Novikova, P. C. M. Christianen, A. M. Balbashov, and R. Pisarev, J. Alloys Compd. **858**, 157633 (2020).

[24] B. Yuan, I. Khait, G.-J. Shu, F. C. Chou, M. B. Stone, J. P. Clancy, A. Paramekanti, and Y.-J. Kim, Phys. Rev. X **10**, 011062 (2020).

[25] M. Elliot, P. A. McClarty, D. Prabhakaran, R. D. Johnson, H. C. Walker, P. Manuel, and R. Coldea, arXiv:2007.04199 (2020).

[26] H. Watanabe, H. Yamauchi, and H. Takei, J. Magn. Magn. Mat. **15–18**, 549 (1980).

[27] R. Küchler, T. Bauer, M. Brando, and F. Steglich, Rev. Sci. Instruments **83**, 095102 (2012).

[28] T. Barth and E. Posnjak, Z. Kristallogr. **88**, 271 (1934).

[29] K. Kabsch, in *International Tables for Crystallography, Vol. F*, edited by M. G. Rossmann and E. Arnold (Kluwer Academic Publishers, Dordrecht, 2001), Chap. 11.3.

[30] *CrysAlisPro*, Agilent Technologies UK Ltd., Oxford (2011).

[31] R. H. Blessing, Acta Cryst. A **51**, 33 (1995).

[32] *SCALE3 ABSPACK, CrysAlisPro*, Agilent Technologies UK Ltd., Oxford (2011).

[33] W. R. Busing and A. Levy, Acta Cryst. **10**, 180 (1957).

[34] G. M. Sheldrick, *SHELXT*, University of Göttingen and Bruker AXS Gmbh, Karlshruhe, Germany (2012–2018).

[35] M. Ruf and B. C. Noll, *Application Note SC-XRD 503*, Bruker AXS Gmbh, Karlshruhe, Germany (2014).

[36] G. Sheldrick, Acta Cryst. A **71**, 3 (2015).

[37] G. M. Sheldrick, *SHELXL-20xx*, University of Göttingen and Bruker AXS Gmbh, Karlshruhe, Germany (2012–2018).

[38] W. Robinson and G. M. Sheldrick, *Crystallographic Computing 4* (IUCr and Oxford University Press, Oxford, UK, 1988).

[39] G. Sheldrick, Acta Cryst. A **64**, 112 (2008).

[40] G. Sheldrick, Acta Cryst. C **71**, 3 (2015).

[41] P. J. Brown, A. G. Fox, H.-C. Hu, J. I. Langford, H. Lipson, E. N. Maslen, M. A. O'Keefe, T. M. Sabine, and B. T. M. Willis, in *International Tables for Crystallography, Vol. C*, edited by E. Prince (Kluwer Academic Publishers, Dordrecht, 2004), 3rd ed., Chap. 6.

[42] P. Azavant and A. Lichanot, Acta Cryst. A **49**, 91 (1993).

[43] S. L. Morelhão, *Computer Simulation Tools for X-ray Analysis* (Springer International Publishing Cham, Switzerland, 2016), Chap. 1.3.1 and Appendix B, http://xraybook.if.usp.br.

[44] A. C. Larson, *Crystallographic Computing* (Munksgaard, Copenhagen, Denmark, 1970).

[45] CSD 2062660 (model A), 2062661 (model B), and 2062662 (model C) contain the supplementary crystallographic data for this paper. These data can be obtained from the Cambridge Crystallographic Data Centre's and FIZ Karlsruhe's joint Access Service via, https://www.ccdc.cam.ac.uk/structures/?

[46] G. Lawes, A. P. Ramirez, C. M. Varma, and M. A. Subramanian, Phys. Rev. Lett. **91**, 257208 (2003).

[47] T. D. Sparks, M. C. Kemei, P. T. Barton, R. Seshadri, E.-D. Mun, and V. S. Zapf, Phys. Rev. B **89**, 024405 (2014).

[48] U. Adem, G. Nénert, Arramel, N. Mufti, G. R. Blake, and T. T. M. Palstra, Eur. Phys. J. B **71**, 393 (2009).

[49] See Supplemental Material at http://link.aps.org/supplemental/10.1103/PhysRevB.103.134438 for up and down sweeps of relative length changes vs magnetic field in the ab-plane and crystal structure of NiTiO$_3$ in the ab-plane at 100 K and 2 K, respectively.

[50] M. K. Wilkinson, J. W. Cable, E. O. Wollan, and W. C. Koehler, Phys. Rev. **113**, 497 (1959).

[51] W. Knafo, C. Meingast, K. Grube, S. Drobnik, P. Popovich, P. Schweiss, P. Adelmann, T. Wolf, and H. v. Löhneysen, Phys. Rev. Lett. **99**, 137206 (2007).

[52] E. V. Gomonaj and V. M. Loktev, Low Temp. Phys. **25**, 520 (1999).

[53] H. Gomonay and V. M. Loktev, J. Phys.: Condens. Matter **14**, 3959 (2002).

[54] Y. Shapira and N. F. Oliveira, Phys. Rev. B **18**, 1425 (1978).

[55] M. Safa and B. Tanner, Phil. Mag. B **37**, 739 (1978).

[56] B. Tanner, Contemp. Phys. **20**, 187 (1979).

[57] T. Yamada, S. Saito, and Y. Shimomura, J. Phys. Soc. Jpn. **21**, 672 (1966).

[58] V. M. Kalita, A. F. Lozenko, and S. M. Ryabchenko, Low Temp. Phys. **26**, 489 (2000).

[59] V. M. Kalita, A. F. Lozenko, and P. A. Trotsenko, Low Temp. Phys. **28**, 263 (2002).

[60] V. M. Kalita and A. F. Lozenko, Low Temp. Phys. **27**, 645 (2001).

[61] V. M. Kalita, A. F. Lozenko, P. A. Trotsenko, and T. M. Yatkevich, Low Temp. Phys. **30**, 27 (2004).

[62] V. M. Kalita, A. F. Lozenko, S. M. Ryabchenko, and P. A. Trotsenko, Low Temp. Phys. **31**, 794 (2005).

[63] M. E. Lines, Phys. Rev. **131**, 546 (1963).

[64] H. Yamaguchi, H. Hiroyoshi, M. Yamada, H. Watanabe, and H. Takei, J. Mag. Magn. Mat. **31–34**, 1071 (1983).

[65] N. B. Weber, H. Ohldag, H. Gomonaj, and F. U. Hillebrecht, Phys. Rev. Lett. **91**, 237205 (2003).

[66] Y. B. Gaididei and V. Loktev, Solid State Commun. **39**, 1077 (1981).

[67] V. G. Bar'yakhtar, M. A. Savchenko, and V. Tarasenko, J. Exp. The. Phys. **22**, 1115 (1966).

[68] A. F. Lozenko and S. M. Ryabchenko, Sov. J. Exp. Theor. Phys. **38**, 538 (1974).

Supplement: Magneto-structural coupling in Ilmenite-type NiTiO$_3$: A combined diffraction and dilatometry study

K. Dey,[1, *] S. Sauerland,[1] B. Ouladdaif,[2] K. Beauvois,[2] H. Wadepohl,[3] and R. Klingeler[1, 4]

[1]*Kirchhoff Institute of Physics, Heidelberg University,*
INF 227, 69120, Heidelberg, Germany

[2]*Institut Laue-Langevin, CS20156, 38042 GRENOBLE Cedex 9 - France*

[3]*Institute of Inorganic chemistry, Heidelberg University, 69120, Heidelberg, Germany*

[4]*Center for Advance Materials (CAM), Heidelberg University,*
INF 227, D-69120, Heidelberg, Germany

(Dated: February 15, 2021)

PACS numbers:
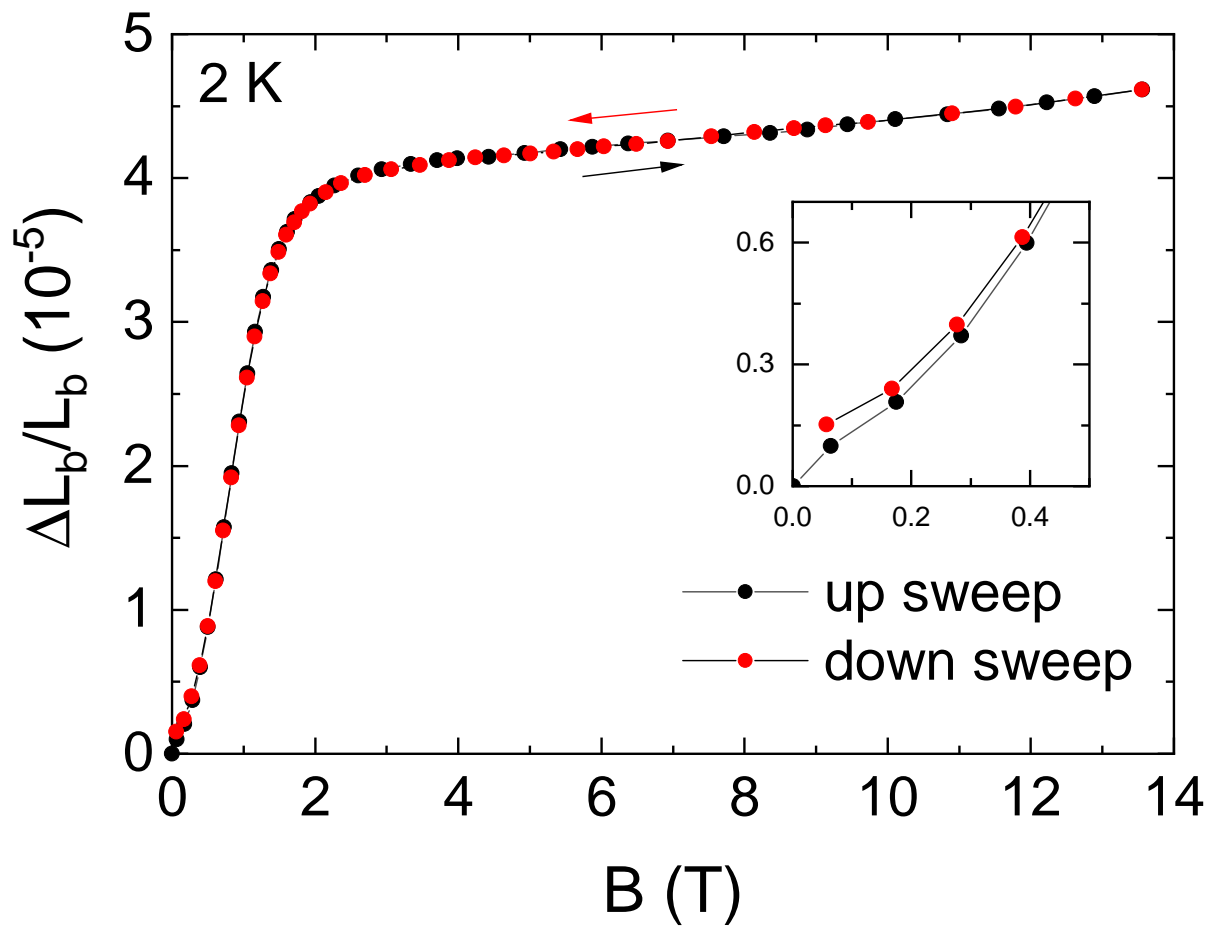
FIG. 1: Relative length changes dL_b/L_b versus magnetic field sweeps in the up and down down directions at 2 K. The inset shows an enlarged view in the low temperature region revealing small remanent magnetostriction.

* email:kaustav.dey@kip.uni-heidelberg.de

(a) 100 K – from single-crystal XRD

∠(Ni-O-Ni) = 90.349(12)°
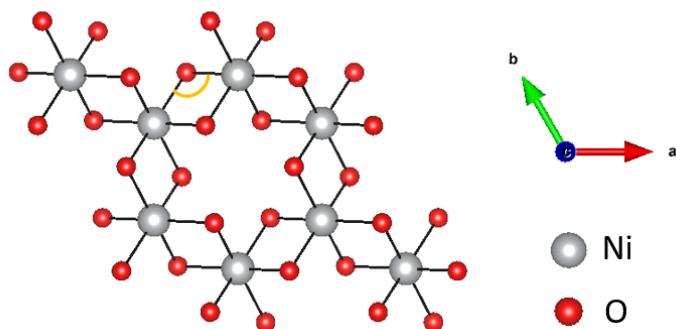
(b) 2 K – fromSingle crystal Neutron

∠(Ni-O-Ni) = 90.3619°
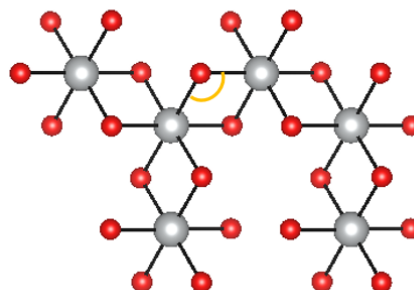
FIG. 2: Crystal structure of NiTiO$_3$ in the *ab*-plane determined at (a) 100 K using single-crystal X-ray diffraction and at (b) 2 K from single-crystal neutron diffraction experiment. The schematic crystal structure is generated using the VESTA software(https://jp-minerals.org/vesta).

2.3   Magnetic phase diagram, magnetoelastic coupling and Grüneisen scaling in CoTiO$_3$

The following section entitled "Magnetic phase diagram, magnetoelastic coupling and Grüneisen scaling in CoTiO$_3$" has been submitted for publication and is currently under review in Physical Review B journal.

In the following, contributions of each co-authors are explained in detail, particularly highlighting the specific contribution of K. Dey who is the co-first author and the communicating author.

- K. Dey performed the single crystal growth and characterization (Fig. 1) and magnetization measurements (SI Fig. 3). K. Dey supported the analysis of the specific heat (Fig. 3(a)), thermal expansion data (Fig. 3(b), 6) and in the construction of the magnetic phase diagram (Fig. 7). K. Dey plotted the final version of the plots, wrote and communicated the manuscript.

- M. Hoffmann is the co-first author of the paper. In the frame of his master thesis, M. Hoffmann performed the thermal expansion measurements (Fig. 3(b), Fig. (6)), analysed the specific heat data (3 (a)) and constructed the magnetic phase diagram (Fig. 7). M. Hoffmann also performed the Grüneisen analysis (Fig. 4 and SI Fig. 2) and wrote parts of the manuscript.

- J. Werner performed the high-field magnetization measurements (Fig. 5) and took part in the discussions.

- R. Bag assisted in the single-crystal growth.

- J. Kaiser in the frame of his bachelor thesis, oriented the single crystal and performed magnetization measurements (Fig. 2 and 5 (b)).

- H. Wadepohl performed and analysed the single-crystal X-ray diffraction experiments. H. Wadepohl assisted in writing the single-crystal x-ray section in the manuscript.

- Y. Skourski was the local contact at HLD-EMFL, Dresden and supervised the high-field magnetization measurements.

- M. Abdel-Hafiez performed the specific heat measurements (Fig. 3(a)).

- S. Singh supervised the single crystal growth experiments.

- R. Klingeler supervised the measurements, supported data analysis and manuscript writing.

- All the authors proofread the manuscript.

Magnetic phase diagram, magnetoelastic coupling and Grüneisen scaling in CoTiO₃

M. Hoffmann [*,1] K. Dey [*,1,†] J. Werner,[1] R. Bag,[2] J. Kaiser,[1] H. Wadepohl,[3]
Y. Skourski,[4] M. Abdel-Hafiez,[5] S. Singh,[2] and R. Klingeler[1,6]

[1]*Kirchhoff Institute of Physics, Heidelberg University,*
INF 227, D-69120, Heidelberg, Germany
[2]*Indian Institute of Science Education and Research, Pune, Maharashtra 411008, India*
[3]*Institute of Inorganic chemistry, Heidelberg University, 69120, Heidelberg, Germany*
[4]*Dresden High Magnetic Field Laboratory (HLD-EMFL),*
Helmholtz-Zentrum Dresden Rossendorf, D-01328 Dresden, Germany
[5]*Department of Physics and Astronomy,*
Uppsala University, Box 516, SE-751 20 Uppsala, Sweden
[6]*Center for Advance Materials (CAM), Heidelberg University,*
INF 227, D-69120, Heidelberg, Germany
(Dated: July 7, 2021)

Abstract

High-quality single crystals of CoTiO₃ are grown and used to elucidate in detail structural and magnetostructural effects by means of high-resolution capacitance dilatometry studies in fields up to 15 T which are complemented by specific heat and magnetization measurements. In addition, we refine the single-crystal structure of the ilmenite ($R\bar{3}$) phase. At the antiferromagnetic ordering temperature T_N pronounced λ-shaped anomaly in the thermal expansion coefficients signals shrinking of both the c and b axes, indicating strong magnetoelastic coupling with uniaxial pressure along c yielding six times larger effect on T_N than pressure applied in-plane. The hydrostatic pressure dependency derived by means of Grüneisen analysis amounts to $\partial T_\mathrm{N}/\partial p \approx 2.7(4)$ K/GPa. The high-field magnetization studies in static and pulsed magnetic fields up to 60 T along with high-field thermal expansion measurements facilitate in constructing the complete anisotropic magnetic phase diagram of CoTiO₃. While the results confirm the presence of significant magnetodielectric coupling, our data show that magnetism drives the observed structural, dielectric and magnetic changes both in the short-range ordered regime well-above T_N as well as in the long-range magnetically ordered phase.

PACS numbers:

---

* both the authors contributed equally
†email:kaustav.dey@kip.uni-heidelberg.de

1

I.   INTRODUCTION

The recent theoretical proposals on $3d^7$ Cobalt-based honeycomb magnets as a promising host for Kitaev model physics has sparked enormous interest in these materials [1, 2]. In the context of Kitaev materials, unlike the conventional $4d$ and $5d$ honeycomb ruthenates and iridates, the spin-obit coupling in $3d$ Co^{2+} ions is comparatively weaker resulting in a combined Kitaev-Heisenberg Hamiltonian with a rich magnetic phase diagram [2, 3]. Following the theoretical proposals, several new experimental materials for example BaCo$_2$(AsO$_4$)$_2$ [4], Na$_3$Co$_2$SbO$_6$ [5], Na$_2$Co$_2$TeO$_6$ [5–7] comprising of Co-based honeycomb structures have been under intense investigation.

In this report, we investigate CoTiO$_3$ belonging to the ilmenite titanates family with the general formula ATiO$_3$, where A is a $3d$ transition metal ion. The crystal structure comprises of alternating layers of corner sharing TiO$_6$ and CoO$_6$ octahedra along the c axis. In a particular ab plane, the magnetic Co^{2+} ions are interconnected via the O^{2-} ions and exhibit a buckled honeycomb-like structure [8]. The neutron-diffraction studies performed as early as 1964 by Newnham *et al.* [9] and more recently by Elliot *et al.* [10] on polycrystalline samples, reveal a long-ranged two-sublattice, easy-plane type antiferromagnetic structure below T_N= 38 K [11, 12], with ferromagnetically aligned Co^{2+} spins lying in the ab plane and the layers being coupled antiferromagnetically along the c axis. The easy-plane type magnetic anisotropy is due to a combined effect of crystal-field effects and spin-orbit coupling on high-spin $3d^7$ Co^{2+} ions effectively leading to a pseudospin-1/2 ground state [13–15].

The recent inelastic neutron scattering (INS) results generated enormous interest in this material. The main features of the magnon dispersion, i.e., the low-energy dispersion of spin waves and the observance of high-energy spin-orbit excitons at 28 meV was captured well with an XXZ-type Hamiltonian [10, 15, 16]. Unusual temperature dependence of the spin-orbit excitation was observed below T_N, which was accounted for by some mixing of the ground state doublet and excited state multiplets [16]. Most importantly, the presence of Dirac magnons at symmetry protected points in k-space was observed [15] which makes CoTiO$_3$ a model system to study non-trivial magnon band topology [10]. Application wise, CoTiO$_3$ has been studied in the past for its adaptability as high-κ dielectrics [17, 18], resonator antennas [19] and more recently for its significant magnetodielectric coupling properties [20, 21]. The mechanism yielding the observed significant magnetodielectric coupling in CoTiO$_3$ is however unclear.

Keeping in mind the fundamental and technological interest of CoTiO$_3$, we study in detail the high-field magnetization and magneto-structural coupling by means of high-resolution dilatometry. Thereby, we elucidate magnetoelastic coupling and establish the anisotropic magnetic phase diagram. Combination of thermal expansion data with specific heat enables us to analyse the relevant energy scales in terms of a Grüneisen analysis.

II.   EXPERIMENTAL METHODS

Macroscopic single crystals of CoTiO$_3$ were grown in a four-mirror optical floating-zone furnace (Crystal System Corporation, Japan) equipped with 4×150 W halogen lamps. Phase purity of the powders and pulverized single crystals was studied at room-temperature by means of powder X-ray diffraction (XRD) measurements on a Bruker D8 Advance ECO diffractometer with Cu-Kα source. Single crystal X-ray studies were performed at 100 K using an Agilent Technologies Supernova-E CCD 4-circle diffractometer (Mo-Kα radiation λ=0.71073 Å, micro-focus X-ray tube, multilayer mirror optics). Laue diffraction in the back scattering geometry was performed to study the crystallinity and to orient the single crystals. The composition analysis was performed

using scanning electron microscope equipped with energy dispersive x-ray (EDX) analysis (Zeiss ultra plus).

Static magnetic susceptibility $\chi = M/B$ was studied in magnetic fields up to 15 T applied along the principal crystallographic axes by means of a home-built vibrating sample magnetometer [22] (VSM) and in fields up to 5 T in a Quantum Design MPMS-XL5 SQUID magnetometer. The angular dependence of magnetisation was measured in a Quantum Design MPMS3 SQUID magnetometer using a horizontal rotator. Pulsed-magnetic-field magnetization was studied up to 60 T at the Helmholtz Zentrum Dresden Rossendorf by an induction method using a coaxial pick-up coil system [23]. The pulse raising time was 7 ms. The pulsed-field magnetization data were calibrated using static magnetic field measurements. Specific heat measurements have been done in a Quantum Design PPMS using a relaxation method. The relative length changes dL_i/L_i were studied on a single crystal of approximate dimensions $1.6 \times 2.0 \times 1.3$ mm^3 by means of a standard three-terminal high-resolution capacitance dilatometer [24, 25]. The measurements were performed in magnetic fields up to 15 T and the uniaxial thermal expansion coefficients $\alpha_i = 1/L_i \cdot dL_i(T)/dT$ were derived from the data.

III. CRYSTAL GROWTH AND CHARACTERIZATION

CoTiO$_3$ powders were synthesized by mixing stoichiometric amounts of Co$_3$O$_4$(99.9 % Alfa Aesar) and TiO$_2$(99.9 % Sigma-Aldrich) and sintering in air, at temperatures ranging from 900 to 1150° C with several intermediate grinding steps, until a single phase material was achieved. For crystal growth, about 7-9 cm of homogeneous and dense rods were obtained by first hydrostatically pressing the phase pure CoTiO$_3$ powders in rubber tubes and then sintering them at 1350° C for 24 h. Owing to its congruently melting nature [26], higher growth rates of 6-8 mm/h were employed for crystal growth. This is in contrast to other incongruently melting ilmenites, for example NiTiO$_3$ where a slower rate of 3 mm/h must be employed to successfully grow macroscopic single crystals [27]. Two growth experiments in differing gas flows comprising of air at ambient pressure and O$_2$ at 1 bar were performed. Both the growths were relatively stable and resulted in macroscopic single crystals. The optimized growth parameters are listed in table II.

TABLE I: Optimized growth parameters, lattice parameters, and phase analysis from the Rietveld refinement of the room temperature powder XRD data of crushed CoTiO$_3$ single crystals of two growth experiments (I and II). Feed and seed rods were counter-rotated at the same rotation speed.

	I	II
atmosphere	air	O$_2$
pressure	ambient	1 bar
growth-rate (mm/h)	6	6
rot. speed (mm/h)	20	20
latt. parameter a (Å)	5.066(7)	5.065(3)
latt. parameter c (Å)	13.918(7)	13.916(2)
composition (Co : Ti)	1 : 1.004	1 : 1.08
secondary phase	TiO$_2$ + Co$_2$TiO$_4$	TiO$_2$ +Co$_2$TiO$_4$

Fig. 1(a) shows a representative CoTiO$_3$ boule grown in O$_2$ atmosphere at 1 bar pressure. The phase analysis by means of Rietveld refinements of powder XRD data of the pulverized single
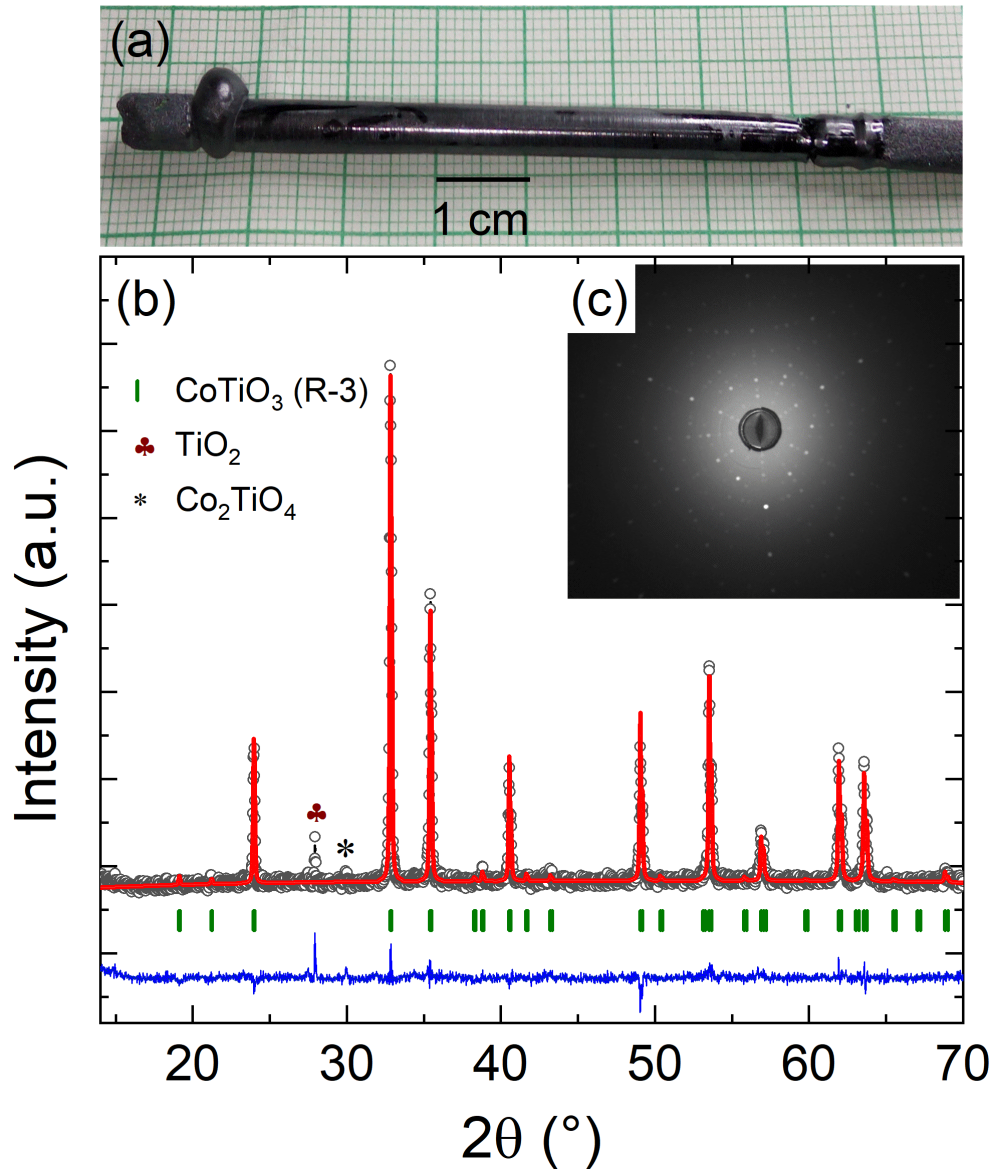
FIG. 1: (a) Picture of an as-grown CoTiO$_3$ boule obtained in O$_2$ atmosphere at 1 bar pressure. (b) Rietveld refinement fit of the room temperature XRD data of a powdered CoTiO$_3$ single crystal. The observed diffraction pattern is shown in black, calculated pattern in red and the difference between observed and calculated pattern is shown in blue. The vertical ticks in green denote the allowed Bragg positions of the ilmenite phase and (c) is a representative Laue pattern of CoTiO$_3$ single crystal.

crystalline pieces (see Fig. 1(b) and Table II) implies the main ilmenite ($R\bar{3}$) phase as well as the secondary TiO$_2$ (Rutile) and the spinel (Co$_2$TiO$_4$) phase in both air and oxygen atmosphere grown crystals. Such secondary phases were observed as inclusions in previously reported CoTiO$_3$ crystals by Balbashov *et al.* [11] and ascribed to high-temperature gradients at the growth interface. A qualitative comparison of the relative intensities of impurity peaks from room temperature XRD data reveals that the spinel Co$_2$TiO$_4$ phase is present in larger proportions in air-grown than in oxygen-grown single crystals (where it is hardly visible; see Fig. 1(b)) in agreement with Balbashov *et al.*. However, the EDX analysis suggests a better stoichiometric proportion of Co:Ti for

air-grown as compared to oxygen-grown crystals. We ascribe this to a slightly increased evaporation of cobalt oxides in oxygen flow as compared to air flow resulting in stoichiometric mismatch which furthermore leads to a higher proportion of precipitated TiO_2 phase in oxygen-grown crystals (see Fig. 1(b)). However, as will be shown below, the sharp anomalies in magnetization and thermodynamic measurements imply negligible effects of the minor stoichiometric mismatch. Importantly, the back-scattered Laue diffraction spots for the oxygen-grown samples are sharp indicating a high-quality (Fig.1(c)) as compared to air-grown crystals where the splitting of spots was observed at various points along the grown boule. Due to relatively low proportions of magnetic spinel impurity and better quality, we employed cut and oriented $CoTiO_3$ single crystals grown in O_2 flow at 1 bar for further studies.

To the best of our knowledge, the earlier studies of ilmenite-type $CoTiO_3$ crystal structure have been limited to powder diffraction experiments only [8, 9, 11]. We have re-investigated the crystal structure of our oxygen-grown single crystals by means of high resolution single crystal XRD at 100 K with Mo Kα radiation ($\lambda = 0.71073$ Å). Experimental and refinement details are given in the supplementary material. Similar to the recent single-crystal X-ray diffraction study on $NiTiO_3$[28], three somewhat different models were employed for the atomic structure factors f_{at} within the independent spherical atoms approximation: conventional f_{at} calculated with neutral atoms for Co, Ti and O (model A) and two "ionic" models[29] (f_{at} for Co^{2+}, Ti^{4+} and O^{2-} (models B and C); for details see SI). The different models refined to essentially the same structure, with a marginally better fit of model B, but only insignificant differences in the key parameters like atom coordinates, R values, U_{eq} for all atoms and residual electron density. Inter-atomic distances agreed within one standard deviation. The structural refinements confirm the assignment of $R\bar{3}$ space group and improve the accuracy of the crystallographic parameters previously obtained. The obtained lattice parameters and relevant crystallographic information are listed in table **??** [30].

TABLE II: Fractional atomic coordinates, Wyckoff positions, site occupation and equivalent isotropic displacement parameters (Å²) of $CoTiO_3$ as obtained from refinement of single-crystal XRD measurements at 100 K using model B (see text for more details). [Space group: $R\bar{3}$ (148), $a = b = 5.0601$ Å, $c = 13.8918$ Å, $\alpha = \beta = 90°$, $\gamma = 120°$; sof denotes the fraction of atom type present at the site after application of crystallographic symmetry;

Atom	Site	x	y	z	sof	$U_{eq}{}^a$
Co	6c	0	0	0.14511(2)	1	0.00297(2)
Ti	6c	0	0	0.35448(2)	1	0.00262(2)
O	18f	0.02051(6)	0.31608(6)	0.25410(2)	1	0.00391(3)

Note: ^{a} U_{eq} is defined as one third of the trace of the orthogonalized U_{ij} tensor. The anisotropic displacement factor exponent takes the form: $-2\pi^2[h^2a^{*2}U_{11} + ... + 2hka^*b^*U_{12}]$.]

IV.   MAGNETOELASTIC COUPLING

The onset of long-range antiferromagnetic order in $CoTiO_3$ at $T_N = 37$ K is associated with pronounced anomalies in the magnetic susceptibility (Fig. 2) as well as in the specific heat and the thermal expansion (Fig. 3). The magnetic susceptibility is nearly isotropic in the ab plane and exhibits a significant anisotropy with respect to the c axis up to the highest measured temperatures of 350 K. For $T \leq T_N$, the susceptibility decreases for magnetic fields B applied in the ab plane and
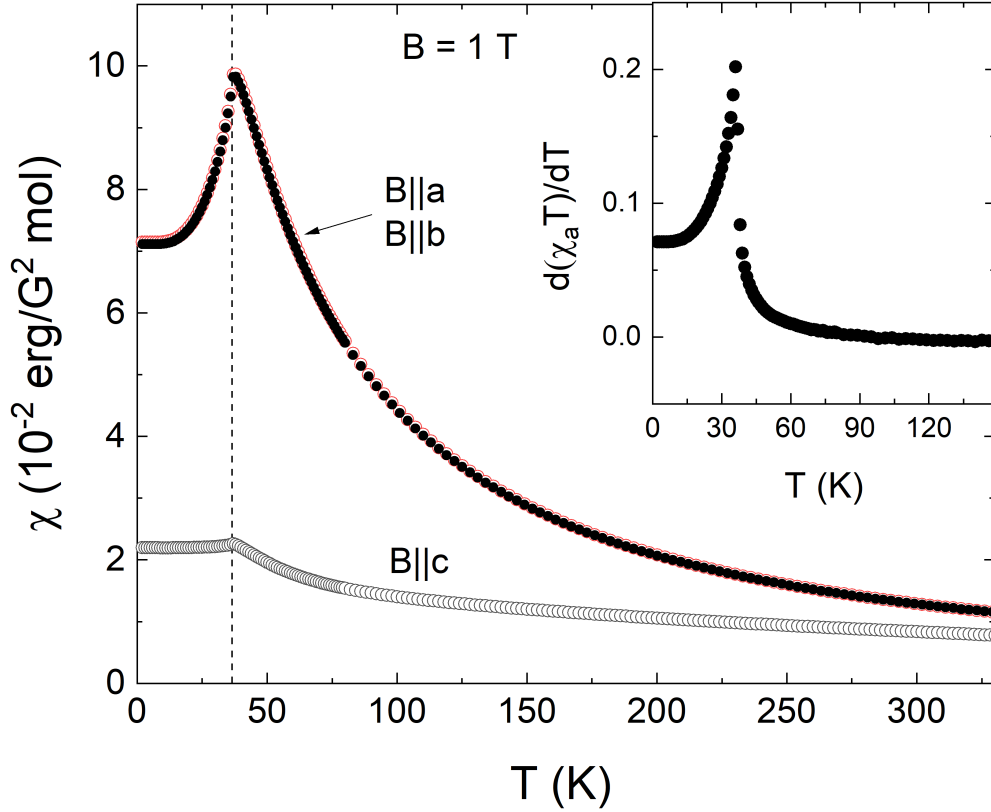
FIG. 2: Temperature dependence of static magnetic susceptibility $\chi = M/B$ at $B = 1$ T applied along the principal crystallographic directions. The inset presents Fisher's specific heat [31] $\partial(\chi T)/\partial T$ at $B\|a=1$ T.

attains a constant value for $B\|c$ axis suggesting an easy-plane-type antiferromagnetic structure. This is in accordance with previous studies on polycrystalline [9, 12] and single crystalline CoTiO$_3$ samples [11, 32]. Above T_N, the persisting anisotropy up to 350 K is attributed to single-ion effects due to the octahedral crystal field and spin-orbit coupling on magnetic Co^{2+} spins which results in an effective spin $J_{eff} = 1/2$ ground state [14, 15]. The high-temperature susceptibility behaviour cannot be accounted for by the Curie-Weiss model with an anisotropic g-factor. This is explained by considerable mixing of the ground state $J_{eff} = 1/2$ with excited state multiplets, i.e., $J_{eff} = 3/2, 5/2...$ as experimentally observed in recent INS studies on CoTiO$_3$ [10, 15, 16] and theoretically described by Goodenough [13]. In the literature, the high-temperature susceptibility of cobaltates comprising of Co^{2+} ions in octahedral crystalline fields is reported to show complicated temperature dependencies for example in CoCl$_2$ [14] and Na$_3$Co$_2$SbO$_6$ [3] among several others.

The sharp λ-shaped anomalies in the specific heat [Fig. 3(a)] and in Fisher's specific heat [31] $\partial(\chi_a T)/\partial T$ (Fig. 2 (inset)) confirm the onset of long-range order at T_N and also the continuous nature of the phase transition. In order to assess the magnetic entropy changes, the phononic contribution to the specific heat (c_p^{ph}) has been estimated by fitting the previously published c_p data from Klemme *et al.* [33] at temperatures well above T_N by an extended Debye model which includes both Debye and Einstein terms [34]. The model fits very well the data at temperatures above 70 K and yields characteristic Debye and Einstein temperatures of $\Theta_D = 626(20)$ K and $\Theta_E = 193(10)$ K, respectively. Integrating the magnetic specific heat (c_p- c_p^{ph})/T yields the magnetic entropy changes $S_{mag} = 5.2(2)$ J/(mol K) which is close to the theoretically predicted value of R$ln(2) = 5.7$ J/(mol K) for $J_{eff} = 1/2$ Co^{2+} spins. The results imply that approximately 15 %
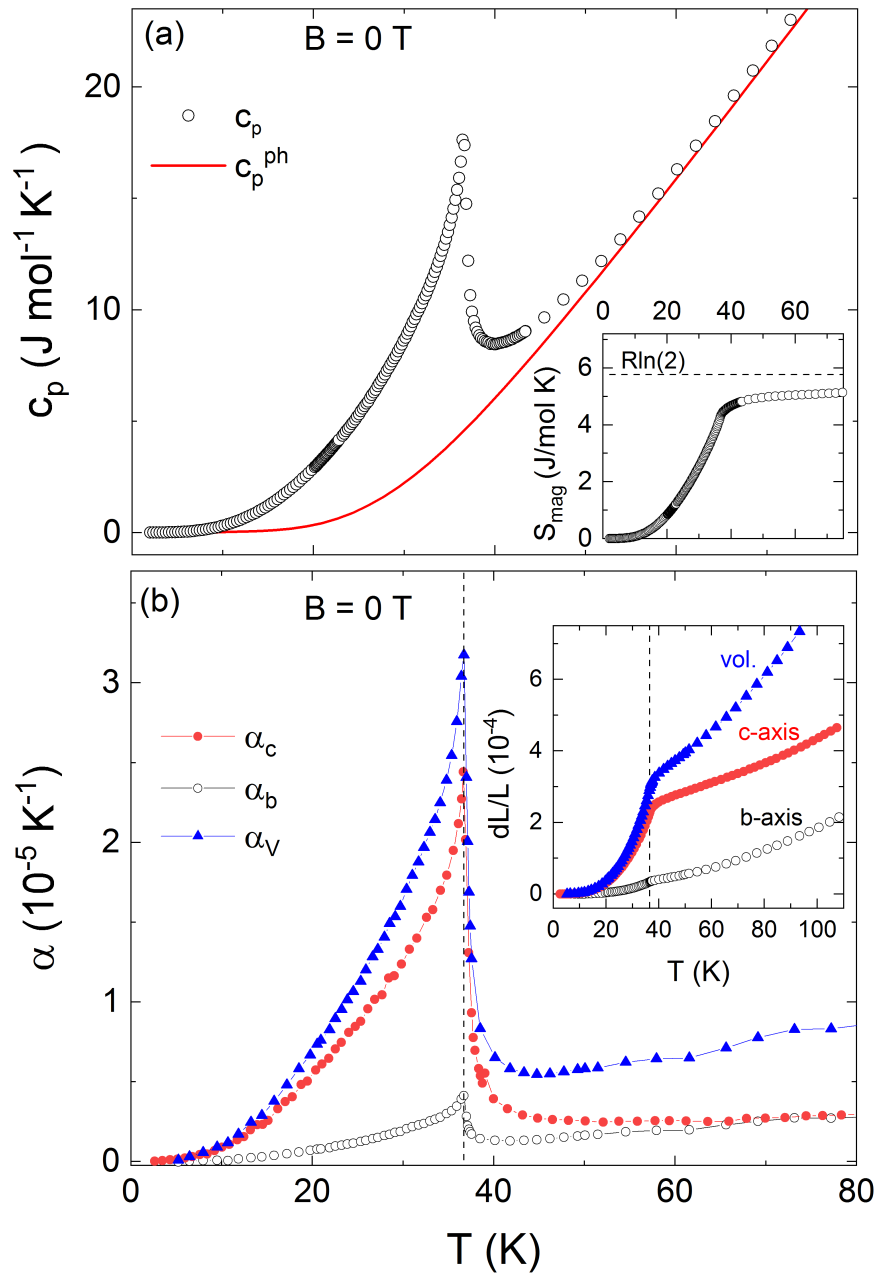
FIG. 3: (a) Temperature dependence of specific heat c_p in zero magnetic field. The solid red line in (a) indicates the phonon specific heat c_p^{ph} obtained by fitting the c_p data with a combined Debye and Einstein model well above the magnetic ordering transition (see the text). The inset to (a) shows the magnetic entropy changes obtained by integrating $(c_p - c_p^{ph})/T$. (b) Thermal expansion coefficients α_i versus temperature along the crystallographic b and c axes and the volume thermal expansion coefficient α_V. The dashed vertical line marks T_N. The inset to (b) shows the associated relative length changes dL_i/L_i versus temperature.

of the total magnetic entropy is consumed between T_N and 70 K, suggesting the presence of considerable short-range correlations precursing the evolution of long-range magnetic order.

The zero-field thermal expansion measurements reveal strong anomalies at T_N in the uniaxial thermal expansion coefficients $\alpha_i (i = b, c)$ and in the relative length changes dL_i/L_i [Fig. 3(b)]. The anomalies demonstrate large spontaneous magnetostriction at T_N and hence the presence of significant magnetoelastic coupling in CoTiO$_3$. The measured relative length changes shown in the inset to Fig. 3(b) signal shrinking of both c and b axes upon the evolution of magnetic order at T_N with the size of the anomaly in α_c about six times larger than in α_b. As these data imply positive uniaxial pressure dependencies both for pressure applied in-plane and along c, the anomaly in the volume thermal expansion coefficient $\alpha_V = \alpha_c + 2\alpha_b$ correspondingly signals a significant positive hydrostatic pressure dependency. Furthermore, α_b and α_c in Fig. 3(b) (also see inset to Fig. 4) evidence structural effects above T_N precursing the onset of long-range order up to around 70 K. This coincides with the temperature regime where magnetic entropy changes mark the presence of short-range magnetic correlations.
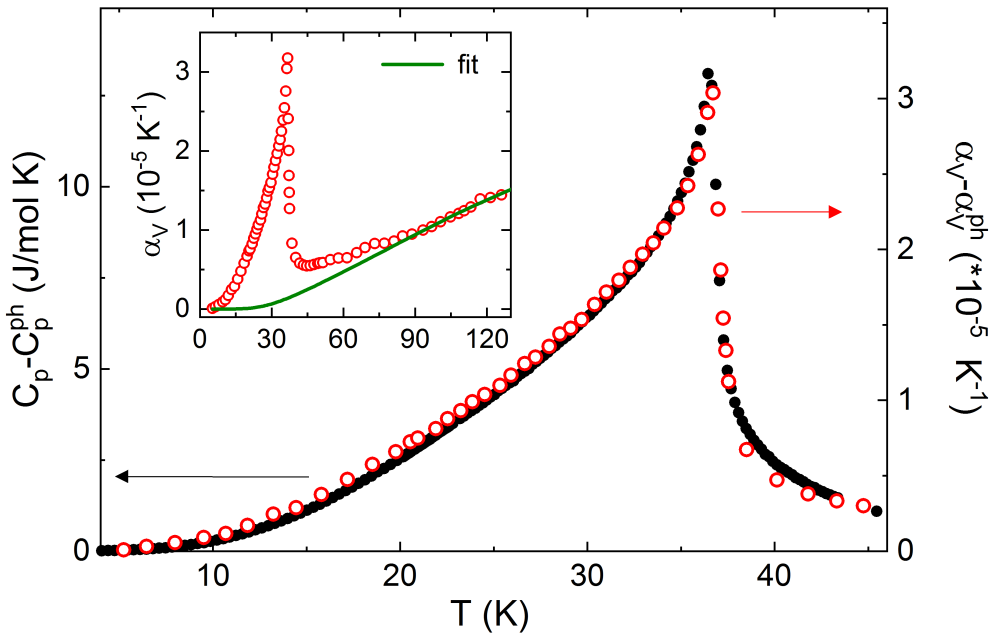
FIG. 4: Grüneisen scaling of the magnetic contributions to the heat capacity c_p^{mag} and volume thermal expansion coefficient α_V^{mag}. Inset: The volume thermal expansion coefficient α_V along with a combined Debye-Einstein fit to the high-temperature data (see the text).

Comparison of the non-phononic contributions to the thermal expansion coefficient and the specific heat enables further conclusions on the nature of the associated entropy changes and on magnetoelastic coupling. Exploiting Grüneisen scaling for the lattice, we have approximated the phononic contribution to the volume thermal expansion coefficient α_V by using the same Θ_D and Θ_E from the background specific heat c_p^{ph} (Fig. 3(a)) and scaling the Debye and Einstein contributions accordingly [27]. As seen in the inset to Fig. 4, the background to α_V is well approximated above 90 K. This procedure yields the lattice Grüneisen parameters $\gamma^{\mathrm{ph}} = \alpha^{\mathrm{ph}}/c_p^{\mathrm{ph}}$ [22] which amount to $\gamma_D = 1.02 \times 10^{-7}$ mol/J and $\gamma_E = 1.0(3) \times 10^{-7}$ mol/J, respectively.

The obtained non-phononic contributions to the thermal expansion coefficient α_V^{mag} are shown with the non-phononic specific heat c_p^{mag} in Fig. 4(a). Both quantities vary proportionately in the entire T-range, i.e., the magnetic Grüneisen parameter is T-independent. This observation implies

the presence of a single dominant energy scale J [22, 35]. Since the entropy changes are of magnetic nature, we conclude that a single dominant magnetic degree of freedom drives the observed non-phononic length and entropy changes. The corresponding magnetic volume Grüneisen parameter amounts to $\Gamma_V^m = \alpha_V^{\mathrm{mag}}/c_p^{\mathrm{mag}} = 24(2) \times 10^{-7}$ mol/J. The hydrostatic pressure (p_h) dependency of T_N is obtained from the Ehrenfest relation $\partial T_N/\partial p_h = T_N V_m \Gamma_V^m = 2.7(4)$ K/GPa. Here, we used the molar volume $V_m = 3.09 \times 10^{-5}$ m^3/mol. Furthermore, Grüneisen scaling for each individual axis is confirmed by good proportionality between the uniaxial thermal expansion coefficients α_b^{mag} and α_c^{mag} and c_p^{mag} (see the SI Fig. 2) from which we read-off $\Gamma_c^m = 1.8(4) \times 10^{-6}$ mol/J and $\Gamma_b^m = 3(1) \times 10^{-7}$ mol/J, respectively. This yields the uniaxial pressure dependencies of $\partial T_N/\partial p_c = 2.1(5)$ K/GPa and $\partial T_N/\partial p_b = 0.3(1)$ K/GPa, respectively.

V. HIGH-FIELD MAGNETIZATION AND THE PHASE DIAGRAM

The saturation fields and moments at $T = 1.5$ K are determined from pulsed-field magnetization studies up to 60 T as shown in Fig. 5(a). The absolute values of magnetization are calibrated with the SQUID data shown in Fig. 5(a,b). The magnetization is anisotropic and for both $B||a$ and $B||c$ shows largely linear behaviour in a wide range of applied magnetic fields. At any particular field, the magnetization is higher for $B||a$ as compared to $B||c$ which is expected for a highly anisotropic easy-plane antiferromagnet. The saturation fields are determined from the peaks in $\partial M/\partial B$ (Fig. 5(a) inset), and we obtain $B_{\mathrm{sat,ab}} = 16.3(5)$ T and $B_{\mathrm{sat,c}} = 46(1)$ T for fields in the ab plane and along the c axis, respectively. Above B_{sat}, the magnetization increases linearly which is ascribed to Van Vleck paramagnetism of the Co^{2+} ions in an octahedral environment. From the magnetization slope determined from linear-fits (dashed lines in Fig. 5(a)) above the saturation fields we obtain the Van Vleck susceptibility as $\chi_{\mathrm{ab}}^{\mathrm{VV}} = 0.013$ erg/(G^{2}mol) and $\chi_c^{\mathrm{VV}} = 0.011$ erg/(G^{2}mol), respectively. These values are similar to those in other Co-based systems [36, 37]. The saturation magnetisation and corresponding g-factors obtained after appropriate Van Vleck correction, amounts to $M_{\mathrm{sat,ab}} = 2.89$ μ_B/f.u. and $g_{\mathrm{ab}} = 5.7(2)$ for the ab plane and $M_{\mathrm{sat,c}} = 1.31$ μ_B/f.u. and $g_c = 2.62(4)$ for the c axis, respectively.

A closer look at the low-field behaviour as shown in Fig. 5(b) at $T = 2$ K, confirms the linearity of M for $B||c$ extending to zero magnetic field whereas a non-linear behaviour (sickle-shaped) up to 4 T is observed for magnetic fields applied in the ab plane. Specifically, the derivative of magnetization with respect to magnetic field shows a broad peak centered at $B^* = 2$ T suggestive of a spin-reorientation process and previously described as a continuous rotation of Co^{2+} moments in the basal plane aided by magnetic field [11]. Increasing temperature has negligible effects on B^* (see SI Fig. 3) resulting in a horizontal phase boundary (Fig. 7). Static magnetic susceptibility measured in magnetic fields up to 15 T [Fig. 5 (c),(d)] confirm the linear respectively non-linear behavior for the different magnetic field directions. For $B||a$ the slight non-linearity below B^* is exhibited by a monotonous change for $T < T_N$ at applied magnetic fields $B \geq 3$ T as compared to $B = 1$ T. Overall, the data confirm spin-reorientation behaviour as for $B \geq 3$ T (i.e. above B^*) the susceptibility attains an almost constant value below T_N whereas it decreases sharply for $B||a = 1$ T. In addition, the data show the effect of external magnetic fields on the long-range spin ordered phase and particularly reveal stronger suppression of T_N for magnetic fields $B = 15$ T applied in the ab plane by $\Delta T_N = 18$ K as compared to the $B||c$ axis with yields $\Delta T_N = 2$ K.

A strongly anisotropic field effect is also evident from Fig. 6 where the thermal expansion coefficients α_i are shown for external magnetic fields up to 15 T. For $B||c$, T_N shifts slightly to lower temperatures along with a considerable increase in anomaly height on increasing magnetic fields. In contrast for $B||b$, suppression of the anomaly height is observed along-with a considerable shift
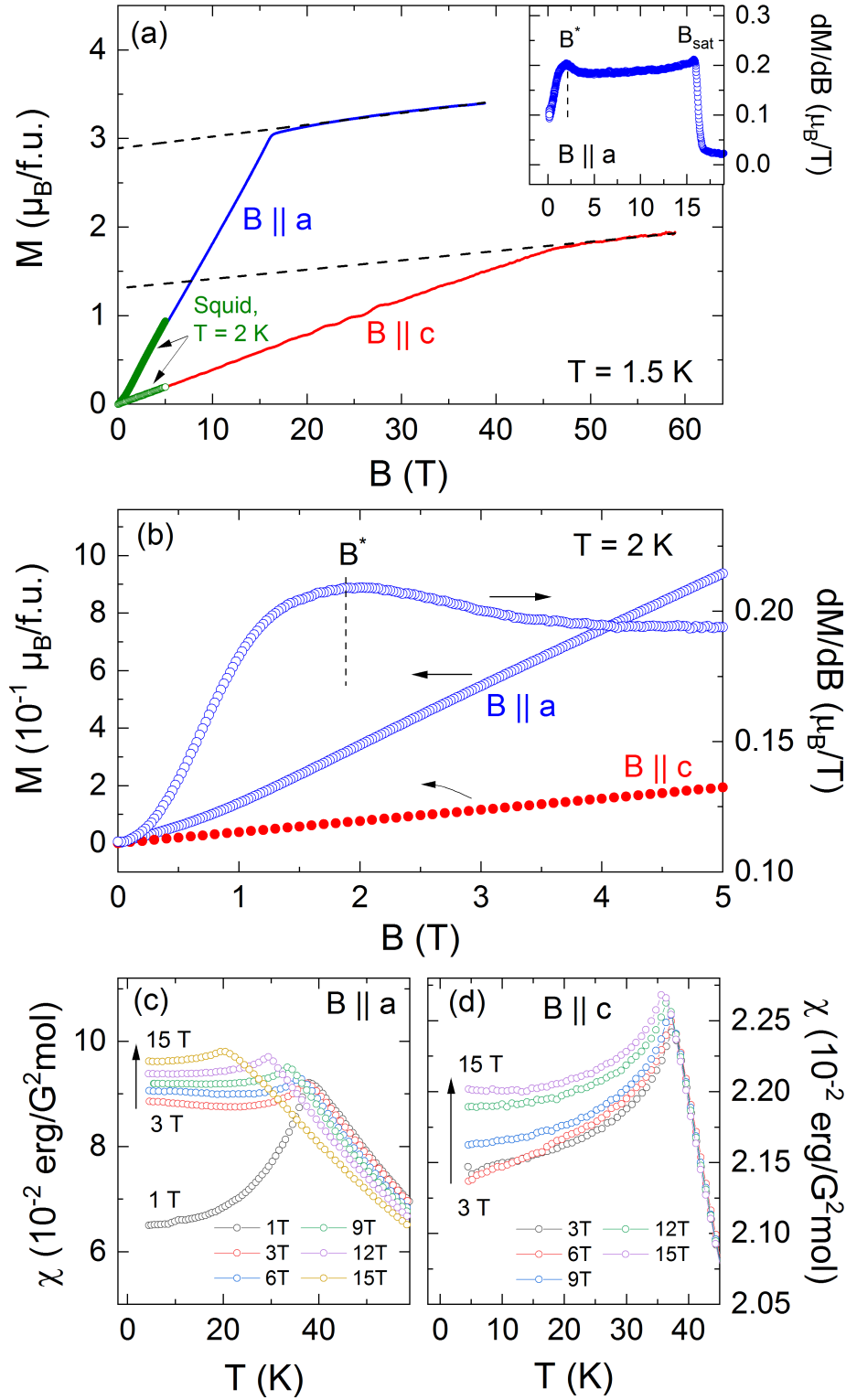
FIG. 5: (a) Pulsed-field magnetization M at $T = 1.5$ K. Dashed lines in (a) denote Van Vleck paramagnetism. The inset to (a) shows the field derivative $\partial M/\partial B$ for $B\|a$. (b) Quasi-static field magnetization M and magnetic susceptibility $\partial M/\partial B$ versus magnetic field along the a and c axes, at $T = 2$ K. (c) and (d) Static magnetic susceptibility $\chi = M/B$ versus temperature for magnetic fields up to 15 T applied along the a- and c axes, respectively.
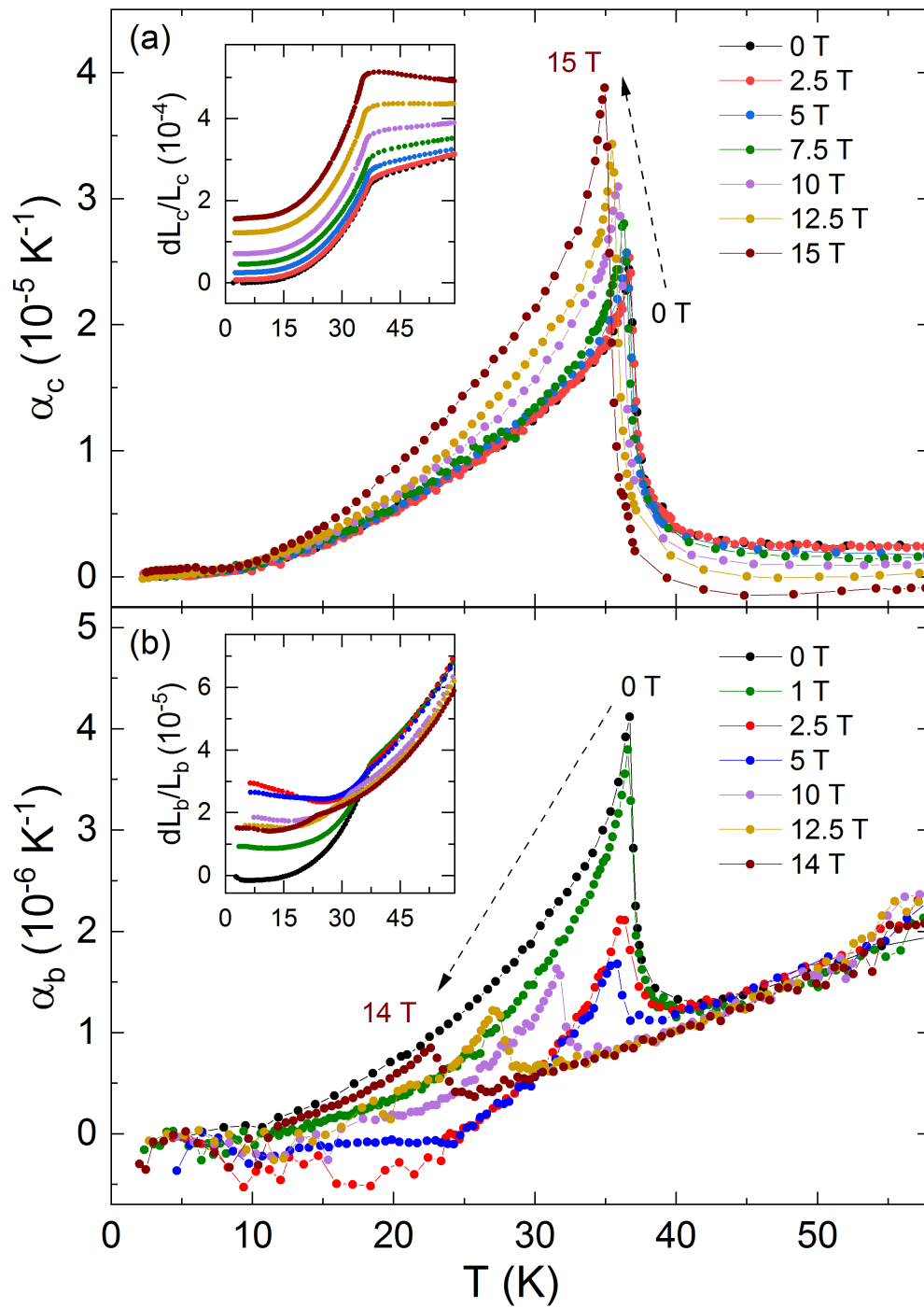
FIG. 6: Thermal expansion coefficients α_i at magnetic fields between 0 and 14 T magnetic fields applied along the (a) c- and (b) b axes, respectively. The insets show the corresponding relative length changes dL_i/L_i shifted by means of experimental magnetostriction curves, at $T = 50$ K (c axis) and 30 K (b axis).

of T_N to lower temperatures for fields above 5 T. The sharp anomalies in α_i facilitates construction of the magnetic phase diagram as shown in Fig. 7.

VI. DISCUSSION

One of the intriguing properties of CoTiO$_3$ is strong magnetoelectric coupling, the microscopic origin of which is still unclear. While our data show and elucidate pronounced magnetoelastic coupling, anomalies in the electrical permitivitty ϵ were observed at T_N for both polycrystalline [20] and single crystalline [21] CoTiO$_3$ samples along with strong field-dependent magnetocapacitance at and above T_N [20].

Comparison of the spontaneous strain, as measured by the relative length changes dL_i/L_i, with the dielectric permitivitty data published by Dubrovin *et al.* [21], sheds light on the coupling mechanism of lattice and dielectric degrees of freedom. As shown in Fig. 8(b) and (c), the non-phononic relative length changes below T_N and the dielectric function ϵ show similar temperature dependence. Note that, the experimentally observed dielectric anomalies at T_N may also arise due to spontaneous deformation of lattice, as is exhibited by the relation $\epsilon = Cd/\epsilon_0 A$, where C, ϵ_0, d and A are sample capacitance, vacuum permitivitty, sample thickness and area, respectively. However, a direct quantitative comparison of dL_i/L_i in Fig. 8(a) and (b) with ϵ_i indicates that this cannot be the case. The relative length changes along b and c axes respectively are about four orders of magnitude smaller than the corresponding magnetic changes in ϵ_b and ϵ_c, respectively. This observation indicates the presence of significant magnetodielectric coupling in CoTiO$_3$. The fact that the driving entropic changes at T_N are purely magnetic in nature as evidenced by Grüneisen analysis above furthermore implies that magnetic degrees of freedom form a single common origin for the observed structural, dielectric and magnetic changes at and below T_N.

The effect of short-ranged magnetic correlations accompanied by a corresponding lattice response existing above T_N is evidenced from specific heat (Fig. 3(a)) and thermal expansion (Fig. 3(b)) measurements. It has been shown that **q**-dependent spin-spin correlations couple to the dielectric response via the coupling of magnetic fluctuations to optical-phonons, thereby causing a significant magnetocapacitive effect [38]. Accordingly, we conclude that the significant magnetocapacitive observed above T_N in polycrystalline CoTiO$_3$ [20] is due to persistent spin-spin correlations.

Our results clearly show that both in-plane and out-of-plane uniaxial pressure enhance antiferromagnetism in CoTiO$_3$. Surprisingly, NiTiO$_3$ which exhibits an easy-plane AFM structure[28, 39] similar to CoTiO$_3$, shows a different behaviour in associated length changes in the ab plane when heating across T_N, i.e., an expansion along the c axis implying dT_N/d$p_c > 0$ but shrinking of the b axis implying dT_N/d$p_b < 0$ [27]. In NiTiO$_3$, the opposing effects of in-plane and out-of-plane pressure are understood by enhanced and reduced strengths of the leading superexchange interactions for the respective uniaxial pressures [27].

In contrast for CoTiO$_3$, uniaxial pressures along both the in-plane and out of plane directions induce an increase of T_N. There are several potential explanations for this qualitatively different behaviour. Firstly, the electronic configuration of the Co^{2+} ions in octahedral environment implies an effective orbital momentum of $l = 1$ as compared to the virtually quenched orbital momentum in Ni^{2+} ions [13, 14]. Following the original work by Callen*et al.* [42, 43], this difference which causes different anisotropy parameters can hence in principle result in opposite signs of magnetoelastic coupling coefficients. This is also demonstrated by magnetostriction studies on easy-plane antiferromagnets NiCl2 and CoCl2 [44] which are isostructural the NiTiO3 and CoTiO3. Furthermore, our results are in-line with Ref. 10, where the presence of finite bond dependent magnetic
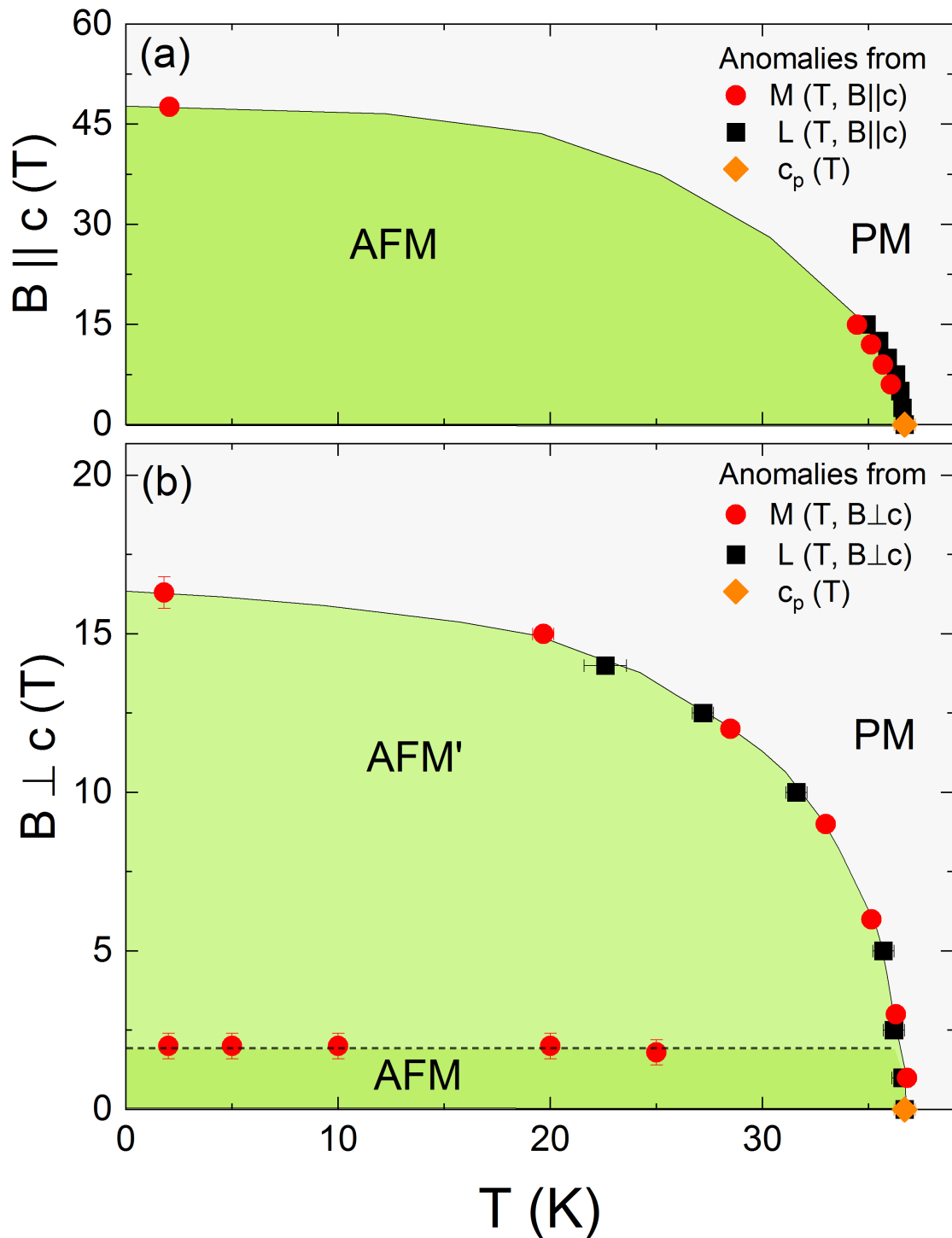
FIG. 7: Magnetic phase diagram of CoTiO$_3$ for (a) $B||c$ axis and (b) $B||ab$ plane constructed from magnetization $M(T, B)$, dilatometry $L(T, B)$, and specific heat data. AFM, AFM' and PM label the antiferromagnetically ordered, spin-reoriented and paramagnetic region, respectively.
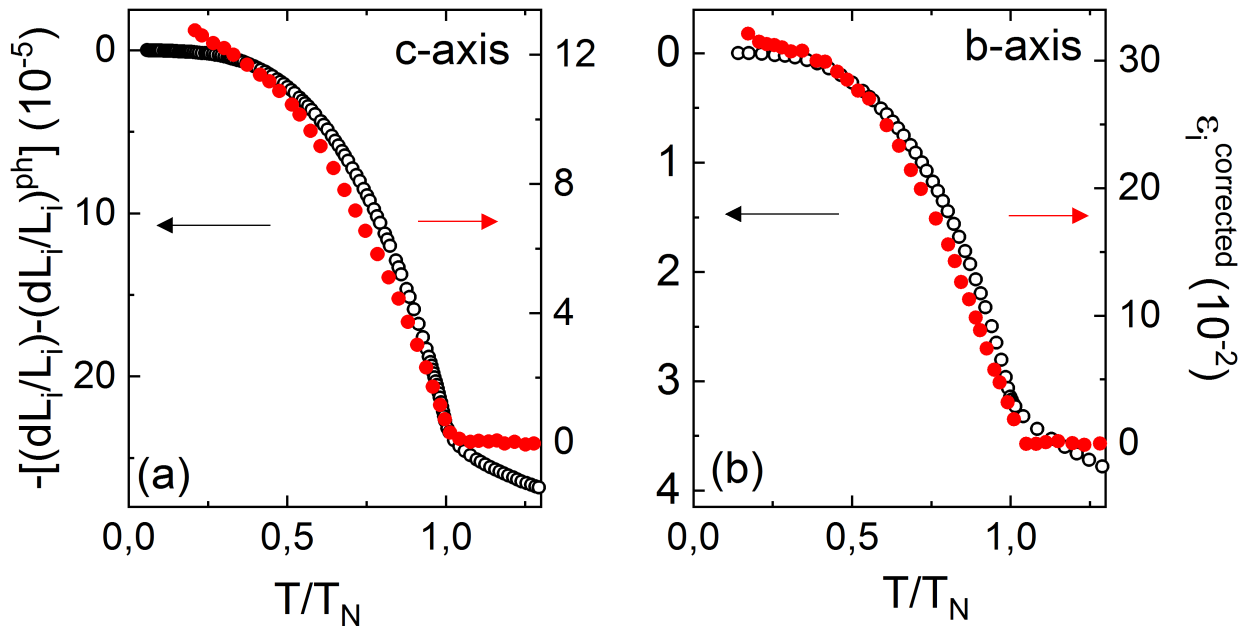
FIG. 8: Scalings of the non-phononic relative length changes dL_i/L_i and corrected dielectric permitivitty ϵ digitized from Dubrovin *et al.* [21] for (a) c and (b) b axis respectively.

frustration has been suggested for CoTiO$_3$. In this case, even small distortions are supposed to lift degeneracy resulting in large pressure effects [40]. Hence, frustration may be partially lifted by application of uniaxial pressure in the ab plane generating additional effective in-plane anisotropy, thereby stabilizing magnetic order, i.e. $dT_N/dp_b > 0$.

We also note that the pressure dependencies of the magnetic anisotropy parameters influence the sign of the uniaxial thermal expansion coefficient (see equation (2) in [41]). Therefore, one may speculate that a sufficiently large variation in the pressure dependencies of anisotropy could also lead to an opposite signs for α in the ab plane in NiTiO$_3$ and CoTiO$_3$.

VII.   CONCLUSIONS

To summarize, high-quality single crystals are used to refine the crystal structure and to study thermodynamic properties of CoTiO$_3$, which clearly demonstrate the presence of strong magnetoelastic coupling in CoTiO$_3$, and constructed its anisotropic magnetic phase diagram. By means of Grüneisen analysis we deduced the positive pressure dependencies of T_N for all crystallographic axes. We find that the magnetic degrees of freedom drive the observed structural, dielectric and magnetic changes both in the short-range ordered regime well-above T_N as well as in the long-range magnetically ordered phase.

VIII.   ACKNOWLEDGMENTS

---

[1] H. Liu and G. Khaliullin, Phys. Rev. B **97**, 014407 (2018).

[2] R. Sano, Y. Kato, and Y. Motome, Phys. Rev. B **97**, 014408 (2018).

[3] H. Liu, J. Chaloupka, and G. Khaliullin, Phys. Rev. Lett. **125**, 047201 (2020).

[4] R. Zhong, T. Gao, N. P. Ong, and R. J. Cava, **6** (2020).

[5] M. Songvilay, J. Robert, S. Petit, J. A. Rodriguez-Rivera, W. D. Ratcliff, F. Damay, V. Balédent, M. Jiménez-Ruiz, P. Lejay, E. Pachoud, et al., Phys. Rev. B **102**, 224429 (2020).

[6] E. Lefrançois, M. Songvilay, J. Robert, G. Nataf, E. Jordan, L. Chaix, C. V. Colin, P. Lejay, A. Hadj-Azzem, R. Ballou, et al., Phys. Rev. B **94**, 214416 (2016).

[7] X. Hong, M. Gillig, R. Hentrich, W. Yao, V. Kocsis, A. R. Witte, T. Schreiner, D. Baumann, N. Pérez, A. U. B. Wolter, et al., arXiv: **2101.12199** (2021).

[8] T. Barth and E. Posnjak, Zeit für Krist. p. 271 (1934).

[9] R. E. Newnham, J. H. Fang, and R. P. Santoro, Acta Cryst. **17**, 240 (1964).

[10] M. Elliot, P. A. McClarty, D. Prabhakaran, R. D. Johnson, H. C. Walker, P. Manuel, and R. Coldea, arXiv: **2007.04199** (2020).

[11] A. Balbashov, A. Mukhin, V. Ivanov, L. Iskhakova, and M. Voronchikhina, Fiz. Nizk. Temp. **43**, 1200 (2017).

[12] J. J. Stickler, S. Kern, A. Wold, and G. Heller, Phys. Rev. **164**, 765 (1967).

[13] J. B. Goodenough and J. J. Stickler, Phys. Rev. **164**, 768 (1967).

[14] M. E. Lines, Phys. Rev. **131**, 546 (1963).

[15] B. Yuan, I. Khait, G.-J. Shu, F. C. Chou, M. B. Stone, J. P. Clancy, A. Paramekanti, and Y.-J. Kim, Phys. Rev. X **10**, 11062 (2020).

[16] B. Yuan, M. B. Stone, G.-J. Shu, F. C. Chou, X. Rao, J. P. Clancy, and Y.-J. Kim, Phys. Rev. B **102**, 134404 (2020).

[17] Tien-Sheng Chao, Wei-Ming Ku, Hong-Chin Lin, D. Landheer, Yu-Yang Wang, and Y. Mori, IEEE Trans. Electron Devices **51**, 2200 (2004).

[18] T. M. Pan, T. F. Lei, and T. S. Chao, J. Appl. Phys **89**, 3447 (2001).

[19] U. Ullah, W. F. F. W. Ali, M. F. Ain, N. M. Mahyuddin, and Z. A. Ahmad, Mater. Des. **85**, 396 (2015).

[20] J. K. Harada, L. Balhorn, J. Hazi, M. C. Kemei, and R. Seshadri, Phys. Rev. B **93**, 104404 (2016).

[21] R. Dubrovin, N. Siverin, M. Prosnikov, V. Chernyshev, N. Novikova, P. Christianen, A. Balbashov, and R. Pisarev, J. Alloys Compd. p. 157633 (2020).

[22] R. Klingeler, B. Büchner, K. Y. Choi, V. Kataev, U. Ammerahl, A. Revcolevschi, and J. Schnack, Phys. Rev. B **73**, 014426 (2006).

[23] Y. Skourski, M. D. Kuz'min, K. P. Skokov, A. V. Andreev, and J. Wosnitza, Phys. Rev. B **83**, 214420 (2011).

[24] R. Küchler, T. Bauer, M. Brando, and F. Steglich, Rev. Sci. Instru. **83**, 95102 (2012).

[25] J. Werner, W. Hergett, M. Gertig, J. Park, C. Koo, and R. Klingeler, Phys. Rev. B **95**, 214414 (2017).

[26] B. Bohuslav and M. Arnulf, J. Inorg. and Nuclear Chem. **31**, 649 (1969).

[27] K. Dey, S. Sauerland, J. Werner, Y. Skourski, M. Abdel-Hafiez, R. Bag, S. Singh, and R. Klingeler, Phys. Rev. B **101**, 195122 (2020).

[28] K. Dey, S. Sauerland, B. Ouladdiaf, K. Beauvois, H. Wadepohl, and R. Klingeler, Phys. Rev. B **103**,

134438 (2021).

[29] R. A. Angel and F. Nestola, Am. Min. **101**, 1036 (2016).

[30] CCDC 2082344 (model A), 2082345 (model B) and 2082346 (model C) contains the supplementary crystallographic data for this paper. These data can be obtained from the Cambridge Crystallographic Data Centre's and FIZ Karlsruhe's joint Access Service via https://www.ccdc.cam.ac.uk/structures/?

[31] M. E. Fisher, Philos. Mag. **7**, 1731 (1962).

[32] H. Watanabe, H. Yamauchi, and H. Takei, J.Magn. Magnetic Mat. **15-18**, 549 (1980).

[33] S. Klemme, W. Hermes, M. Eul, C. H. Wijbrans, A. Rohrbach, and R. Pöttgen, Chem. Cent. J. **5**, 54 (2011).

[34] N. W. Ashcroft and N. Mermin (Cengage Learning, Inc, 1976), ISBN 9780030839931.

[35] P. Gegenwart, Rep. Prog. Phys. **79**, 114502 (2016).

[36] L. Yin, Z. W. Ouyang, J. F. Wang, X. Y. Yue, R. Chen, Z. Z. He, Z. X. Wang, Z. C. Xia, and Y. Liu, Phys. Rev. B **99**, 134434 (2019).

[37] T. Susuki, N. Kurita, T. Tanaka, H. Nojiri, A. Matsuo, K. Kindo, and H. Tanaka, Phys. Rev. Lett. **110**, 267201 (2013).

[38] G. Lawes, A. P. Ramirez, C. M. Varma, and M. A. Subramanian, Phys. Rev. Lett. **91**, 257208 (2003).

[39] G. Shirane, S. Pickart, and Y. Ishikawa, J. Phys. Soc. Japan **14**, 1352 (1959).

[40] R. Küchler, C. Stingl, Y. Tokiwa, M. S. Kim, T. Takabatake, and P. Gegenwart, Phys. Rev. B **96**, 241110 (2017).

[41] H. W. Willemsen, R. L. Armstrong, and P. P. M. Meincke, J. Low Temp. Phys **26**, 299 (1977).

[42] E. Callen, and H. B. Callen, Phys. Rev. **139**, A455-A471 (1965).

[43] E. Callen, J. Appl. Phys. **39**, 519 (1968).

[44] V. M. Kalita, A. F. Lozenko, S. M. Ryabchenko, and P. A. Trotsenko, Low Temp. Phys. **31**, 794 (2005).

Supplement: Magnetic Phase Diagram, Magnetoelastic coupling and Grüneisen scaling for CoTiO$_3$

M. Hoffmann *,[1] K. Dey * ,[1,†] J. Werner,[1] R. Bag,[2] J. Kaiser,[1]

H. Wadepohl,[3] Y. Skourski,[4] M. Abdel-Hafiez,[5] S. Singh,[2] and R. Klingeler[1,6]

[1]Kirchhoff Institute of Physics, Heidelberg University,

INF 227, D-69120, Heidelberg, Germany

[2]Indian Institute of Science Education and Research, Pune, Maharashtra 411008, India

[3]Institute of Inorganic chemistry, Heidelberg University, 69120, Heidelberg, Germany

[4]Dresden High Magnetic Field Laboratory (HLD-EMFL),

Helmholtz-Zentrum Dresden Rossendorf, D-01314 Dresden, Germany

[5]Department of Physics and Astronomy,

Uppsala University, Box 516, SE-751 20 Uppsala, Sweden

[6]Center for Advance Materials (CAM), Heidelberg University,

INF 227, D-69120, Heidelberg, Germany

(Dated: July 6, 2021)

PACS numbers:

---

* both the authors contributed equally

SINGLE CRYSTAL X-RAY DIFFRACTION

A single crystal splinter of size 0.16×0.14×0.01 mm^3 was broken of from larger specimen and used for data collection. A full shell of intensity data was collected up to 0.4 Å resolution with an average multiplicity of observations 14.3. Detector frames (ω-scans, scan width 0.5°) were integrated by profile fitting [1]. Data were corrected for air and detector absorption, Lorentz and polarization effects [2] and scaled essentially by application of appropriate spherical harmonic functions [2–4]. Absorption by the crystal was treated with a semi-empirical multiscan method (as part of the scaling procedure), and augmented by a spherical correction [4, 5]. Space group $R\bar{3}$ was assigned based on systematic absences and intensity statistics (trigonal obverse centered unit cell on hexagonal axes, Hall group -R 3). This choice was confirmed by analysis of the symmetry of the phases obtained ab initio in P1. The structure was solved by intrinsic phasing [6–8] and refined by full-matrix least-squares methods based on F^2 against all unique reflections [9–12]. Atomic structure factors f_{at} for neutral atoms (used for model A), Co^{2+} and Ti^{4+} (used for models B and C) were taken from ref. [13], those for O^{2-} from ref. [14] (used for model B) or ref. [15], respectively (used for model C). An empirical secondary extinction correction [10, 16] was applied in each case but proved insignificant. The different models refined to essentially the same structure, with a marginally better fit of model B but only insignificant differences in key parameters like atom coordinates, R factors, U_{eq} for all atoms and residual electron density. Co-O and Ti-O bond lengths agreed within one standard deviation. There was no evidence of cation mixing and fully occupied sites were employed for all atoms. Merohedral twinning within the holohedry -3m was considered in a separate refinement employing the method advocated by Jameson [17] but proved to be absent in our crystal, as indicated by a vanishing fractional contribution (0.0021(8)) of the second twin component.

———————

[†] email:kaustav.dey@kip.uni-heidelberg.de

[1] K. Kabsch, *International Tables for Crystallography*, vol. F (Kluwer Academic Publishers, Dordrecht, 2001).

[2] *CrysAlisPro*, Agilent Technologies UK Ltd., Oxford (2011).

[3] R. H. Blessing, Acta Cryst. **A51** (1995).

[4] *SCALE3 ABSPACK, CrysAlisPro*, Agilent Technologies UK Ltd., Oxford (2011).

[5] W. R. Busing and A. Levy, Acta Cryst. **10** (1957).

[6] *SHELXT*, University of Göttingen and Bruker AXS Gmbh, Karlshruhe, Germany (2012-2018).

[7] *M. Ruf, B. C. Noll, Application note SC-XRD 503*, Bruker AXS Gmbh, Karlshruhe, Germany (2014).

[8] G. sheldrick, Acta Cryst. **A71** (2015).

[9] *SHELXL-20xx*, University of Göttingen and Bruker AXS Gmbh, Karlshruhe, Germany (2012-2018).

[10] W. Robinson and G. M. Sheldrick, *Crystallographic Computing 4* (IUCr and Oxford University Press, Oxford, UK, 1988).

[11] G. sheldrick, Acta Cryst. **A64** (2008).

[12] G. sheldrick, Acta Cryst. **C71** (2015).

[13] P. J. Brown, A. G. Fox, H. H.-C., J. I. Langford, H. Lipson, E. N. Maslen, M. A. O'Keefe, T. M. Sabine, and B. T. M. Willis, *International Tables for Crystallography*, vol. C (Kluwer Academic Publishers, Dordrecht, The Netherlands,, 2004), 3rd ed.

[14] P. Azavant and A. Lichanot, Acta Cryst. **A49** (1993).

[15] Morelhão, *Computer simulation tools for X-ray analysis* (Springer International Publishing Cham, Switzerland, 2016), 3rd ed., URL http://http://xraybook.if.usp.br.

[16] A. C. Larson, *Crystallographic computing* (Munksgaard, Copenhagen, Denmark, 1970).

[17] J. B. Jameson, Acta Cryst. **A38** (1982).
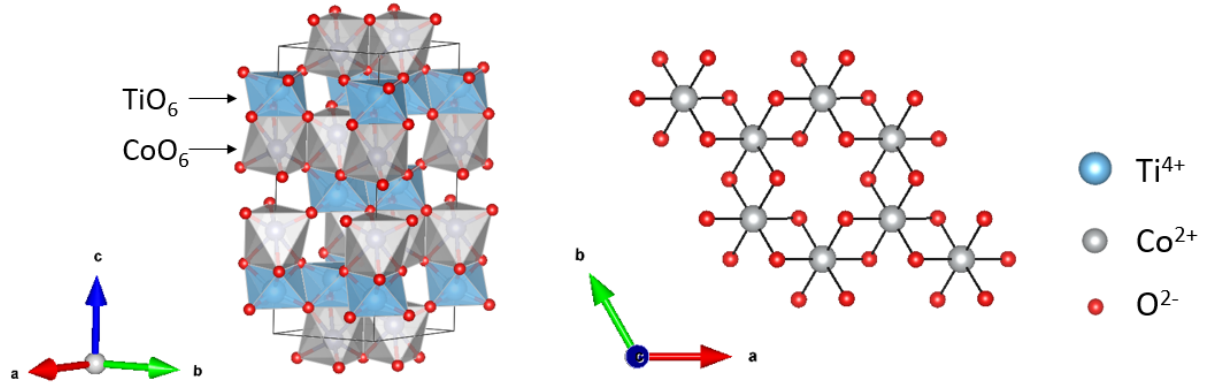
FIG. 1: Ilmenite-type crystal structure of CoTiO$_3$.

TABLE I: Selected crystallographic parameters of CoTiO$_3$.

Empirical formula	CoTiO$_3$
Formula weight	154.32
T(K)	100(1)
Crystal system, space group	trigonal, $R\bar{3}$ (*IT* Nr. 148)
Unit cell dimensions	
a (Å)	5.06009(6)
c (Å)	13.89182(17)
V (Å^3)	308.040(8)
Z, Calculated density (g cm^{-3})	6, 4.991
Absorption coefficient for Mo-Kα (mm^{-1})	11.624
Transmission factors: max, min	1.000, 0.397
Theta range for data collection	4.4° to 60.2°
Reflections collected / independent	14863 / 1042 [R$_{int}$ = 0.023]
observed reflections [$I > 2\sigma(I)$]	1031
data/restraints/parameters	1042/0/17

TABLE II: Details of crystal structure refinement of CoTiO$_3$.

Model	A	B	C
Gof on F^2	1.118	1.185	1.201
R indices$[F > 4\sigma(F_0)]$ $R(F), wR(F^2)$	0.0115, 0.0337	0.0115, 0.0318	0.0125, 0.0343
R indices (all data) $R(F), wR(F^2)$	0.0116, 0.0337	0.0116, 0.0318	0.0127, 0.0344
extinction coefficient	0.0054(8)	0.0055(7)	0.0071(8)
largest residual praks, rms,max, min /e.Å^3	0.119,1.102,-0.551	0.115, 0.865, -0.738	0.123, 0.920, -0.699
CCDC deposition number	2082344	2082345	2082346
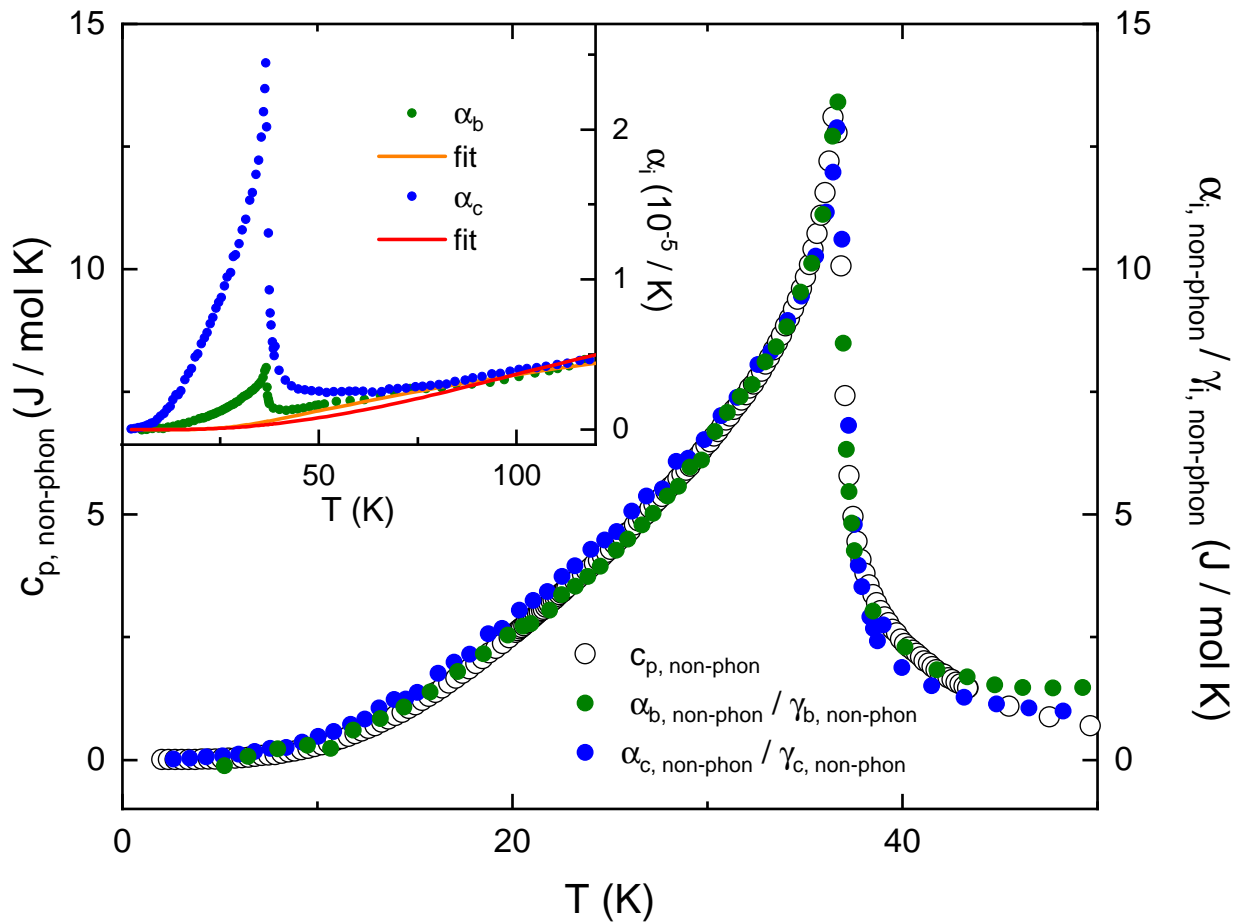
FIG. 2: Grüneisen scaling as described in the main text for b- and c-axis individually. The resulting magnetic Grüneisen ratios are $2.7(2)\,10^{-7}$ mol/J and $1.8(2)\,10^{-7}$ mol/J, respectively.
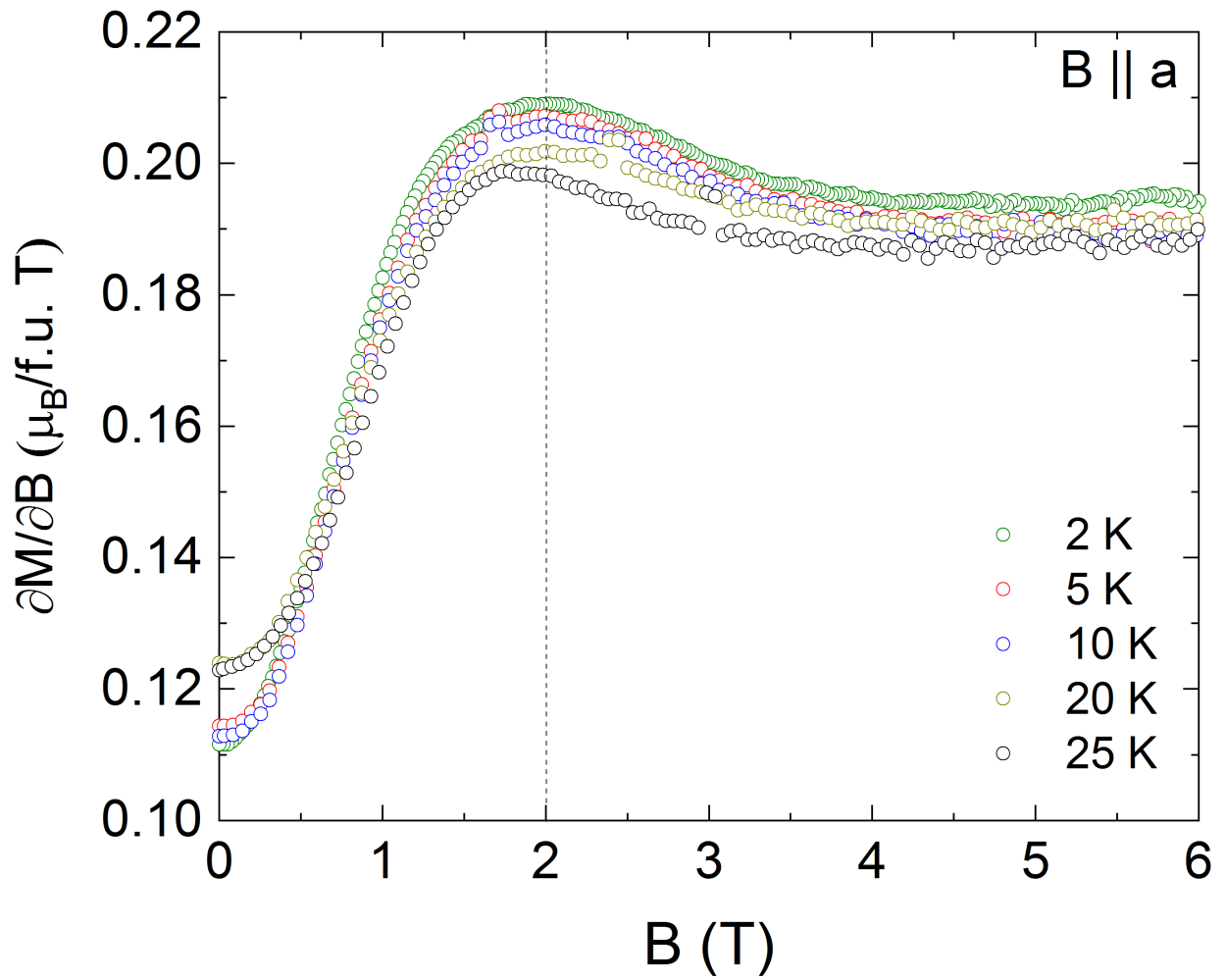
FIG. 3: Magnetic susceptibility $\partial M/\partial B$ versus magnetic field along a-axis.
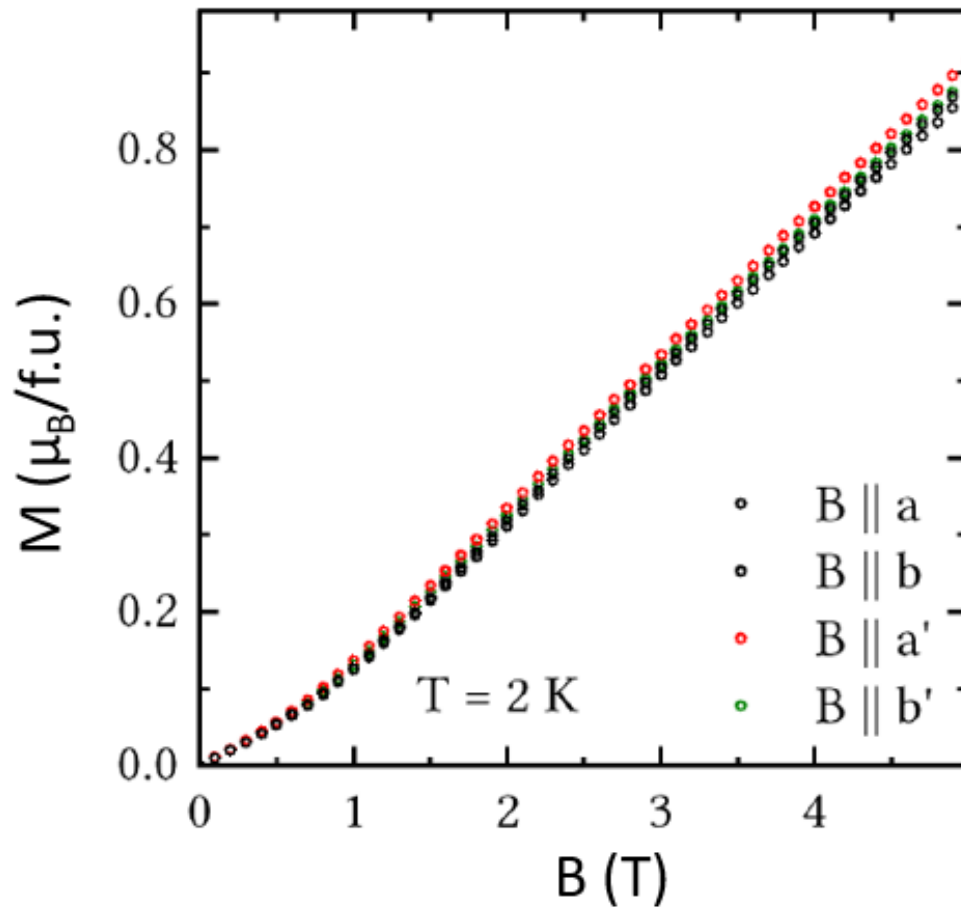
FIG. 4: Magnetization vs. magnetic-field along a, b, a' and b'-directions in CoTiO$_3$ at $T = 2$ K. Here $a' = [1, 1, 0]$ and $b' = [1, -1, 0]$.

2.4   Magnetostriction and magnetostructural domains in CoTiO$_3$

The following section entitled "Magnetostriction and magnetostructural domains of CoTiO$_3$" has been submitted for publication and is currently under review in Physical Review Materials journal.

In the following, contributions of each co-authors are explained in detail, particularly highlighting the specific contribution of K. Dey who is the first author and the communicating author.

- K. Dey assisted in the analysis of the magnetostriction data. K. Dey planned and suggested the anisotropic magnetostriction measurements Fig. 4. The domain analysis by means of phenomenological models was suggested by K. Dey. K. Dey assited in successfully applying the domain model (Fig. 7 and Fig. 8) and in performing the rotational magnetization measurements (Fig. 5). K. Dey made all the final plots and wrote the manuscript draft.

- M. Hoffmann in the frame of his master thesis performed the magnetostriction measurements and rotational magnetization measurements (Fig. 5). M. Hoffmann analysed the data and supported in manuscript writing.

- R. Klingeler supervised the measurements and supported data analysis and manuscript writing.

- All the authors proofread the manuscript.

Magnetostriction and magnetostructural domains in CoTiO$_3$

K. Dey,[1, *] M. Hoffmann,[1] and R. Klingeler[1, 2]

[1]*Kirchhoff Institute of Physics, Heidelberg University,*
INF 227, D-69120, Heidelberg, Germany
[2]*Center for Advance Materials (CAM), Heidelberg University,*
INF 225, D-69120, Heidelberg, Germany
(Dated: June 16, 2021)

Abstract

We report the magnetostrictive length changes of CoTiO$_3$ studied by means of high-resolution dilatometry in magnetic fields (B) up to 15 T. In the long-range antiferromagnetically ordered phase below T_N = 38 K, the easy-plane type spin structure undergoes a spin-reorientation transition in the ab plane in magnetic fields $B||ab \approx 2$ T. We observe pronounced length changes driven by external magnetic field in this field region indicating significant magnetoelastic coupling in CoTiO$_3$. Specifically, we observe anisotropic deformation of the lattice for fields applied in the ab plane. While, for $B \lesssim 2$ T, in-plane magnetostriction shows that the lattice expands (contracts) parallel (perpendicular) to the field direction, the opposite behaviour appear at higher fields. Furthermore, there are remarkable effects of slight changes in the applied uniaxial pressure on the magnetostrictive response of CoTiO$_3$ persisting to temperatures well above T_N. The data evidence the presence of magnetic domains below T_N as well as of structural ones in CoTiO$_3$. The presence of magnetic domains in the spin ordered phase is further evidenced by an additional 3-fold magnetic anisotropy appearing below T_N. We discuss the effects of rotational magnetic domains on isothermal magnetization and magnetostriction and interpret our results on the basis of a multi-domain phenomenological model.

---

[*] email:kaustav.dey@kip.uni-heidelberg.de

I.   INTRODUCTION

Research in antiferromagnetic spintronics has garnered enormous interest over the past decades due to its high-frequency (THz) dynamics, long distance spin-wave transport, spin-orbit effects and robustness against external magnetic field perturbations, making them attractive for practical applications (see Refs. [1 and 2] and references therein). In particular, considerable efforts have been made to understand and manipulate the magnetic domain structure [3], spin-wave scattering at the domain walls [4] and domain wall motion [5, 6]. Understanding the domain wall structure and dynamics is not only relevant from an application point of view, but also has profound effects on the macroscopic thermodynamics and transport properties of strongly correlated electron systems [7–11].

In this report, we investigate CoTiO$_3$ belonging to the ilmenites titanates family (MTiO$_3$; $M =$ Co, Ni, Mn, Fe), which have been studied quite extensively in the recent years due their significant magnetoelectric and magnetoelastic properties [11–16]. All the ilmenite titanates crystallize in the rhombohedral $R\bar{3}$ structure with the magnetic M^{2+} ions in the basal ab plane arranged in a buckled honeycomb-like structure (see Fig. 1). In particular for CoTiO$_3$, early magnetization [17, 18] and neutron diffraction experiments [19] indicated a long-ranged easy-plane type antiferromagnetic structure below T_{N} = 38 K. Furthermore, recent inelastic neutron scattering experiments on CoTiO$_3$ exhibited the presence of Dirac magnons [20] and rendered it as a model system to study non-trivial magnon band topology [21, 22]. Here, we present macroscopic magnetization and magnetostriction ($dL(B)/L$) measurements on CoTiO$_3$. In particular, we observe pronounced effects of rotational magnetic domains on the macroscopic measurements and interpret our results on the basis of multi-domain phenomenological theories. Also above T_{N}, the magnetostrictive response is extremely sensitive to small changes in the applied external uniaxial pressure, indicating the presence of magnetostructural domains in CoTiO$_3$.
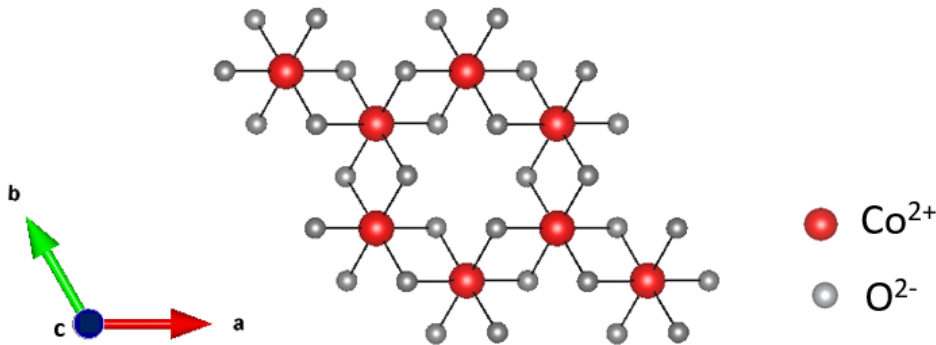
FIG. 1. Crystallographic arrangement of cobalt and oxygen ions in a basal hexagonal ab plane of the ilmenite CoTiO$_3$ structure [23]. The buckling is along the c axis and hence is not visible here.

II.   EXPERIMENTAL METHODS

Macroscopic single crystals of CoTiO$_3$ were grown by the optical floating-zone technique as reported elsewhere [24]. Static magnetic susceptibility $\chi = M/B$ was studied in magnetic fields up to 15 T applied along the principal crystallographic axes by means of a home-built vibrating

sample magnetometer [25] and in fields up to 5 T in a Quantum Design MPMS-XL5 SQUID magnetometer. The angular dependence of magnetisation was measured in a Quantum Design MPMS3 SQUID magnetometer using the rotator option. The relative length changes dL_i/L_i were studied on a single crystal of approximate dimensions $1.6 \times 2.0 \times 1.3$ mm^3 by means of a standard three-terminal high-resolution capacitance dilatometer [26, 27]. The field induced uniaxial length changes $dL_i(B)/L_i$ were measured at various fixed temperatures in magnetic fields up to 15 T and the longitudinal magnetostriction coefficients $\lambda_i = 1/L_i \times dL_i(B)/dB$ were derived with the same dilatometer. In both cases, magnetic fields were applied along the direction of measured length changes. To further study the length changes transverse to applied external magnetic fields, a second setup comprising of a mini-dilatometer on a rotator [28] inside a Physical Properties Measurement System (Quantum Design) was applied.

III. RESULTS

The application of external magnetic-field yields pronounced changes in the lattice parameters of CoTiO$_3$. As shown in Fig. 2(b), a monotonic increase of the c axis driven by $B||c$ up to 15 T is observed at all the measured temperatures, i.e., between 2 and 200 K. In contrast, for $B||b$ a pronounced increase of the associated lattice parameter is observed in the low-field region, i.e., $B < 3$ T, followed by a relatively smaller decrease in higher fields as seen in Fig. 2(a). For $T \lesssim T_{\rm N}$, small anomalies in the magnetostriction (i.e., in the data obtained at 33 and 35 K) at higher field indicate the phase boundary to the paramagnetic phase (cf. also Fig. 3(b) and Fig. 6).

The region of significant lattice changes below 3 T applied in-plane coincides with the non-linear region in magnetization M vs. B measurements [18], signalling a spin-reorientation process in the ab-plane. This is particularly evident in Fig. 3(a) where the corresponding derivatives of both, i.e., of the magnetization $\partial M/\partial B$ and of the relative length changes λ are presented. However, these quantities peak at different positions which is contrary to the expectations of bare spin-orientation associated with an anomaly in the magnetostriction due to finite spin-lattice coupling [29–31]. Instead, it is reminiscent of rotational domain behaviour as observed in Ising-like BaCo$_2$V$_2$O$_8$ [32] or in easy-plane type BaNi$_2$V$_2$O$_8$ [33] and NiTiO$_3$ [11]. As described below, the presence of domains has to be involved and in the following we will present clear evidence that the data represent a crossover from a low-field multi-domain state to a high-field homogeneous state with spins nearly perpendicular to the applied magnetic field.

The lattice changes in the hexagonal ab plane are further investigated by measuring the length changes dL_b/L_b in longitudinal and transversal magnetic fields applied in-plane. As shown in Fig. 4(a), the longitudinal length changes $(dL_b(B||b)/L_b)$ exhibit an almost equal and opposite behaviour as compared to transverse length changes where the field is applied $\perp bc$, i.e., along the perpendicular-to-b in-plane direction $(dL_b(B \perp bc)/L_b)$. Specifically, while above 3 T the spins are nearly perpendicular to B, the data imply an anisotropic deformation of the ab plane. This behaviour does not comply to the perfect $R\bar{3}$ structure but reveals an in-plane anisotropy induced by applied external magnetic field. The field-direction induced deformation can be estimated as the difference in magnetostrictive length changes for $B||b$ and $B \perp b$ which, at 3 T, amounts to $\approx 2.6 \times 10^{-4}$ at $T = 2$ K. Tentatively, as the field lifts the hexagonal lattice symmetry and rotates spins perpendicularly to B, this quantity may be interpreted as an orthorhombic distortion. Above the spin-crossover region, i.e., at $B \geq 3$ T, the data reveal that the hexagonal basal plane shrinks parallel to the field-direction (i.e., perpendicular to the spin direction), whereas it elongates perpendicular to the field direction (parallel to the spin direction).

In a capacitance dilatometer, uniaxial pressure amounting to a few MPa is applied to the sample
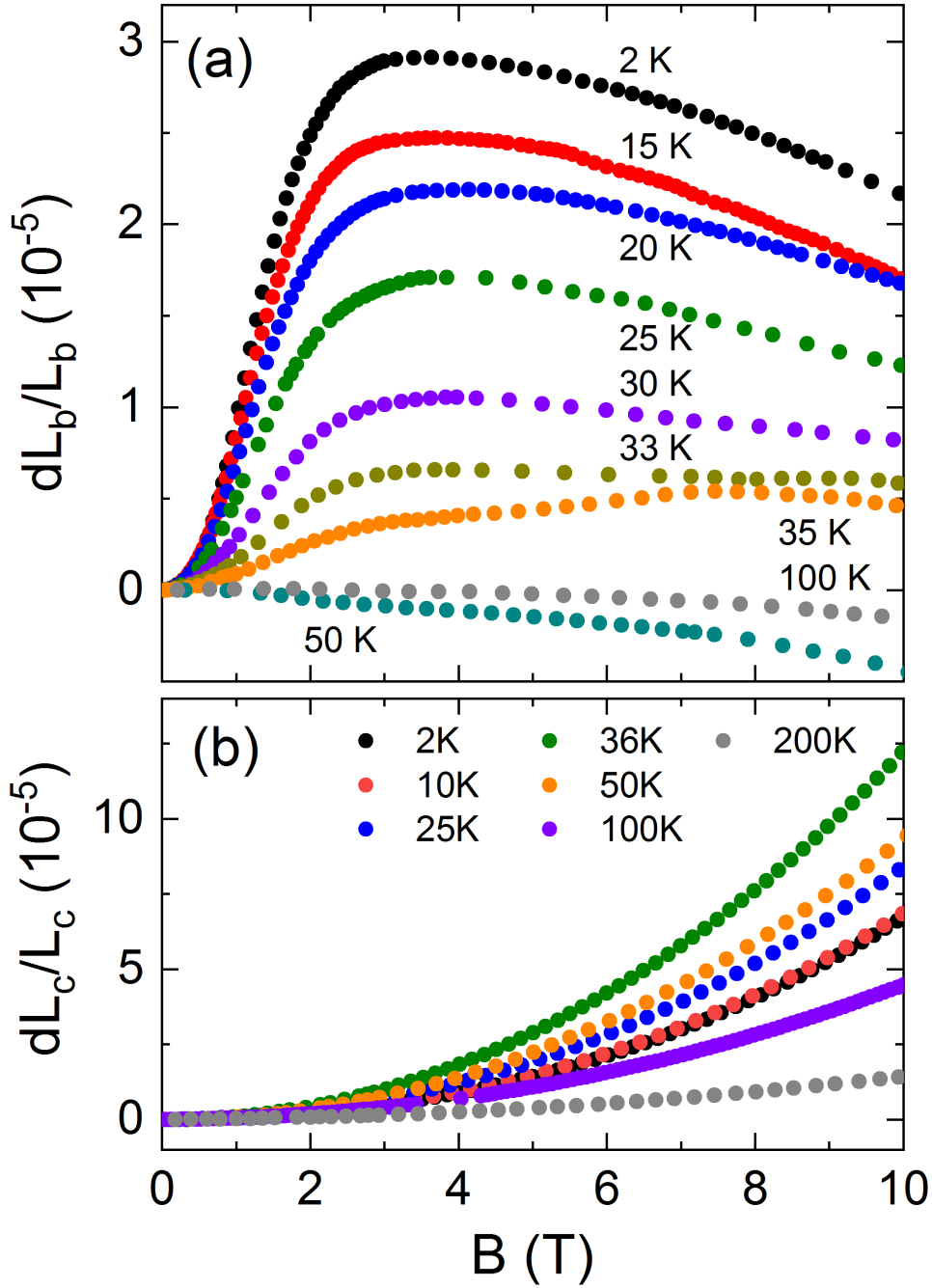
FIG. 2. Relative length changes dL_i/L_i versus magnetic field for (a) $B||b$ (2.5 MPa) and (b) $B||c$ at different temperatures.

during magnetostriction measurements resulting in very small anisotropic strain [34], [?]. Since pressures in the GPa range are required to induce significant elastic deformation in solids, such tiny distortions inevitably associated with the measurement setup are usually irrelevant. Notably, for CoTiO$_3$ we observe quite remarkable effects of tiny pressures applied by the dilatometer in magnetostriction measurements. As seen in Fig. 4(b) and (c), an increase in the uniaxial pressure by mere 0.5 MPa applied by tightening the dilatometer screw results in two significant changes in
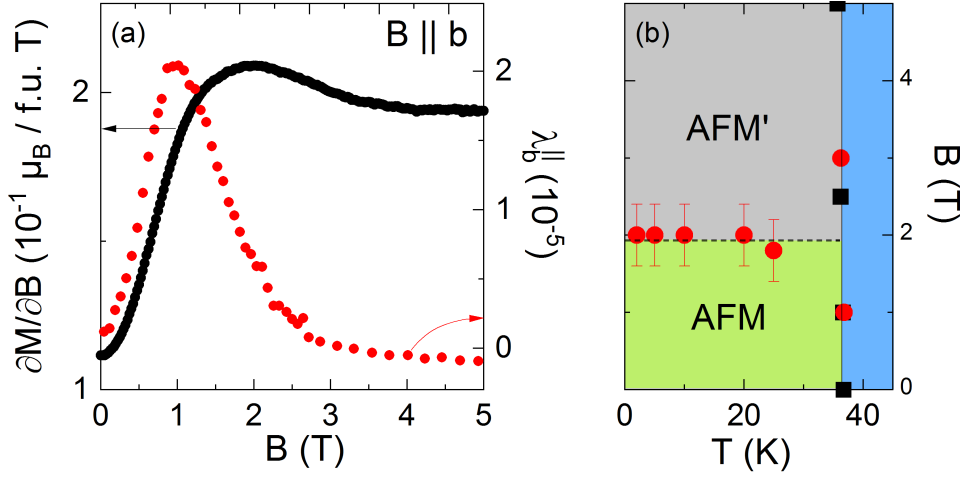
FIG. 3. (a) Field derivative of the isothermal magnetization $\partial M/\partial B$ and magnetostriction coefficient λ_b for $B||b$ axis, at 2 K. The maxima of both quantities are found at different fields. (b) Magnetic phase diagram for $T \leq 42$ K and B up to 5 T. Red (black) markers represent positions of magnetisation (thermal expansion) anomalies. Lines and colours are guide to the eye.

the magnetostrictive behaviour: (1) there is a complete reversal in the dL_b/L_b vs. B behaviour in the whole field range up to 15 T under study and up to 100 K and (2) a shift in the spin crossover field B_{cr} marked by the vertical dashed lines in Fig. 4(b) to lower magnetic fields. Note, that the measurements are performed in a single-run without removing the sample. We argue below that observations (1) and (2) indicate the presence of magnetostructural domains in CoTiO$_3$ single crystal [32, 33].

In particular at $T = 2$ K and $B > 5$ T, a closer look at the data in Fig. 4(b) reveals a switch from lattice contraction to expansion upon increasing the uniaxial pressure from 2.5 MPa to 3.0 MPa. This pressure dependent reversal effect persists up to 100 K (see Fig. 4(c)) which is well above T_{N}, suggesting a purely crystallographic origin. Interestingly, such pressure dependent reversal effect in the dL_b/L_b behaviour has been previously observed in other systems and ascribed to the presence of crystallographic structural twins [32]. It is to note that, the recent neutron diffraction studies on CoTiO$_3$ [21] confirm the presence of two almost equal-weighted structural twins related by a [110] mirror plane. Rigorous X-ray Laue pattern investigations on our CoTiO$_3$ single crystals excludes the possibility of more than one crystallographic grain. Hence, the findings above leads to the conclusion that, the observed change from positive to negative magnetostriction upon increasing the uniaxial pressure in CoTiO$_3$, is due to the presence of structural twins. Consequently, the experimentally measured length changes reflect the superposition response from all the individual twins whose relative population is altered by the applied external uniaxial pressure, resulting in a complete reversal in dL_b/L_b behaviour at a particular pressure.

In addition to structure domains evidenced above, the low-temperature spin ordered phase in principle may host magnetic domains, too. Specifically, the crystallographic symmetry is C_3 in the easy-hexagonal plane, which may result in the presence of three equally populated magnetic domains with spins rotated by $120°$ between them. Such a domain structure is often found in easy-plane type antiferromagnets [33, 35] and more recently in NiTiO$_3$, which is isostructural to CoTiO$_3$ [11]. The presence of magnetic domains below T_{N} is indeed evidenced by the angle-dependent magnetization measurements M vs. θ in the ab plane, as exhibited in Fig. 5. In the paramagnetic region, i.e., at 300 K, the data reveal a C_2 ($180°$) anisotropy which amounts to
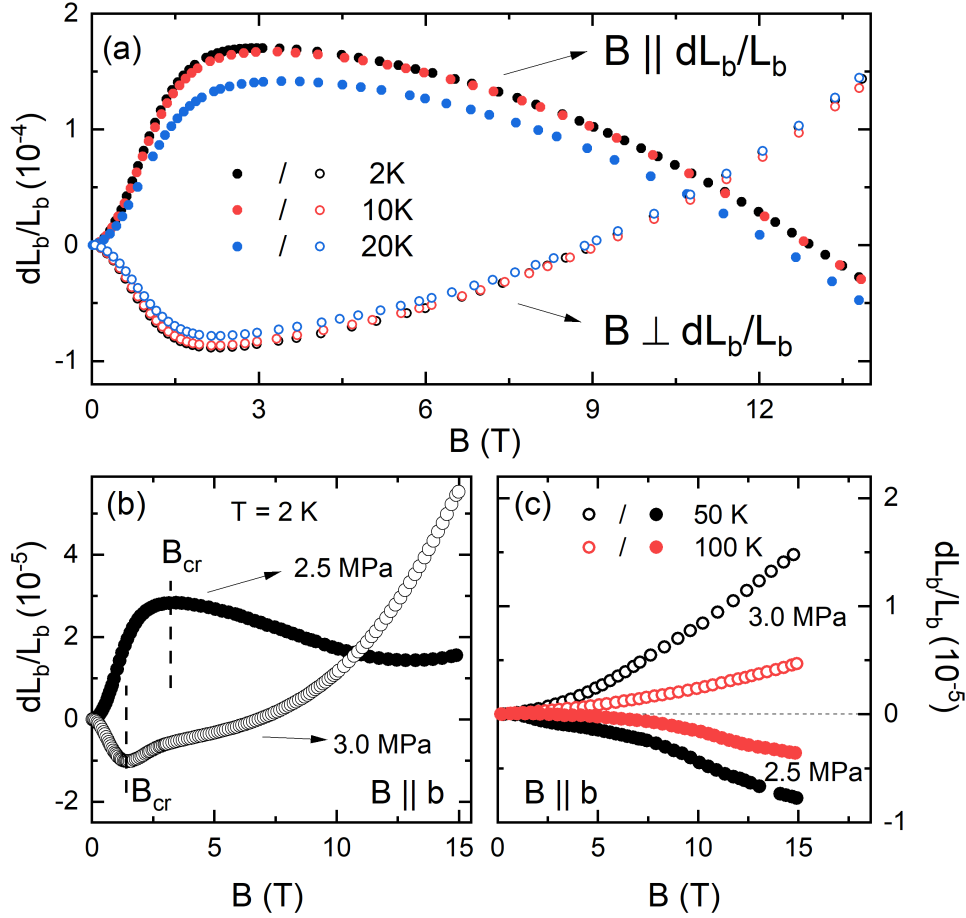
FIG. 4. (a) Magnetostriction dL_b/L_b versus magnetic field $B||b$ and $B \perp b$ (both in-plane), respectively, at different temperatures. (b) dL_b/L_b vs. B, at $T = 2$ K, with different uniaxial pressure applied along the b direction, and (c) in the paramagnetic phase at 50 K and 100 K, respectively. The vertical dashed lines in (b) indicates approximately the crossover from magnetic multi-domains to the monodomain region. See the text for details.

$\approx 2 \times 10^{-4}$ μ_B/f.u. in the plane. In contrast, as seen in Fig. 5(b), we observe additional peaks in the angle dependence of the magnetisation in the magnetically ordered phase at $T = 2$ K $< T_N$. Tracking the maximum position of the peaks reveals an approximate 60° spacing between each of them which is indicative of a C_3 anisotropy in the easy ab-plane. We conclude the presence of a magnetic multi-domain ground state in CoTiO$_3$. Fingerprints of magnetic domains are also visible in the magnetostriction data as will be further discussed below.

IV. DISCUSSION

As shown in Fig. 3, reorientation of the spins around $B \approx 2$ T is associated which lattice changes which derivative peaks well below the actual spin crossover field. Moreover, the characteristic field scale of the magnetostrictive lattice changes and even the sign of magnetostriction drastically depends on tiny changes of the strain applied in the experiment. These findings imply the presence of structural twins well above T_N and further support the scenario of magnetic
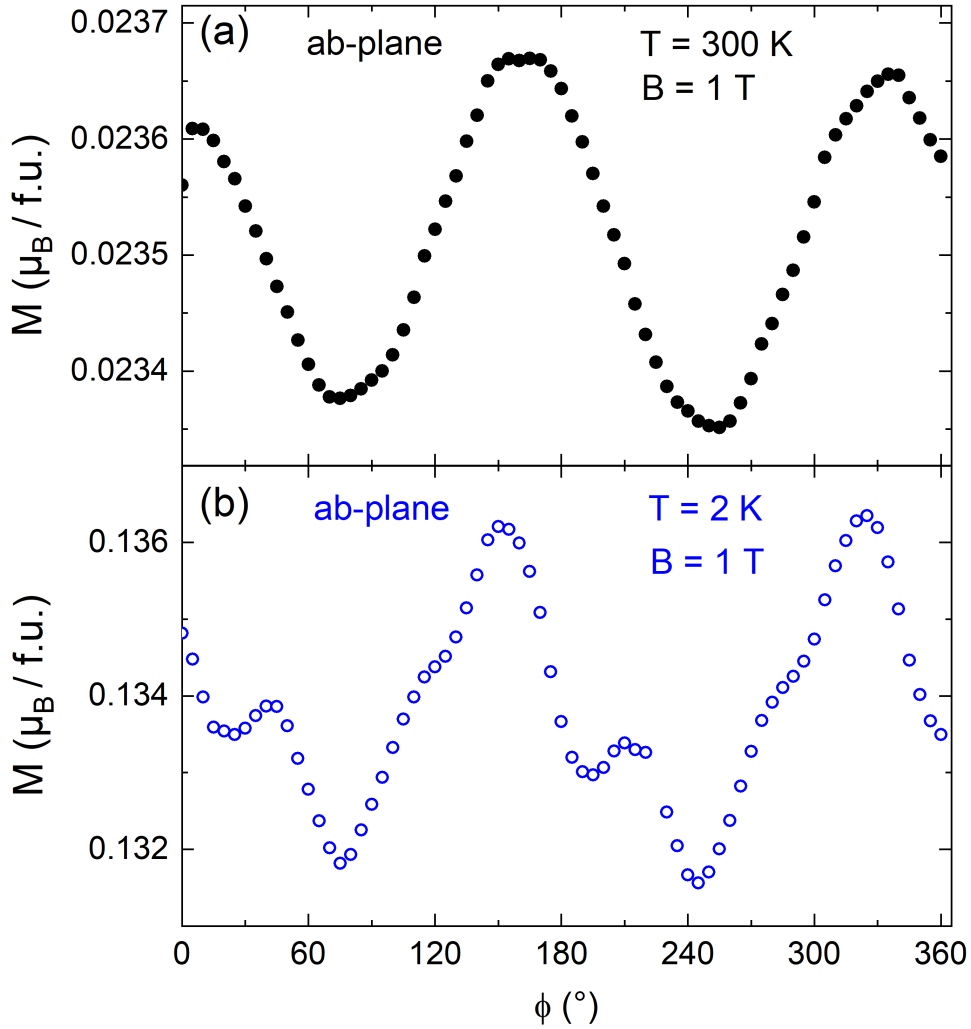
FIG. 5. The angle dependence of the magnetization at $B = 1$ T obtained by rotating the single crystal in the ab plane at (a) 300 K and at (b) 2 K. An additional asymmetry observed in the magnetic ordered phase is interpreted as a signature of magnetic domains.

domains at low temperatures. It also implies that the anomalies in the magnetostriction for $B||b$ cannot be analysed in terms of thermodynamic relations.

In contrast, magnetostriction along the c axis is not affected by the presence of in-plane twins. $dL_c(B)$ exhibits a monotonic field-driven increase which is an order of magnitude larger than the in-plane length changes (cf. Fig. 2). Notably, for a linear in-field magnetization, i.e., $M = \chi B$, which is realised for the c axis [14, 17] and in general for the paramagnetic region, exploiting the Maxwell relation $1/L_i \times (\partial L_i/\partial B)|_p = -1/V \times (\partial M/\partial p_i)|_B$ results in $(dL_i/L_i)|_p = -(1/2V)(\partial \chi/\partial p_i)|_B \times B^2$, where V denotes the molar volume. Indeed, for $B||c$ the data in Fig. 2(b) and SI Fig. 1 confirm the square-field dependency $dL_c/L_c \propto B^2$ for $B \leq 15$ T. Furthermore, the data enable reading off $\partial(\ln \chi_c)/\partial p_c \simeq -21$ % GPa^{-1} at 2 K. For $dL_b(B)$, in contrast, at 100 K, which is well in the paramagnetic regime, the Maxwell relation described above would imply a change in sign of $\partial \chi_b/\partial p_b$ upon increasing the pressure from 2.5 to 3.0 MPa which is unreasonable. Instead, this behaviour is associated to the presence of structural domains in-plane
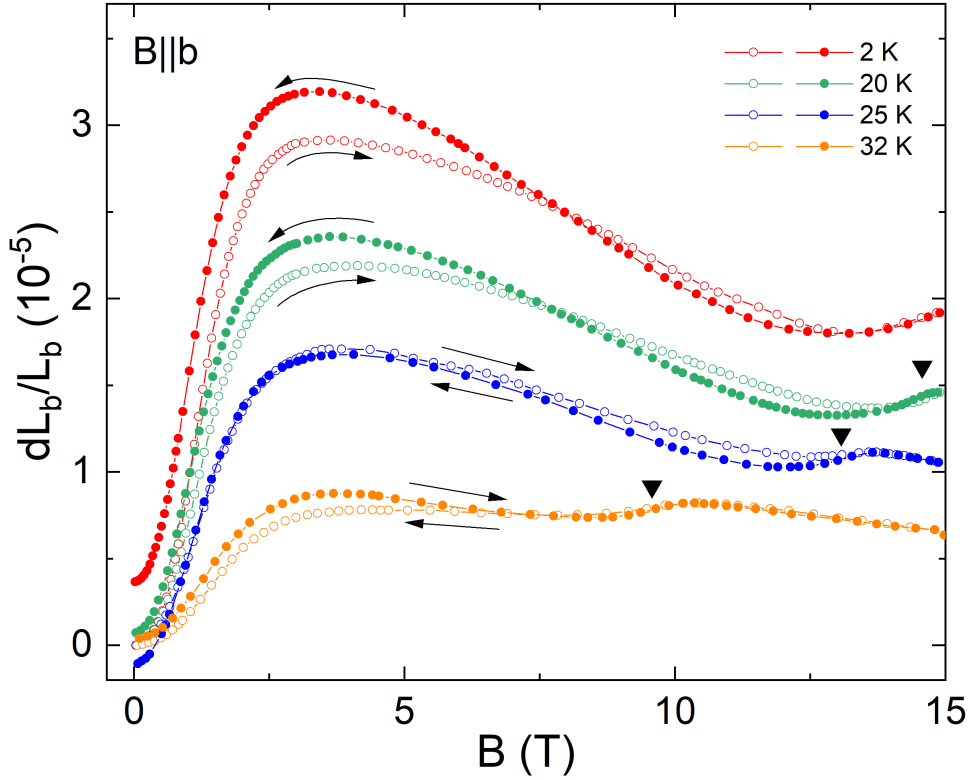
FIG. 6. Magnetostriction along the b axis during imposition (open markers, up-sweep) and removal (full markers, down-sweep) of the magnetic field at different temperatures and at an estimated uniaxial pressure of 2.5 MPa. Small discontinuities in the magnetostriction at higher fields indicated by the black triangles signal the antiferromagnetic to paramagnetic phase boundary.

and the obtained magnetostrictive behaviour is a superposition of the response of two structural twins whose relative proportions are changed due to change in uniaxial pressure, resulting in the sign changes in dL_b/L_b behaviour.

In the long-range spin ordered phase, increasing the uniaxial pressure in the few-MPa regime described above, shifts the crossover field B_{cr} as observed in Fig. 4(b). This is attributed to changes in the magnetic domain distribution of the ground state. Hence, as stated above and in-line with our expectations, the broad-hump observed in dL_b/L_b (see Figs. 2(a) and 4(b)) is not the signature of a thermodynamic phase transition but signals the crossover from the multi-domain spin ground state to a uniform phase comprising of spins pointing nearly perpendicular to the external magnetic field direction.

Interestingly, the up- and down-sweeps in magnetostriction feature a small remanent striction in the antiferromagnetic phase (see Fig. 6). This observation further evidences the presence of antiferromagnetic domains as it is straightforwardly explained by irreversibility due to the pinning of domain walls by defects and crystalline imperfections [7]. The remanent striction amounts to 3.7×10^{-6} at 2 K and 2.5 MPa. The small hysteresis at higher fields has an opposite sign as compared to the low-field one and might indicate either the presence of few strongly pinned domain walls persisting in the whole antiferromagnetic phase or a weak discontinuous character of the antiferromagnetic phase boundary at high fields.

The overall scenario is, therefore, that application of external magnetic fields leads to rotation of
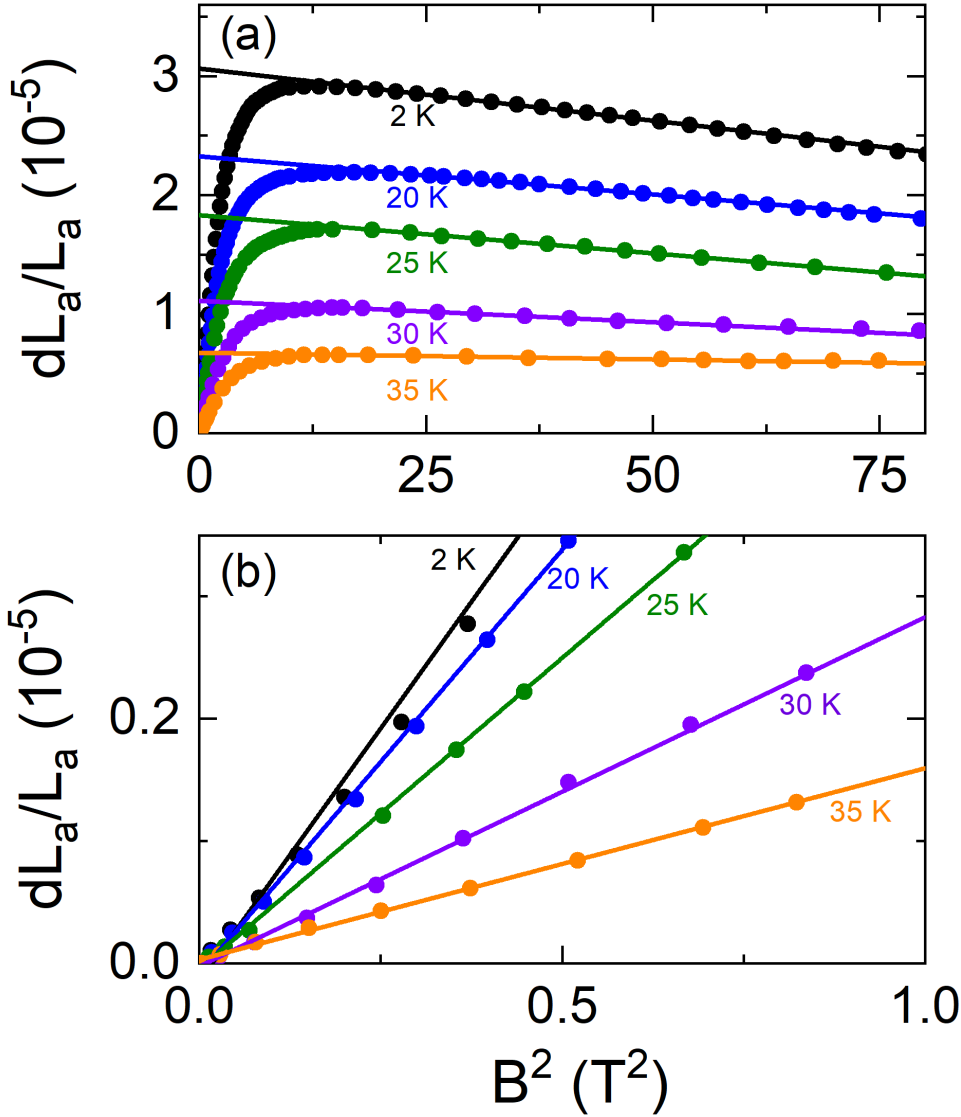
FIG. 7. dL_b/L_b versus B^2 in the (a) high-field homogeneous state and (b) low-field multi-domain state, respectively. The solid lines are corresponding linear fits using Eqs. (1) and (2), respectively. See the text for details.

spins facilitated by domain wall motion. In the multi-domain ground state, the macroscopic magnetization and relative length changes in magnetic fields ($B \lesssim 3$ T) undergo continuous changes and are characterized by broad anomalies in the corresponding field derivatives which maxima however do not coincide (see Fig. 3). Such behaviours have been previously observed in several easy-plane type, high-symmetry cubic [36, 37] and hexagonal antiferromagnets [8, 11, 33, 38]. We hence in the following apply the phenomenological models developed by Kalita *et al.* [8, 38–41] to describe magnetization and magnetostriction in CoTiO$_3$. Both in the multi-domain region $B < 1$ T and in the homogeneous state at $B > 3$ T, the induced striction dL_b/L_b varies as a square of magnetic field as shown in Fig. 7. At higher fields, i.e., in the homogeneous phase characterized by spins perpendicular to the applied field direction, the magnetostriction is described well by [8]

$$\left(\frac{dL_b}{L_b}\right)(T,B) = \left(\frac{dL_b}{L_b}\right)_0 (T) + \alpha(T) \cdot B^2 \tag{1}$$

where $(dL_b/L_b)_0$ is the hypothetical spontaneous magnetostriction that would be observed if the magnetoelastic domains did not appear at low fields; $\alpha(T)$ is a temperature-dependent prefactor.

The large magnetostrictive response in the multi-domain region is facilitated by domain effects and can be described by [8]

$$\left(\frac{dL_b}{L_b}\right)(T,B) = \left(\frac{dL_b}{L_b}\right)_0 (T) \times \left(\frac{B}{B_d}\right)^2 \tag{2}$$

where B_d is a phenomenological parameter. Note, that the slope of the $(B/B_d)^2$-behaviour is again the hypothetical spontaneous magnetostriction $(dL_b/L_b)_0$ which is accessible from fitting the experimental data using Eq. (1). As seen clearly in Fig. 7, the equations (1) and (2) describe the ab plane $dL(B)/L$ data well in both the multi-domain and the homogeneous state. We note that, while Fig. 7 shows the analysis of magnetostriction data obtained at the external pressure of 2.5 MPa, the B^2-behaviour is also found at different external pressure (cf. Fig. 4(b)), in both regimes $B < 0.5$ T and $B > 3$ T, respectively.
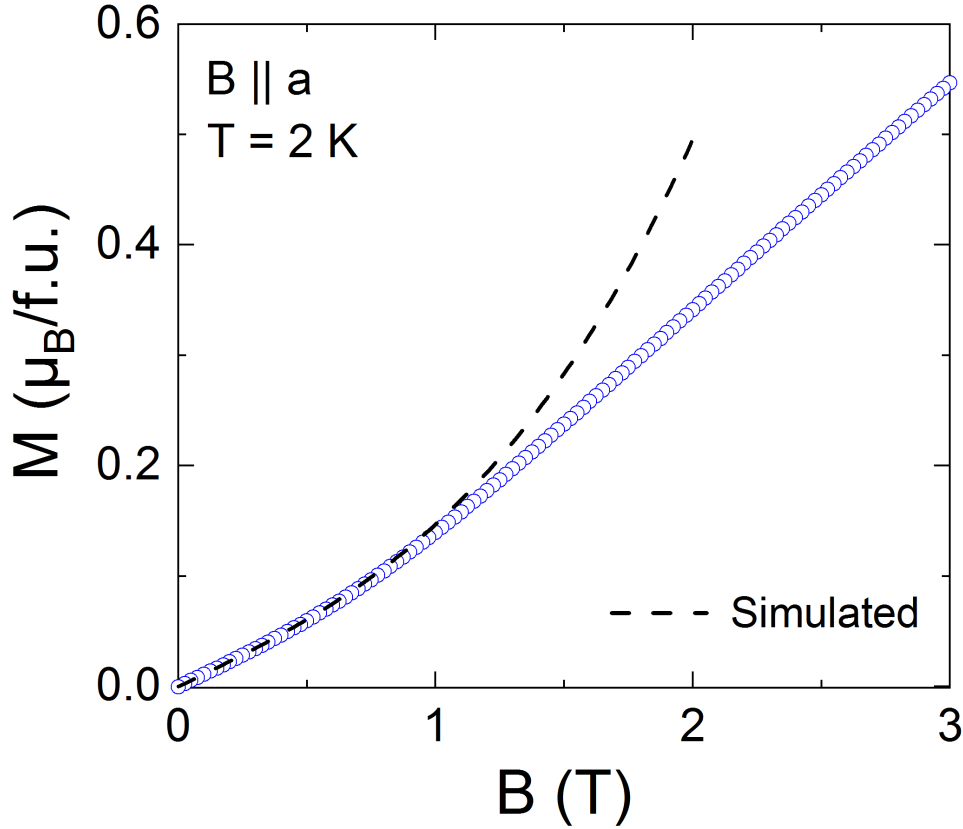
FIG. 8. Magnetization M, at $T = 2$ K, versus applied magnetic field $B||a$-axis. The dashed black line shows a simulation to M at low fields (see the text for more details).

Following the phenomenological models, a smooth non-linear (sickle-shaped) variation of $M(B)$ is expected at low magnetic fields. It is a characteristic of a multi-domain ground state where spin-reorientation gradually takes place by displacement of domain walls [37]. It may be described by [8]

$$M(B) = \frac{1}{2}\chi_e B \left(1 + \frac{(dL_b/L_b)_{rem}}{(dL_b/L_b)_0} + \frac{B^2}{B_d^2} \right).$$ (3)

where χ_e is the magnetic susceptibility in the high-field linear (homogeneous phase) region. A linear fit to the M vs B data at $B > 4$ T yields $\chi_e = 0.19(1)$ μ_B/ T f.u.. We note that Eq. (3) does not include any free fitting parameters. Using B_d, $(dL_b/L_b)_{rem}$ and $(dL_b/L_b)_0$ from the analysis of the magnetostriction data, we simulate the field dependence of M in the low-field region. As seen in Fig. 8, the simulated black line using Eq. (3) yields a good description of magnetization up to 0.7 T, thereby further confirming the applied phenomenological model.

V.   CONCLUSIONS

To summarize, we report the magnetostriction of CoTiO$_3$ single crystals in magnetic fields up to 15 T obtained by high-resolution dilatometry experiments. The results evidence structural domains at high temperatures as well as magnetic domains in the long-range antiferromagnetically ordered phase. Below T_N, we observe pronounced magnetostrictive length changes corresponding to spin-reorientation in the ab plane. Upon application of an in-plane magnetic field, there is an anisotropic deformation breaking the rhombohedral $R\bar{3}$ symmetry in the ab plane. At $B = 3$ T, the difference of in-plane lattice distances amounts to 2.6×10^{-4} which is hardly accessible by diffraction studies. Remarkably, there are drastic effects of small external uniaxial pressure on the magnetostrictive response both above and below T_N which is attributed to the presence of rotational magnetic and twin domains in CoTiO$_3$. We discuss the effects of domains on the magnetisation and magnetostriction on the basis of multi-domain phenomenological models. While the validity of such models and in particular the observed gigantic pressure effects on the magnetostriction are clear fingerprints of magnetostructural domains, our data also imply that even the sign of macroscopic magnetostriction in such materials hosting a multi-domain ground state can depend on tiny changes of the external parameters such as uniaxial strain.

[1] S. Fukami, V. O. Lorenz, and O. Gomonay, J. Appl. Phys. **128**, 070401 (2020).

[2] M. B. Jungfleisch, W. Zhang, and A. Hoffmann, Phys. L. A **382**, 865 (2018).

[3] T. Conzelmann, S. Selzer, and U. Nowak, J. Appl. Phys. **127**, 223908 (2020).

[4] A. Ross, R. Lebrun, O. Gomonay, D. A. Grave, A. Kay, L. Baldrati, S. Becker, A. Qaiumzadeh, C. Ulloa, G. Jakob, et al., Nano Let. **20**, 306 (2020).

[5] S.-H. Yang, K.-S. Ryu, and S. Parkin, Nat. Nanotech. **10**, 221 (2015).

[6] P. Shen, Y. Tserkovnyak, and S. K. Kim, J. Appl. Phys. **127**, 223905 (2020).

[7] E. V. Gomonaj and V. Loktev, Low Temp. Phys. **25**, 520 (1999).

[8] V. M. Kalita, A. F. Lozenko, S. M. Ryabchenko, and P. A. Trotsenko, Low Temp. Phys. **31**, 794 (2005).

[9] B. Náfrádi, T. Keller, F. Hardy, C. Meingast, A. Erb, and B. Keimer, Phys. Rev. Lett. **116**, 047001 (2016).

[10] E. Dagotto, Science **309**, 257 (2005).

[11] K. Dey, S. Sauerland, B. Ouladdiaf, K. Beauvois, H. Wadepohl, and R. Klingeler, Phys. Rev. B **103**, 134438 (2021).

[12] J. K. Harada, L. Balhorn, J. Hazi, M. C. Kemei, and R. Seshadri, Phys. Rev. B **93**, 104404 (2016).

[13] R. Dubrovin, N. Siverin, M. Prosnikov, V. Chernyshev, N. Novikova, P. Christianen, A. Balbashov, and R. Pisarev, J. Alloys Compd. p. 157633 (2020).

[14] K. Dey, S. Sauerland, J. Werner, Y. Skourski, M. Abdel-Hafiez, R. Bag, S. Singh, and R. Klingeler, Phys. Rev. B **101**, 195122 (2020).

[15] N. Mufti, G. R. Blake, M. Mostovoy, S. Riyadi, A. A. Nugroho, and T. T. M. Palstra, Phys. Rev. B **83**, 104416 (2011).

[16] M. Charilaou, D. Sheptyakov, J. F. Löffler, and A. U. Gehring, Phys. Rev. B **86**, 024439 (2012).

[17] H. Watanabe, H. Yamauchi, and H. Takei, J.Magn. Magnetic Mat. **15-18**, 549 (1980).

[18] A. Balbashov, A. Mukhin, V. Ivanov, L. Iskhakova, and M. Voronchikhina, Fiz. Nizk. Temp. **43**, 1200 (2017).

[19] R. E. Newnham, J. H. Fang, and R. P. Santoro, Acta Cryst. **17**, 240 (1964).

[20] B. Yuan, I. Khait, G.-J. Shu, F. C. Chou, M. B. Stone, J. P. Clancy, A. Paramekanti, and Y.-J. Kim, Phys. Rev. X **10**, 11062 (2020).

[21] M. Elliot, P. A. McClarty, D. Prabhakaran, R. D. Johnson, H. C. Walker, P. Manuel, and R. Coldea, arXiv: **2007.04199** (2020).

[22] B. Yuan, M. B. Stone, G.-J. Shu, F. C. Chou, X. Rao, J. P. Clancy, and Y.-J. Kim, Phys. Rev. B **102**, 134404 (2020).

[23] Schematic generated using the VESTA software (https://jp-minerals.org/vesta/en/) by accessing the crystallographic information file (CIF) with the CCDC 2082345 in the FIZ Karlsruhe's joint Access Service via https://www.ccdc.cam.ac.uk/structures/?

[24] M. Hoffmann, K. Dey, J. Werner, R. Bag, J. Kaiser, H. Wadepohl, Y. skourski, M. Abdel-Hafiez, S. Singh and R. Klingeler (to be published).

[25] R. Klingeler, B. Büchner, K. Y. Choi, V. Kataev, U. Ammerahl, A. Revcolevschi, and J. Schnack, Phys. Rev. B **73**, 014426 (2006).

[26] R. Küchler, T. Bauer, M. Brando, and F. Steglich, Rev. Sci. Instru. **83**, 95102 (2012).

[27] L. Wang, J. Werner, A. Ottmann, R. Weis, M. Abdel-Hafiez, J. Sannigrahi, S. Majumdar, C. Koo, and R. Klingeler, **20**, 063045 (2018).

[28] R. Küchler, A. Wörl, P. Gegenwart, M. Berben, B. Bryant, , and S. Wiedmann, Rev. Sci. Instrum. **88**, 083903 (2017).

[29] M. Rotter, A. Barcza, M. Doerr, M. D. Le, J. Brooks, E. Jobiliong, and J. Perenboom, Phys. Rev. B **76**, 144421 (2007).

[30] M. Ackermann, L. Andersen, T. Lorenz, L. Bohatý, and P. Becker, New J. Phys. **17**, 013045 (2015).

[31] J. Werner, W. Hergett, M. Gertig, J. Park, C. Koo, and R. Klingeler, Phys. Rev. B **95**, 214414 (2017).

[32] S. K. Niesen, G. Kolland, M. Seher, O. Breunig, M. Valldor, M. Braden, B. Grenier, and T. Lorenz, Phys. Rev. B **87**, 224413 (2013).

[33] W. Knafo, C. Meingast, K. Grube, S. Drobnik, P. Popovich, P. Schweiss, P. Adelmann, T. Wolf, and H. v. Löhneysen, Phys. Rev. Lett. **99**, 137206 (2007).

[34] F. Scaravaggi, S. Sauerland, L. Wang, R. Kappenberger, P. Lepucki, A. P. Dioguardi, X. Hong, F. Caglieris, C. Wuttke, C. Hess, et al., Phys. Rev. B **103**, 174506 (2021).

[35] M. K. Wilkinson, J. W. Cable, E. O. Wollan, and W. C. Koehler, Phys. Rev. **113**, 497 (1959).

[36] M. Safa and B. K. Tanner, Philos. Mag. B **37**, 739 (1978).

[37] B. K. Tanner, Contemp. Phys. **20**, 187 (1979).

[38] V. M. Kalita, A. F. Lozenko, and S. M. Ryabchenko, Low Temp. Phys. **26**, 489 (2000).

[39] V. M. Kalita and A. F. Lozenko, Low Temp. Phys. **27**, 358 (2001).

[40] V. M. Kalita, A. F. Lozenko, and P. A. Trotsenko, Low Temp. Phys. **28**, 263 (2002).

[41] V. M. Kalita, A. F. Lozenko, P. A. Trotsenko, and T. M. Yatkevich, Low Temp. Phys. **30**, 27 (2004).

Supplement: Magnetostriction and magnetostructural domains in CoTiO$_3$

K. Dey,[1,*] M. Hoffmann,[1] and R. Klingeler[1,2]

[1]*Kirchhoff Institute of Physics, Heidelberg University,*
INF 227, D-69120, Heidelberg, Germany

[2]*Center for Advance Materials (CAM), Heidelberg University,*
INF 227, D-69120, Heidelberg, Germany

(Dated: July 1, 2021)

---

[*] email:kaustav.dey@kip.uni-heidelberg.de
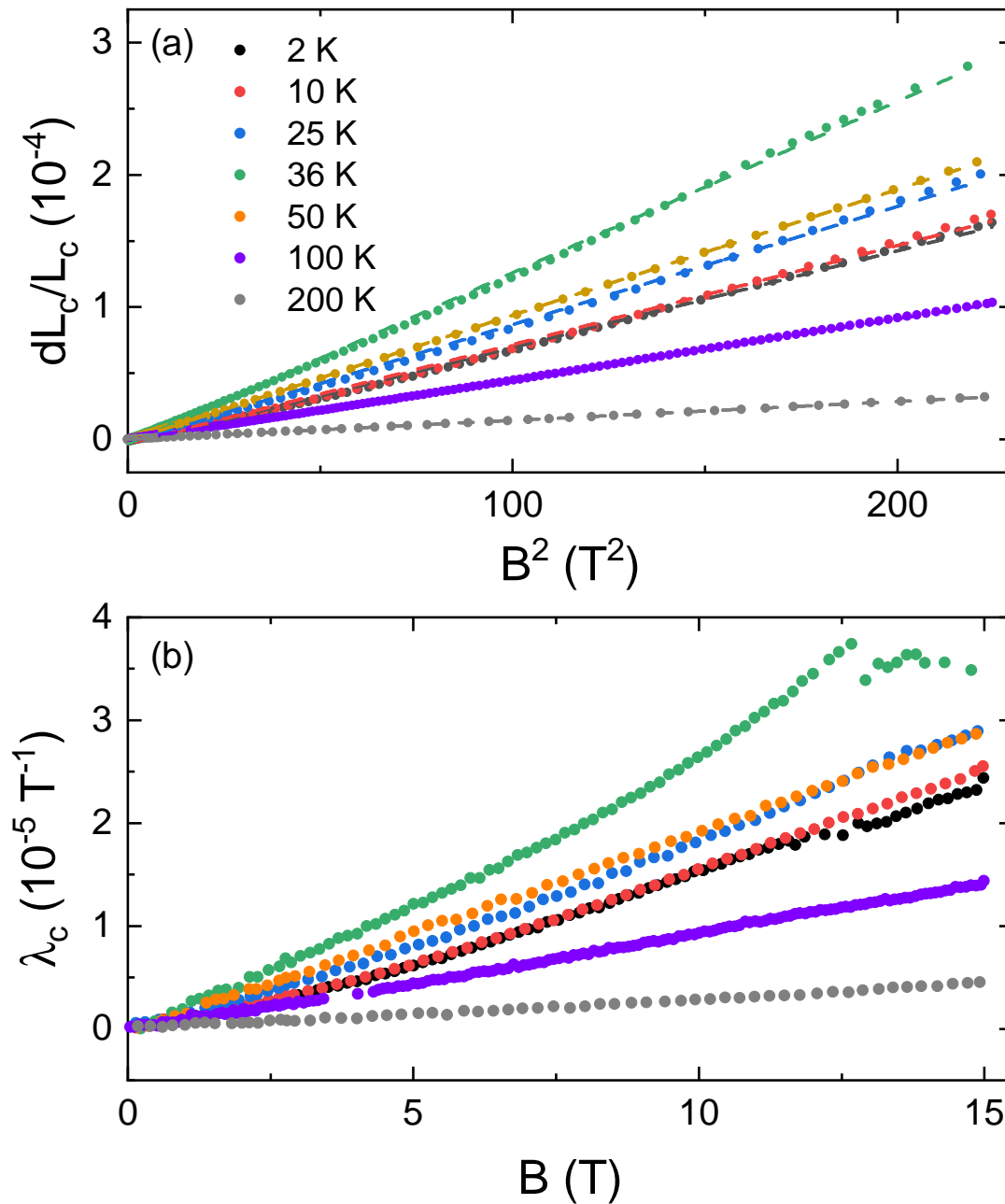
FIG. 1. (a) Fitting lines (dashed lines) to the relative length changes dL_c/L_c plotted versus B^2 allows to determine the pressure dependencies of the magnetic susceptibility; (b) Magnetostriction coefficients $\lambda_c = 1/L_c \cdot dL_c/dB$ at several temperatures for $B||c$. Generally, a linear field dependence is found. Near to the Néel temperature (at 36 K) at high fields, a diffuse feature marks the saturation field.

Chapter 3

High-pressure single-crystal growth and magnetic properties of LaNiO$_3$

The following chapter has been published in the Journal of Crystal Growth under the title 'Magnetic properties of high-pressure optical floating-zone grown LaNiO$_3$ single crystals' [113] Copyright ©2021 Elsevier B.V.All rights reserved

In the following, the contributions of each co-authors are explained in detail, particularly highlighting the specific contribution of K. Dey who is the first and the communicating author.

- Almost all the measurements except specific heat (Fig. 5(b) and 6(b)) and TGA measurements (supplement Fig. 1) and the data analysis were performed by K. Dey. All the plots making and manuscript writing was done by K. Dey.

- W. Hergett assisted K. Dey in single-crystal growth.

- P. Telang performed the TGA measurements (supplement Fig. 1).

- M. Abdel-Hafiez performed the specific heat measurements (Fig. 5(b) and 6(b)).

- R. Klingeler supervised the measurements and supported data analysis and manuscript writing.

- All the authors proofread the manuscript.
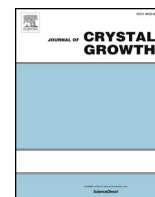
Magnetic properties of high-pressure optical floating-zone grown LaNiO₃ single crystals

Kaustav Dey[a,*], Waldemar Hergett[a], Prachi Telang[b], Mahmoud M. Abdel-Hafiez[a,c], Rüdiger Klingeler[a,d]

[a] Kirchhoff Institute for Physics, Heidelberg University, 69120 Heidelberg, Germany
[b] Department of Physics, Indian Institute of Science Education and Research, Pune, Maharashtra 411008, India
[c] Harvard University, Cambridge, MA 02138, USA
[d] Centre for Advanced Materials (CAM), Heidelberg University, 69120 Heidelberg, Germany

ABSTRACT

Macroscopic cm-sized single crystals of distorted perovskite LaNiO₃ have been grown by means of the optical floating-zone method at oxygen pressures of 40 and 80 bar, respectively. Depending on the growth parameters, the crystals feature a transition to long-range antiferromagnetic order as indicated by magnetic susceptibility and specific heat studies or lack of magnetic order. Our findings resemble recent contradictory reports which either imply the presence of unexpected antiferromagnetism (Guo et al., 2018) or the absence of magnetic order (Zhang et al., 2017; Wang et al., 2018). Our data indicate that long-range magnetic order is not intrinsic to LaNiO₃.

1. Introduction

Rare earth nickelate perovskites RNiO₃ (R = Pr-Lu, Y) are an extensively studied class of compounds, exhibiting band-width controlled metal-insulator (MI) transition as a function of temperature that varies with the rare-earth size [4,5]. Apart from LaNiO₃, which exhibits Pauli paramagnetism, all RNiO₃ compounds show MI transition with antiferromagnetic ground state [5]. However, for nearly three decades intense research on bulk RNiO₃ compounds has been restricted to polycrystalline samples only as single-crystals had not been accessible due to necessity of high temperature and pressure to keep nickel in the unusual +3 valence state [6,7]. Recent technological advances in the field of crystal growth enable growth of high-quality single crystals of previously non-accessible systems, e.g., by applying high pressure [8–17]. In fact, single crystals of LaNiO₃ were grown recently, for the first time, using the high-pressure optical floating zone furnace employing pressures as high as 150 bar [1,2]. Subsequent magnetic studies on LaNiO₃ single crystals revealed a markedly different behaviour [1,2] as compared to the polycrystalline LaNiO₃ samples [18–20]. Contradictory reports on the magnetic ground state of LaNiO₃ have been published recently. Guo et al. by means of magnetisation, specific heat and neutron diffraction experiments on LaNiO₃ single crystals report an antiferromagnetic metallic ground state [1] whereas no long range

order was observed by Zhang et al. [2]. Recent DFT calculations [21] find the *Pnma* structure to be marginally favoured compared to the experimentally reported *R3̄c* structure and antiferromagnetic order could be stabilized in both phases. It is important to re-investigate the intrinsic nature of magnetism in LaNiO₃, as it could provide important clues towards understanding the driving mechanism responsible for the MI transition in the RNiO₃ perovskite nickelates.

In the present work, we report the successful growth of LaNiO₃ single crystals by the high O₂-pressure optical floating-zone technique. Laue analysis implies the presence of macroscopic single crystalline grains and phase purity is confirmed by means of room temperature X-ray diffraction. The static magnetic susceptibility $\chi = M/B$ vs. temperature of LaNiO₃ single crystals grown under 40 bar and 80 bar is reported. Crystals extracted from areas well separated from the molten zone regions display magnetic susceptibilities in accordance with Zhang et al.[2]. In particular, the crystals do not exhibit anomalies as observed by Guo et al. [1]. In contrast, single crystals extracted nearby the molten zone region exhibit kinks in χ at around 155 K and corresponding jumps in the specific heat. Based on magnetisation and specific heat measurements on our LaNiO₃ single crystals, we conclude that long range ordering in LaNiO₃ may not be intrinsic and that the effect of oxygen deficient phases, i.e, LaNiO₃₋δ needs to be considered seriously when interpreting the physical properties of LaNiO₃.

* Corresponding author.
  E-mail address: kaustav.dey@kip.uni-heidelberg.de (K. Dey).

2. Experimental details

Precursors for the crystal growth were prepared via standard solid state reaction method. La_2O_3 was calcined overnight at 900 °C to remove absorbed water. Stoichiometric amounts of La_2O_3 and NiO were thoroughly ground in an agate mortar and the resulting mixture was sintered at 1000 °C for 24 h in O_2 flow of 250 sccm. The obtained powder was re-ground, densely packed in a rubber tube and isostatically pressed at 60 MPa to obtain cylindrical shaped rods of 6–8 cm in length and 5 mm in diameter. These rods were sintered at 1150 °C in air for several days and used as feed and seed rods. The crystal growth was carried out in a high-pressure optical floating-zone (FZ) furnace (HKZ, SciDre) [9]. A Xenon arc lamp operating at 3.5 kW was employed and the growth was performed inside a sapphire chamber of 72 mm in length and 20 mm wall thickness. All the growth experiments were performed in O_2 atmosphere at elevated pressures of 40 and 80 bar, maintaining an O_2 flow rate of 0.1 l/min. The feed and seed rods were counter rotated at 10 rpm for homogeneous mixing and thermal stability of the zone. The feed rod was pulled at 7 mm/h and the seed rod was pulled at about 4–6 mm/h to ensure enough liquid volume in the zone and to maintain the zone stability. *In-situ* temperature profiles of the sample and molten zone were obtained stroboscopically by means of a two-color pyrometer which can be moved vertically along the growth chamber during the growth process.

Phase purity was studied by means of X-ray diffraction (XRD) measurements on a Bruker D8 Advance ECO diffractometer with Cu $K\alpha$ source. Data have been collected at room temperature in the 2θ range of 10–70° with 0.02° step-size and integration time of 180 s per step. Rietveld refinement of the obtained patterns was done using the FullProf Suite 2.0 [22]. Oxygen content was determined by thermogravimetry (TGA) using the STA 449 F1 Jupiter by NETZSCH equipped with a WRe type thermocouple. Pulverized samples (≈ 60 mg) were placed in an alumina crucible and heated at the rate of 10 K/min up to 550 °C with dwell time of two hours at the highest temperature. The measurements were done under reducing Ar-10%/H_2 gas flow at 40 ml/min. Magnetisation was measured using a superconducting quantum interference device (SQUID) magnetometer (Quantum Design MPMS-XL5). Specific heat measurements were carried out in a Quantum Design PPMS using the relaxation method.

3. Results and discussions

The crystal growth was carried out successfully by maintaining a stable zone in the presence of an elevated O_2 pressure between 40 and 80 bar. Elevated pressure is required to obtain phase pure $LaNiO_3$ single crystals which contains Ni in unusual $+3$ oxidation state [2]. Simple solid state reaction of the precursors at high temperatures ($T > 800$ °C) and ambient pressure leads to the formation of other oxide phases (Ruddlesden-Popper) containing Ni in its usual $+2$ state [23]. One of challenges we faced in the high-pressure optical growth of $LaNiO_3$ is the cracking of the feed and seed rods during the growth. The density of the cracks formed during 80 bar growth is higher than at 40 bar. We attribute this to the fact that increasing the gas pressure leads to a sharper temperature gradient along the rod facilitating the crack formation [24]. The larger number of cracks at 80 bar made it difficult to form and maintain a stable zone, sometimes leading to the breaking and falling of the feed rod. To avoid the cracking issue, highly dense feed rods have been made. Sintering the rods at a higher temperature, i.e., at 1150 °C, with longer dwelling time of about 4–6 days was found suitable to completely overcome cracking. During the growth, the feeding rate is kept higher than the crystal pulling rate to maintain a stable zone leading to the formation of broad crystals of about 5–6 mm in diameter. The length of the longest as-grown single crystal rod obtained in our experiment at 40 bar O_2 pressure is about 1.4 cm as shown in Fig. 2.

Fig. 1 shows the floating-zone formed during the growth along with the respective temperature profile of the sample and the molten region.
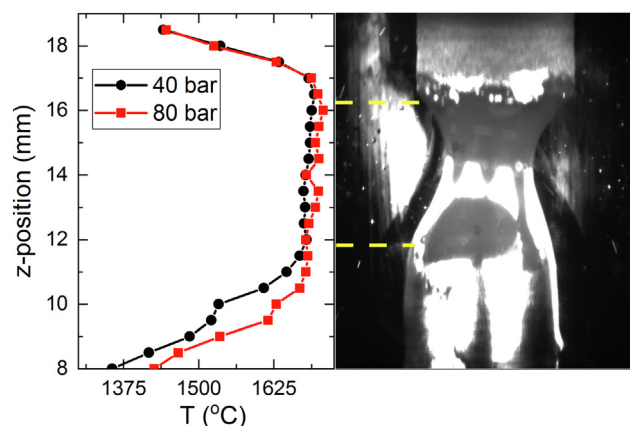
Fig. 1. Vertical in situ temperature profile of the sample at and around the melting zone during the growth as measured by the pyrometer (left) and real-time image of a typical $LaNiO_3$ floating zone (right).

The profile demonstrates a plateau-like shape showing a broad central region corresponding to the melt. The temperature of the liquid floating-zone amounts to 1681 ± 5 °C at 40 bar and 1696 ± 8 °C at 80 bar O_2 pressure, respectively. The near vertical profile in the temperature of the floating-zone indicates that the zone-temperature is near constant. This indicates that counter rotation of feed and seed rods at 10 rpm is appropriate to achieve a homogeneous temperature distribution in the floating-zone. The resulting as-grown $LaNiO_3$ boule is shown in Fig. 2. Laue diffraction performed at several spots along the length of the boule to detect single-crystalline grains confirms cm-size single-crystalline grains in the obtained samples with good crystallinity.

To study the phase purity of the grown single crystals, powder XRD was performed on several crushed and pulverized single crystalline pieces cut along the length of the grown rods. Fig. 3 shows Rietveld refinements of the obtained XRD patterns for the growths performed at 40 and 80 bar, respectively. The results imply that our single crystals exhibit the $R\bar{3}c$ space group and confirm phase purity within the accuracy of the powder XRD measurements. The lattice parameters obtained from Rietveld analysis of the room temperature XRD patterns is listed in Table 1. Note that the Ni-O-Ni bond angle is less than 180° indicating that $LaNiO_3$ has a distorted perovskite structure. The oxygen content of the $LaNiO_3$ crystals grown under 40 bar was determined to be 2.976(1) by TGA measurements which implies $\delta \approx -0.023(8)$ vacancies per formula unit. For the samples grown at 80 bar the oxygen content amounts to 2.979(1), i.e. $\delta \approx -0.020(9)$. Note that the oxygen deficiency is in a similar range as reported by Zhang et al. [2]. In contrast, the crystals extracted close to the molten floating zone (LNO40.1) exhibit a significantly larger oxygen deficiency of $\delta \approx -0.183(8)$ vacancies per formula unit resulting in an oxygen content of 2.816(9). As noted in Table 1, the Ni−O−Ni bond angle as well as the lattice parameters increase with increase in oxygen vacancies but no change is observed in the crystal structure symmetry from XRD measurements on the most oxygen deficient samples.

Fig. 4 shows the static magnetic susceptibility $\chi = M/B$ vs. T for several $LaNiO_3$ single crystals grown under 40 and 80 bar, respectively.
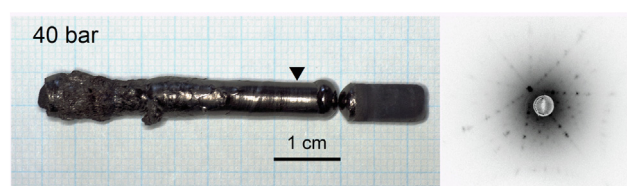
Fig. 2. As-grown boule of $LaNiO_3$ grown at 40 bar O_2-pressure and representative back-scattered Laue pattern taken along the growth direction at the position marked by the black triangle.
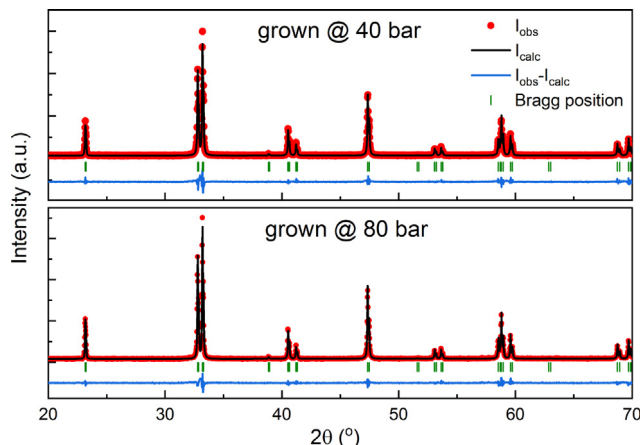
Fig. 3. Room temperature XRD-patterns and corresponding Rietveld refinements of powdered LaNiO$_3$ single crystals grown at 40 and 80 bar O$_2$ pressure, respectively. The observed diffraction patterns are shown in red, calculated patterns in black, and the difference between the observed and calculated patterns is shown in blue. Vertical green ticks denote the allowed Bragg positions.The R parameters of the fits are R_{wp} = 15.5, R_e = 8.85, χ^2 = 3.05 for 40 bar and R_{wp} = 14, R_e = 9.42, χ^2 = 2.21 for 80 bar respectively. (For interpretation of the references to colour in this figure legend, the reader is referred to the web version of this article.)

Table 1

Lattice constants, Ni−O−Ni bond angle of $R\bar{3}c$-LaNiO$_3$ as determined from Rietveld analysis of room temperature X-ray diffraction data, and oxygen vacancy content δ. Samples marked as LNO40 and LNO80 are taken from two different boules grown at 40 and 80 bar, respectively. $*$ mark indicates a sample extracted close to the solidified floating-zone (about 2 mm away) which exhibits anomalies in the susceptibility and specific heat data (cf. Figs. 4 and 5). All other crystals are extracted far from the solidified zone and exhibit no such anomalies. Refer the text for further information.

Sample	a (Å)	c (Å)	∢ Ni−O−Ni (°)	δ
LNO40.1*	5.459(2)	13.136(2)	169.9	−0.183(8)
LNO40.2	5.457(3)	13.130(4)	165.3(7)	−0.023(8)
LNO80.1	5.457(2)	13.130(1)	164.8(3)	−0.020(9)
LNO80.2	5.457(6)	13.129(7)	164.8(3)	–

The overall behaviour $\chi(T)$ is consistent with previous reports on single crystals by Zhang et al. [2] and Guo et al. [1], but markedly differ from the magnetic susceptibility of polycrystalline LaNiO$_3$[18,20] (refer to the digitized data in Fig. 4). While χ is of the same order of magnitude, it demonstrates only very weak temperature dependence in polycrystals and is quantitatively well described by the sum of Pauli paramagnetism and a Curie contribution. Instead, the data in Fig. 4 shows a broad maximum in addition to the Curie-like upturn at low temperatures which may be associated to quasi-free magnetic impurities, e.g., due to the presence of Ni^{2+} in the $\lesssim$ 1% range [2,19]. A smaller upturn in susceptibility, as observed (Fig. 4) in the crystals grown under 80 bar to that of 40 bar implies less quasi-free moments suggesting that higher pressure reduces the presence of Ni^{2+} defects in the grown LaNiO$_3$ single crystals.

Detailed inspection of the magnetic susceptibility in the region of the maximum exhibits no anomalies for crystals grown at 40 and 80 bar (see Fig. 4). The susceptibility results are in accordance with Zhang et al. Surprisingly, the single crystalline pieces extracted nearer, i.e., about 2 mm away from the solidified zone of one of the boules (LNO40.1) and which possess the highest oxygen deficiency as obtained from the TGA data, exhibit a kink in χ at T_N = 151 K (see Fig. 4). In fact, several pieces extracted from a region close to the solidified floating-zone exhibit similar anomalies at temperatures 151–157 K as shown in Fig. 4. The corresponding specific heat data for one of these single
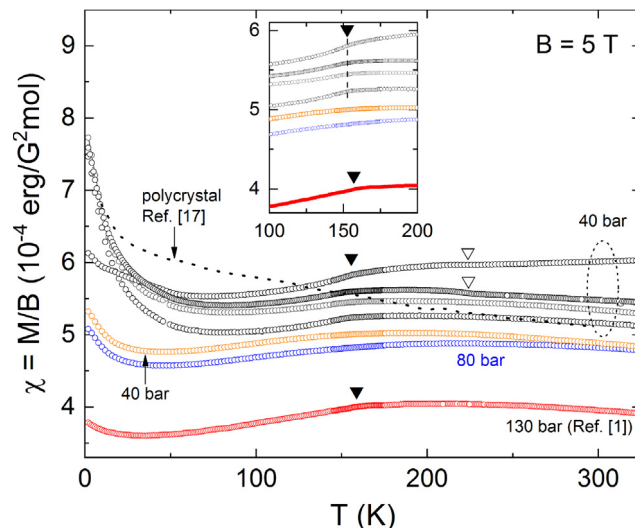
Fig. 4. Temperature dependence of the static magnetic susceptibility $\chi = M/B$ of several LaNiO$_3$ single crystals grown under 40 and 80 bar O$_2$ pressure, respectively, at B = 5 T. The inset shows χ in the temperature range 100 K $\leqslant$ T $\leqslant$ 200 K, i.e., highlighting the regime where some of the samples evolve antiferromagnetic order. Anomalies signaling the evolution of antiferromagnetism are marked by filled triangles. Open triangles mark anomalies indicative of a ferromagnetic impurity phase (see the text).
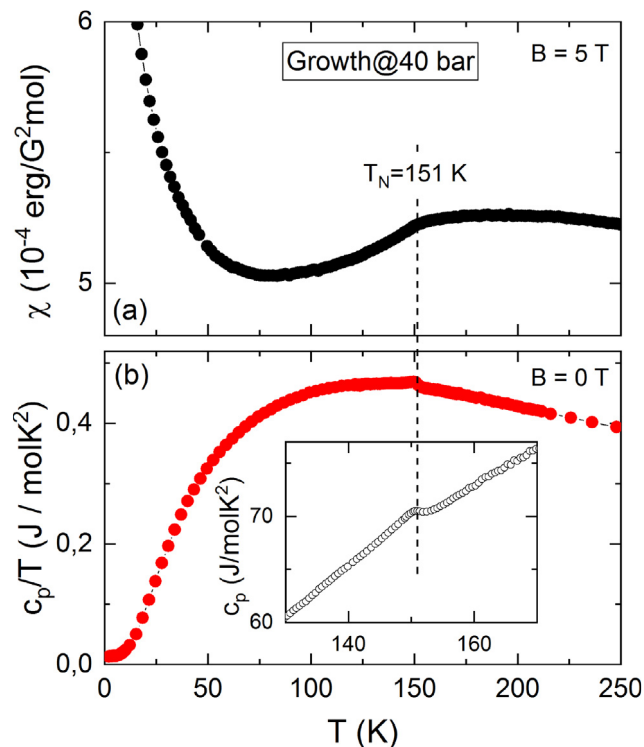
Fig. 5. Temperature dependence of (a) magnetic susceptibility and (b) heat capacity of a LaNiO$_3$ single crystal grown under 40 bar of O$_2$ pressure.

crystalline pieces (Fig. 5b) show a small jump Δc_p at T_N which is usually indicative of the onset of long-range order. Note that the observed anomalies are in the same temperature range as previously reported by Guo et al. [1] where anomalies in the susceptibility and the specific heat were observed at 157 K (see the digitized data in Fig. 4). Quarter integer peaks in single crystal neutron diffraction enabled them to conclude the presence of long-range antiferromagnetic order. These findings challenged all previous studies where LaNiO$_3$ was reported to
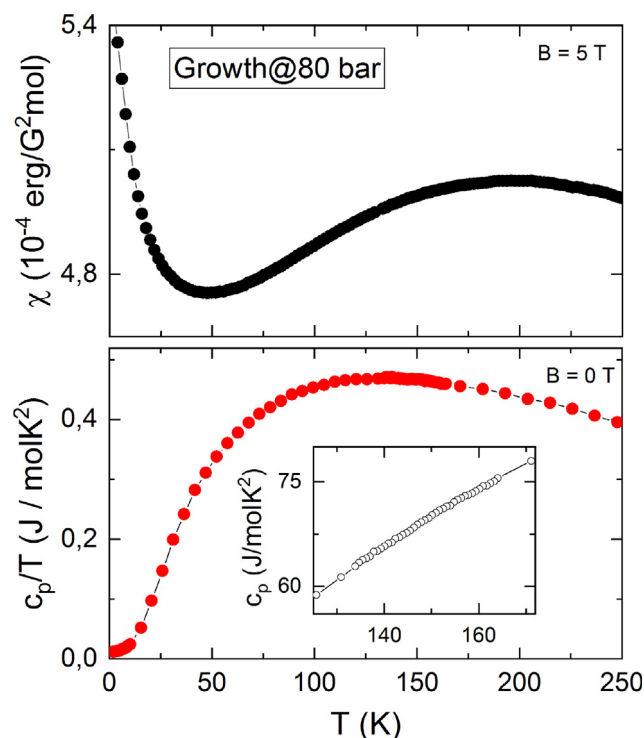
Fig. 6. Temperature dependence of (a) magnetic susceptibility and (b) heat capacity of a LaNiO$_3$ single crystal grown under 80 bar of O$_2$ pressure.

be a Pauli paramagnetic metal. As shown in Figs. 4 and 5, we observe similar anomalies in χ and c_p only for the single crystals extracted very close to the solidified zones. The specific heat data for a single crystalline piece grown at 80 bar pressure (i.e. LNO80.1 and LNO80.2) and taken far away from the zone exhibits no anomaly (see Fig. 6). This indicates an extrinsic nature of the observed anomalies. Note, that the oxygen deficient phases of LaNiO$_3$, i.e., LaNiO$_{3-\delta}$, show various anomalies in magnetic studies depending on δ. For example, LaNiO$_{2.5}$ reportedly shows antiferromagnetism at $T_N = 140$ K [25] whereas LaNiO$_{2.75}$ shows ferromagnetism at $T_C = 230$ K [26]. Indeed, depending on growth conditions of the samples and vicinity to the solidified floating zone, the susceptibility indicates a ferromagnetic impurity phase, presumably LaNiO$_{2.75}$, as shown by a feature at $T \approx 225$ K (see open triangles in Fig. 4). Comparison of the anomaly with data on LaNiO$_{2.75}$ from Ref. [26] suggests ~5(2)% of this impurity phase in crystals taken from direct vicinity of the molten zone. Notably, Wang et. al. [3] reduced LaNiO$_3$ a single crystal without any anomalies in χ to LaNiO$_{3-\delta}$ which resulted in the appearance of clear features at 150 K (showing antiferromagnetism) as well as at 225 K (showing ferromagnetism). If oxygen deficiency is a parameter governing the presence of antiferromagnetism, details of the growth process and in particular the distance of the crystalline grain under study from the zone will be crucial. We emphasize that all crystals showing the above mentioned anomalies have been taken from a region within 2 mm from the frozen floating-zone of the respective boules which in fact exhibits the largest oxygen deficiency. In contrast, LaNiO$_3$ single crystals taken well away from the frozen floating-zone possess a smaller oxygen deficiency and show the behaviour exemplified by Fig. 6.

4. Conclusions

We have successfully grown macroscopic single crystals of LaNiO$_3$ at oxygen pressures of 40 and 80 bar, respectively. Anomalies in static

magnetic susceptibility and heat capacity were observed only in single crystals grown under 40 bar pressure and extracted from a region close to the zone. Our results indicate an extrinsic nature of the observed anomalies, most likely arising due to oxygen deficient phases LaNiO$_{3-\delta}$.

Declaration of Competing Interest

The authors declared that there is no conflict of interest.

Appendix A. Supplementary material

Supplementary data associated with this article can be found, in the online version, at https://doi.org/10.1016/j.jcrysgro.2019.125157.

References

[1] H. Guo, Z.W. Li, L. Zhao, Z. Hu, C.F. Chang, C.Y. Kuo, W. Schmidt, A. Piovano, T.W. Pi, O. Sobolev, D.I. Khomskii, L.H. Tjeng, A.C. Komarek, Nat. Commun. 9 (1) (2018) 43.
[2] J. Zhang, H. Zheng, Y. Ren, J.F. Mitchell, Cryst. Growth Des. 17 (5) (2017) 2730–2735.
[3] B.-X. Wang, S. Rosenkranz, X. Rui, J. Zhang, F. Ye, H. Zheng, R.F. Klie, J.F. Mitchell, D. Phelan, Phys. Rev. Mat. 2 (6) (2018).
[4] M.L. Medarde, J. Phys. Condens. Matt. 9 (8) (1997) 1679–1707.
[5] G. Catalan, Phase Trans. 81 (7–8) (2008) 729–749.
[6] J.A. Alonso, M.J. Martínez-Lope, M.T. Casais, J.L. García-Muñoz, M.T. Fernández-Díaz, Phys. Rev. B 61 (2000) 1756–1763.
[7] P. Lacorre, J. Torrance, J. Pannetier, A. Nazzal, P. Wang, T. Huang, J. Sol. State Chem. 91 (2) (1991) 225–237.
[8] C. Neef, H. Wadepohl, H.-P. Meyer, R. Klingeler, J. Cryst. Growth 462 (2017) 50–59.
[9] N. Wizent, G. Behr, W. Löser, B. Büchner, R. Klingeler, J. Cryst. Growth 318 (1) (2011) 995–999.
[10] D. Souptel, W. Löser, G. Behr, J. Cryst. Growth 300 (2) (2007) 538–550.
[11] J. Zhang, H. Zheng, C.D. Malliakas, J.M. Allred, Y. Ren, Q. Li, T.-H. Han, J. Mitchell, Chem. Mater. 26 (24) (2014) 7172–7182.
[12] H.B. Cao, Z.Y. Zhao, M. Lee, E.S. Choi, M.A. McGuire, B.C. Sales, H.D. Zhou, J.-Q. Yan, D.G. Mandrus, APL Mater. 3 (6) (2015) 062512.
[13] W.A. Phelan, J. Zahn, Z. Kennedy, T.M. McQueen, J. Sol. State Chem. 270 (2019) 705–709.
[14] H. Guo, Z. Hu, T.-W. Pi, L.H. Tjeng, A.C. Komarek, Crystals 6 (8) (2016).
[15] N. Wizent, N. Leps, G. Behr, R. Klingeler, B. Büchner, W. Löser, J. Cryst. Growth 401 (2014) 596–600.
[16] W. Hergett, C. Neef, H. Wadepohl, H.P. Meyer, M.M. Abdel-Hafiez, C. Ritter, E. Thauer, R. Klingeler, J. Cryst. Growth 515 (2019) 37–43.
[17] N. Wizent, G. Behr, F. Lipps, I. Hellmann, R. Klingeler, V. Kataev, W. Löser, N. Sato, B. Büchner, J. Cryst. Growth 311 (5) (2009) 1273–1277.
[18] K. Sreedhar, J.M. Honig, M. Darwin, M. McElfresh, P.M. Shand, J. Xu, B.C. Crooker, J. Spalek, Phy. Rev. B 46 (10) (1992) 6382–6386.
[19] X.Q. Xu, J.L. Peng, Z.Y. Li, H.L. Ju, R.L. Greene, Phys. Rev. B 48 (2) (1993) 1112–1118.
[20] J.S. Zhou, L.G. Marshall, J.B. Goodenough, Phys. Rev. B 89 (24) (2014).
[21] A. Subedi, SciPost Phys. 5 (2018) 20.
[22] J. Rodríguez-Carvajal, Phys. B: Condens. Matt. 192 (1) (1993) 55–69.
[23] G. Li, J. Yang, Y. Fan, S. Tian, C. Zheng, J. Sol. State Chem. 141 (2) (1998) 457–461.
[24] S. Koohpayeh, D. Fort, J. Abell, Prog. Cryst. Growth Character. Mater. 54 (3) (2008) 121–137.
[25] T. Moriga, O. Usaka, T. Imamura, I. Nakabayashi, I. Matsubara, T. Kinouchi, S. Kikkawa, F. Kanamaru, Bull. Chem. Soc. Japan 67 (3) (1994) 687–693.
[26] R.D. Sánchez, M.T. Causa, A. Caneiro, A. Butera, M. Vallet-Regí, M.J. Sayagués, J. González-Calbet, F. García-Sanz, J. Rivas, Phys. Rev. B 54 (1996) 16574–16578.

Magnetic properties of high-pressure optical floating-zone grown LaNiO₃ single crystals
Supplementary Information

Kaustav Dey[a,*], Waldemar Hergett[a], Prachi Telang[b], Mahmoud M. Abdel-Hafiez[a,c], Surjeet Singh[b], Rüdiger Klingeler[a,d]

[a]*Kirchhoff Institute for Physics, Heidelberg University, 69120 Heidelberg, Germany*
[b]*Department of Physics, Indian Institute of Science Education and Research, Pune, Maharashtra-411008, India*
[c]*Harvard University, Cambridge, MA 02138, USA*
[d]*Centre for Advanced Materials (CAM), Heidelberg University, 69120 Heidelberg, Germany*
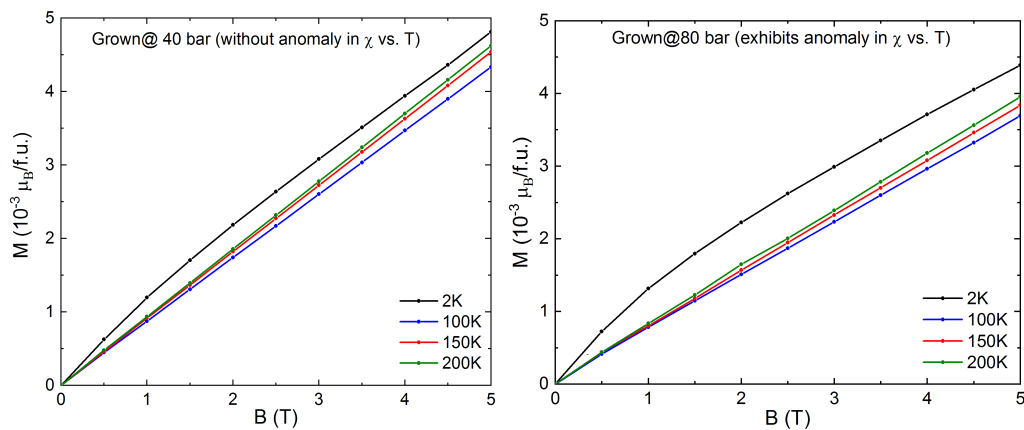
Figure 1: DC magnetization vs field at various temperatures for single crystalline pieces grown at (a) 40 bar and (b) 80 bar respectively.
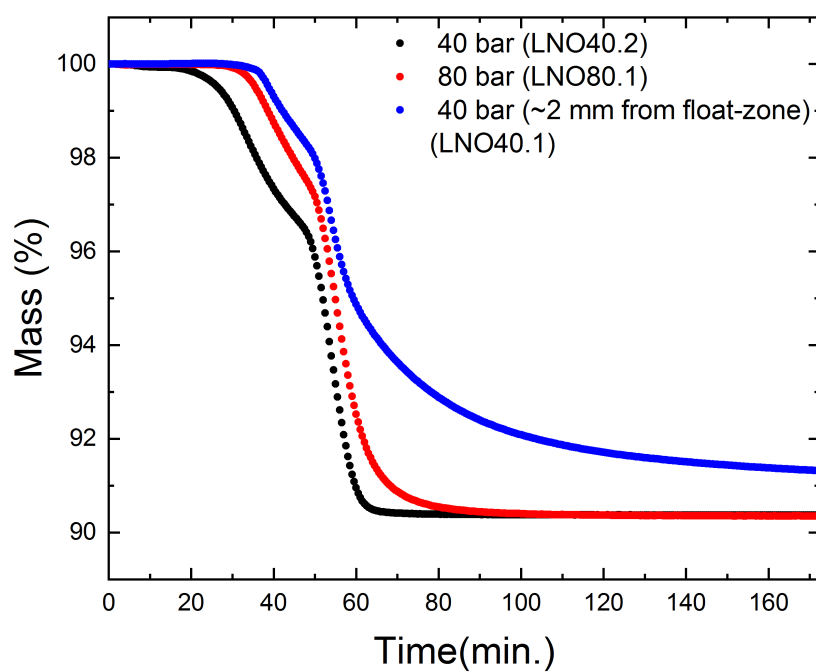
Figure 2: TGA measurements showing the temporal dependance of the sample mass of the LaNiO3 single crystals grown at 40 bar and 80 bar respectively.

Chapter 4

Conclusions

One of the principal aims of this thesis is the growth of bulk single-crystals of ilmenite titanates and lanthanum nickelates. For this, the optical floating-zone method was employed in the recently available high-pressure optical furnace (Sci-Dre, 150 bar) and additionally in the widely available four-mirror optical furnace (CSC, 10 bar). The titanates $NiTiO_3$ and $CoTiO_3$ and the nickelate $LaNiO_3$ have been grown. Additional single-crystals of other members of the ilmenite family - $MnTiO_3$ (Appendix B) and $Ni_{0.25}Mn_{0.75}TiO_3$ (Appendix C) and Ruddlesden-Popper $La_4Ni_3O_{10}$ (Appendix D) have also been grown. In particular, the four-mirror furnace was found to be better suited for the growth of titanates and the high-pressure furnace proved to be the only way to grow the lanthanum nickelates, since pressures greater than 10 bar was needed to stabilize the right phase. Table 4.1 summarizes the most suitable parameters optimized for the growths of macroscopic single-crystals.

Table 4.1. The table summarizes the growth parameters namely the atmosphere (atm.), growth and feeding rate, the employed pressure p and the rotation speed of the counter rotating rods for the most-stable growth of the ilmenite titanates and lanthanum nickelates.

material	atm. (flow rate)	growth rate	feed rate	p (bar)	rot. speed (rpm)
$NiTiO_3$	air (3 l/min)	3 mm/h	3 mm/h	ambient	20
$CoTiO_3$	O_2 (0.05 l/min)	6 mm/h	6 mm/h	ambient	20
$MnTiO_3$	Ar (0.5 l/min)	5 mm/h	5 mm/h	5	10
$Ni_{0.25}Mn_{0.75}TiO_3$	Ar (0.3 l/min)	2 mm/h	2 mm/h	5	10-15
$LaNiO_3$	O_2 (0.1 l/min)	7 mm/h	4-6 mm/h	40/80	10
$La_4Ni_3O_{10}$	O_2 (0.1 l/min)	6 mm/h	4 mm/h	20	12-15

All the synthesized materials were characterized in detail by means of powder and single-crystal X-ray diffraction, EDX, polarized microscopy and magnetization measurements. The resulting single-crystalline pieces were oriented ($\approx$ few mm^3 dimensions) typically along prin-

cipal crystallographic directions. Detailed magnetic and thermodynamic studies were carried out on specifically - $NiTiO_3$, $CoTiO_3$ and $LaNiO_3$ which form the bulk of this thesis. Below a summary of important results from each chapter is presented.

4.1 Summary

Chapter 2

A detailed investigation of the magnetoelastic coupling in the optical floating-zone grown $NiTiO_3$ single-crystal is presented in **section 2.1**. It is observed by means of high-resolution thermo-dilatometry experiments that the lattice spontaneously deforms upon the evolution of long-ranged antiferromagnetic order below T_N = 22.5 K. The measured relative length changes $dL_i/L_i (i = a, c)$ signal shrinking of c axis and increase of a axis upon decreasing temperature across T_N indicating significant magnetoelastic coupling in $NiTiO_3$. The corresponding thermal expansion coefficients (α_i) exhibited significant lambda shaped anomalies at T_N and the signs of the anomaly help determine the sign of the uniaxial pressure dependency, i.e., $dT_N/dP_a < 0$ and $dT_N/dP_c > 0$ for $NiTiO_3$. The scaling of the non-phononic contribution to the thermal expansion coefficient (α_V^{mag}) and the specific heat (C_p^{mag}) revealed a single temperature independent Grüneisen parameter amounting to $\gamma_m = 1.18(3) \times 10^{-6}$. The Grüneisen analysis indicated a single dominant energy scale ϵ across T_N and enabled estimating the hydrostatic pressure dependency of T_N, amounting to $dT_N/dP = 1.12(4)$ K/Gpa using the Ehrenfest relation. The positive sign of hydrostatic pressure dependency imply that the nearest neighbour ferromagnetic interactions in the ab plane supposedly increase on application of hydrostatic pressure. Furthermore, we constructed the complete magnetic phase diagram of $NiTiO_3$ for the first time using high-field dilatometry (15 T) and magnetization studies in static (15 T) and pulsed (60 T) magnetic fields. While the shape of anomalies in α were not significantly affected by magnetic fields, T_N expectantly and isotropically shifted to lower temperature for both a and c axes. Magnetization data in the pulsed-magnetic fields indicated that the magnetic saturation for both a and c axes is achieved at $B_{sat} = 36.0(5)$ T. The resulting saturation magnetization amounted to $M_{sat} = 2.23(5)$ $\mu_B/f.u.$ and for $S = 1$ (for Ni^{2+}) this yielded an isotropic g-factor of 2.23(5). The g-factor value agrees very well with electron spin-resonance experiments [39] and from Curie-Weiss fit to the static magnetic susceptibility data. While the magnetization exhibited a linear behaviour for all $B||c$, a non-linear sickle-shaped behaviour indicative of spin-reorientation was observed at low magnetic-fields ($B \leq 2$ T) applied in the hexagonal ab plane. The in-plane magnetostriction measurements, i.e., dL_a/L_a vs. B corresponding to the spin-reorientation exhibited significant length changes amounting to $\Delta L_a/L_a = 4.8 \times 10^{-5}$ at 2 K. The corresponding phase boundary $B(T)$ of the spin-reorientation was constructed using

the half-heights from the magnetostriction data and indicated negligible entropy change across the transition.

Following the results of section 2.1 where the magnetoelastic coupling was established for the first time in $NiTiO_3$, a detailed investigation establishing finite magnetoelectric coupling in $NiTiO_3$ is presented in section 2.2. In particular, single-crystal X-ray and neutron diffraction data are presented and compared to that of magnetization and thermo-dilatometry results presented in section 2.1. The single-crystal XRD measurements performed at 100 K reconfirmed the assignment of $R\bar{3}$ space group and improved on the accuracy of the previously reported crystallographic parameters from polycrystalline XRD and neutron measurements [28,34]. Furthermore, the neutron diffraction study of nuclear structure at 2 K which is well below $T_N = 22.5$ K revealed that the macroscopic $R\bar{3}$ symmetry is preserved until the lowest temperatures. Hence, the data clearly indicated that the spontaneous lattice deformation of $NiTiO_3$ at T_N as revealed from the thermal expansion data in section 2.1 is symmetry preserving one. Additional satellite magnetic Bragg-peaks corresponding to the propagation vector (0,0,1.5) were also observed at $T = 2$ K in the neutron data which enabled re-confirming the easy-plane type spin-structure (A-type) of $NiTiO_3$. In fact the magnetic ground state of $NiTiO_3$ comprises of three equally populated 120° rotational domains owing to the C_3 symmetry of the hexagonal ab plane. Comparison of the magnetic order parameter 'L', the relative volume changes (from dilatometry measurements in section 2.1) and the reported dielectric function 'ϵ' [44], revealed that ϵ varies as L^2. This is in-line with the predictions of Landau theory and clearly indicates finite magnetoelectric coupling in $NiTiO_3$. The detailed structural studies as described above further suggested that a spin-phonon coupling rather than an exchange striction mechanism is possibly the responsible microscopic mechanism behind the observed magnetoelectric effect in $NiTiO_3$. Furthermore, the results from in-field neutron diffraction (up to 6 T) with magnetic field applied in the ab plane are also presented and compared to magnetostriction and magnetization measurements. In-field neutron data clearly revealed the continuous evolution of multidomain ground state to a single domain (for $B \geq 2$ T) comprising of spins aligned perpendicular to the applied external magnetic field. The in-plane spin-reorientation process for $B < 2$ T is in fact responsible for the observed sickle-shaped behaviour in magnetization and pronounced increase in magnetostriction measurements as described in section 2.1. The measurements further revealed that the thermodynamic quantities $\partial M/\partial B$ and λ^a peak at different points which is uncharacteristic for a spin-reorientation transition (e.g. spin-flop), but is a feature of multi-domain rearrangement process. The macroscopic magnetization and magnetostriction measurements were successfully described by means of magnetoelastic multi-domain phenomenological theories, and a linear scaling of the thermodynamic quantities $\partial\chi/\partial B$ and λ^a in the multidomain state in-line with the predictions of the theory.

In **section 2.3**, the magnetic and thermodynamic investigations as described above on $NiTiO_3$

was extended to another member of the ilmenite titanates family namely $CoTiO_3$. In particular, $CoTiO_3$ has a similar crystallographic and A-type magnetic structure [35] as $NiTiO_3$. However, the difference in magnetism arises from the spin-orbit coupled pseudospin-1/2 ground state in $CoTiO_3$ which is fundamentally different from the spin-1 ground state with nearly quenched orbital momentum realised for $NiTiO_3$. As a result, the magnetic susceptibility is highly-anisotropic in $CoTiO_3$ with a non Curie-Weiss behaviour at high-temperatures due to considerable mixing of the ground J_{eff} = 1/2 state with the higher J_{eff} = 3/2, 5/2... multiplets. The structural refinements of the single-crystal x-ray diffraction data at 100 K re-confirm the $R\bar{3}$ space group [28]. The zero-field thermal expansion measurements revealed strong anomalies at T_N= 37 K with shrinking of both c and b axes indicative of strong magnetoelastic coupling. The data imply positive uniaxial pressure dependencies $dT_N/dp_c > 0$ and $dT_N/dp_b > 0$ contrary to what was observed for $NiTiO_3$ (where $dT_N/dp_b < 0$). It is speculated that unlike $NiTiO_3$, the presence of bond-anisotropic frustration in the hexagonal plane of $CoTiO_3$ [45] can be lifted by an externally applied uniaxial pressure, hence resulting in a positive pressure dependency. The magnetic Grüneisen analysis indicated a single-dominant magnetic degree of freedom driving the observed non-phononic length and entropic changes and further enabled estimating a hydrostatic pressure dependency of $dT_N/dp = 2.7(4)$ K/GPa. Interestingly, the quantitative comparison of the measured relative length changes dL_i/L_i with the published dielectric data [114] enabled us to establish the presence of significant magnetodielectric coupling in $CoTiO_3$. Thermal expansion measurements in external magnetic fields of up to 15 T and magnetization measurements up to 60 T enabled constructing the full magnetic phase diagram of $CoTiO_3$ for the first time. An anisotropic magnetic saturation due to the $3D$-XY nature of the Co^{2+} was achieved at $B_{sat,ab} = 16.3(5)$ T and $B_{sat,c} = 46(1)$ T resulting in $g_{ab} = 5.7(2)$ and $g_c = 2.62(4)$. A strong anisotropic field effect was also observed in thermal expansion coefficients where the T_N shifted considerably more to lower temperatures for magnetic fields applied in ab-plane than along c axis. The sharp peaks in α coincided well with the anomalies from static susceptibility χ vs T data measured in various fields up to 15 T and hence enabled constructing the PM to AFM phase boundary. Additionally, a non-linear sickle-shaped behaviour corresponding to a spin-reorientation transition similar to $NiTiO_3$ was observed in magnetization M vs. B measurements. Following the temperature evolution of this transition by performing M vs. B scans at different $T < T_N$ resulted in a nearly horizontal AFM to spin-reoriented phase boundary.

In section 2.4, the magnetostrictive data of $CoTiO_3$ up to 15 T is presented and the analyzed in the framework of magnetic and structural domains. The uniaxial magnetostriction for $B||c$ is observed to vary as square of the applied external magnetic field i.e. $dL_c/L_c \propto B^2$. In contrast for $B||b$, pronounced increase in lattice parameters is observed at low-fields i.e., $B < 3$ T concomitant with the spin-reorientation region marked by non-linear magnetization. Above the spin-reorientation, a relatively smaller decrease in length changes is observed up to 15 T. Not

surprisingly, the thermodynamic quantities $\partial M/\partial B$ and magnetostriction coefficient λ, peak at different positions suggesting the presence of magnetic domains similar to $NiTiO_3$. Clear evidence of magnetic domains is observed in rotational magnetization measurements (M vs. θ) which exhibits a C_3 anisotropy corresponding to three domains and also in magnetostriction measurements which exhibit a hysteresis in the up and down magnetic field sweeps. Interestingly, the longitudinal and transverse magnetostriction measurements in the ab plane reveals an anisotropic deformation of lattice at 2 K, indicating the breaking of the $R\bar{3}$ symmetry. This is the first ever measurement in the ilmenite titanates family in which the breaking of structural symmetry by means of external magnetic field is reported. This indicates the strong coupling of spins and lattice degrees of freedom, which is a manifestation of significant spin-orbit coupling in $CoTiO_3$. Remarkably, we observed a complete reversal in the magnetostrictive behaviour dL_b/L_b in the entire field range on slightly increasing the applied uniaxial pressure (by the dilatometer) from 2.5 MPa to 3 MPa. This pressure dependent reversal effect persists until 100 K which is well above T_N indicating the the presence of structural domains (crystallographic twins) in $CoTiO_3$. Consequently, the magnetostrictive behaviour in $CoTiO_3$ results from the superposition of the response from both the structural twins and magnetic domains. Finally, we successfully describe our in-plane magnetostriction data in the multi-domain and the homogeneous state and low-field magnetization by means of magnetoelastic phenomenological theories similar to $NiTiO_3$.

Chapter 3

In chapter 3, high-pressure single-crystal growth and detailed characterization of $LaNiO_3$ is presented. In particular, in-homogeneity of stoichiometry was observed for $LaNiO_3$ single-crystals extracted at different longitudinal positions along the grown boule. In particular, the pieces extracted close to the floating-zone (≈ 2 mm) exhibit clear anomalies in the magnetic susceptibility and specific heat measurements at ≈ 150 K and some of them also exhibits an additional anomaly at 230 K. In contrast, the pieces which were extracted farther away from the zone exhibited no such anomalies. The oxygen vacancy characterization by means of TGA measurements indicated that the pieces extracted close to the floating-zone are significantly more oxygen-deficient than the pieces extracted farther away. As there exit several oxygen-deficient lanthanum nickelates $LaNiO_{3-x}$ which exhibit anomalies depending on x at around 150 K and 230 K respectively, hence our measurements explicitly indicate that the observed anomalies are extrinsic and that $LaNiO_3$ is a paramagnetic metal down to 2 K. Overall, our work solves the ambiguity concerning the magnetic ground state of bulk-$LaNiO_3$ ([92], [20]) using an uncommon way of characterization of different crystalline pieces extracted along the longitudinal direction of an optically floating-zone grown boule and in general emphasizes the

effects of oxygen-vacancy defects in nickelates.

4.2 Future work

This thesis tries to answer some of the fundamental questions pertaining to the magnetoelastic and magneto-electric coupling in the ilmenite titanates and the magnetic ground state of lanthanum nickelate. On the hindsight, the research in ilmenite titanates started in the 1950s and for lanthanum nickelates in the 1970s. However, as is always the case, the technological advances in experimentation, the improvement in our understanding as time passes and discovery of new theoretical principles leaves a plenty of room at the bottom. The effort in this thesis has been to add to the current understanding and in this process try and establish some general principles which has a wider applicability. Keeping this in mind, some of the most exciting directions to carry forward from this work is as the following.

- The preliminary single-crystal neutron diffraction study of the magnetic ground state of $CoTiO_3$ (see Appendix A) has surprisingly revealed that there is a possibility of a two-K magnetic ground state instead of the previously reported single-K magnetic structure [35]. This suggests a more complicated magnetic ground state than previously thought. Bearing in mind the recent interest in $CoTiO_3$ due to it's unconventional topological magnon-band properties [42, 45, 115], revisiting the magnetic ground state of $CoTiO_3$ is of utmost importance.

- The observance of linear magneto-electric coupling in $MnTiO_3$ in 2011 by Mufti *et al.* [58] as described earlier led to the resurgence of interest in ilmenites in the past decade. Following that, a flurry of research has been directed towards the understanding of the underlying responsible microscopic mechanism. Although a $p - d$ hybridization mechanism between the transition metal ion and the ligand has been proposed [63] behind the magnetism induced ferroelectricity, the recent X-ray [66] and neutron results [67] have indicated that the importance of spin-lattice coupling cannot be neglected. In this work, high-quality single-crystals of $MnTiO_3$ have been grown at an elevated pressure of 5 bar in argon atmosphere (see Appendix B), which as a matter of fact is the first time that an ilmenite single crystal has been grown at such pressures. These crystals have been grown for further investigation into the magnetoelastic coupling and specifically field-induced lattice changes (magnetostriction) measurements by means of high-resolution dilatometry. These measurements will shed more light into the spin-lattice coupling and the magnetoelectric mechanism in $MnTiO_3$.

- The mixed compound $Ni_xMn_{1-x}TiO_3$ exhibits an interesting concentration versus temperature phase diagram with a variety of magnetic phases which includes a spin-glass

phase (0.4<x<0.5) and the mixed phases reentered (0.3<x<0.4 and 0.5<x<0.55) from the antiferromagnetic ones [116]. Such a system with competing anisotropies and exchange frustrations can be an extremely interesting model system to study the spin-lattice coupling and the magnetoelectric coupling in different magnetic phases.
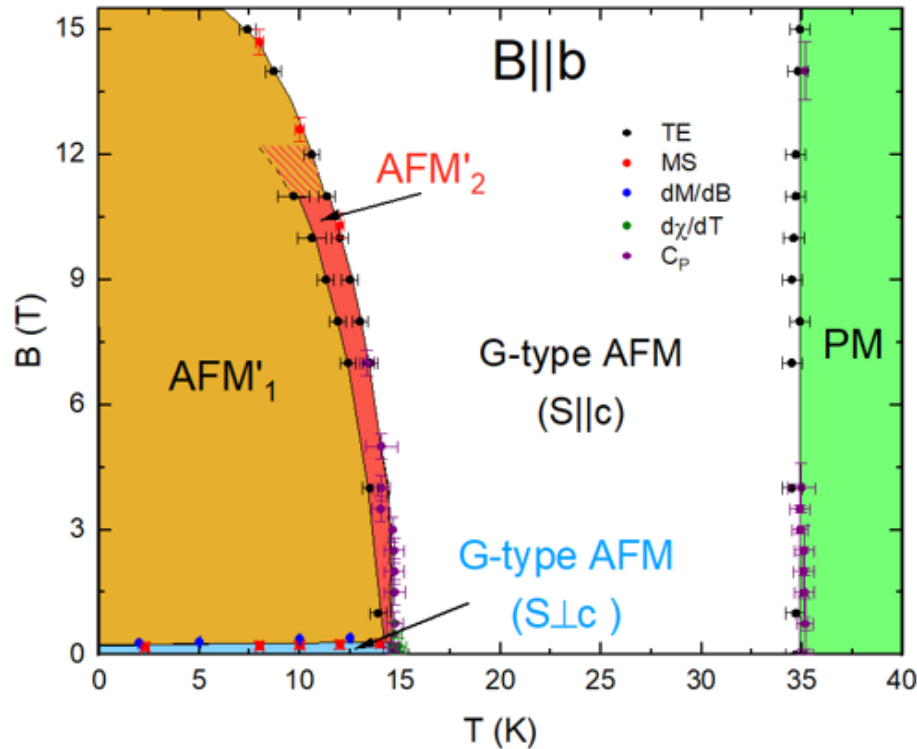
Figure 4.1. The magnetic phase diagram of $Ni_{0.25}Mn_{0.75}TiO_3$ for B$||b$ constructed using the thermal expansion (TE), magnetostriction (MS), specific heat (C_p) and magnetization measurements (M) in magnetic fields of up to 15 T. The TE and MS measurements were performed by Lukas Gries and the cp measurements were performed by Ahmed Elghandour of the Kirchhoff Institute for Physics, Heidelberg University.

In this work, taking cue from the details of single crystal growth of the parent compounds, i.e., $NiTiO_3$ and $MnTiO_3$, the $Ni_{0.25}Mn_{0.75}TiO_3$ single-crystals were grown successfully in 5 bar argon atmosphere (See Appendix C for details of growth and characterization). Furthermore, the magnetic phase diagram was constructed (Fig. 4.1) by magnetization, specific heat and high-resolution dilatometry measurements in magnetic fields up to 15 T. As expected, the doped compound exhibits a very interesting phase diagram where for $T < 35$ K a G-type AFM order, which is similar to the ME active $MnTiO_3$ is realized. Interesting, a spin-reorientation transition is observed below 15 K where another G-type order with spins lying in the ab plane is realized. This type of order is not realized for any of the parent ilmenites (see Fig. 1.3) and is only accessible for the mixed compounds. Moreover, application of magnetic fields resulted in two additional field-induced phase

AFM'$_1$ and AFM'$_2$, where the later is still unreported. Investigating the magnetoelectric and magnetoelastic properties and additionally the magnetic structure of the field induced phases by means of neutron diffraction would be extremely interesting in the doped titanates.

- Following the work on the longitudinal characterization of oxygen in-homogeneity in the LaNiO$_3$ grown boule (see chapter 3) in 2019, a radial characterization was also performed for LaNiO$_3$ single crystals by Zheng *et al.* in 2020 [104]. They observed that the samples extracted from the peripheral region are more stoichiometric than those extracted from the central region. Both of the works in general emphasis on the kind of inhomogeneities that one needs to mind while performing an high-pressure optical floating zone growth. This is extremely important in the context of nickelate research which has attracted intense attention in the past decades due to it's interesting properties (ex. CDW+SDW order in La$_4$Ni$_3$O$_{10}$ [117] - See appendix D) and especially since 2019 due to the discovery of superconductivity in the thin films of Nd$_{0.8}$Sr$_{0.2}$NiO$_2$ [118]. The efforts are now focused on observing the superconductivity in the bulk single-crystals where a high-pressure optical floating-zone growth is the preferred method of choice [119].

Appendix A

Single-crystal neutron diffraction of $CoTiO_3$
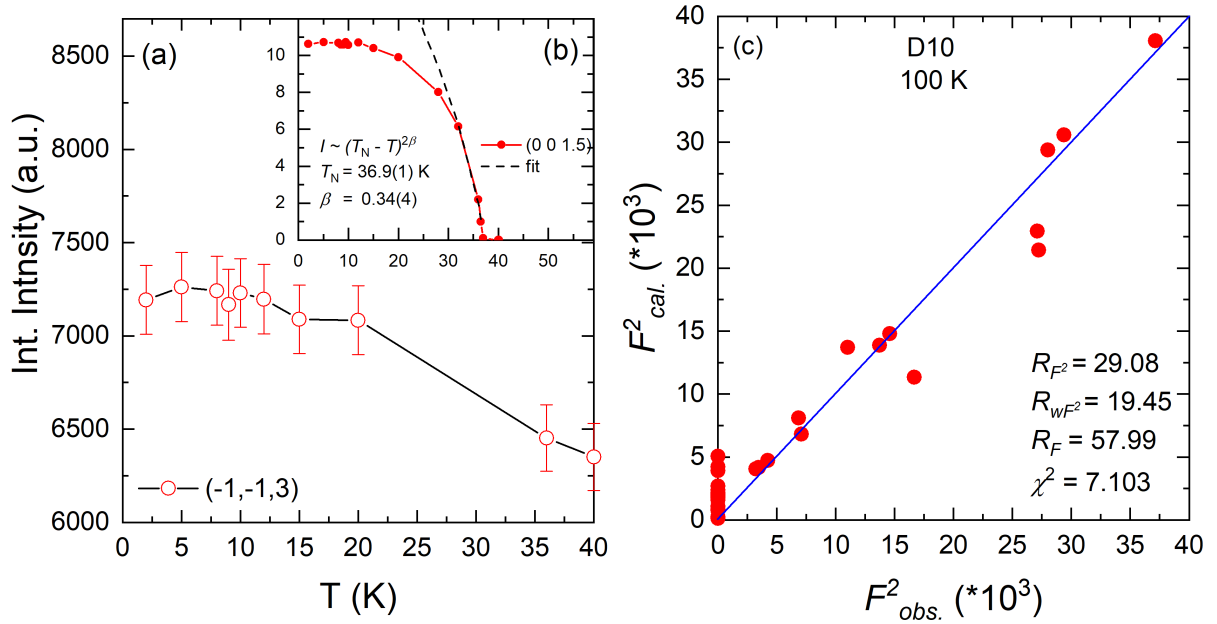
Figure A.1. Single-crystal neutron diffraction of $CoTiO_3$ has been performed at the d10 instrument in ILL, Grenoble. (a) Integrated intensity I vs. T of the nuclear Bragg peak (-1,-1,3) for $CoTiO_3$. The inset shows the I vs. T of the magnetic (0,0,1.5) Bragg peak. The dashed black curve shows a fit to the data. (b) Observed vs. calculated structure factors of the nuclear Bragg reflections at 100 K for $CoTiO_3$.

Single-crystal neutron diffraction experiments on a $CoTiO_3$ single-crystal of size $2 \times 1.85 \times 1$ mm^3 were performed at $B = 0$ T on the D10 instrument at the Institut-Laue Langevin. An incident neutron beam of wavelength of 2.36 Å using the pyrolytic graphite monochromator was employed. In the time-span of 1.5 days, 120 nuclear reflections (37 independent) corresponding to the $R\bar{3}$ space group were obtained at 100 K and 12 K respectively. In total, 334 satellite

magnetic reflections (assuming $K = (0,0,0.5)$ in $P-1$ space group) were obtained at 2 K. The temperature evolution of several nuclear and magnetic peaks were followed in the range 2 K to 40 K. Integrated intensity I vs. T of a representative magnetic Bragg peak (0,0,1.5) is shown in the inset to Fig. A.1(a). The power-law fit in the critical region reveals T_N = 36.9(1) K, in-line with the macroscopic measurements. The position of the new satellite reflections suggests a propagation vector of $K = (0,0,3/2)$ in-line with the polycrystalline neutron data [35, 45]. However, several nuclear peaks exhibit a small but visible increase in intensity at 12 K (below T_N) as compared to 100 K. As shown in Fig. A.1 (a), a clear increase in the integrated intensity of the nuclear Bragg peak (-1,-1,3) is observed below T_N. This observation suggests an additional magnetic moment propagating with $K = (0,0,0)$ indicating a more complicated magnetic ground state of $CoTiO_3$ than previously reported [35, 45]. The nuclear structure at 100 K could not be refined satisfactorily owing to the current limited data set and the weak intensity structure factor being wrongly calculated under the given model as shown in Fig. A.1 (b). Tentatively this is ascribed to multiple scattering effects. Using a smaller single-crystal piece and a larger incident neutron beam wavelength can prove beneficial against multiple scattering. Obtaining a reliable and extensive data set is essential in completely solving the magnetic ground state of $CoTiO_3$.

Appendix B

Single-crystal growth and magnetization of MnTiO$_3$

Table B.1. The stable parameters employed during the optical floating zone growths of MnTiO$_3$ single-crystal. The phase analysis is performed using the Rietveld refinements of the room temperature powder XRD data of pulverized MnTiO$_3$ single-crystals and the magnetization (M vs. B) data.

	I	II	III	IV
Atmosphere	O$_2$	O$_2$	Ar	Ar
Flow rate	0.2 l/min	0.2 l/min	0.5 l/min	0.5 l/min
Pressure	Ambient	10 bar	5 bar	15 bar
Feeding rate	3 mm/h	3-4 mm/h	5 mm/h	3 mm/h
Growth rate	3 mm/h	3-4 mm/h	5 mm/h	3 mm/h
rotation rate	20 rpm	20 rpm	10 rpm	20 rpm
Growth	stable	unstable-zone	stable	stable
Secondary phases (appr.)	TiO$_2$ (5%) + Mn$_3$O$_4$ (0.06%)	-	TiO$_2$(1%)	Mn$_3$O$_4$ (0.1%)

All the MnTiO$_3$ single-crystal growths were performed using the Sci-Dre HKZ furnace [98]. The first growth which was performed in the O$_2$ flow and ambient pressure resulted in excessive evaporation with red colour deposits on the inner protection glass tube. Although a phase analysis of the deposit was not performed, it is ascribed to a manganese oxide deposition. Consequently the growths were performed under elevated pressures to reduce evaporation and obtain stoichiometric single-crystals. In particular, a growth experiment performed under 10 bar O$_2$ pressure proved futile due to excessive bubbling and breaking of the floating zone. Hence argon atmosphere was chosen and the growth could be stabilized at elevated pressures of 5 bar

and 15 bar respectively. Although some deposits were still observed on the inner glass tube post-growth under 5 bar Ar flow but were significantly reduced as compared to the ambient pressure growth. In fact, negligible deposition was seen for the 15 bar growth. Large cm-sized single-crystals with high-quality Laue patterns were obtained for growth numbers I, III and IV as shown in Tab. B.1 respectively. In this work, the high-quality $MnTiO_3$ single-crystals were grown for the first time at such elevated pressures. Furthermore, analysis of the phase by means of Rietveld refinements and magnetization data (for details see below) indicate that the growth performed under 5 bar Ar pressure (col. III of Tab. B.1) resulted in the best quality single crystals.
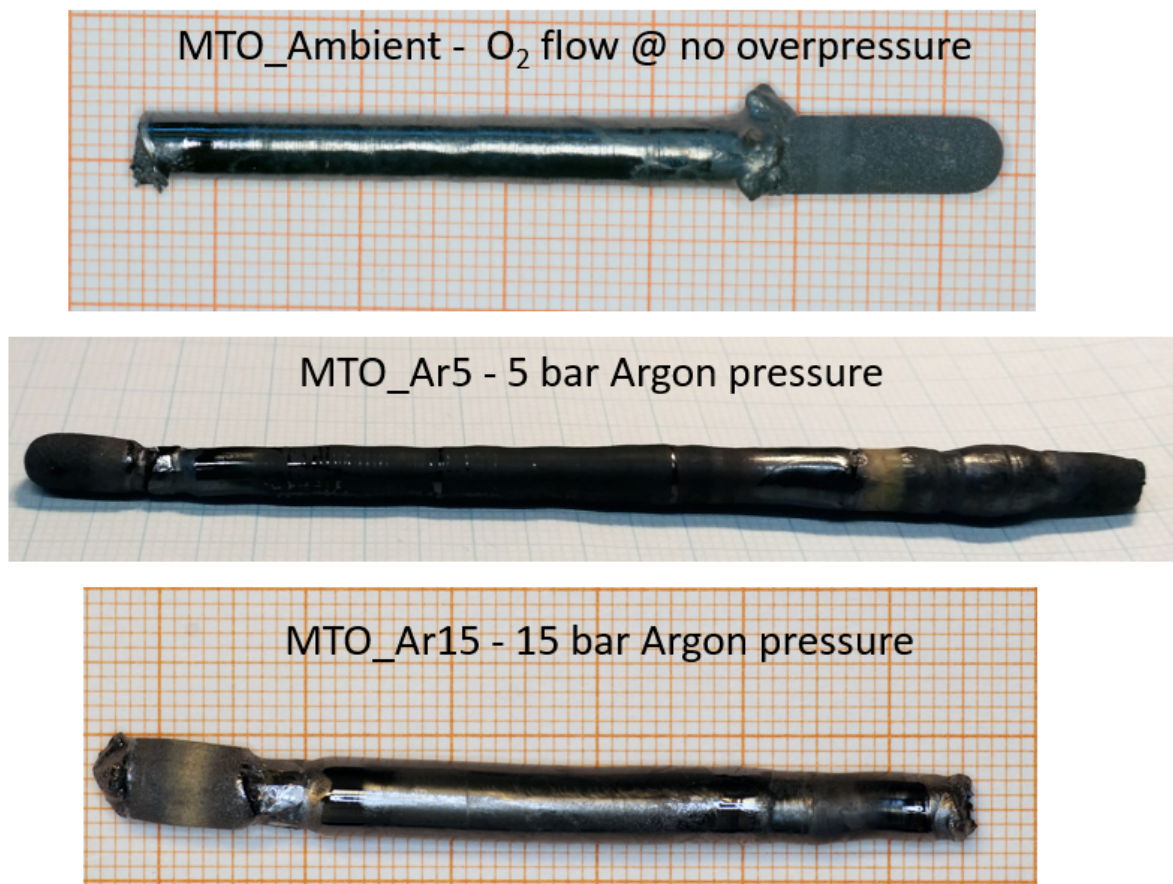
Figure B.1. Pictures showing the optical floating-zone grown boules of $MnTiO_3$ at different atmospheres and pressure. All the boules have been grown in the Sci-Dre HKZ [98] furnace.
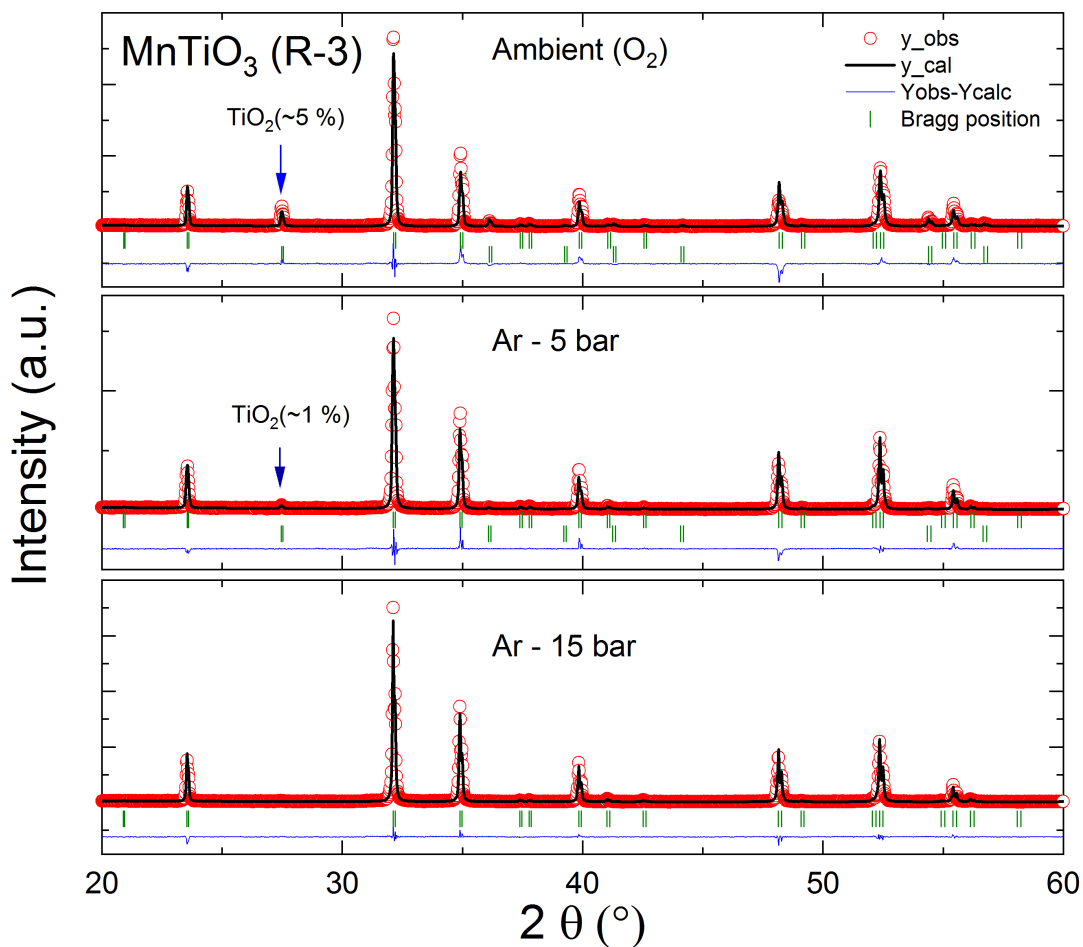
Figure B.2. Two-phase (ilmenite and rutile) Rietveld refinement fits to the room-temperature XRD data of pulverized $MnTiO_3$ single-crystals grown at different atmospheres and pressures. The observed diffraction (y-obs) pattern is shown in red, the calculated pattern (y-cal) in black and the difference between the observed and the calculated pattern is shown in blue. The upper vertical ticks in green denote the allowed Bragg positions of the ilmenite-phase ($R\bar{3}$) and the lower ticks denote the Bragg positions of the rutile TiO_2 phase.

Table B.2. The lattice parameters and the goodness of fit (R-factors) parameters obtained from the Rietveld refinement fits to the room-temperature XRD data (see Fig. B.2).

Growth	Ambient	5 bar Ar	15 bar Ar
Space group	$R\bar{3}$	$R\bar{3}$	$R\bar{3}$
$a = b$ (Å)	5.1358(1)	5.1383(1)	5.1395(1)
c (Å)	14.2778(4)	14.2796(2)	14.2824(2)
R_{Bragg}	14.58	8.20	5.24
R_{wp}	24.6	18.2	15.7
R_{exp}	11.85	11.26	10.98
χ^2	4.31	2.61	2.14

Table B.3. Crystal data and structure refinement from single-crystal X-ray diffraction performed at 100 K on the $MnTiO_3$ single crystals grown under 5 bar argon pressure. Note: The single-crystal X-ray diffraction experiments were performed by Prof. Hubert Wadepohl of the Inorganic-Chemical institute of Heidelberg University.

Empirical formula	$MnTiO_3$
Formula weight	150.33
T(K)	100(1)
wavelength	Mo K_α, 0.71073 Å
Crystal system, space group	trigonal, $R\bar{3}$ (*IT* Nr. 148)
Unit cell dimensions	
a (Å)	5.13393(6) ; $\alpha = 90°$
c (Å)	14.26879(15) ; $\beta = 90°, \gamma = 90°$
V (Å^3)	325.700(8)
Z, Calculated density (g cm^{-3})	6, 4.598
Absorption coefficient for Mo-Kα (mm^{-1})	9.169
Crystal size (mm^3)	$0.20 \cdot 0.11 \cdot 0.02$ (plate)
Transmission factors: max, min	1.000, 0.365
Theta range for data collection	4.3° to 60.2°
Reflections collected / independent	29329 / 1107 [R_{int} = 0.0551]
observed reflections [$I > 2\sigma(I)$]	1078
data/restraints/parameters	1107/0/17
Goodness-of-fit on F^2	1.206
Final R indices[$F > 4\sigma(F_0)$] $R(F), wR(F^2)$	0.0149, 0.0364
R indices (all data) $R(F), wR(F^2)$	0.0155, 0.0367
extinction coefficient	0.0029(9)
X-ray source	microfocus X-Ray tub
Diffractometer	Agilent SuperNova, Dual, Cu at home/near, Eos

Table B.4. Fractional atomic coordinates, Wyckoff positions, site occupation and equivalent isotropic displacement parameters (Å^2) of $MnTiO_3$ as obtained from the refinement of single-crystal XRD measurements at 100 K. sof denotes the fraction of atom type present at the site after application of crystallographic symmetry; ^{a} U_{eq} is defined as one third of the trace of the orthogonalized U_{ij} tensor. The anisotropic displacement factor exponent takes the form: $-2\pi^2[h^2a^{*2}U_{11} + ... + 2hka^*b^*U_{12}]$.

Atom	Site	x	y	z	sof	$U_{eq}{}^a$
Mn	6c	0.33333	0.666667	0.52623(2)	1	0.00402(2)
Ti	6c	1	1	0.64762(2)	1	0.00339(2)
O	18f	0.69740(7)	0.65222(7)	0.58931(2)	1	0.00475(4)
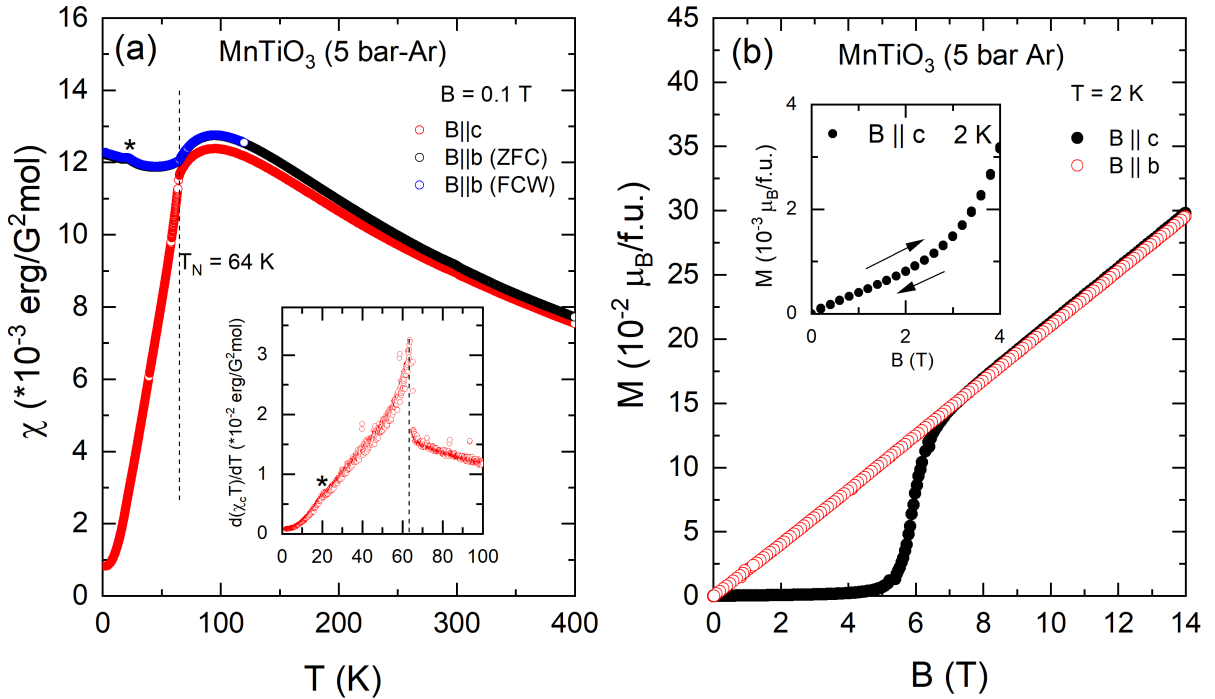
Figure B.3. (a) The static magnetic susceptibility $\chi = M/B$ vs. T of $MnTiO_3$ single-crystal grown at 5 bar Ar pressure for magnetic-field $B = 0.1$ T, applied along principle crystallographic directions. The inset to (a) shows the Fisher's specific heat $\partial\chi_cT/\partial T$ vs. T [120]. The vertical dashed lines indicate T_N. The broad hump above T_N is due to the crossover from 3D to quasi-2D behaviour [53, 54, 121]. The tiny anomaly indicated by the black star at $T \approx 20$ K is tentatively ascribed to small amount of δ-MnO_2 (exhibits PM to AFM transition below 20 K) [122] impurity phase. (b) M vs. B data as measured using the VSM-option in the PPMS at $T = 2$ K. The spin-flop transition is observed at 6 T for $B||c$. The inset to (b) shows the up and down sweeps as measured in the MPMS.
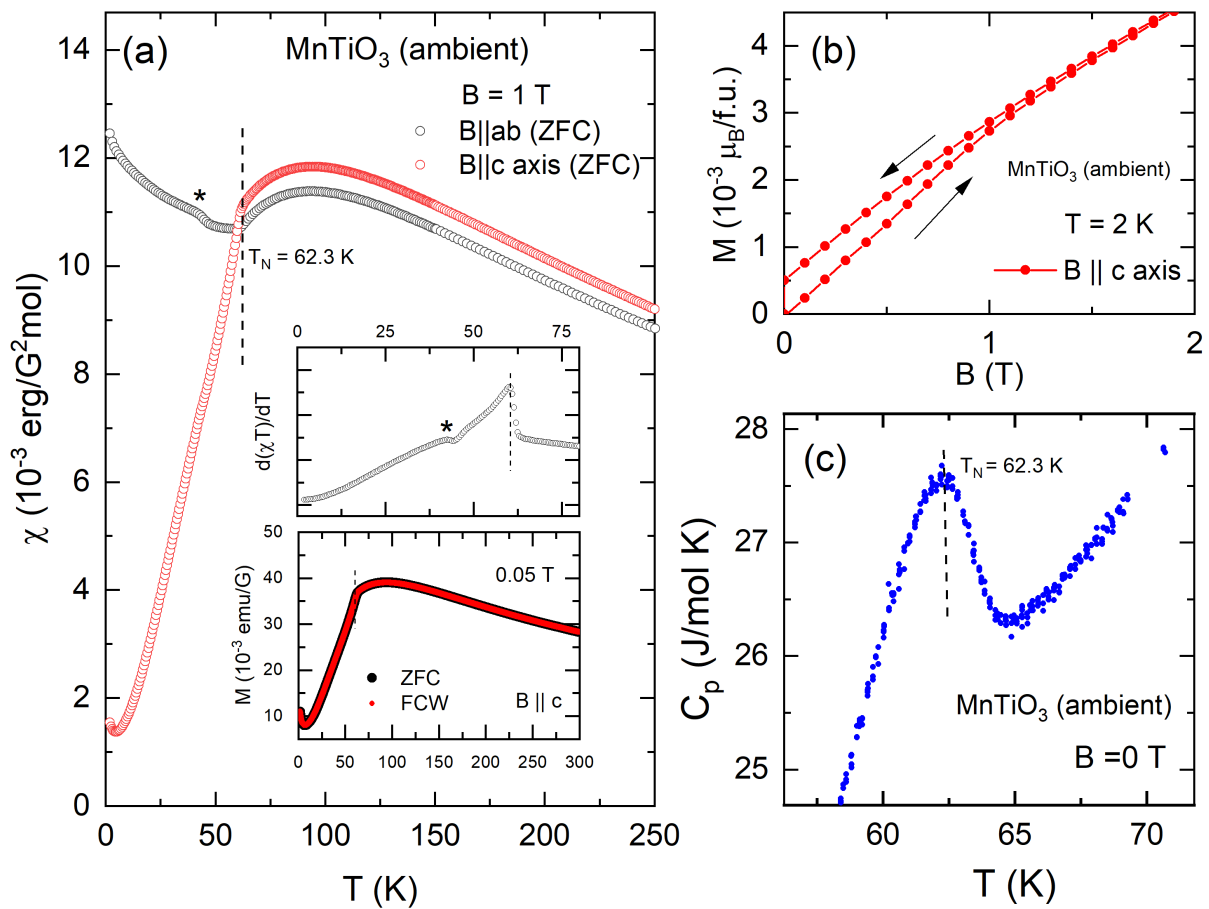
Figure B.4. (a) The static magnetic susceptibility $\chi = M/B$ vs. T of a $MnTiO_3$ single-crystal grown at ambient pressure in O_2 flow, for magnetic-field $B = 0.05$ T applied along the principle crystallographic directions (DC measurement). The top right inset to (a) shows Fisher's specific heat [120]. The vertical dashed lines indicate T_N. The tiny anomaly marked by the black star is ascribed to Mn_3O_4 impurity which is a ferrimagnet with $T_C \approx 43$ K [123]. The bottom right right inset to (a) shows the reversibility in the magnetization measured in the entire temperature range with two different protocols - FCW and ZFC (VSM-Squid measurement). (b) M vs. B data for $B||c$ at $T = 2$ K. An unexpected small hysteresis is observed due to the presence of Mn_3O_4 impurity. The impurity phase is estimated to be about 0.06 % from remanent magnetization value [123]. (c) The zero-field specific-heat data showing an anomaly corresponding to long-range antiferromagnetic transition at T_N. The anomaly is rather broad indicating the poor quality of the grown single-crystal. Note: The specific heat measurement was performed by Dr. Mahmoud M. Abdel-Hafiez at Goethe University, Frankfurt, Germany.
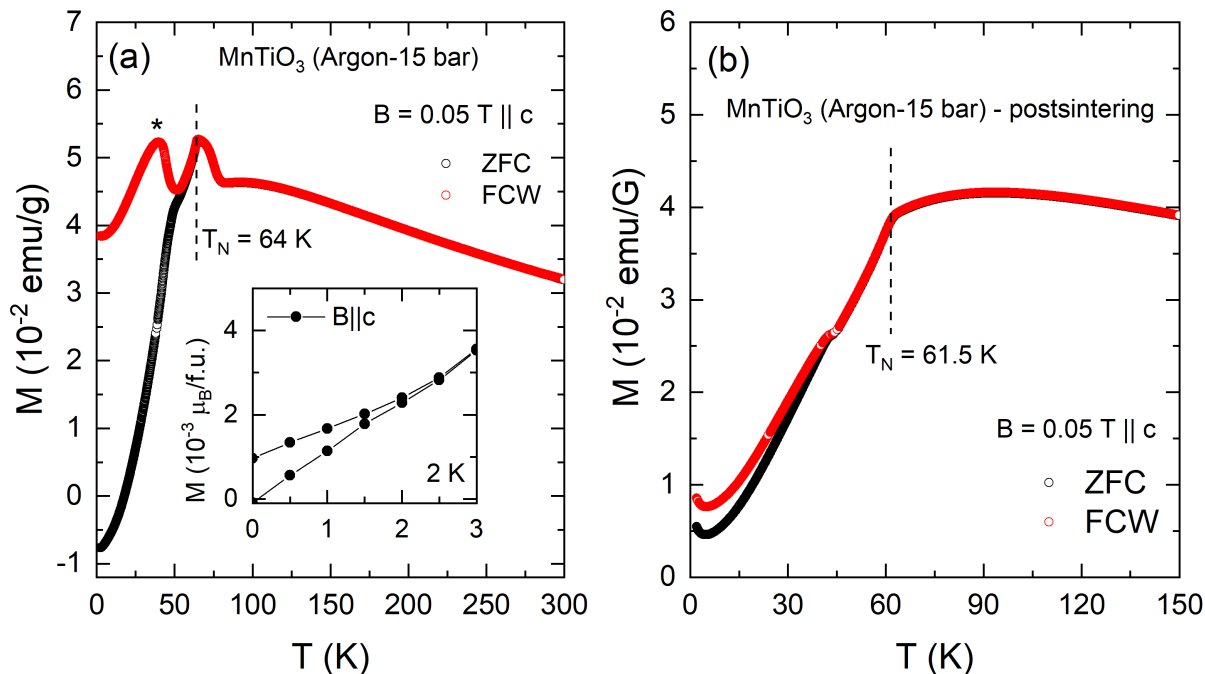
Figure B.5. (a) The static magnetic susceptibility $\chi = M/B$ vs. T of MnTiO$_3$ single-crystal grown at 15 bar pressure in Argon flow, for magnetic-field $B = 0.05$ T applied along the principle crystallographic directions (VSM-Squid measurement). There exists irreversibility in the ZFC and FCW measurements below 50 K which is ascribed to some impurity magnetic nano-regions precipitated during the crystal-growth. The peak in FCW curve as marked by black star is at ≈ 43 K and is possibly arising due to Mn$_3$O$_4$ impurity. The inset to (a) shows the M vs. B data at $T = 2$ K. The observed hysteresis is assumed to be only due to Mn$_3$O$_4$ impurity and amounts to approx. 0.1 % calculated using the remanent magnetization value. (b) The χ vs. T data of the same MnTiO$_3$ single-crystal as in (a) after sintering in air at 800°C for 5 h. The irreversibility between ZFC and FCW data still features below 43 K but is significantly deceased as compared to (a). Note that such features below T_N have been observed in the literature but have not been discussed in detail [58, 66, 121]. The fact that these features appear at different temperatures depending on the growth conditions of MnTiO$_3$ single-crystal, indicate the extrinsic nature of them. Also some variations in the Néel temperature is observed in the single-crystals grown under different conditions indicating that some disorder maybe present in the system.

Appendix C

Single-crystal growth and characterization of $Ni_{0.25}Mn_{0.75}TiO_3$
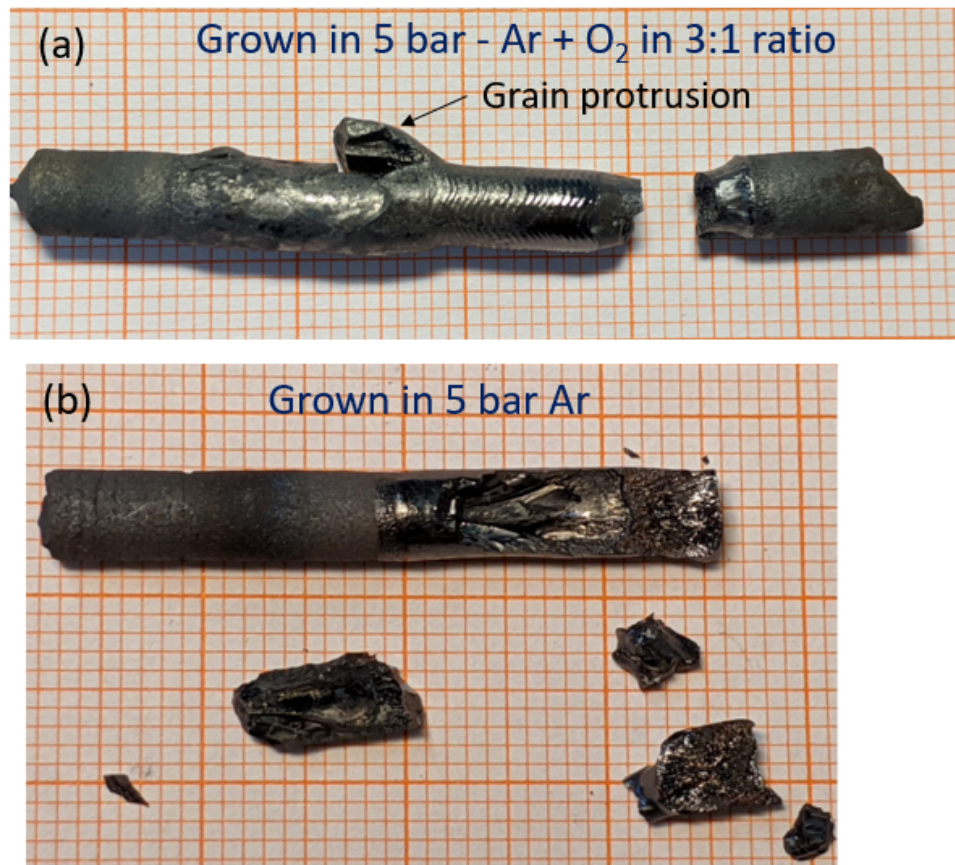
Figure C.1. $Ni_{0.25}Mn_{0.75}TiO_3$ boules as-grown under (a) 5 bar - Ar (0.75 l/min) + O_2 (0.25 l/min) atmosphere and (b) 5 bar Ar (0.3 l/min) atmosphere. The grain protrusion as indicated in (a) affects the zone stability and is one of the major challenges faced while growing $Ni_{0.25}Mn_{0.75}TiO_3$. The boule in (b) yielded the best quality single-crystals.

Precursors for the crystal growth were prepared via the standard solid state reaction. NiO

was sintered overnight at 1000°C and MnO_2 and TiO_2 were sintered at 120°C for three days to remove absorbed water. Stoichiometric amounts of the above precursors were thoroughly ground in an agate mortar until a homogeneous mixture is obtained. The mixture was then sintered at 1000°C for 30 hours. The obtained powder was reground and densely packed in a rubber tube and isostatically pressed at 50 MPa to obtain cylindrical shaped rods of length 4-6 cm and 5 mm in diameter. The obtained rods were further sintered at 1200°C for 24 h to obtain feed and seed rods for the crystal growth.

The crystal growth was performed in the high-pressure optical floating zone furnace (HKZ, SCI-Dre) using a 3.5 kW Xe arc lamp. An elevated pressure of 5 bar was employed to circumvent the manganese evaporation issue (See Appendix B). Several crystal growth experiments were performed in a mixed 3:1 - Ar (0.75 l/min) : O_2 (0.25 l/min) atmosphere using differing growth rates of 1-2 mm/h with counter-rotating rods at 10-25 rpm. Although the growths in the mixed atmosphere were relatively stable, the obtained boules were largely polycrystalline in nature and no macroscopic single-crystalline grain could be extracted. Consequently, only argon with a flow rate of 0.3 l/min and 5 bar pressure was employed. The growth experiment was carried out with 16.5% of shutter opening and the growth rate was maintained at 2 mm/h. The rods were counter rotated at 15 rpm. The obtained boule as shown in fig. C.1(b) resulted in a very good Laue pattern and a macroscopic single-crystalline piece extracted from the central region was oriented along $b \times (2, -1, 0) \times c$ ($2 \times 3 \times 1$ mm^3). One of the major challenges during the growth experiments was that of grain protrusion as indicated in Fig. C.1(a). During the grain competition process (usually at the beginning of crystal growth) it was observed that a portion of seed cracks and separates, hampering the floating-zone stability. Varying the parameters such a changing the rotation speeds, power and growth rates couldn't circumvent the issue. It is possible that the cracking takes place at the grain boundaries due to the high thermal stress along the rods. In particular, the individual pieces which broke off from the boule grown in Ar atmosphere (as seen in Fig. C.1) also exhibited good crystallinity in Laue diffraction experiments.

The phase analysis by means of room-temperature powder XRD data indicate that the pieces extracted from the boule grown under 5 bar Ar pressure are phase pure, whereas the pieces extracted from the boules grown in mixed 3:1 - Ar+O_2 atmosphere show impurity peaks corresponding to the rutile phase. Rigorous edx measurements were performed by Lennart Singer of the Kirchhoff Institute for Physics, Heidelberg University on the oriented single crystalline piece (grown under 5 bar Ar). EDX analysis indicates an average proportion of Ni:Mn of 0.235(5):0.765(5) and (Ni+Mn):Ti of $\approx$ 1:1. The refinements of the single crystal XRD data at 100 K using the neutral atomic scattering factors (f_{at}) resulted in the Ni:Mn proportion of 0.27:0.73 and using the preferred ionic scattering factors (Tab. C.2) resulted in Ni:Mn of 0.21:0.79. Note that the EDX measurements are more reliable in estimating the elemental com-
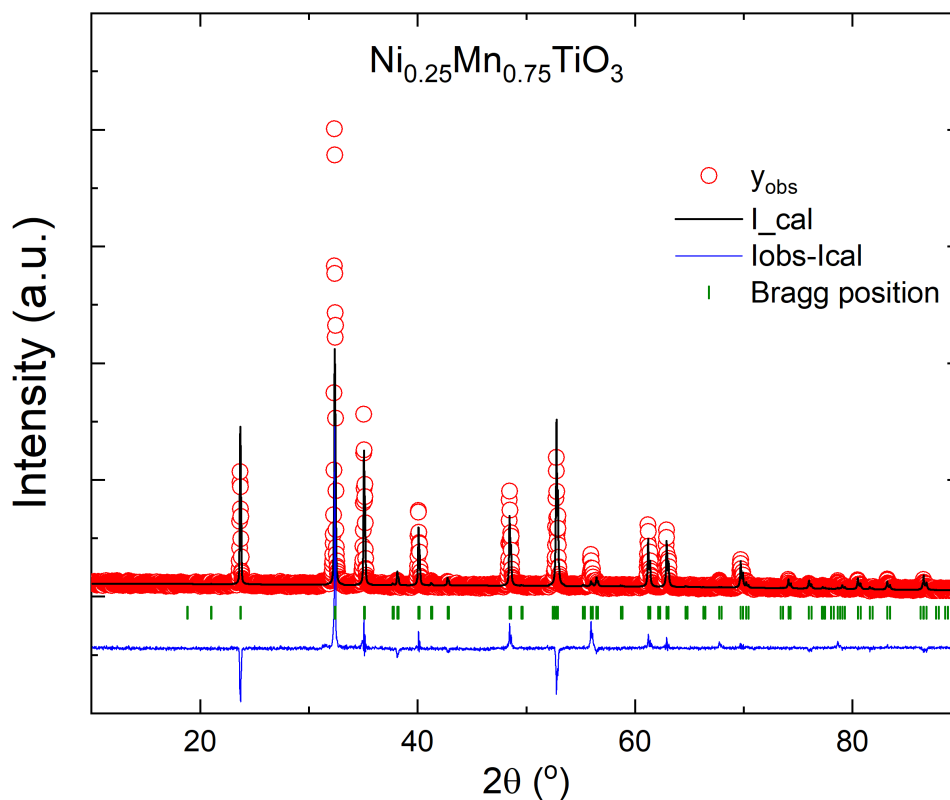
Figure C.2. The Rietveld refinement fit to the room-temperature XRD data of pulverized $Ni_{0.25}Mn_{0.75}TiO_3$ single-crystal grown at 5 bar Argon atmosphere. All the observed Bragg reflections match with the expected $R\bar{3}$ space group (green ticks) indicating phase purity. Full occupancy of all the cations were assumed for the fit. Poor estimation of the fit to the highest intensity peak ($2\theta \approx 35^0$) could be due to the variation from the assumed full occupation or due to in-homogeneous grinding prior to the XRD experiment.

position as compared to intensity refinements of the diffraction data which depends on a various other parameters such as absorption and transmission factors etc.

Table C.1. Fractional atomic coordinates, Wyckoff positions, site occupation and equivalent isotropic displacement parameters (Å^2) of $Ni_{0.25}Mn_{0.75}TiO_3$ as obtained from refinement of single-crystal XRD measurements at 100 K. sof denotes the fraction of atom type present at the site after application of crystallographic symmetry; [a] U_{eq} is defined as one third of the trace of the orthogonalized U_{ij} tensor. The anisotropic displacement factor exponent takes the form: $-2\pi^2[h^2a^{*2}U_{11} + ... + 2hka^*b^*U_{12}]$.

Atom	Site	x	y	z	sof	U_{eq}[a]
Ni	6c	0.33333	0.666667	0.52391(2)	0.214(6)	0.00388(2)
Mn	6c	0.33333	0.666667	0.52391(2)	0.786(6)	0.00388(2)
Ti	6c	1	1	0.64673(2)	1	0.00303(2)
O	18f	0.69388(6)	0.65114(6)	0.58857(2)	1	0.00463(3)

Table C.2. Crystal data and structure refinement (using ionic atom scattering factors F_{at}) from single-crystal X-ray diffraction performed at 100 K on the $Ni_{0.25}Mn_{0.75}TiO_3$ single crystals grown at 5 bar argon pressure. Note: The single-crystal X-ray diffraction experiments were performed by Prof. Hubert Wadepohl of the Inorganic-Chemical institute of Heidelberg University.

Empirical formula	$Ni_{0.21}Mn_{0.79}TiO_3$
Formula weight	151.14
T(K)	100(1)
wavelength	Mo K_α, 0.71073 Å
Crystal system, space group	trigonal, $R\bar{3}$ (*IT* Nr. 148)
Unit cell dimensions	
a (Å)	5.10799(4) ; $\alpha = 90°$
c (Å)	14.12863(11) ; $\beta = 90°, \gamma = 90°$
V (Å^3)	319.250(5)
Z, Calculated density (g cm^{-3})	6, 4.717
Absorption coefficient for Mo-Kα (mm^{-1})	9.981
Crystal size (mm^3)	$0.21 \cdot 0.15 \cdot 0.08$ (irregular)
Transmission factors: max, min	1.000, 0.591
Theta range for data collection	4.8° to 59.3°
Reflections collected / independent	14885 / 1065 [R$_{int}$ = 0.023]
observed reflections [$I > 2\sigma(I)$]	1052
data/restraints/parameters	1065/0/18
Goodness-of-fit on F^2	1.127
Final R indices[$F > 4\sigma(F_0)$] $R(F), wR(F^2)$	0.0113, 0.0272
R indices (all data) $R(F), wR(F^2)$	0.0115, 0.0273
extinction coefficient	0.0039(4)
X-ray source	microfocus X-Ray tub
Diffractometer	Agilent SuperNova, Dual, Cu at home/near, Eos

Appendix D

Single-crystal growth of La$_4$Ni$_3$O$_{10}$

Figure D.1. Picture showing the optical floating-zone grown La$_4$Ni$_3$O$_{10}$ boule at 20 bar oxygen pressure.

The Ruddlesden-Popper (n=3) La$_4$Ni$_3$O$_{10}$ single crystal was grown using the high-pressure optical floating zone furnace at an elevated oxygen pressure of 20 bar (flow rate - 0.1 l/min). Employing high-O$_2$ pressures is typical for rare-earth nickelates growth [20, 21] and in this case is crucial to stabilize the optimal phase containing a high valence state of Ni (nominal +2.67). The growth experiment in this work has been performed following the work of Zhang *et al.* [117], where they report the single crystal growth of La$_4$Ni$_3$O$_{10}$ for the first time and show that 20 bar O$_2$ pressure is necessary to obtain phase purity. In this work, a 3.5 kW Xe-lamp was used to melt the feed rod ($\approx$ 6 cm long) and the seed rod ($\approx$ 2.5 cm long) to form a molten-zone. As the growth progressed, the molten-zone exhibited a tendency to thin. This was tackled by using a higher feeding rate of 6 mm/h as compared to the growth rate of 4 mm/h, hence resulting in a thick ($\approx$ 7 mm in diameter) as-grown boule (see Fig. D.1). The zone was stabilized at 34.8 % of the shutter opening and the counter-rotation of feed and seed rods at 12.5 rpm ensured good mixing. Towards the end, the growth process was stopped by quickly turning down the power and quenching the zone.

Previously, Zhang *et al.* [117] reported that La$_4$Ni$_3$O$_{10}$ crystallizes predominately in the $P2_1/a$ space group. An additional meta-stable phase with $Bmab$ space group could also be

present due to the rapid post-growth cooling which is typical of floating-zone process. It was shown that depending on the lattice symmetry, $La_4Ni_3O_{10}$ exhibits a metal to metal transition at $\approx$ 146 K in $Bmab$ phase and at 138.6 K in $P2_1/a$ phase [117]. In particular, it was also found that on post-annealing at 1000° under 20 bar O_2 pressure, only a single transition at 138 K remained in physical properties measurements indicating that the $P2_1/a$ phase is more stable [117]. In this work, about 1 cm (from the quenched zone) of the grown boule was cut and two samples labelled as LNO4310-2.1 (extracted $\approx$ 2 mm from zone) and LNO4310-2.2 (extracted farther away from zone)) were extracted from this piece. The remaining as-grown boule was mounted at the seed position of the HKZ-furnace and was subsequently annealed under 20 bar O_2 pressure with 10% shutter opening. The temperature reading of the pyrometer was maintained below 1000°C and the rod was annealed for about 2 hours. Finally, the process was stopped by quickly removing the rod out of focus. The piece extracted post-annealing is labelled as LNO4310-2.3.

Preliminary phase analysis by means of X-ray diffraction data of the pulverized post-growth pieces (extracted from the boule shown in Fig. D.1) exhibited predominately $La_4Ni_3O_{10}$ phase. While tiny impurities of the (n = 2) Ruddelsden-Popper phase $La_3Ni_2O_7$ was found in the pieces extracted from the as-grown boule, i.e., LNO4310-2.1 and LNO4310-2.2, the piece extracted post-annealing i.e., LNO4310-2.3 exhibited phase purity. The lab-based XRD data proved inadequate in distinguishing the minor structural differences between the $Bmab$ or $P2_1/a$ space groups as indicated by other reports [117, 124]. The back-scattered Laue experiment surprisingly showed good quality images with sharp spots only for the central regions of the boule and bad quality for peripheral regions. This indicates that the crystallinity varies in the radial direction with better quality limited to the central region. With careful Laue analysis, the bad quality peripheral regions were cut out and a high-quality single-crystalline piece was obtained from the central region (in this work only for LNO4310-2.1). In fact, the phase purity as indicated by the powder XRD data exhibited no radial variation.
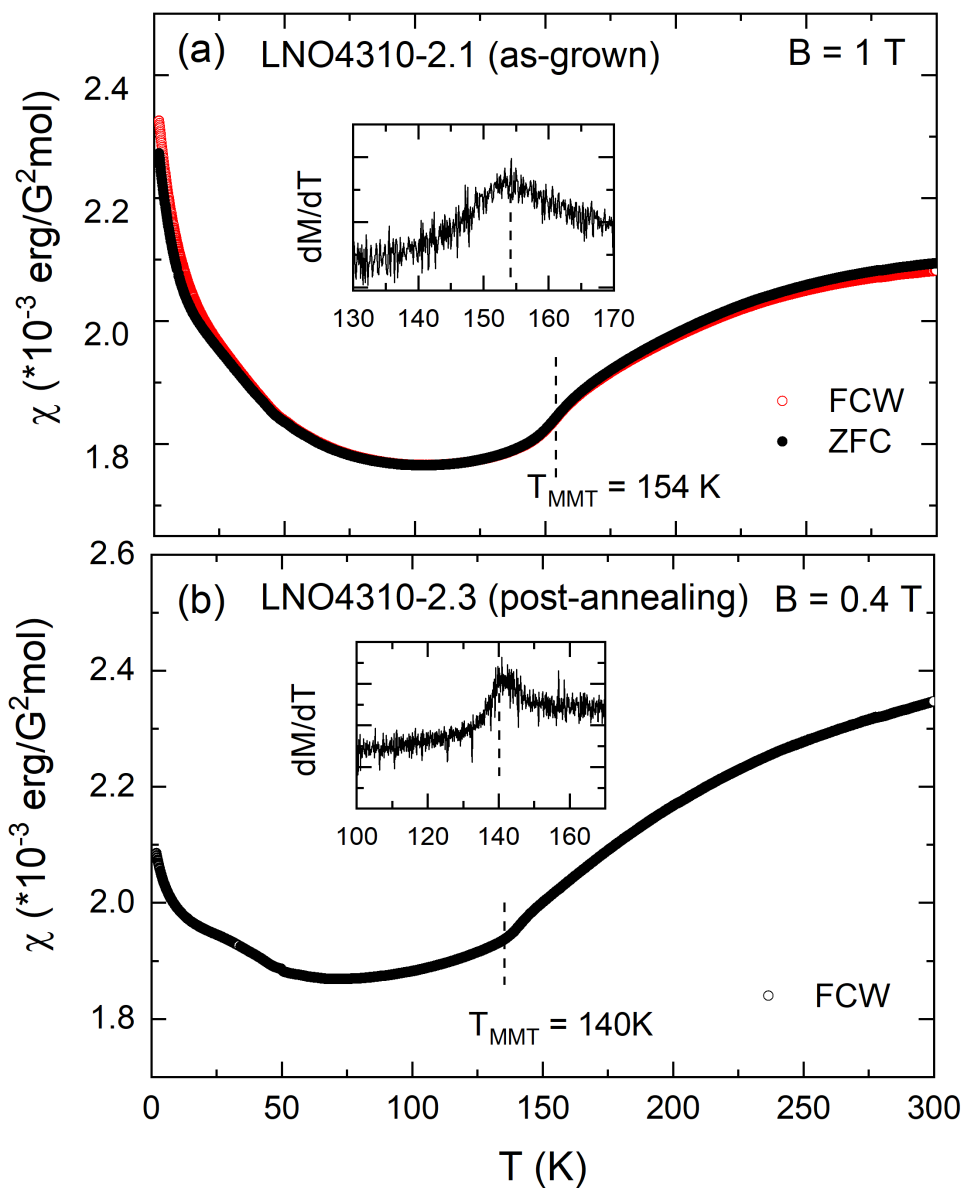
Figure D.2. (a) The static magnetic susceptibility $\chi = M/B$ vs. T of a non-oriented $La_4Ni_3O_{10}$ single-crystal piece extracted from the central region of the as-grown boule LNO4310-2.1 as shown in Fig. D.1. The metal-to-metal transition (T_{MMT}) is at 154 K indicating that the sample is predominately in $Bmab$ phase [117]. (b) The χ vs. T data of the single crystal piece - LNO4310-2.3 extracted from the central region of the as-grown boule annealed at 20 bar O_2 pressure. Note that the (T_{MMT}) is at a lower temperature of 140 K indicating that the post-annealed sample is predominately in $P2_1/a$ phase.

Bibliography

[1] C. N. R. Rao. Transition metal oxides. *Annu. Rev. Phys. Chem.*, 40:291–326, 1989.

[2] A. Alexandradinata and N.P. Armitage et. al. The future of strongly correlated electron problem. *arXiv2010.00584*, 2020.

[3] Y. Tokura. Correlated-electron physics in transition-metal oxides. *Phys. Today*, 56:7, 2003.

[4] Y. Tokura and N. Nagaosa. Orbital physics in transition-metal oxides. *Science*, 288(5465):462–468, 2000.

[5] J. G. Bednorz and K. A. Müller. Possible hightc superconductivity in the Ba−La−Cu−O system. *Zeitschrift für Physik B Condensed Matter*, 64:189–193, 1986.

[6] B. Keimer and J.E. Moore. The physics of quantum materials. *Nat. phys.*, 13:1045–1055, 2017.

[7] M. Angst. *Strongly correlated electrons, Chapter 12 in Lectures of the JCNS Laboratory Course*. Forschungszentrum Jülich GmbH, 52425 Jülich, Germany, 2012, 2012.

[8] John B. Goodenough. Perspective on engineering transition-metal oxides. *Chem. of Mat.*, 26(1):820–829, 2014.

[9] G. Binasch, P. Grünberg, F. Saurenbach, and W. Zinn. Enhanced magnetoresistance in layered magnetic structures with antiferromagnetic interlayer exchange. *Phys. Rev. B*, 39:4828–4830, 1989.

[10] M. N. Baibich, J. M. Broto, A. Fert, F. N. Van Dau, F. Petroff, P. Etienne, G. Creuzet, A. Friederich, and J. Chazelas. Giant magnetoresistance of (001)fe/(001)cr magnetic superlattices. *Phys. Rev. Lett.*, 61:2472–2475, 1988.

[11] S. W. Cheong and M. Mostovoy. Multiferroics: a magnetic twist for ferroelectricity. *Nat. Mat.*, 6:13–20, 2007.

[12] D. Khomskii. Classifying multiferroics: Mechanisms and effects. *Phys.*, 2:20, 2009.

[13] S. Dong, J.-M. Liu, S. W. Cheong, and Z. Ren. Multiferroic materials and magneto-electric physics: symmetry, entanglement, excitation, and topology. *Advances in Phys.*, 64(5-6):519–626, 2015.

[14] N. Samarth. Quantum materials discovery from a synthesis perspective. *Nat. Mat.*, 16:10–68–1076, 2017.

[15] R. Dingle, H. L. Störmer, A. C. Gossard, and W. Wiegmann. Electron mobilities in modulation doped semiconductor heterojunction superlattices. *Applied Phys L.*, 33(7):665–667, 1978.

[16] T. Kimura, T. Goto, H. Shintani, K. Ishizaka, T. Arima, and Y. Tokura. Magnetic control of ferroelectric polarization. *Applied Phys. L.*, 426:55–58, 2003.

[17] H. A. Dabkowska and A. B. Dabkowski. *Crystal Growth of Oxides by Optical Floating Zone Technique*, pages 367–391. Springer Berlin Heidelberg, 2010.

[18] Paul C Canfield. New materials physics. *Reports on Progress in Phys.*, 83(1):016501, 2019.

[19] Julian L. Schmehr, Michael Aling, Eli Zoghlin, and Stephen D. Wilson. High-pressure laser floating zone furnace. *Review of Scientific Instruments*, 90(4):043906, 2019.

[20] J. Zhang, H. Zheng, Y. Ren, and J. F. Mitchell. High-pressure floating-zone growth of perovskite nickelate $LaNiO_3$ single crystals. *Crystal Growth & Design*, 17(5):2730–2735, 2017.

[21] Y. M. Klein, M. Kozłowski, A. Linden, P. Lacorre, M. Medarde, and D. J. Gawryluk. $ReNiO_3$ single crystals (RE = Nd, Sm, Gd, Dy, Y, Ho, Er, Lu) grown from molten salts under 2000 bar oxygen-gas pressure. *Crystal Growth and Design*, 2021.

[22] D. Souptel, W. Löser, and G. Behr. Vertical optical floating zone furnace: Principles of irradiation profile formation. *J. Cryst. Growth*, 300(2):538–550, 2007.

[23] G. Behr, W. Löser, N. Wizent, P. Ribeiro, M. O. Apostu, and D. Souptel. Influence of heat distribution and zone shape in the floating zone growth of selected oxide compounds. *J. Mat. Sci.*, 45(8):2223–2227, 2010.

[24] W. Hergett, C. Neef, H. Wadepohl, H.-P. Meyer, M. M. Abdel-Hafiez, C. Ritter, E. Thauer, and R. Klingeler. High-pressure optical floating-zone growth of Li_2FeSiO_4 single crystals. *Journal of Crystal Growth*, 515:37–43, 2019.

[25] Vesta- visualization for crystallographic and structural analysis. `https://jp-minerals.org/vesta/en/download.html`.

[26] `https://en.wikipedia.org/wiki/Ilmenite#cite_note-7`.

[27] T.F.W. Barth and E. Posnjak. The crystal structure of ilmenite. *Zeit für Krist.*, page 265, 1934.

[28] T.F.W. Barth and E. Posnjak. Notes on some structures of the ilmenite type. *Zeit für Krist.*, page 271, 1934.

[29] J. B. Goodenough and J. J. Stickler. Theory of the magnetic properties of the ilmenites $m\text{Tio}_3$. *Phys. Rev.*, 164:768, 1967.

[30] M. E. Lines. Magnetic properties of $CoCl_2$ and $NiCl_2$. *Phys. Rev.*, 131:546–555, 1963.

[31] B. Bleaney and K. W. H. Stevens. Paramagnetic resonance. *Reports on Progress in Phys.*, 16(1):108–159, jan 1953.

[32] Daniel I. Khomskii. *Transition Metal Compounds*. Cambridge University Press, 2014.

[33] J. J. Stickler, S. Kern, A. Wold, and G. Heller. Magnetic resonance and susceptibility of several ilmenite powders. *Phys. Rev.*, 164:765, 1967.

[34] G. Shirane, S.J. Pickart, and Y. Ishikawa. Neutron diffraction study of antiferromagnetic $MnTiO_3$ and $NiTiO_3$. *J. Phys. Soc. Japan*, 14(10):1352–1360, 1959.

[35] R. E. Newnham, J. H. Fang, and R. P. Santoro. Crystal structure and magnetic properties of $CoTiO_3$. *Acta Cryst.*, 17:240–242, 1964.

[36] Y. Yamaguchi, H. Kato, H. Takei, A.I. Goldman, and G. Shirane. Re-examination of the magnetic structure of $FeTiO_3$. *Solid State Comm.*, 59(12):865–868, 1986.

[37] H. Kato, Y. Yamaguchi, M. Ohashi, M. Yamada, H. Takei, and S. Funahashi. On the obliqueness of the easy axis in collinear antiferromagnetic $FeTiO_3$. *Solid State Comm.*, 45(8):669–672, 1983.

[38] M. Charilaou, D. Sheptyakov, J. F. Löffler, and A. U. Gehring. Large spontaneous magnetostriction in $FeTiO_3$ and adjustable magnetic configuration in Fe(III)-doped $FeTiO_3$. *Phys. Rev. B*, 86:024439, Jul 2012.

[39] Johannes Werner. *Experimental studies of Magnetization and Electron spin resonance in transition metal compounds with competing interactions*. PhD thesis, Heidelberg University, 2019.

[40] H. Watanabe, H. Yamauchi, and H. Takei. Magnetic anisotropies in $MTiO_3(M = Co, Ni)$. *J.Magn. Magnetic Mat.*, 15-18:549 − 550, 1980.

[41] K. Dey, S. Sauerland, J. Werner, Y. Skourski, M. Abdel-Hafiez, R. Bag, S. Singh, and R. Klingeler. Magnetic phase diagram and magnetoelastic coupling of $NiTiO_3$. *Phys. Rev. B*, 101:195122, 2020.

[42] B. Yuan, I. Khait, G.-J. Shu, F. C. Chou, M. B. Stone, J. P. Clancy, A. Paramekanti, and Y.-J. Kim. Dirac magnons in a honeycomb lattice quantum *XY* magnet $CoTiO_3$. *Phys. Rev. X*, 10:11062, 2020.

[43] J. J. Stickler and G. S. Heller. Proceedings of the seventh conference on magnetism and magnetic materials. pages 1302–1303, Boston, MA, 1962. Springer US.

[44] J. K. Harada, L. Balhorn, J. Hazi, M. C. Kemei, and R. Seshadri. Magnetodielectric coupling in the ilmenites $MTiO_3$ $(M = Co, Ni)$. *Phys. Rev. B*, 93:104404, 2016.

[45] M. Elliot, P. A. McClarty, D. Prabhakaran, R. D. Johnson, H. C. Walker, P. Manuel, and R. Coldea. Visualization of isospin momentum texture of dirac magnons and excitons in a honeycomb quantum magnet. *arXiv:*, 2007.04199, 2020.

[46] R.S. Singh, T.H. Ansari, R.A. Singh, and B.M. Wanklyn. Electrical conduction in $NiTiO_3$ single crystals. *Mat. Chem. and Phys.*, 40(3):173–177, 1995.

[47] O. Masataka, T. Kiyoaki, M. Fumiyuki, and T. Humihiko. Electron-density distribution in ilmenite-type crystals iii. nickel (ii) titanium (iv) trioxide, $NiTiO_3$. *Mineralogical J.*, 14(4):133–144, 1988.

[48] A. Balbashov, A. Mukhin, V. Ivanov, L. Iskhakova, and M. Voronchikhina. Electric and magnetic properties of titanium-cobalt-oxide single crystals produced by floating zone melting with light heating. *Fiz. Nizk. Temp.*, 43:1200–1206, 08 2017.

[49] H. Takei. Preferentially orientated precipitation in $MnTiO_3$ single crystals. *J. Mat. Sci.*, 16(5):1310–1316, 1981.

[50] H. Yamauchi, H. Hiroyoshi, M. Yamada, H. Watanabe, and H. Takei. Spin flopping in $MnTiO_3$. *J. of Magnetism and Magnetic Mat.*, 31-34:1071–1072, 1983.

[51] J. Akimitsu, Y. Ishikawa, and Y. Endoh. On the two-dimensional antiferromagnetic character of $MnTiO_3$. *Solid State Comm.*, 8(2):87–90, 1970.

[52] C. C. Stephenson and D. Smith. Heat capacity of manganese titanate from 30 to 300 k. *J. of Chemical Phys.*, 49(4):1814–1818, 1968.

[53] J. Akimitsu and Y. Ishikawa. Neutron scattering study of anisotropic spin correlations in quasi two-dimensional antiferromagnet $MnTiO_3$. *Solid State Comm.*, 15(6):1123–1127, 1974.

[54] J. Akimitsu and Y. Ishikawa. Magnetic critical behavior of a quasi two-dimensional antiferromagnet $MnTiO_3$. *J. Phys. Soc. of Japan*, 42(2):462–469, 1977.

[55] Y. Todate, Y. Ishikawa, K. Tajima, S. Tomiyoshi, and H. Takei. Spin dynamics in a quasi-two dimensional antiferromagnet $MnTiO_3$. *J. Phys. Soc. of Japan*, 55(12):4464–4476, 1986.

[56] K. Tajima, Y. Todate, and H. Ikeda. Magnetic excitations in low-dimensional antiferromagnets measured with the max spectrometer. *Physica B: Condensed Matter*, 156-157:301–304, 1989.

[57] J. Akimitsu and H. Yamazaki. Critical behavior of the e.s.r. line widths in a quasi two-dimensional antiferromagnet $MnTiO_3$. *Phys. Let. A*, 55(3):177–178, 1975.

[58] N. Mufti, G. R. Blake, M. Mostovoy, S. Riyadi, A. A. Nugroho, and T. T. M. Palstra. Magnetoelectric coupling in $MnTiO_3$. *Phys. Rev. B*, 83:104416, Mar 2011.

[59] Judy G. Cherian, Takahisa D. Tokumoto, Haidong Zhou, Eun Sang Choi, and Stephen A. McGill. Electronic structure and magnetic symmetry in $MnTiO_3$ analyzed by second harmonic generation. *Phys. Rev. B*, 87:214411, Jun 2013.

[60] V. J. Folen, G. T. Rado, and E. W. Stalder. Anisotropy of the magnetoelectric effect in Cr_2O_3. *Phys. Rev. Lett.*, 6:607–608, Jun 1961.

[61] Y. F. Popov, A. M. Kadomtseva, D. V. Belov, G. P. Vorob'ev, and A. K. Zvezdin. Magnetic-field-induced toroidal moment in the magnetoelectric Cr_2O_3. *J. Exp. and Theo. Phys.*, 69:330–335, 1999.

[62] H. Toyosaki, M. Kawasaki, and Y. Tokura. Atomically smooth and single crystalline $MnTiO_3$ thin films with a ferrotoroidic structure. *Appl. Phys. Let.*, 93(7):072507, 2008.

[63] S. W. Chen, P. A. Lin, H. T. Jeng, S. W. Fu, J. M. Lee, J. F. Lee, C. W. Pao, H. Ishii, K. D. Tsuei, N. Hiraoka, D. P. Chen, S. X. Dou, X. L. Wang, K. T. Lu, and J. M. Chen. Exchange interaction mediated ferroelectricity in multiferroic $MnTiO_3$ with anisotropic orbital hybridization and hole delocalization. *Appl. Phys. Let.*, 104(8):082104, 2014.

[64] H. Murakawa, Y. Onose, S. Miyahara, N. Furukawa, and Y. Tokura. Ferroelectricity induced by spin-dependent metal-ligand hybridization in $Ba_2CoGe_2O_7$. *Phys. Rev. Lett.*, 105:137202, Sep 2010.

[65] C. Jia, S. Onoda, N. Nagaosa, and J. H. Han. Microscopic theory of spin-polarization coupling in multiferroic transition metal oxides. *Phys. Rev. B*, 76:144424, Oct 2007.

[66] R. K. Maurya, N. Singh, S. K. Pandey, and R. Bindu. Evidence of spin lattice coupling in $MnTiO_3$: An x-ray diffraction study. *Europhys. Let.*, 110(2):27007, 2015.

[67] Harlyn J. Silverstein, Elizabeth Skoropata, Paul M. Sarte, Cole Mauws, Adam A. Aczel, Eun Sang Choi, Johan van Lierop, Christopher R. Wiebe, and Haidong Zhou. Incommensurate crystal supercell and polarization flop observed in the magnetoelectric ilmenite $MnTiO_3$. *Phys. Rev. B*, 93:054416, 2016.

[68] H. Liu, J. Chaloupka, and G. Khaliullin. Kitaev spin liquid in $3d$ transition metal compounds. *Phys. Rev. Lett.*, 125:047201, 2020.

[69] H. Liu and G. Khaliullin. Pseudospin exchange interactions in d^7 cobalt compounds: Possible realization of the kitaev model. *Phys. Rev. B*, 97:014407, Jan 2018.

[70] H. Takagi, T. Takayama, G. Jackeli, G. Khaliullin, and S. E. Nagler. Concept and realization of kitaev quantum spin liquids. *Nat. Rev. phys.*, 1:264–280, 2019.

[71] J. Zaanen, G. A. Sawatzky, and J. W. Allen. Band gaps and electronic structure of transition-metal compounds. *Phys. Rev. Lett.*, 55:418–421, 1985.

[72] R. Zhong, T. Gao, N. P. Ong, and R. J. Cava. Weak-field induced nonmagnetic state in a co-based honeycomb. *Science Advances*, 6(4), 2020.

[73] M. Songvilay, J. Robert, S. Petit, J. A. Rodriguez-Rivera, W. D. Ratcliff, F. Damay, V. Balédent, M. Jiménez-Ruiz, P. Lejay, E. Pachoud, A. Hadj-Azzem, V. Simonet, and C. Stock. Kitaev interactions in the co honeycomb antiferromagnets $Na_3Co_2SbO_6$ and $Na_2Co_2TeO_6$. *Phys. Rev. B*, 102:224429, Dec 2020.

[74] E. Lefrançois, M. Songvilay, J. Robert, G. Nataf, E. Jordan, L. Chaix, C. V. Colin, P. Lejay, A. Hadj-Azzem, R. Ballou, and V. Simonet. Magnetic properties of the honeycomb oxide $Na_2Co_2TeO_6$. *Phys. Rev. B*, 94:214416, 2016.

[75] C. Wong, M. Avdeev, and C. D. Ling. Zig-zag magnetic ordering in honeycomb-layered $Na_3Co_2SbO_6$. *J. of Solid State Chem.*, 243:18–22, 2016.

[76] S. Shivam, R. Coldea, R. Moessner, and P. McClarty. Neutron scattering signatures of magnon weyl points. *arXiv1712.08535*, 2017.

[77] S Catalano, M Gibert, J Fowlie, J Íñiguez, J-M Triscone, and J Kreisel. Rare-earth nickelates $RNiO_3$: thin films and heterostructures. *Reports on Progress in Phys.*, 81(4):046501, feb 2018.

[78] María Luisa Medarde. Structural, magnetic and electronic properties of RNiO$_3$ perovskites (R = rare earth). *Journal of Phys.: Cond. Mat.*, 9(8):1679–1707, 1997.

[79] G. Catalan. Progress in perovskite nickelate research. *Phase Transitions*, 81(7-8):729–749, 2008.

[80] G. Demazeau, A. Marbeuf, M. Pouchard, and P. Hagenmuller. Sur une série de composés oxygènes du nickel trivalent derivés de la perovskite. *J. of Solid State Chem.*, 3(4):582–589, 1971.

[81] P. Lacorre, J.B. Torrance, J. Pannetier, A.I. Nazzal, P.W. Wang, and T.C. Huang. Synthesis, crystal structure, and properties of metallic PrNiO$_3$: Comparison with metallic NdNiO$_3$ and semiconducting SmNiO$_3$. *J. of Solid State Chem.*, 91(2):225–237, 1991.

[82] J A Alonso, A Muñoz, A Largeteau, and G Demazeau. Crystal growth of NdNiO$_3$ perovskite under high oxygen pressure. *J. of Phys.: Cond. Mat.*, 16(14):S1277–S1281, mar 2004.

[83] S. Middey, J. Chakhalian, P. Mahadevan, J.W. Freeland, A.J. Millis, and D.D. Sarma. Physics of ultrathin films and heterostructures of rare-earth nickelates. *Annual Review of Materials Research*, 46(1):305–334, 2016.

[84] J.-S. Zhou, L. G. Marshall, and J. B. Goodenough. Mass enhancement versus stoner enhancement in strongly correlated metallic perovskites: LaNiO$_3$ and LaCuO$_3$. *Phys. Rev. B*, 89:245138, Jun 2014.

[85] K. Sreedhar, J. M. Honig, M. Darwin, M. McElfresh, P. M. Shand, J. Xu, B. C. Crooker, and J. Spalek. Electronic properties of the metallic perovskite LaNiO$_3$: Correlated behavior of 3d electrons. *Phys. Rev. B*, 46:6382–6386, Sep 1992.

[86] X. Q. Xu, J. L. Peng, Z. Y. Li, H. L. Ju, and R. L. Greene. Resisitivity, thermopower, and susceptibility of RNiO$_3$ (R = La, Pr). *Phys. Rev. B*, 48:1112–1118, 1993.

[87] J. L. García-Muñoz, J. Rodríguez-Carvajal, P. Lacorre, and J. B. Torrance. Neutron-diffraction study of RNiO$_3$ (R = La, Pr, Nd, Sm): Electronically induced structural changes across the metal-insulator transition. *Phys. Rev. B*, 46:4414–4425, Aug 1992.

[88] A Wold, B Post, and E Banks. Rare earth nickel oxides. *Journal of the American Chemical Society (U.S.)*, 79, 9 1957.

[89] B. Li, D. Louca, S. Yano, L. G. Marshall, J. Zhou, and J. B. Goodenough. Insulating pockets in metallic LaNiO$_3$. *Advanced Electronic Mat.*, 2(2):1500261, 2016.

[90] J. Shamblin, M. Heres, H. Zhou, S. Joshua, L. Maik, N. Joerg, J. A. Alonso, and H. John-ston. Experimental evidence for bipolaron condensation as a mechanism for the metal-insulator transition in rare-earth nickelates. *Nat. Comm.*, 9:86, 2018.

[91] Alaska Subedi. Breathing distortions in the metallic, antiferromagnetic phase of $LaNiO_3$. *Sci Post*, 5:020, 2018.

[92] H. Guo, Z. W. Li, L. Zhao, Z. Hu, C. F. Chang, C. Y. Kuo, W. Schmidt, A. Piovano, T. W. Pi, O. Sobolev, D. I. Khomskii, L. H. Tjeng, and A. C. Komarek. Antiferromagnetic correlations in the metallic strongly correlated transition metal oxide $LaNiO_3$. *Nat. Commun.*, 9(1):43, 2018.

[93] R. D. Sánchez, M. T. Causa, A. Caneiro, A. Butera, M. Vallet-Regí, M. J. Sayagués, J. González-Calbet, F. García-Sanz, and J. Rivas. Metal-insulator transition in oxygen-deficient $LaNiO_{3-x}$ perovskites. *Phys. Rev. B*, 54:16574–16578, 1996.

[94] J.M. González-Calbet, M.J. Sayagués, and M. Vallet-Regí. An electron diffraction study of new phases in the $LaNiO_{3-x}$ system. *Solid State Ionics*, 32-33:721–726, 1989.

[95] Toshihiro Moriga, Osamu Usaka, Tomomi Imamura, Ichiro Nakabayashi, Ichiro Matsub-ara, Tsuneo Kinouchi, Shinichi Kikkawa, and Fumikazu Kanamaru. Synthesis, crystal structure, and properties of oxygen-deficient lanthanum nickelate $LaNiO_{3-x}$ ($0 \leq x \leq 0.5$). *Bulletin of the Chemical Society of Japan*, 67(3):687–693, 1994.

[96] Bi-Xia Wang, S. Rosenkranz, X. Rui, Junjie Zhang, F. Ye, H. Zheng, R. F. Klie, J. F. Mitchell, and D. Phelan. Antiferromagnetic defect structure in $LaNiO_{3-x}$ single crystals. *Phys. Rev. Mat.*, 2(6), 2018.

[97] S.M. Koohpayeh, D. Fort, and J.S. Abell. The optical floating zone technique: A review of experimental procedures with special reference to oxides. *Progress in Cryst. Growth and Characterization of Mat.*, 54(3):121–137, 2008.

[98] SCIDRE. High-pressure high-temperature optical floating zone furnace hkz. `https://scidre.de/index.php?id=12`, 2009.

[99] Crystal Impact. Match! phase analysis using powder diffraction. `http://www.crystalimpact.com/match/`.

[100] Bruker. Diffrac.eva. `https://www.bruker.com/content/bruker/int/en/products-and-solutions/diffractometers-and-scattering-systems/x-ray-diffractometers/diffrac-suite-software/diffrac-eva.html`.

[101] J. R. Carvajal. Recent advances in magnetic structure determination by neutron powder diffraction. *Physica B: Cond. Mat.*, 192(1):55–69, 1993.

[102] FIZ Karlsruhe. Icsd. `https://icsd.products.fiz-karlsruhe.de/`.

[103] Christian Linkenheld. Axio scope.a1. `https://www.mikroskopie.de/?page_id= 225`.

[104] H. Zheng, B.-X. Wang, D. Phelan, J. Zhang, Y. Ren, M. J. Krogstad, S. Rosenkranz, R. Osborn, and J. F. Mitchell. Oxygen inhomogeneity and reversibility in single crystal $LaNiO_{3-\delta}$. *Crystals*, 10(7), 2020.

[105] Photonic Science. Psl viewer. `https://photonicscience.com/products/ laue-crystal-orientation-system/`.

[106] Clip- cologne laue indexation program. `http://clip4.sourceforge.net/`.

[107] Qauntum Design. Magnetic property measurement system. `https://qd-europe.com/ de/en/product/mpms3-squid-magnetometer/`.

[108] Qauntum Design. Mpms 3 horizontal rotator option user's manual. `https:// qd-europe.com/de/en/product/mpms3-squid-magnetometer/`.

[109] Qauntum Design. Physical property measurement system. `https://qd-europe.com/ de/en/product/mpms3-squid-magnetometer/`.

[110] Institut Laue-Langevin. D10- single-crystal four-circle diffractometer with three-axis energy analysis. `https://www.ill.eu/users/instruments/instruments-list/ d10/description/instrument-layout`.

[111] T. Roisnel and J. Rodríguez-carvajal. Winplotr: a windows tool for powder diffraction analysis. In *Materials Science Forum. Proceedings of the European Powder Diffraction Conf. (EPDIC 7)*, 2001.

[112] K. Dey, S. Sauerland, B. Ouladdiaf, K. Beauvois, H. Wadepohl, and R. Klingeler. Magnetostructural coupling in ilmenite-type $NiTiO_3$.

[113] K. Dey, W. Hergett, P. Telang, M. M. Abdel-Hafiez, and R. Klingeler. Magnetic properties of high-pressure optical floating-zone grown $LaNiO_3$ single crystals. *Journal of Crystal Growth*, 524:125157, 2019.

[114] R.M. Dubrovin, N.V. Siverin, M.A. Prosnikov, V.A. Chernyshev, N.N. Novikova, P.C.M. Christianen, A.M. Balbashov, and R.V. Pisarev. Lattice dynamics and spontaneous magnetodielectric effect in ilmenite $CoTiO_3$. *J. Alloys Compd.*, page 157633, 2020.

[115] B. Yuan, M. B. Stone, G.-J. Shu, F. C. Chou, X. Rao, J. P. Clancy, and Y.-J. Kim. Spin-orbit exciton in a honeycomb lattice magnet $CoTiO_3$: Revealing a link between magnetism in d- and f-electron systems. *Phys. Rev. B*, 102:134404, 2020.

[116] A. Ito, H. Kawano, H. Yoshizawa, and K. Motoya. Magnetic properties and phase diagram of $Ni_xMn_{1-x}TiO_3$. *J. Magn. and Magnetic Mat.*, 104-107:1637–1638, 1992.

[117] J. Zhang, H. Zheng, Y.-S. Chen, Y. Ren, M. Yonemura, A. Huq, and J. F. Mitchell. High oxygen pressure floating zone growth and crystal structure of the metallic nickelates $R_4Ni_3O_{10}$ $(R = La, Pr)$. *Phys. Rev. Materials*, 4:083402, 2020.

[118] D. Li, K. Lee, B. Y. Wang, M. Osada, S. Crossley, H. R. Lee, Y. Cui, Y. Hikita, and H. Y. Hwang. Superconductivity in an infinite-layer nickelate. *Nat.*, 572:624–627, 2019.

[119] J. Zhang and X. Tao. Review on quasi-2d square planar nickelates. *Crystal Eng. Comm.*, 23:3249–3264, 2021.

[120] Michael E. Fisher. Relation between the specific heat and susceptibility of an antiferromagnet. *The Philosophical Magazine: A J. of Theor. Exp. and Appl. Phys.*, 7(82):1731–1743, 1962.

[121] I. Y. Hwang, K. H. Lee, J.-H. Chung, K. Ikeuchi, V. O. Garlea, H. Yamauchi, M. Akatsu, and S. Shamoto. Spin wave excitations in honeycomb antiferromagnet $MnTiO_3$. *J. Phys. Soc. of Japan*, 90(6):064708, 2021.

[122] C. Zhou, J. Wang, X. Liu, F. Chen, Y. Di, S. Gao, and Q. Shi. Magnetic and thermodynamic properties of α, β, γ and δ-MnO_2. *New J. Chem.*, 42:8400–8407, 2018.

[123] I. Jacobs. Evidence for triangular moment arrangements in $MO·Mn_2O_3$. *J. of Phys. and Chem. of Solids*, 11:1–11, 1959.

[124] D. Rout, S. R. Mudi, M. Hoffmann, S. Spachmann, R. Klingeler, and S. Singh. Structural and physical properties of trilayer nickelates $R_4Ni_3O_{10}$ $(R = La, Pr, and Nd)$. *Phys. Rev. B*, 102:195144, 2020.

Acknowledgements